



Development of thermal energy harvesting systems

Natalia Salamon

► To cite this version:

Natalia Salamon. Development of thermal energy harvesting systems. Electric power. Université Grenoble Alpes; Politechnika Łódzka, 2018. English. NNT : 2018GREAI011 . tel-01797966

HAL Id: tel-01797966

<https://theses.hal.science/tel-01797966>

Submitted on 23 May 2018

HAL is a multi-disciplinary open access archive for the deposit and dissemination of scientific research documents, whether they are published or not. The documents may come from teaching and research institutions in France or abroad, or from public or private research centers.

L'archive ouverte pluridisciplinaire **HAL**, est destinée au dépôt et à la diffusion de documents scientifiques de niveau recherche, publiés ou non, émanant des établissements d'enseignement et de recherche français ou étrangers, des laboratoires publics ou privés.

THÈSE

Pour obtenir le grade de

DOCTEUR DE LA COMMUNAUTÉ UNIVERSITÉ GRENOBLE ALPES

Spécialité : MEP : Mécanique des fluides Energétique, Procédés
Arrêté ministériel : 25 mai 2016

Présentée par

Natalia SALAMON

Thèse dirigée par **Simon PERRAUD**, chef de Projet CEA Grenoble

préparée au sein du **Laboratoire CEA
Grenoble/LITEN/DTNM/SERE/LRME**

dans l'École Doctorale I-MEP2 – Ingénierie - Matériaux, Mécanique,
Environnement, Energétique, Procédés, Production

Developpement de systèmes de récupération d'énergie thermique

Development of thermal energy harvesting systems

Thèse soutenue publiquement le **24 janvier 2018**,
devant le jury composé de :

Monsieur Frédéric LEFEVRE

Professeur, INSA de Lyon, Rapporteur

Monsieur Luc FRECHETTE

Professeur, Université de Sherbrooke, Rapporteur

Monsieur Daniel BELLET

Professeur, Université de Grenoble Alpes, Président

Monsieur Paul MURALT

Professeur, École Polytechnique Fédérale de Lausanne, Examineur

Monsieur Simon PERRAUD

Ingénieur de Recherche, CEA Grenoble, Directeur de thèse

Monsieur Ulrich SOUPREMANIEN

Ingénieur de Recherche, CEA Grenoble, Examineur



Acknowledgements	1
Introduction	1
1. STATE OF THE ART	3
1.1. WASTE ENERGY RECOVERY	3
1.2. ENERGY HARVESTING SOURCES	4
1.3. ENERGY HARVESTING METHODS	5
1.3.1. Mechanic energy conversion: development of kinetic transducers	5
1.3.1.1. Electrostatic energy conversion: capacitive transducers	5
1.3.1.2. Magnetic energy conversion based on Faraday's Law	7
1.3.1.3. Energy conversion based on piezoelectric effect: piezoelectric transducers	8
1.3.2. Electromagnetic energy conversion: development of photovoltaic and RF transducers	10
1.3.2.1. Solar energy conversion: photovoltaic transducers	10
1.3.2.2. Energy conversion based on rectifying antenna: RF transducers	13
1.3.3. Thermal energy conversion	14
1.3.3.1. Carnot cycle	14
1.3.3.2. Thermoelectric generators: Seebeck Effect	14
1.3.3.3. MEMS-based micro heat engines	18
1.3.3.4. Vapor-based generator operating due to micro-vibrations	21
1.3.3.5. Pulsating Heat Pipes	22
1.3.3.6. Concept of thermal energy transducer applying two-phase energy conversion	24
1.4. SUMMARY OF THE CHAPTER	27
2. ELECTROMECHANICAL CONVERSION APPLYING PIEZOELECTRIC MATERIALS	28
2.1. HISTORICAL DEVELOPMENT AND APPLICATIONS OF PIEZOELECTRIC MATERIALS	28
2.2. CLASSIFICATION OF PIEZOELECTRIC MATERIALS	29
2.2.1. Inorganic piezoelectric materials	29
2.2.2. Organic piezoelectric materials	33
2.2.3. Piezoelectric composites	33
2.3. ELECTRO-MECHANICAL PROPERTIES OF PIEZOELECTRIC MATERIALS	34
2.3.1. Boundary conditions	34
2.3.2. Properties of piezoelectric materials and piezoelectric coefficients	34
2.3.2.1. Elastic properties and coefficients of piezoelectric materials	35
2.3.2.2. Electrical properties and coefficients of piezoelectric materials	36
2.3.3. Piezoelectric equations	40
2.4. SUMMARY OF THE CHAPTER	41
3. ANALYSIS OF PIEZOELECTRIC CONVERTERS EXPOSED TO PULSE OF PRESSURE	42
3.1. EXPERIMENTAL SETUP DESCRIPTION	42
3.2. ANALYSIS OF FLEXIBLE PVDF TRANSDUCERS	45
3.2.1. Electrical response of PVDF to the pressure pulse: cantilever mode	45

TABLE OF CONTENTS

3.2.2.	Electrical response of PVDF to the pressure pulse: strain mode.....	47
3.2.3.	Comparison of PVDF films operating in cantilever and strain mode	52
3.3.	ANALYSIS OF CIRCULAR PIEZOELECTRIC CERAMICS PZT	52
3.3.1.	Piezoelectric material determination	54
3.3.2.	Electrical response of PZT to the pressure pulse: stress mode.....	56
3.3.3.	Electrical response of PZT to the pressure pulse: strain mode.....	58
3.3.4.	Comparison of PZT-based ceramics operating in stress and strain mode.....	60
3.4.	COMPARISON BETWEEN PVDF AND PZT-BASED TRANSDUCERS.....	61
3.5.	NUMERICAL MODELING	61
3.5.1.	Comparison between simulation and experimental results	62
3.5.2.	Size optimization.....	64
3.5.2.1.	Influence of PZT thickness.....	65
3.5.2.2.	Influence of PZT radius.....	67
3.5.2.3.	Miniaturization	67
3.6.	SUMMARY OF THE CHAPTER	69
4.	CONCEPT OF A THERMAL ENERGY CONVERTER BASED ON PHASE- CHANGE PHENOMENON	71
4.1.	THE PROTOTYPES APPLYING PHASE-CHANGE PHENOMENON TO HARVEST THERMAL ENERGY 71	
4.1.1.	Microfluidic heat engine based on explosive boiling.....	71
4.1.2.	Self-Oscillating Fluidic Heat Engine (SOFHE)	74
4.1.3.	Thermo-mechanical oscillating system at macroscale	76
4.2.	CONCEPT OF THE SILICON-BASED DEMONSTRATOR IN MICROSCALE	80
4.2.1.	Technological challenges	81
4.2.1.1.	Type of the working fluid.....	81
4.2.1.2.	Channel design	83
4.2.1.3.	Filling ratio.....	88
4.2.1.4.	Hot surface temperature	91
4.2.1.5.	Type of piezoelectric.....	92
4.3.	SUMMARY OF THE CHAPTER	93
5.	TECHNOLOGICAL REALIZATION OF THE SILICON-BASED DEMONSTRATOR	95
5.1.	SELECTION OF TECHNOLOGICAL PROCESSES.....	96
5.1.1.	Silicon etching process.....	96
5.1.1.1.	Dry etching approach	96
5.1.1.2.	Wet etching approach	97
5.1.2.	Surface wettability.....	103
5.1.3.	Silicon bonding	106
5.1.3.1.	Wafer preprocessing.....	107
5.1.3.2.	Silicon bonding techniques	107
5.1.3.3.	Adhesive bonding.....	108

5.1.4.	PZT montage – challenges and limitations	110
5.2.	PROCESS FLOW OF ENERGY HARVESTER FABRICATION	111
5.3.	SUMMARY OF THE CHAPTER	113
6.	CHARACTERIZATION OF THE PROTOTYPE STRUCTURES	114
6.1.	PARAMETERS OF INFLUENCE: HIERARCHY OF IMPORTANCE.....	115
6.1.1.	Ranking of the parameters.....	115
6.2.	PRELIMINARY EXPERIMENTS	116
6.2.1.	Determining the working conditions ensuring oscillation mechanism	116
6.2.1.1.	Fixed parameters: device structure.....	116
6.2.1.2.	Variable parameters: oscillations nature	118
6.2.2.	Working conditions summary	120
6.3.	OPERATION OF THE DEVICE WITH A COOLING SYSTEM.....	120
6.3.1.	Uncertainty analysis and experimental repeatability.....	120
6.3.2.	Experimental setup description	120
6.3.3.	Electric response to the pressure pulses	122
6.3.3.1.	Impact of T_H for 10% filling ratio	122
6.3.3.2.	Impact of T_H for 20% filling ratio	124
6.3.3.3.	Impact of T_H for 30% filling ratio	127
6.3.3.4.	Summary of the experiments.....	128
6.4.	OPERATION OF THE DEVICE WITHOUT A COOLING SYSTEM	129
6.5.	SUMMARY OF THE CHAPTER	132
	Conclusions	133
	Appendix A	137
	Appendix B	139
	Appendix C	141
	Bibliography.....	147
	List of figures	152
	List of tables.....	157

Acknowledgements

The research presented in this manuscript is the result of a cooperation between STMicroelectronics, Lodz University of Technology, CEA-Liten and University of Grenoble Alpes and a number of people contributed to this work.

In the first place I would like to thank the committee members for their valuable comments and suggestions, as well as for the lively and interesting discussion during the viva.

I would like to thank professor Zbigniew Lisik from Lodz University of Technology for entrusting me with this work, for his scientific support and our long discussions.

I am very grateful to Simon Perraud from CEA-Liten for accepting the responsibility of supervising this work despite his numerous commitments, his great advice regarding the direction of the project and the final presentation. I would also like to thank him for his moral support in the difficult moments of this challenging work.

I would like to address the special acknowledgements to Ulrich Soupremanien from CEA-Liten for his mentoring, all the fruitful discussions, and the willingness to share his knowledge. I am very grateful for his availability, trust and most of all, for his kindness and friendship.

I would like to thank Stéphane Monfray from STMicroelectronics for his support, supervising, understanding and culturally rich collaboration. I am thankful also for his inestimable help in navigating through the formal complexities of an international collaboration.

I would like to express my sincere gratitude to Thomas Skotnicki from STMicroelectronics for giving me the chance to work in a cutting edge environment for an eye-opening experience. I would like to thank him for all his help throughout the duration of this PhD and for motivating discussions that allowed me to improve.

I am grateful also to Emmanuel Ollier from CEA-Liten for his warm welcome, positive energy, and friendly atmosphere in the lab.

I would like to thank Łukasz Ruta from the Department of Semiconductor and Optoelectronics Devices of TUL for passing me all the knowledge regarding silicon technology, the number of hours spent in clean room, and all his contribution to the technological ideas and solutions used in this work. His friendship made it easier to overcome the challenges faced during this time.

I am grateful to Roman Gozdur from Lodz University of Technology for sharing his huge knowledge and experience in the field of electronics, many practical ideas regarding experimental setups development and for discovering together a domain totally new to both of us... energy harvesting.

Many thanks to Marcin Turczyński from Lodz University of Technology for our friendship, and for all the reports and documents always delivered on time even when I was far.

I am grateful also to Adam Miklaszewski from Lodz University of Technology for his technical support and for not being afraid of fabricating even the craziest of my designs.

To all the colleagues from Lodz University of Technology Ewa, Kasia, Marysia, Emilia, Agnieszka, Natalia, Zbyszek, Maciek, Andrzej, Tomek, Jacek, Bartek, Janusz, Marek thank you for your support, positive energy and the good atmosphere that made each working day much brighter.

ACKNOWLEDGEMENTS

Finally, I would like to thank my family from the bottom of my heart - my parents and brother who always believed in me and encouraged to work further, and my husband Onoriu for his patience, understanding, and both emotional and scientific support.

Introduction

The research presented in this manuscript has been focused on the domain of energy harvesting that has received recently a great deal of interest in the scientific community. The trend of continuous miniaturization of integrated circuits and the huge progress in wireless communication, as well as the rising availability of Ultra-Low Power devices, led to the development of the devices that generate small amounts of electrical energy from their ambient, without a contribution of any additional power source. There is a number of energy sources that exist in the environment and in the proximity to human, and they can be classified by the type of provided energy. Amongst kinetic, electromagnetic and thermal energy, the one that is the most easily available and can be used for low power electronic supply is kinetic energy. Due to the high energy density and high efficiency of power conversion, the kinetic transducers operating based on piezoelectric effect have been identified as interesting for energy harvesting applications.

The present work was aimed at the development of a thermal energy harvesting device that operates applying piezoelectric conversion. There are several systems working based on thermal energy conversion in the domain of energy harvesting. The most well-known amongst them, are these applying Seebeck effect. However, despite the undoubted advantages of these thermoelectric generators, they have also some drawbacks, mainly related to the materials of which they are composed. First of all, they must exhibit at the same time high electric conductivity and low thermal conductivity, which are the parameters of an opposite nature. Additionally, some of the materials can be expensive, rare and harmful to the environment. Moreover, it is necessary to enhance the thermal characteristics of the thermoelectric generators by using heat sinks, which exclude them from the small-scaled applications. Hence, the question: is it possible to fabricate a device that does not apply Seebeck effect and is able to harvest thermal energy, arises.

The goal of this work was to design and fabricate a pressure oscillating device of small dimensions – up to 2 cm of diameter and 2 mm of thickness, applying liquid to gas phase-change phenomenon, which is capable of generating electrical energy from a constant source of heat by means of piezoelectric transducer. Additionally, the device should be characterized by a simplicity of construction, ease of manufacture with the conventional equipment and common materials. Moreover, it should not contain any moving parts. The additional advantage would be the operation without an enhancement of a cooling system. To face these requirements and to open out wide perspectives of the device implementation in variety of silicon microsystems, the well-known, conventional silicon technology has been selected.

The concept proposed in this work implied two steps of energy conversion: firstly thermal energy should be converted into mechanic energy by means of abrupt evaporation and condensation of a working fluid, resulting in a local overpressure, transformed in a second step into electrical energy by means of a piezoelectric element. The uniqueness of this concept consisted in the first step of conversion being the result of a cyclic evaporation and condensation of a working fluid enclosed in a micro-confinement.

INTRODUCTION

The design process of the prototype included establishment of the device's geometry, a bonding method of several silicon wafers of the device, as well as a working fluid and a piezoelectric element selection.

1. State of the art

1.1. Waste energy recovery

Nowadays a large amount of energy is wasted every day by car exhaust, household appliances and, most of all, by a number of industrial facilities and limitations of the power conversion processes. The United States Department of Energy informs that even 50% of energy coming from fuels burned in U.S., used for power generation in conventional power plants, is wasted and transferred thereafter to the atmosphere in a form of heat [1]. The largest losses are related to the heating processes and involve exhaust and fuel gasses, heated air, thermoelectric generation, steam leaks, heat exchangers, cooling liquids and gasses, furnaces, hot surfaces, turbines, engines etc. Figure 1.1 shows the energy losses in diverse industrial sectors, which were estimated by Energetics Incorporated for U.S. Department of Energy, Industrial Technology Programs [2].

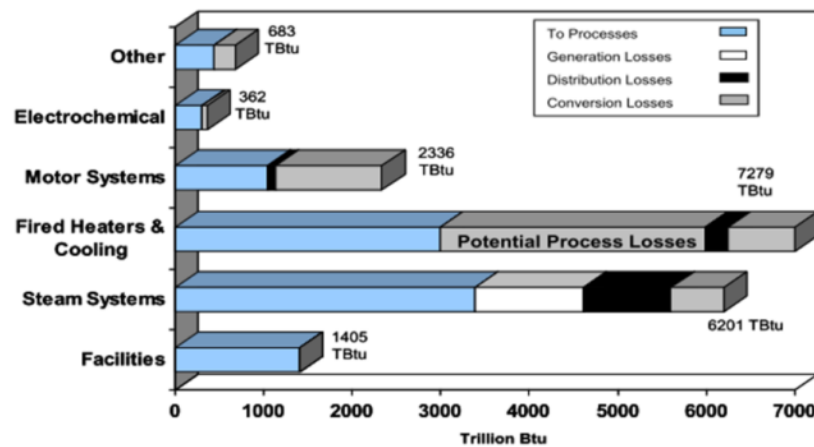


Figure 1.1: Estimation of energy losses for major energy use areas in manufacturing [2].

Taking into account the limited sources of energy and at the same time the continuously increasing demand for the industrial products, the great efforts have been done to develop more efficient, sustainable and economical technologies of energy conversion. As a result, the costs and the use of fuel decrease with the simultaneous rise of productivity. Additionally, efficient use of energy impacts positively on the environment by reducing pollutants emission. An economic method of increasing the overall efficiency of the industrial systems is known as Waste Heat Recovery. During this process the waste heat is recuperated and used afterwards, depending on the application, for the processes such as heating or clean energy generation. According to the research, the energy loose from industry could fulfill up to 20% of domestic electricity need and result in 20% reduction of greenhouse gas emissions [1,3].

Another approach of using waste energy, but in smaller scale, is energy harvesting. In this process various forms of energy, normally dissipated and lost in the environment, are extracted and converted into electricity that can be employed afterwards to supply the electronic devices of low power consumption [4]. Nowadays, the evolution of electronics is heading towards

miniaturization. At the same time the power consumption of diverse electronic devices decreases. Recently, the most developing field of electronics is focused on mobile devices, hence one of the key features studied by industry is autonomy. From this point of view energy harvesting is a very promising technique as it ensures mobility and it could be a base for the development of alternative or additional power supplies [5]. The main drawback of this method is, that the energy generated by environmental sources is relatively low, variable and often unpredictable. Nevertheless, the significant improvement in efficiency of integrated circuits and raising availability of Ultra Low Power (ULP) systems led to the increased interest in the devices that generate small amounts of electrical energy from their ambient, without any additional power source [6]. Currently, ULP devices can be supplied with power in the range of several dozen and several hundreds of microwatts. In order to maintain them in stand-by mode, less than $1\text{ }\mu\text{W}$ is required [4,6]. As an example, less than 100 nW is enough to maintain ARM (Advanced RISC Machine) core, developed by ARM Silicon, in stand-by mode and $600\text{ }\mu\text{W/MHz}$ allows to perform its continuous operation [9]. In such cases, the possibility of powering electronic circuits by conventional batteries or energy harvesting devices appears [10]. Another system that could be supplied by energy harvesting devices is Wireless Sensor Network (WSN) that is the network constituted by a large number of autonomous sensors communicating between each other and monitoring the environmental conditions. This system is undoubtedly interesting and promising, as it can be used in many areas such as health monitoring or smart buildings, its application however is challenging mainly due to a requirement of a large number of batteries. Due to the fact that the WSN can contain thousands of nodes installed very often in isolated areas, using conventional batteries that have limited lifetime can be troublesome. Hence, in order to supply these systems, it is desired to replace the batteries with the alternative power sources. Taking into account that one WSN node typically consumes only up to $100\text{ }\mu\text{W}$ in an operation mode, the use of energy harvesters as supplies appears to be promising [11]. As an example, a wireless pulse oximeter sensor developed by Torfs et al. [12] requires approximately $89\text{ }\mu\text{W}$ for a 15 second measurement interval and it can be fully powered by watch-style thermoelectric generator. Moreover, it turns out that in order to measure and transmit temperature value every 5 seconds $10\text{ }\mu\text{W}$ is nowadays sufficient [13].

The benefits derived from the development of energy harvesting techniques stay not only in new technological opportunities but also in the fact that they are more environmentally friendly as compared to conventional batteries.

1.2. Energy harvesting sources

The number of research conducted in the domain of energy harvesting showed, that there is no universal energy source and its choice strongly depends on the application of energy harvesting device. The diverse energy sources that exist in the environment and in the vicinity of human can be classified according to the type of energy that they provide - typically mechanical, electromagnetic or thermal, coming either from natural or industrial sources. The examples of possible sources depending on the type of provided energy [11,12] are listed in Table 1.1.

Table 1.1: Examples of energy sources depending on the type of provided energy.

Type of energy	Possible sources of energy	
	Natural	Industrial
Mechanical	wind, air, water flow, ocean currents, human body (e.g.: while walking or running)	all sources of mechanical vibrations, stresses and strains that come from machines
Electromagnetic	EM waves, RF signals, acoustic waves, sunlight	inductors, coils, transformers, indoor room light
Thermal	temperature gradient, heat of human body	heat energy variations from furnaces, heaters, chillers, fans, friction sources, car engines

1.3. Energy harvesting methods

1.3.1. Mechanic energy conversion: development of kinetic transducers

One of the most attractive and easily available energy that can be used for supplying low power electronic devices is kinetic energy coming from mechanical vibrations, air and water flow or human activity. Kinetic energy harvesting is based on the mechanical deformation or on the displacement of a moving element, contained inside the converter.

Taking into consideration their mechanical construction, two classes of kinetic transducers can be specified: internal and non-internal. In the first type of the converter, kinetic energy is generated by the vibrations or the displacement of a proof mass, and the energy obtained in this process depends on this mass. It has to be taken into account that the devices applying spring-mass system resonate at a particular frequency and, in order to obtain the maximum value of energy, the vibrations must occur at this resonance. Therefore, the main problem that appears with a process of the device miniaturization is an increase of the resonance frequency that significantly exceeds the characteristic frequencies of most of the mechanical energy sources. In case of non-internal converters, the pressure is applied by an external element and it is transformed into a form of elastic energy, causing a deformation that is further converted into electrical energy by a piezoelectric material. Obtained energy does not depend on the mass of the transducer but on its deformation. The parameters playing the significant role in the value of produced energy are geometric dimensions and material constraints such as Young's Modulus [16]. There are three mechanisms that can be applied to convert kinetic energy into electricity: piezoelectric, electrostatic and magnetic [17].

1.3.1.1. Electrostatic energy conversion: capacitive transducers

In electrostatic energy harvesters, known also as capacitive transducers, the generation of energy occurs due to a movable converter that changes its position against an electric field. The main element of the electrostatic harvester is a variable capacitor with one electrode fasten to an oscillating mass that is suspended by beams. In response to a force applied to the mass, a change either in dielectric gap (in case of an in-plane gap-closing converter) or in the overlap surface (for an overlap varying converter) takes place. To compensate the bias voltage, the

capacitance changes and the additional charges gather on the electrodes [17]. Figure 1.2a-b) shows a schematic of the comb gap-closing and the overlap electrostatic energy harvesters, respectively.

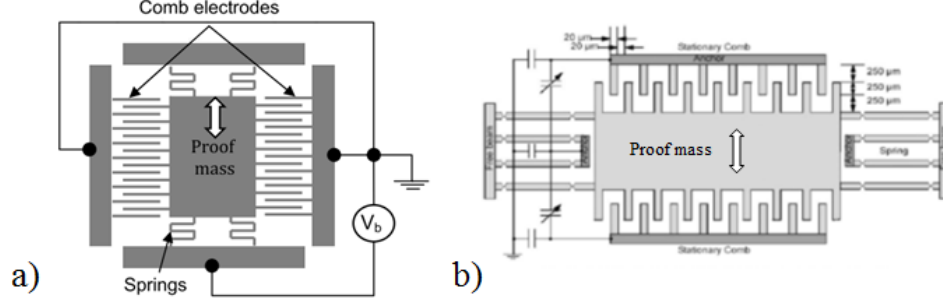


Figure 1.2: (a) Comb gap-closing and (b) overlap electrostatic energy harvester [17].

There are two types of electrostatic energy harvesting devices: electret-free and electret-based converters. The transducers from the first group, work based on the conversion cycles of charging and discharging of the capacitor and they require an active electronic circuit that can apply the charge cycle to the structure [18]. In case of constant charge accumulated in the capacitor and accompanying decrease of the capacitance, the value of voltage rises. This can be obtained either by the reduction of an overlap between the plates or by the increase of a distance between them. When the voltage on the capacitor is constant and the capacitance decreases, the charge rise occurs. The most common cycles enabling the conversion of mechanical energy into electricity are charge-constrained and voltage-constrained cycles shown in Figure 1.3.

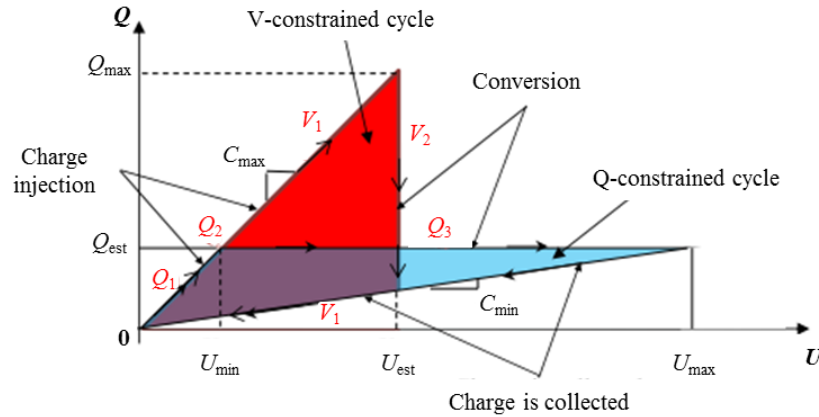


Figure 1.3: Charge-constrained and voltage-constrained energy conversion cycles for electret-free electrostatic devices [18].

Both conversion cycles start when the capacitance of the device is at maximum. At this point the capacitor is charged by a voltage source to an initial value, in order to polarize it. The energy harvested in the process is given by the total path of the cycle [16].

One of the most significant drawback of the electret-free electrostatic harvester is the requirement of an external supply source ensuring the capacitor pre-charging. The alternative solution that enables to overcome this issue, is to add to one or two plates of the capacitor and the electret layers that are electrically charged. This enables to avoid the energy cycles and gives the possibility of converting mechanical energy directly into electricity. This is the second group of electrostatic energy harvesters, so-called electret-based converters [18].

The power generated by the capacitive transducers at a centimeter scale stands at the values between $1 \mu\text{W}/\text{cm}^3$ and $10 \mu\text{W}/\text{cm}^3$ for the frequencies in the range of 10 Hz. However, the best properties of these transducers are observed in microscale when the electromechanical coupling is improved due to the augmented electric field [19].

1.3.1.2. Magnetic energy conversion based on Faraday's Law

The principle of magnetic energy harvesters is based on Faraday's Law, according to which the changes of magnetic flux Φ_B through an electric circuit result in electric field generation. This law can be expressed by Eq.(1.1):

$$\varepsilon = - \frac{d\Phi_B}{dt} \quad \text{Eq.(1.1)}$$

where ε is the electromotive force. Typically, this kind of converter works in two configurations and it consists either a movable magnet and a static coil or a fixed magnet, whose flux is linked with a movable coil.

Figure 1.4 shows the model of a simple magnetic induction transducer in which a relative displacement of an oscillating mass is converted into electrical energy.

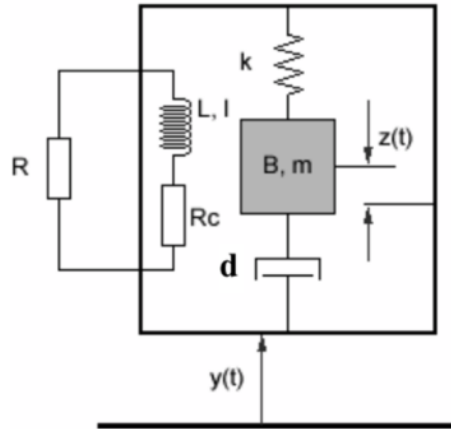


Figure 1.4: The model of the magnetic induction transducer [20].

In terms of a frequency bandwidth and an optimal load, these converters present complementary behavior as compared to the piezoelectric transducers and they are recommended for low frequency, small impedance and medium size applications. Most of the commercially

available devices are made at a centimeter scale [17]. The main drawback of these devices is their low output voltage that requires a rectification. Moreover, a volumetric energy density decreases at low scale.

The volumetric power density generated by these converters equals to around $100 \mu\text{W}/\text{cm}^3$ at the frequency range of 100 Hz and it depends on the acceleration caused by the vibrations and the movable mass [6].

1.3.1.3. Energy conversion based on piezoelectric effect: piezoelectric transducers

Piezoelectric transducers convert mechanical energy into electric charge based on direct piezoelectric effect that is a phenomenon during which certain materials being exposed to mechanical stress produce an electric field. This occurs due to a movement of the atoms in the crystals' molecules. The atoms forming the piezoelectric compounds have either gained or lost electrons, which means that the piezoelectric crystals are composed of positive and negative ions in an alternating fashion. Due to a mechanical deformation, these ions move away from each other resulting in an energy gradient across the crystal. This leads to a generation of a potential difference between the opposite surfaces of the material. The output piezoelectric voltage is a function of stress. Figure 1.5a-b) shows a simplified schematic of two configurations of silicon and oxygen ions inside the quartz: when there is no stress applied to the crystal and when it is exposed to the external force, respectively. In the first case, all the charges are compensated due to a symmetry of ions location. In the second case, the application of stress results in a lattice deformation and the charges of different signs appear on the opposite sides of the material.

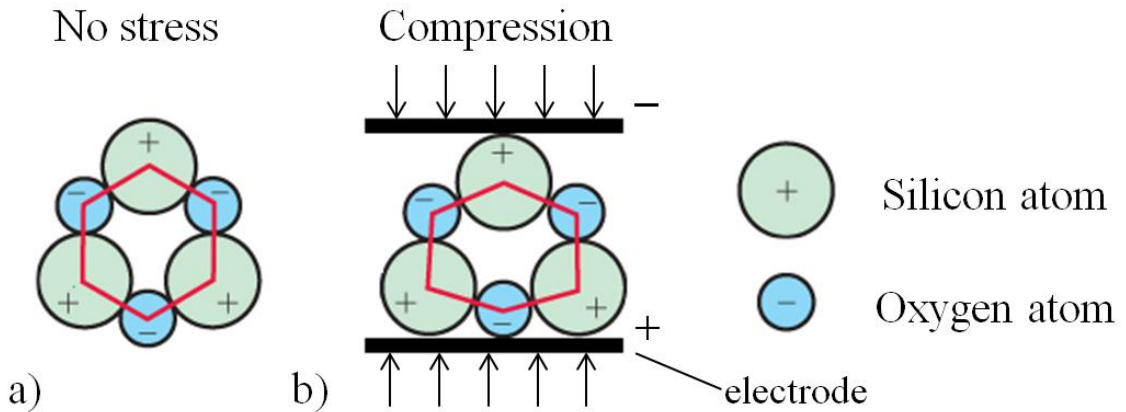


Figure 1.5: Simplified configuration of silicon and oxygen ions inside the quartz (a) when there is no stress applied to the crystal; (b) when the crystal is exposed to the stress.

Piezoelectric materials show also the converse effect, where the mechanical deformation in the crystal is caused by the application of an electric field. The volumetric power density generated by the piezoelectric transducers stands at the value of about $100 \mu\text{W}/\text{cm}^3$ for the frequencies of around 50 Hz [6].

The reason of increasing interest in energy harvesters operating based on piezoelectric effect is their high energy density in comparison with electrostatic and electromagnetic generators [21], as well as their high power conversion efficiency and relatively simple operating mechanism [22]. Due to their high electromechanical coupling coefficients, the most often used piezoelectric materials for energy harvesting applications are generally ceramics, amongst which easily available PZT (Lead Zirconate Titanate) is the best known. The most common applications of piezoelectric structures in electromechanical transducers use a geometry of a cantilever beam with one end fixed, piezoelectric thin layer deposited on its surface and an additional tip mass that regulates the frequency of random vibrations of a system (Figure 1.6).

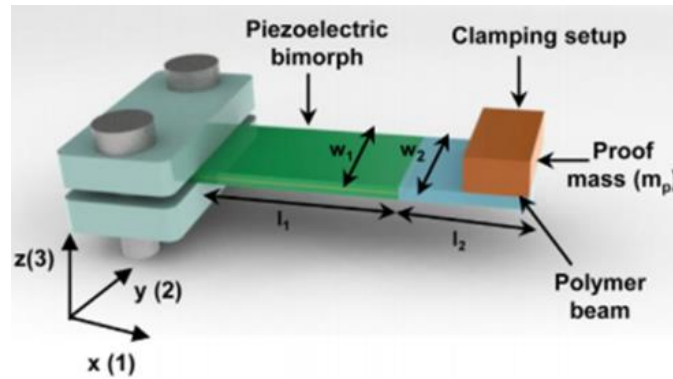


Figure 1.6: Design of a piezoelectric energy harvester working in a form of a cantilever beam [23].

Although the cantilever construction is the most commonly used in piezoelectric converters, more and more often the other geometries are considered. These are typically low-cost, widely available piezoelectric diaphragms consisted of a cylinder-shaped PZT layer mounted on a metal substrate [24].

The optimum energy for piezoelectric materials is obtained in a narrow frequency bandwidth, close to their resonance frequency, which in most cases, is comprised within the range of kHz and vary depending on the configuration, size and loading conditions [25]. The main drawback of using piezoelectric materials for energy harvesting applications consists in an irregular nature of ambient vibration sources and their low frequency. As a consequence, each application requires a dedicated energy harvesting device. The resonance frequency of the piezoelectric transducer can be lowered in several ways. One of the method is to increase a diameter of the element. Figure 1.7 shows the size influence on the value of resonance frequency for circular unimorph and bimorph PZT-based structures composed of one and two PZT layers. The parameters changed during the experiment were the diameters of the metal support and the PZT layer. The diameter of PZT was always 2.5 mm lower than the metal layer diameter. The results presented in Figure 1.7 show that the frequency decreased by one order of magnitude when the diameter of the whole structure raised four times. Another way to reduce the resonance frequency, which is shown in Figure 1.7, is to add more piezoelectric layers to the transducer, creating a multimorph structure [15].

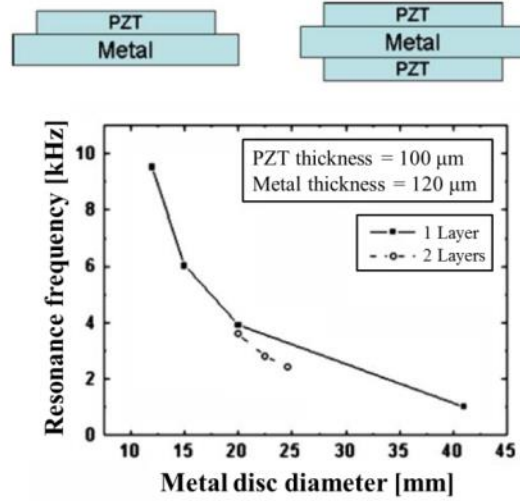


Figure 1.7: Resonance frequency evolution regarding the circular diaphragm diameter [15].

Despite the undoubted advantages of piezoelectric systems, such as their ability of high voltage generation, and their high power density per unit of volume, there are several inconveniences that become significant for the microscale devices. First of all, it has to be taken into account that with miniaturization the piezoelectric coupling decreases drastically and in order to reach the optimal working point, large load impedances are necessary. Moreover, the phenomena of aging, depolarization and fragility of the material should be considered. Recently, the piezoelectric materials that are receiving more and more interest, especially for low frequency applications, are piezoelectric thin films PVDF (polyvinylidene fluoride) especially due to their flexibility and durability. These features make them attractive for such applications like e.g.: wearable sensors [17].

1.3.2. Electromagnetic energy conversion: development of photovoltaic and RF transducers

1.3.2.1. Solar energy conversion: photovoltaic transducers

Currently, one of the most widely used sources of energy is light. The energy coming from the sun or from the devices producing artificial light is converted into electricity with the usage of photovoltaic cells. A typical structure of a single solar cell is composed of p-type and n-type semiconductor layers with two metal contacts and a barrier layer with space-charge region placed between them. The schematic of a silicon-based solar cell and the principle of its operation are presented in Figure 1.8. When the light illuminates the silicon p-n junction from the top of the cell, a separation of photons into negatively charged electrons and positively charged holes occurs. This enables the electrons to move freely to the second level, and as a result, the electrons and holes are separated by the space-charge region. The electrons are further collected by the front contacts of the cell. When the two electrodes are connected to an external load, the electrons flow through the circuit and the electricity is created.

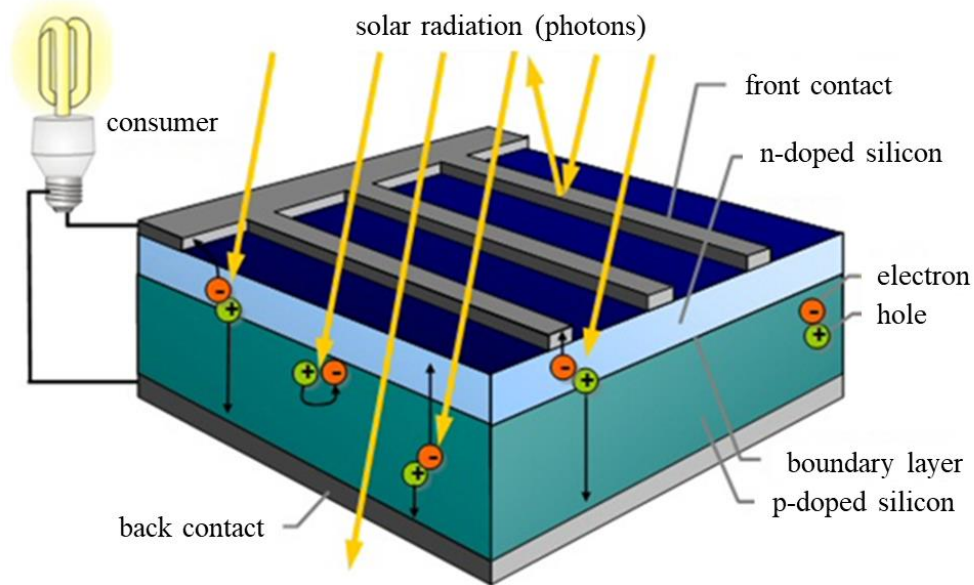


Figure 1.8: The principal structure of a single solar cell [26].

It has to be taken into account that when the photon energy is too low, the separation of the electron from the hole is not possible. On the other hand, when the energy is too high only some part of this energy is required to enable the separation of the particles. Hence, many photons are either reflected or pass through the cell [26].

The amount of energy harvested from the light strongly depends on an insolation. For instance, in full sun, the density of luminous power stays at around 100 mW/cm^2 , whereas the power density given by an artificial light source comprises in the range of $10\text{-}100 \text{ }\mu\text{W/cm}^2$. A solar module with 15% of efficiency can provide 15 mW/cm^2 of power when it is exposed to the sunlight. Table 1.2 shows the dependence of luminous and electric power density on the different lighting conditions.

Table 1.2: Luminous power density and electric power density provided by a single solar cell with 15% of efficiency [27].

Conditions	Luminous power density [mW/cm ²]	Electric power density [mW/cm ²]
Full sun	100.0	15.0
Hazy sun	50.0	7.5
Cloudy sky	5.0-20.0	0.75-3.00
Indoors - artificial light source	0.1-1.5	0.015-0.225
Indoors – office	0.5	0.075
Night	0.0	0

The information placed in Table 1.2 shows, that solar panels are the efficient energy harvesting devices adapted to the applications working in luminous areas.

Due to the fact that the light is an easily accessible source of energy and that solar cells produce relatively high power as compared to the other ambient energy harvesting devices, they can be used for the wide range of applications, and they can supply both ultra-low power devices, e.g.: wireless sensor nodes, as well as high power batteries [28].

The efficiency of photovoltaic cells depends not only on the lighting conditions but also on the fabrication technology. The most common technologies are based on silicon and, in general, the efficiency of such a module is not higher than 20%. The solution alternative to silicon is the application of III-IV compounds. Due to the fact that they can be made in diverse compositions, their energy gap varies between 0.16 eV and 2.24 eV. This means that their junctions can be sensible to several parts of the solar spectrum, and as a result, they are characterized by high light absorption and high efficiency. In recent years, one could observe a rising interest in solar cells based on organic materials. Although their efficiency that currently stays at around 11%, is still relatively low, they present a very desirable feature of long lifetime.

Another interesting alternative to the standard photovoltaic cells are the structures based on photo electrochemical technology. Their main advantage is a flexible construction that opens up new opportunities for diverse applications. The module developed by EPFL presents 14,1% of efficiency [19]. Figure 1.9 depicts the time evolution of photovoltaic cells efficiency depending on their fabrication technology [NREL].

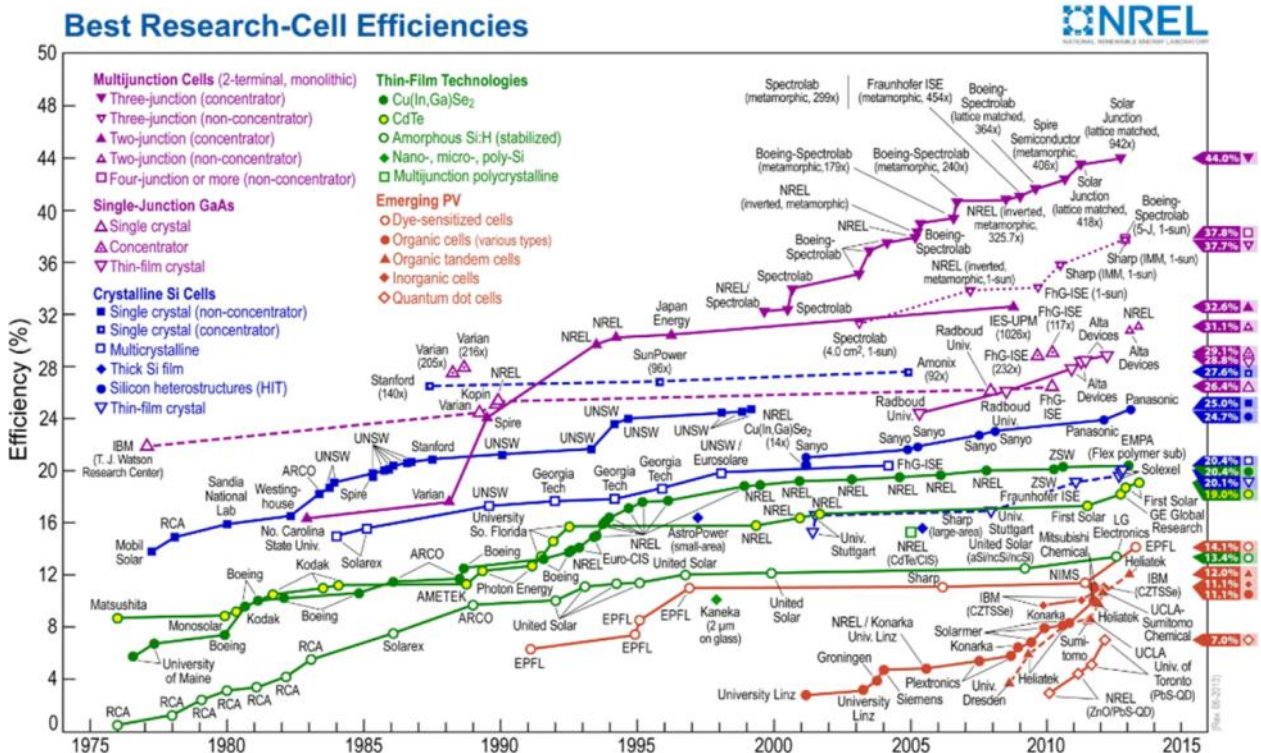


Figure 1.9: Time evolution of photovoltaic cells efficiency depending on their fabrication technology [NREL].

1.3.2.2. Energy conversion based on rectifying antenna: RF transducers

These energy harvesting devices extract the energy from radio frequency (RF) electromagnetic waves. Radio waves that are the part of electromagnetic spectrum, carry the information thanks to the change of amplitude, phase and frequency combination of the wave within a frequency band. The contact of electromagnetic radiation with a conductor, such as antenna, results in a generation of an electric current on the surface of the conductor [29].

Although, compared to the other energy harvesting techniques, RF transducers present the lowest energy density, the accessibility of ubiquitous radio views in proximity to humans, especially in big, crowded agglomerations, make them attractive for supplying low-power electronics. A few examples of the radiation sources, such as television set, radio, mobile phone, wireless LAN, etc. as well as the principle of typical RF energy harvesting system are shown in Figure 1.10a-b), respectively.

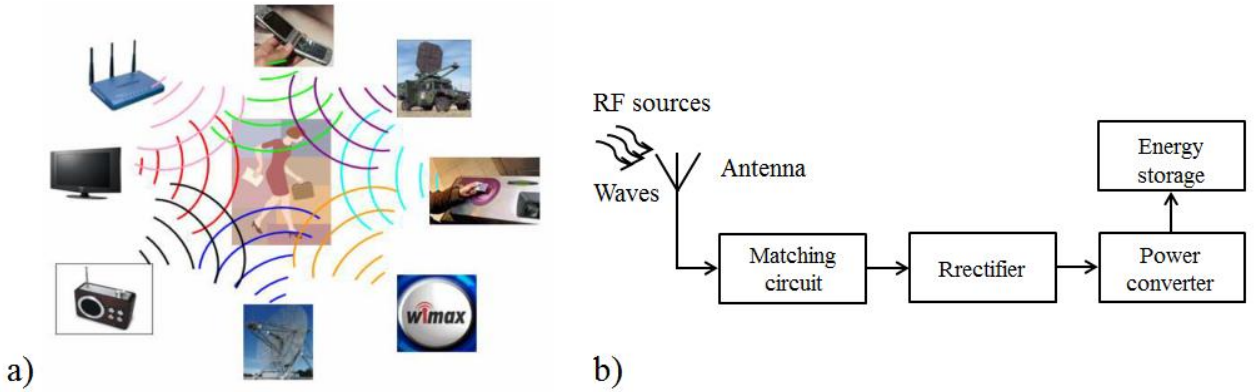


Figure 1.10: (a) Diverse sources of radio waves [30]; (b) principle of a typical RF energy harvesting system.

When the signal generated by the radiation source is collected by the antenna, it passes through a matching circuit, a rectifier and a power converter that generates the voltage necessary to charge an energy storage system. In order to recover all the signals available in the ambience, and as a result, to maximize the efficiency of the system, typically the omni-directional broadband antennas are used [29].

The power densities of these transducers strongly depend on the RF source, as well as on the distance between the source and the antenna, and they are relative low, standing at around $100 \mu\text{W}/\text{cm}^2$, which imposes an application of a large surface receiving antenna [31].

The comparison of capacitive, magnetic, piezoelectric, photovoltaic and RF transducers in terms of electric power density is given in Table 1.3. It has to be taken into consideration that these values vary depending on the working conditions, as well as on the size and mechanical construction of each converter.

Table 1.3: Electric power density provided by different energy transducers.

Type of energy conversion	Type of the transducer	Power density
Mechanical	Capacitive	1-10 $\mu\text{W}/\text{cm}^3$; at $f = 10$ Hz
	Magnetic	100 $\mu\text{W}/\text{cm}^3$; at $f = 100$ Hz
	Piezoelectric	100 $\mu\text{W}/\text{cm}^3$; at $f = 50$ Hz
Electromagnetic	Photovoltaic	15-15000 $\mu\text{W}/\text{cm}^2$
	RF	100 $\mu\text{W}/\text{cm}^2$

1.3.3. Thermal energy conversion

1.3.3.1. Carnot cycle

Each thermodynamic system that passed through a series of different states to finally return to its initial state, performs a thermodynamic cycle. While going through this cycle, the system makes the work on its surroundings acting as a heat engine. The ideal heat engine cycle allowed by physical laws, so-called Carnot cycle, consists of two isothermal and two adiabatic processes. This cycle is a theoretical thermodynamic cycle that provides a formula enabling to determine the maximum efficiency, η , that can be achieved by every thermodynamic engine during a process of heat to work conversion. If the maximum hot temperature reached by the working fluid is given by T_H and T_C is the coldest temperature during the cycle, the efficiency of the heat conversion can be calculated from Eq.(1.2).

$$\eta = \frac{T_H - T_C}{T_H} \quad \text{Eq.(1.2)}$$

The Carnot cycle assumes that the process performed during the heat engine cycle is reversible and that no changes of entropy occur. Due to the fact that in practice a fully reversible engine processes do not exist and all physical processes involve an entropy increase, the Carnot cycle is a theoretical construct. However, it gives a possibility of establishing the highest value of efficiency for any engine cycle operating between hot, T_H , and cold, T_C , temperatures.

1.3.3.2. Thermoelectric generators: Seebeck Effect

One of the most popular methods of converting thermal energy into electricity is based on Seebeck effect that is related to a spatial temperature gradient. The value of electric power generated during the conversion depends on a temperature difference, as well as on a material forming the structure. The Seebeck effect occurs when the junction of two different conductive materials, whose endings are placed at the ambient temperature, is subjected to a source of heat. Due to the fact that the charge carriers migrate from the hot temperature zones towards the cold zones, a potential difference appears resulting in an electromotoric force generation. As the best thermoelectric properties are observed in semiconductors, a typical structure of the generator operating on the grounds of Seebeck effect is composed of two semiconductor bars, where one is doped with n and another with p carriers. Placing this structure between the hot and cold sources

and loading it with a resistance, leads to an electric current generation [32]. The principle of Seebeck effect and Seebeck generator composed of pn junction are schematically illustrated in Figure 1.11a-b).

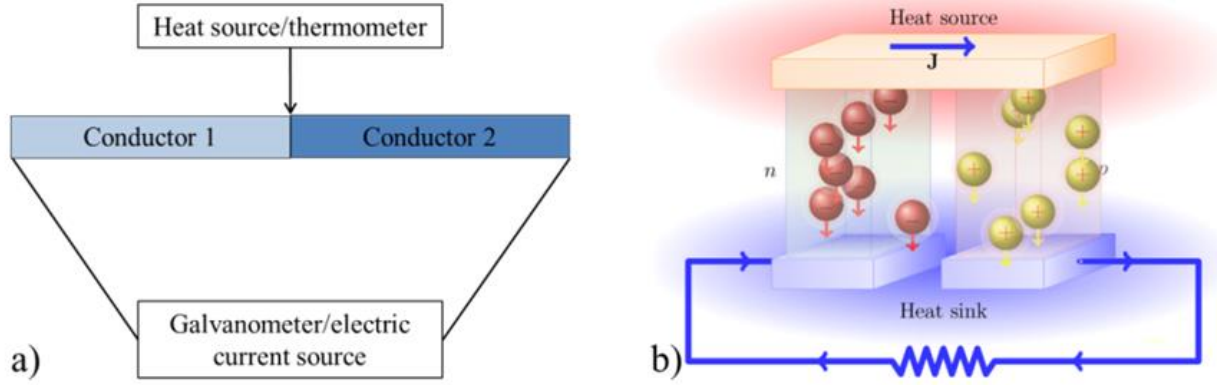


Figure 1.11: (a) Principle of Seebeck effect; (b) pn junction thermoelectric generator [33].

This configuration given in Figure 1.11a) is commonly used in thermocouples due to the fact that the generated voltage is proportional to the temperature difference accordingly to Eq.(1.3).

$$V = \alpha_{AB} \cdot \Delta T \quad \text{Eq.(1.3)}$$

where α_{AB} is a Seebeck coefficient of the junction. The current intensity is expressed by Eq.(1.4).

$$I = \frac{(\alpha_p - \alpha_n)(T_H - T_C)}{R_p R_n R_L} \quad \text{Eq.(1.4)}$$

where α_p and α_n are the Seebeck coefficients of p and n material, respectively; R_p and R_n are the resistances of these materials; R_L is the load resistance; T_H and T_C are the temperatures of a hot and a cold source, respectively.

The electric power that represents a part of the heat flux that passes through the structure is given by Eq.(1.5) and it depends on the thermoelectric properties of the material, as well as on the load resistance.

$$P = I^2 R_L = \left[\frac{(\alpha_p - \alpha_n)(T_H - T_C)}{R_p R_n R_L} \right]^2 R_L \quad \text{Eq.(1.5)}$$

The maximum possible thermoelectric efficiency is given by Eq.(1.6).

$$\eta = \frac{\sqrt{1 + ZT} - 1}{\sqrt{1 + ZT} + \frac{T_C}{T_H}} \cdot \frac{T_H - T_C}{T_H} \quad \text{Eq.(1.6)}$$

where $(T_H - T_C)/T_H$ is the Carnot efficiency. In the efficiency expression of the thermoelectric energy conversion, the combination of the conductors properties, such as electrical and thermal conductivities and Seebeck coefficient, is known as a figure of merit, ZT . In order to optimize this parameter, expressed by Eq.(1.7), for the whole structure of the generator, it is mandatory to optimize the figures of merit, z , related to each material separately, which is described by Eq.(1.8).

$$ZT = \frac{(\alpha_p - \alpha_n)^2}{(\sqrt{k_{tp}\rho_p} + \sqrt{k_{tn}\rho_n})^2} T_m \quad \text{Eq.(1.7)}$$

$$z = \frac{\alpha^2}{k_t \rho} \quad \text{Eq.(1.8)}$$

where T_m is the mean of the hot and cold temperature; k_t is the thermal conductivity and ρ is electrical resistivity of a semiconductor material [19].

To increase the figure of merit z , it is necessary to reduce thermal conductivity of the material and at the same time to increase its electrical conductivity. As these two tendencies are contradicting, the enhancement of the generator properties is a challenge. In general, the heat transfer through the material can occur by means of electrons or phonons. The materials that express a good electric conduction due to the presence of electrons are metals. This is a positive effect in terms of thermoelectric generators. The same electrons however are the reason of high heat conduction, which means that the conductive materials are characterized by both, good electrical and thermal conductivity at the same time. As a consequence, the figure of merit of the conductors is not sufficient for energy harvesting applications. On the other hand, the electrical insulators, such as glass, present desirably low thermal conductivity, including the conductivity by phonons, but their electrical conductivity is close to zero. Thus, the ideal material for thermal generators should combine the electrical properties of metals and the heat resistance of insulators. The compromise has been reached by using semiconductor materials that present relatively high electrical and relatively low thermal conductivity. The figure of merit for semiconductors can be maximized by the control of the dopant concentration, as it is shown in Figure 1.12a). Given that the physical properties of thermoelectric materials depend also on the temperature, the figure of merit expresses the maximum value at the specific range of temperatures, which is illustrated in Figure 1.12b). It is worth to note that n-doped materials might present the optimal performances for different ranges of temperatures than the same materials doped by p-type carriers. The most efficient n-type material for the applications operating at the temperatures close to ambient is tellurium of bismuth, Bi_2Te_3 , and its figure of

merit ZT is close to 1. The p-type material that is the most suitable for the ambient temperatures is tellurium of antimony Sb_2Te_3 . Other materials commonly used in the thermoelectric generators are $\text{Bi}_2(\text{Te}_{0.8}\text{Se}_{0.2})$ and $(\text{Sb}_{0.8}\text{Bi}_{0.2})_2\text{Te}_3$ operating at temperatures of 200°C and 600°C , and the alloys of silicon germanium SiGe dedicated for temperatures higher than 600°C .

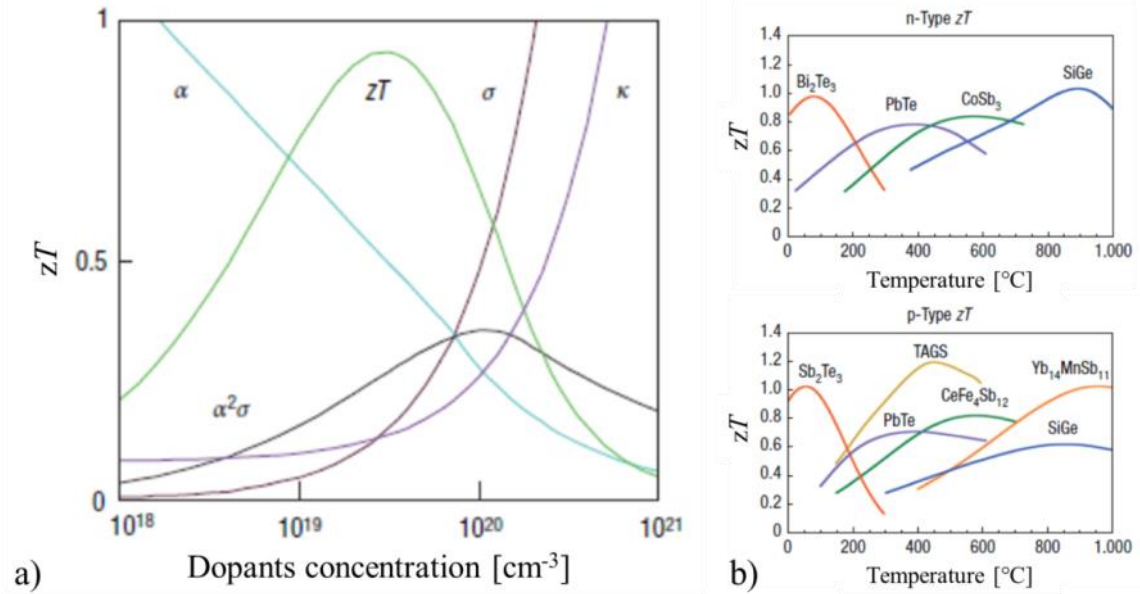


Figure 1.12: (a) The evolution of Bi_2Te_3 figure of merit zT in a function of dopants concentration; (b) figure of merit of different thermoelectric materials in temperature function [34].

Despite the indisputable advantages of thermal generators based on Seebeck effect, they express some inconveniences, especially due to the physical properties of applied thermoelectric materials:

- most of the competitive materials, such as tellurium or antimony, can pose a health risk due to their high toxicity,
- tellurium, amongst other drawbacks, is extremely rare,
- the alloy of SiGe , which is composed of easily available and safe materials, does not present the interesting thermoelectric properties except from the possibility of operating at very high temperatures. It is therefore difficult to find a thermoelectric material that can operate in low temperatures and at the same time is not dangerous for the environment,
- mechanical properties of the thermoelectric materials resemble the ones of the ceramics, which means that the forces to which they can be submitted are limited, hence the structures are fragile,
- the modules are not flexible and their surfaces are relatively large, in the range of centimeters. Thus, in order to reduce the cost of the production, less efficient materials are used [19],
- maintaining a high temperature difference between hot and cold sides of the device is very challenging.

In order to ensure a sufficient temperature gradient enabling the operation of the module a heat sink is required [34]. This makes the whole structure much larger, which exclude its application in limited spaces. The research focused on a thermal conductivity reduction of the thermoelectric materials concerns mainly the mechanism based on phonons. This is due to the fact that thermal conduction generated by electrons is inevitable. This domain is barely investigated and requires the understanding of fundamental physics of conductivity as well as developing the materials of complex chemical compositions, which makes the production process more expensive [35].

All these drawbacks of the thermoelectric materials lead to the research of the devices that could be fabricated in both small and large scales, which are flexible and the production costs are not too high.

1.3.3.3. MEMS-based micro heat engines

Whalen et al. [36] developed a P^3 micro heat engine that was one of the first MEMS dynamic heat engines driven by an external heat source, operating on the grounds of expansion and compression of a two-phase working fluid. A unit-cell device, given schematically in Figure 1.13, was composed of a silicon membrane with a thin PZT-based component, a middle spacer containing a 60 μm thick cavity and a silicon membrane with a resistance heater. The cavity was filled with two-phase working fluid 3MTM PF5060DL. The heat was alternately conducted in and out of the system.

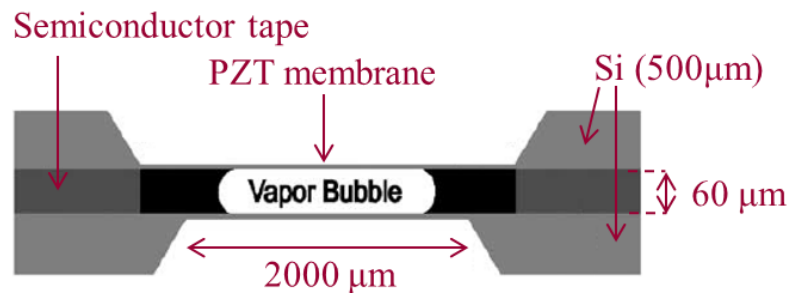


Figure 1.13: Cross-section of a unit-cell micro heat engine prototype [36].

The mechanism of the device operation occurred in 4 steps that are schematically depicted in Figure 1.14:

- 1) The heat was conducted into the working fluid through the silicon membranes.
- 2) The volume of saturated mixture increased, performing mechanical work and as a consequence, the piezoelectric film deformed acting as a generator.
- 3) The heat was conducted out from the device.
- 4) The volume of the working fluid decreased, deforming the piezoelectric film, which resulted in a charge generation.

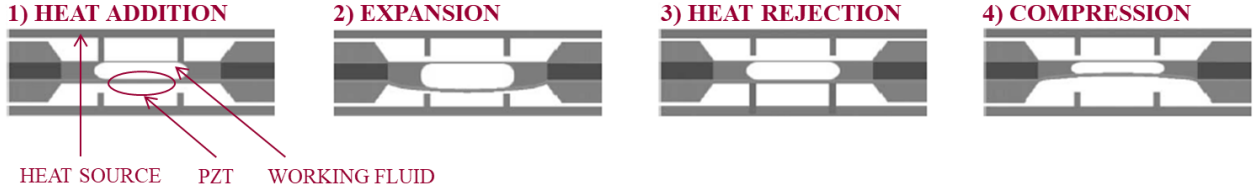


Figure 1.14: Working cycle of unit-cell micro heat engine [36].

In order to characterize the dynamics of the micro heat engine, the authors applied a resistance heater to the device. The heater was electrically pulsed by means of a square wave, with a controllable voltage amplitude, frequency and pulse width. When the micro heat engine operated in its resonance frequency of 240 Hz, the open-circuit voltage varied between 63 mV and 135 mV, as presented in Figure 1.15a). A peak power generated by the system reached its maximum for 14 k Ω load resistance and it was equal to 0.8 μ W. The power dependence on the load resistance is depicted in Figure 1.15b).

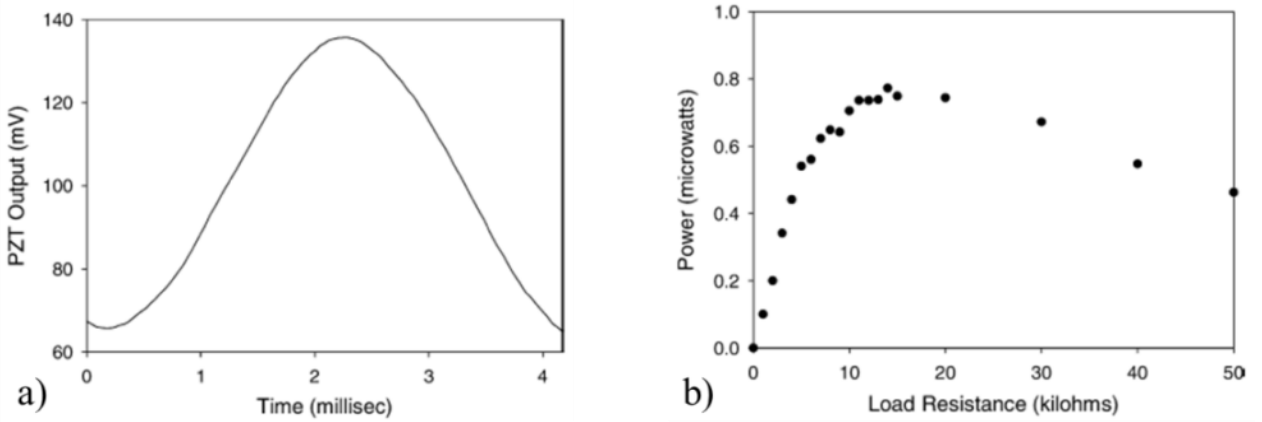


Figure 1.15: (a) Open-circuit voltage versus time and (b) power dependence on the load resistance generated by the micro heat engine [36].

The system could be composed either of a unit-cell engine or the array comprising many unit-cell engines, which gave a great flexibility in terms of its assembly and power generation. Although the results presented by the authors were very interesting, the main drawback of this solution consists in the fact that in order to drive the micro heat engine, an external pulse circuit and a power supply was required.

Huegsen et al. [37] proposed a micro heat engine fabricated in silicon technology, which operated based on a bistable membrane and a phase-change of a working fluid enclosed inside a cavity. The system placed between a heat source and a heat sink was composed of the cavity filled with methoxy-nanofluorobutane $C_4F_9OCH_3$, known as HFE7100, playing the role of the fluid, a thermal insulating layer, a mechanically bistable membrane and a mechanical connector. The device operated in two mechanically stable states – “down-state” and “up-state”. The full cycle, illustrated in Figure 1.16, occurred in 4 steps:

1) In “down-state” the device was in contact with the heat source, as shown in Figure 1.16a). Heat was transferred into the chamber, resulting in thermal expansion of the working fluid enclosed in the device.

2) When a defined threshold pressure was exceeded inside the chamber, the device snapped into the “up-state” position, as shown in Figure 1.16b), due to strongly nonlinear behavior of the bistable membrane.

3) The heat was rejected to the heat sink and pressure inside the working fluid decreased.

4) When the value of pressure inside the chamber dropped below a threshold pressure, the device came back to the “down-state” position and the cycle repeated.

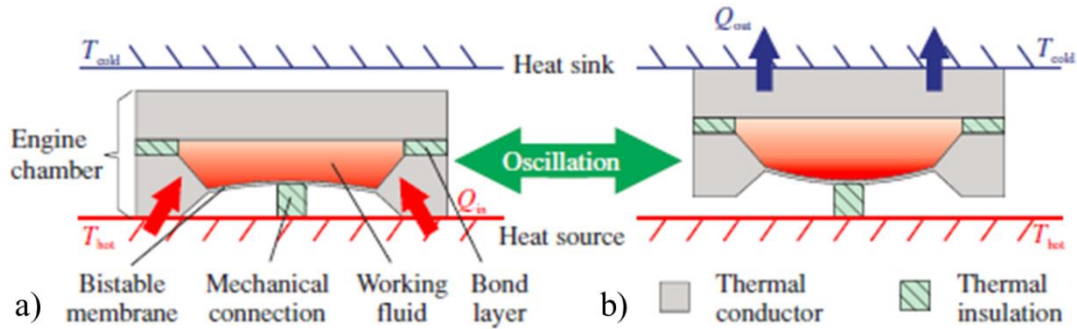


Figure 1.16: Schematic cross-section of the micro heat engine operating in (a) “down-state” and (b) “up-state”[37].

In the first stage of their study the authors simulated the behavior of the system in a thermal network model implemented in P-Spice. This allowed determining the operation frequency and the mechanical output power of the engine, depending on the temperature difference. Accordingly to the simulations, the maximum frequency of 0.72 Hz could be obtained for a temperature difference of 37 K and the mechanical output power should be equal to 1.29 μ W. The theoretical model was confirmed by the experiments that resulted in the value of frequency equal to 0.71 Hz. The main challenge regarding this micro heat engine was related to a complicated fabrication process and a critical step of a final assembly. Moreover, the results presented by the authors referred only to the mechanical power of the engine and no solution enabling its conversion into electricity had been applied to the system.

Formosa et al. performed thorough analysis aimed at defining scaling laws for FPSE (free piston Stirling engines) that are characterized by relatively simple construction and high thermodynamic performance. The authors selected the FPSE for their study on miniaturization due to its simple construction and the lack of a complex kinematic linkage. Additionally, this type of the device can operate in several configurations – engine, cooler or heat pipe. The generic schematics of FPSE is shown in Figure 1.17. the main components of FPSE, playing an important role in the research of Formosa et al. [38] were: two heat exchangers – heater and cooler – that allowed the gas to be maintained at the constant hot and cold temperatures, respectively; a regenerator that periodically stored and released heat from and to the gas, which resulted in

lowering the external heat value required to maintain the hot temperature of the gas; two pistons ensuring the proper dynamics of the FPSE.

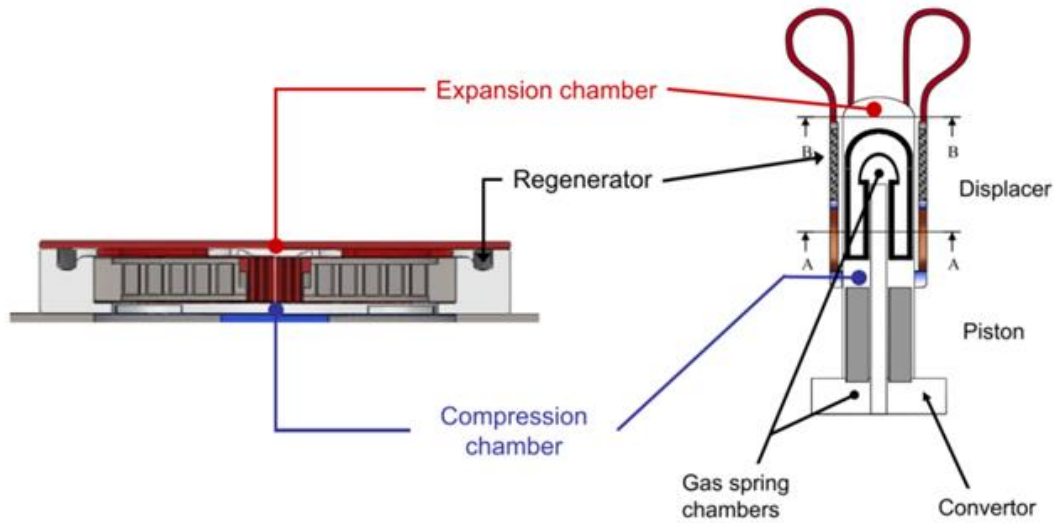


Figure 1.17: The simplified schematic of FPSE geometry [39].

The authors analyzed the effects of size reduction on the performances of FPSEs and proposed a simple first order model enabling to make a preliminary design of the engine and to anticipate the potential power and efficiency of Stirling cycle engines at a millimeter scale. Amongst other, the geometrical parameters of heat exchangers and the regenerator, such as length, hydraulic radius or number of channels, were estimated. The main conclusion driven from this research suggests that the power of the FPSE could significantly increase with scale reduction of the system.

1.3.3.4. Vapor-based generator operating due to micro-vibrations

Hsieh et al. [40] proposed a system operating due to micro-vibrations of a PVDF-based cantilever beam, which were generated by a vapor impact. The main goal of this study was to design an optimal geometry of the beam that would allow adjusting its resonance frequency to the output frequency of the vapor-based generator. The numerical analysis were performed using COMSOL Multiphysics and genetic algorithm. The experimental system given in Figure 1.18a), designed to verify the simulation results was composed of a heater, a working fluid tank and a PVDF cantilever placed at the nozzle of the tank. In this research, water was used as a working fluid. The heat applied to a bottom part of the tank caused the water vaporization at boiling temperature. The vapor expansion impacted the PVDF layer resulting in its deformation and as a consequence, a generation of an electrical charge.

Due to the fact that the natural resonance frequency of tested PVDF was much higher than the resonance frequency of the system, a geometrical optimization of the cantilever was mandatory. The authors performed a numerical modeling, thanks to which they established the cantilever

geometry that allowed reducing resonance frequency from 127.44 Hz down to 60 Hz. This resulted in higher amplitudes of the oscillations and the increase of efficiency by 293.38%. Figure 1.18b-c) illustrate the PVDF cantilever geometry before and after optimization process, respectively.

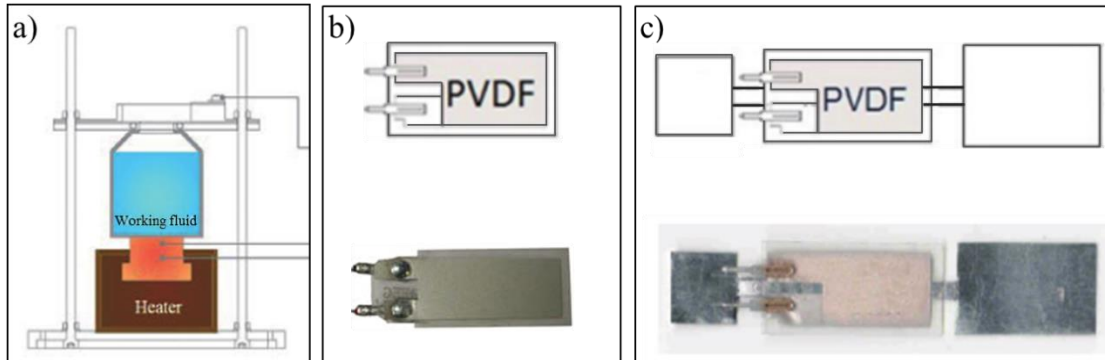


Figure 1.18: Schematic cross-section of vapor-generator [40].

The analysis performed by the authors showed that the geometry of the piezoelectric element plays a significant role in the value of the output voltage generated by the systems operating based on these transducers.

In general, all the devices described in sections 1.3.3.3 and 1.3.3.4 required an additional factor enabling to conduct the heat controlling the oscillations generation. The objective of present work was to develop an oscillating system operating under passive conditions that does not contain any rotating elements aimed at the heat conduction. This means, that the heat provided to the system, being the only source of energy, should be constant and should not oscillate. The devices of the same principle, widely presented in the literature and described briefly in section 1.3.3.5, are pulsating heat pipes (PHP).

1.3.3.5. Pulsating Heat Pipes

Essentially, the PHP is a non-equilibrium heat transfer device, typically employed to transfer large amount of heat in cooling systems. It is made from a meandering tube of inner diameter close to a capillary length, which has several turns and is partially filled with a working fluid. There are two main types of these systems:

- Opened Loop Pulsating Heat Pipes (OLPHP), where ends of the tube are not connected, as presented in Figure 1.19a).
- Closed Loop Pulsating Heat Pipes (CLPHP), where tube ends are connected to each other creating an endless tube, as shown in Figure 1.19b).

Additionally, these systems consist of at least one heat-receiving zone, so-called evaporator or heater, and one heat-dissipating zone, known as condenser or cooler. Before the first operation, the device is partially filled with a working fluid. The fluid forms liquid-vapor plugs and bubbles that are distributed naturally inside the capillary tube. Distribution of the initial plug/bubble inside the tube is not controlled externally. When one end of the tube bundle receives heat,

an oscillating action of this liquid-vapor system transfers it to another end. The transport of vapor bubbles and liquid slugs occur due to the pressure pulsations generated inside the system. Thanks to the device's construction the pressure oscillations are fully thermally driven and no external power source is required to ensure the transport of the fluid. Figure 1.19c) shows the operation mechanism of a typical PHP.

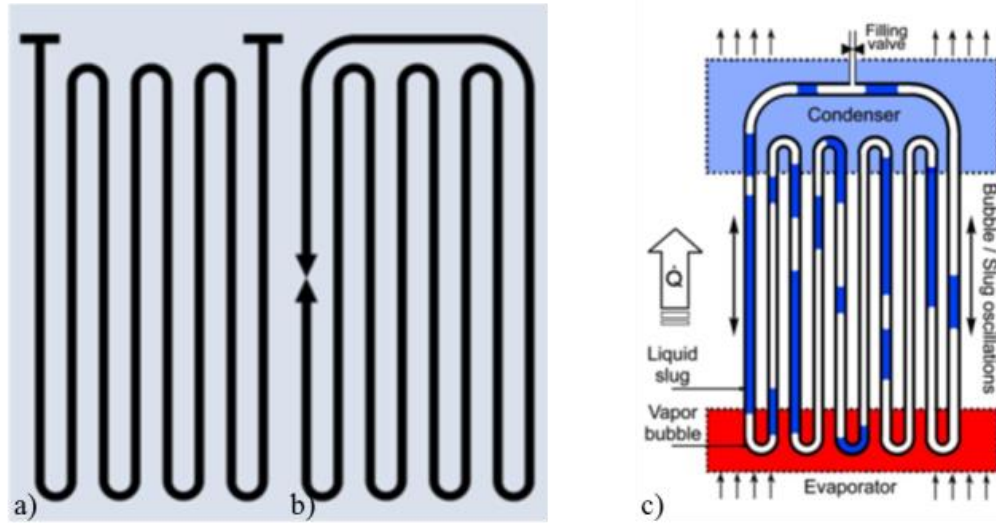


Figure 1.19: Schematic of (a) an open loop without a flow check valve and (b) a closed loop with a flow check valve; (c) operation mechanism of PHP [41].

A number of studies [32,33,35,34,41,42,43] performed in the domain of PHP technologies resulted in a better understanding of the oscillation mechanism occurring in these systems and led to several conclusions regarding the conditions that ensure their best operation. The aspects studied and described in the literature, which could bring a contribution to the design of the oscillating device presented in this work were, amongst others, as follow:

- what is the filling ratio that ensures the oscillations occurrence?
- what is the optimal filling ratio in terms of thermal performance of the system?
- what is the range of inner tube diameter value, which ensures the oscillations incipience and what is the optimal value of this parameter in terms of their thermal performance?
- what is the impact of the working fluid on thermal and mechanical properties of the device?

The analysis performed by [36,42,40,35,41] allow drawing several conclusions regarding these questions. It had been found out that the filling ratio, α , strongly influences the nature of the oscillations and in order to initiate the oscillation mechanism, its specific value is required. Khandekar et al. [49] demonstrated that to ensure the oscillations in a single close loop of a capillary dimension, partially made of cooper and glass, the filling ratio must be comprised between 20% and 80%, when water is considered as a working fluid. Moreover, according to the study of Lips et al. [44], to minimize the overall thermal resistance of the system, the filling ratio should be comprised between 40% and 60%. In general, the authors studying PHP systems that

operate with water report that the optimal value of this parameter, which ensures the most preferable behavior of PHPs in terms of their thermal performance stands at 50%, and it varies slightly depending on the gravity orientations [43]. The research of Xu et al. [46] however, showed that the value of this parameter strongly depends on a type of the working fluid. The authors established experimentally that the filling ratio giving the best thermal performance in their system filled with FC-72 is 70%.

Lin et al. [43] observed that there is a critical, minimal value of the inner tube diameter. The authors did not observe any oscillations for the diameter lower than 0.4 mm. Lips et al. [44] observed the same tendency and noted that with diameter reduction the oscillations disappeared. On the other hand Khandekar [41] states, that in order to ensure the flow oscillations, the cross-section of the tube should not be too large, and its critical diameter D_{crit} , is described by Eq.(1.9).

$$D < D_{\text{crit}} = C \cdot \sqrt{\frac{\gamma}{g(\rho_l - \rho_v)}} = C \cdot \lambda_c \quad \text{Eq.(1.9)}$$

where D is a hydraulic diameter [m]; D_{crit} is a critical diameter [m]; γ is surface tension of a working fluid [N/m]; g is the gravitational acceleration [m/s^2]; ρ_l and ρ_v are liquid and vapor density [kg/m^3], respectively; C given in the literature is usually close to 2 and λ_c is the capillary length [m].

Although the PHP systems present similar operation mechanism to the device proposed in this work, they have a complex structure, typically composed of a number of capillary tubes and they are usually applied to transfer heat in the cooling systems. One of the goals of this work was to develop the device converting thermal energy, which is characterized by the simplicity of the construction and it was assumed that its single cell should comprise only one capillary tube.

1.3.3.6. Concept of thermal energy transducer applying two-phase energy conversion

The research described in present work was conducted on the ground of a patent filed by Skotnicki [50], related to a device capable of generating electricity from a constant heat source. This concept implies energy conversion in two steps: firstly, thermal energy is converted into mechanical by means of an abrupt evaporation and condensation of a working fluid, resulting in a local overpressure. In the second step this overpressure is transformed into electric energy by means of a piezoelectric element.

The device proposed by the author, illustrated schematically in Figure 1.20, is composed of two horizontal walls – one being in contact with a source of heat, another connected to a cold source; a piezoelectric material layer connected to output terminals; two dielectric layers placed on both sides of the piezoelectric material; and a thermal insulating ring. The space comprised between a hot wall and a lower dielectric layer creates a bottom cavity, whereas the space limited by an upper dielectric layer and a cold wall forms a top cavity. Both, bottom and top cavities are spanned by a number of channels drilled through the piezoelectric and dielectric layers.

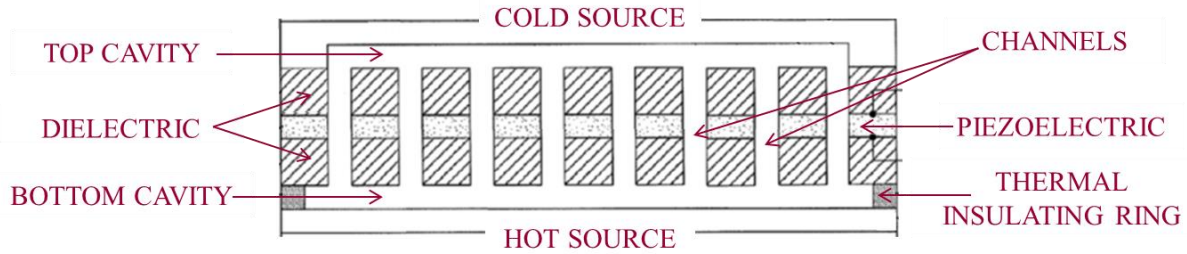


Figure 1.20: Simplified cross-section of the thermoelectric device.

The operating principle of the invention is illustrated in Figure 1.20 and it can be divided into 5 steps:

1) Before the sealing process, a portion of liquid is introduced into a space formed by the channels, the top and the bottom cavity. The liquid must be selected in a way that its boiling temperature is lower than a temperature of the hot wall and higher than the cold wall temperature.

2) When a drop of liquid runs down through one of the channels towards the bottom cavity and reaches the hot wall, it abruptly changes its phase from liquid to vapor, which results in a high overpressure and strong mechanical stress generation in the limited space of the channel, as depicted in Figure 1.21a). The stress occurs mainly due to small dimensions of the channel and to the small height of the bottom cavity.

3) Mechanical stress generated due to this rapid phase-change of the working fluid is transmitted to the piezoelectric layer and by this means transformed into an electric signal.

4) After the evaporation process, vapor condenses on the cold wall surface and liquid accumulates on this wall, as presented in Figure 1.21b).

5) With the increasing mass of the liquid forming on the cold surface, drops fall back again through the channels towards the hot surface, which is shown in Figure 1.21b). From this point, a whole process can start again and it will repeat periodically as long as the relevant values of hot and cold temperatures are maintained.

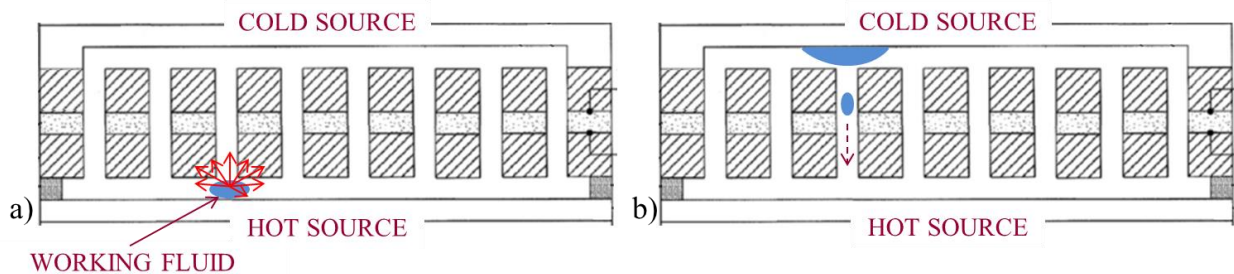


Figure 1.21: Operating principle of the invention.

Although there is a number of existing devices that are able to generate electricity either by thermal or by mechanical energy conversion, despite their undoubted advantages, they all have some drawbacks. For instance, the piezoelectric microgenerators that transform electricity from mechanical vibrations caused by the user's movements can be installed only in portable devices

such as mobile phones or watches. The use of thermoelectric generators based on Seebeck effect, ensuring direct conversion of heat is limited mainly to the measurement applications. Another interesting approach that uses thermoelectric devices applying microturbines integrated to electronic components is costly and difficult to fabricate.

The innovativeness of the concept proposed by Skotnicki [50] consists in the first step of the energy conversion process, namely in heat conversion into pressure variations, being the result of a cyclic evaporation and condensation of the working fluid enclosed within a micro-confinement. Even though in the literature there are many publications describing the research concerning the devices that employ phase-change phenomenon, as it was briefly described in sections 1.3.3.3, -1.3.3.5, they are all characterized by some inconveniences, such as a requirement of an external power source to conduct the heat for the oscillations control [31,32], large size [33,34] or a complex mechanical construction [35,36].

The aim of the patent filed by Skotnicki was to provide an invention of a device transforming thermal energy into electricity, which would be able to overcome at least partially the drawbacks of the solutions described in sections 1.3.3.2 - 1.3.3.5, would be easy to manufacture and integrate with conventional equipment. This patent initiated a wide studies of several research groups, which were aimed at designing and fabricating:

- a microfluidic heat engine based on explosive boiling, performed in the Department of Mechanical Engineering of Sherbrooke University, Canada,
- a self-oscillating fluidic heat engine (SOFHE), developed thanks to a collaboration between the Laboratory of Nanotechnologies and Nanosystems CNRS UMI-3463 of Sherbrooke University, Canada; the University Savoie Mont Blanc, France; and the STMicroelectronics, France,
- a thermo-mechanical oscillating system developed by the Solar energy, Harvesting, Thermal management research group of CEA-Liten, Grenoble, France.

The results of these works are described broadly in sections 4.1.1, 4.1.2 and 4.1.3, respectively. The study presented in this manuscript was conducted under the cooperation with CEA-Liten and the results were obtained partially thanks to the knowledge of this research group. This collaboration led to another research related to the patent [50], which was aimed at developing a small scale silicon-based, thermo-mechanical device applying phase-change phenomenon. This study was performed in the Department of Semiconductor and Optoelectronics Devices at Lodz University of Technology and was the subject of present thesis.

Taking into account the theoretical analysis presented in this chapter, according to which the piezoelectric energy transducers are one of the most promising in terms of energy conversion, as well as the fact that it was decided to design and fabricate a device on the ground of the patent that assumed the application of piezoelectric effect, the need of analyzing thoroughly this phenomenon appeared. The detailed study on piezoelectric materials and electromechanical energy conversion based on piezoelectric effect has been presented in *Chapter 2*.

1.4. Summary of the chapter

The main conclusions driven from *Chapter 1* are the following:

- the large amount of waste energy generated every day, stimulates the demand for more efficient technologies of energy recuperation and conversion,
- numerous sources of waste energy, continuous miniaturization and increasing availability of Ultra-Low Power systems contribute to the development of energy harvesting devices aimed at generating small amounts of electrical energy from their ambient, without additional power source,
- there is no universal energy source for energy harvesting devices and its type strongly depends on the application,
- one of the most attractive and easily available types of energy that can be used for supplying low power electronics is kinetic energy,
- compared to electrostatic and electromagnetic, the piezoelectric transducers are characterized by high energy density, high power conversion efficiency and relatively simple operation mechanism,
- amongst diverse piezoelectric materials, there are two that present the worthwhile features: PZT-based, easily accessible ceramics exhibiting high electromechanical coupling coefficients; flexible PVDF used for low-frequency applications. The deep study on piezoelectric effect and on piezoelectric materials is presented in *Chapter 2*,
- the main drawbacks of different devices that operate based on thermal energy conversion are, amongst others: a need of an external power supply; large size; complex mechanical construction; high costs, toxic or rare materials; fragility,
- a new concept of the device converting thermal energy into electricity in two steps of conversion, operating applying phase-change phenomenon and piezoelectric effect has been proposed. The main objectives for this device were: small scale (up to 2 cm of diameter and 2 mm thickness), simplicity of fabrication with the usage of conventional equipment, no need of external power source. This concept has posed a motivation to initiate the research described in present manuscript.

2. Electromechanical conversion applying piezoelectric materials

2.1. Historical development and applications of piezoelectric materials

In 1880, brothers Jacques and Pierre Curie discovered that certain crystalline minerals, such as Quartz and Tourmaline, display surface charges when they are subjected to a mechanical force. They observed that tension and compression of the material generates voltage of opposite polarity, which was proportional to the applied force. This phenomenon was defined as piezoelectric effect. Soon after, in 1881 Gabriel Lippmann assumed, based on thermodynamic laws, that the same crystals should display also an inverse behavior, which means that under an external field they would exhibit a strain. This theory was later experimentally confirmed by Curie brothers. They proved that when these crystals are exposed to an external electric field they lengthen or shorten according to the polarity of the field and that the deformation was proportional to the strength of the field. This phenomenon was labeled as an inverse piezoelectric effect. The mechanism of direct piezoelectric effect, when the charges inside piezoelectric displace from their equilibrium position to both surfaces in response to the strain, is shown in Figure 2.1a). Figure 2.1b) presents the mechanism of inverse piezoelectric effect, during which an external electric field induces elastic displacement of charges, resulting in a material deformation [51,52].

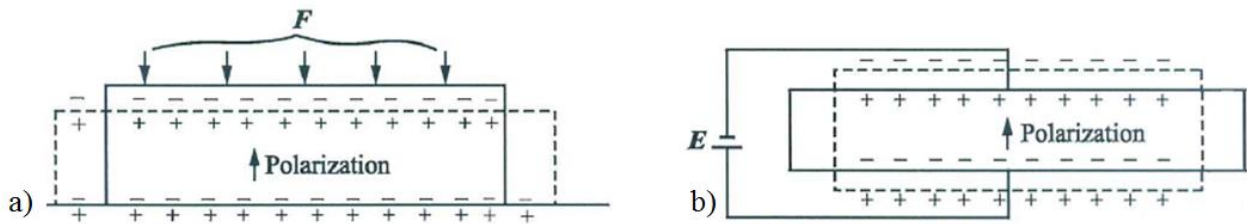


Figure 2.1: Mechanism of (a) direct piezoelectric effect – piezoelectric element responding to an external force; (b) inverse piezoelectric effect – piezoelectric element responding to an external electric field [53].

Due to the fact that the behavior of these crystals is analogical to the behavior of ferromagnetic materials, they are often called ferroelectrics although usually they do not contain iron [52].

One of the first practical applications of piezoelectric effect, developed in 1916 by Langevin, was an ultrasonic transducer that was used for submarine detection [54]. The huge progress in the development of piezoelectric materials has been made during Second World War when the BaTiO₃ (Barium Titanate) ceramics that exhibit piezoelectric characteristics at a useful scale was discovered [55]. The main advantage of this material stands in the fact that it can be easily formed into specific shapes and poled in arbitrary directions [53].

Nowadays, the direct and inverse piezoelectric effects are widely used in industry and piezoelectric materials find a number of applications in everyday use, as well as in specialized devices. The direct effect is typically used for sensing, e.g. in the displacement or force sensors, whereas inverse effect in the actuation applications, such as motors, or in generating sonic and

ultra-sonic signals [52]. The examples of the typical piezoelectric materials applications in various industries are listed in Table 2.1.

Table 2.1: Examples of typical applications of piezoelectric materials [54].

Industry	Application
Automotive	air bag sensors, air flow sensors, audible alarms, fuel atomizers, keyless door entries, seat belt buzzers, knock sensors
Computer	disc drives, inkjet printers
Consumer	cigarette lighters, depth finders, fish finders, humidifiers, jewelry cleaners, musical instruments, speakers, telephones
Medical	disposable patient monitors, foetal heart monitors, ultrasonic imaging
Military	depth sounders, guidance systems, hydrophones, sonar

In all presented applications, the piezoelectric elements are used for sensing or actuation. The new domain, being developed recently, so-called energy harvesting, is focused on designing the systems that apply piezoelectric materials to recuperate and convert the environmental energy into electricity that could be used for powering electronic devices.

2.2. Classification of piezoelectric materials

2.2.1. Inorganic piezoelectric materials

Some crystals without a center of symmetry, which display piezoelectric properties, together with the piezoelectric ceramics create a group of inorganic piezoelectric materials. Although the natural monocrystalline materials such as Quartz, Tourmaline or Seignette salt display relatively small piezoelectric effect, for many years they had been the exclusive sources of piezoelectric properties and they had been used for the development of number of products and applications, such as vibrators controlling standard frequencies, high-selectivity filters or high-temperature ultrasonic transducers [53]. Since the 1960 however, piezoelectric single crystals have been replaced in many applications by the polycrystalline ferroelectric ceramics, such as BaTiO_3 or PZT (Lead Zirconate Titanate), which exhibit much larger displacements and induce higher electric voltages [51,54]. Due to the strong piezoelectric effect, high dielectric constant and relatively simple fabrication technology, piezoelectric ceramics are nowadays the most widely used materials in the devices working based on piezoelectric effect [53].

From a crystallographic point of view, a traditional piezoelectric ceramics exhibit Perovskite crystalline structure, which means that each unit of crystal contains a small tetravalent metal ion, typically Zr (Zirconium) or Ti (Titanium), in a lattice of the large divalent metal ions, such as Pb (Lead) or Ba (Barium) and O^{2-} ions [52]. Above a characteristic temperature, so-called Curie temperature, T_c , the lattice of these materials is cubic and the arrangement of positive and negative charges is symmetric, which means that there are no dipoles in the structure and the material is not ferroelectric. However, below the Curie point, the lattice structure of the ceramics

deforms from electrically neutral face-centered cubic to tetragonal or rhombohedral. This results in a formation of the dipoles and a spontaneous polarization of the ceramics, which makes them interesting for piezoelectric technology [55]. The crystal structure of the piezoelectric ceramics above and below Curie temperature is presented in Figure 2.2a-b), respectively.

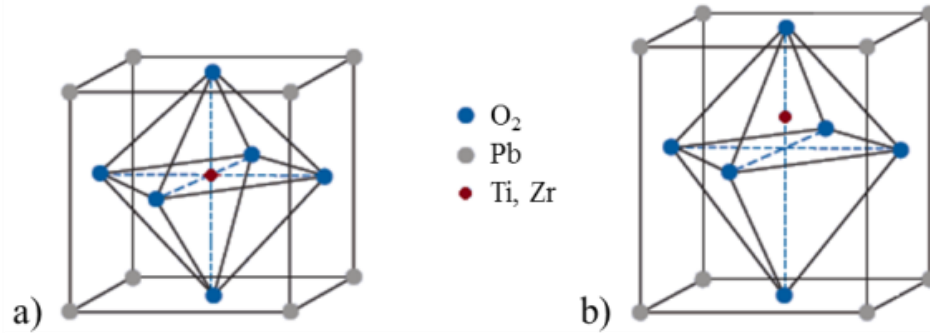


Figure 2.2: Crystal structure of a piezoelectric ceramics (a) above Curie temperature – symmetrical, cubic Perovskite structure; (b) below Curie temperature – tetragonal structure with electric dipole.

Due to the fact that piezoelectric ceramics belong to the group of ferroelectric materials, they display a spontaneous polarization when no electric field is being applied. A ferroelectric crystal is divided into several spatial regions of different polarization directions, so-called domains. Each of the domain formed inside the solid ferroelectric crystal is defined by a physically bounded area, inside which the direction and the absolute value of the vectors of spontaneous polarization are the same.

Random distribution of the domain orientations in ceramic material causes that no macroscopic piezoelectric effect occur, as shown in Figure 2.3a). The individual crystallites are made of only a few domains bonded by the walls and their number depends on the size of the poly-crystalline ceramic material. When the material is exposed to a strong external field or a mechanical stress, different domains can be reoriented, and as a result, the polarity of the whole regions can be reversed, which is shown in Figure 2.3b). After the polarization process, the ceramics exhibits piezoelectric behavior and it can change its dimensions after the application of an electric voltage. However, if the operating temperature is higher than Curie temperature, the polarized ceramics depolarizes and the material loses its piezoelectric properties. The degree of depolarization depends on the Curie temperature of the material [55]. During the poling process, the domains that are aligned similarly to the direction of the electric field expand at the expense of the domains oriented differently, and as a result, the elongation of the ceramic in the direction of the electric field occurs. When the electric field is removed, the directions of the domains remain nearly unchanged, as it is shown in Figure 2.3c), which leads to the permanent polarization and deformation of the material. The ceramics is anisotropic and its properties vary depending on the direction of the measurement [52]. The whole process of poling in the electric field is shown in Figure 2.3.

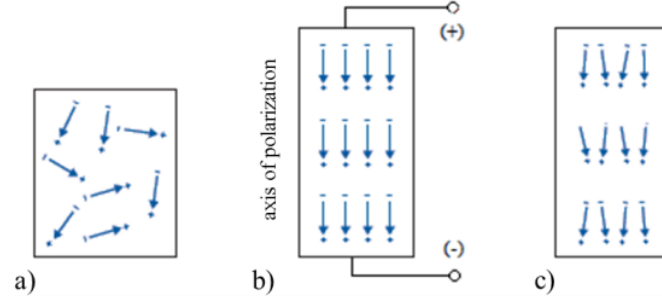


Figure 2.3: (a) Unpolarized dipoles in ferroelectric domains when no electric field is being applied; (b) reorientation of the domains in the strong electric field; (c) remnant polarization after the removal of the electric field [55].

Figure 2.4a) shows a typical strain, S , curve of the ferroelectric piezo ceramics under the influence of the electric field, E . Initially, with the increase of the electric field, the dipoles of all domains are being aligned in the direction of the field, to eventually approach the physical limit of the distortion. During this process, the strain increase occurs. After the reverse of the field, the strain decreases with the decrease of the electric field, which causes the change in the dipole orientations. When the field reaches its negative value, the dipoles are changing their original orientations and at a critical point they completely reverse their directions. As a result, the material is polarized in the opposite direction. Then, the piezoelectric ceramic expands again up to a physical strain limit. When the electric field is reversed again, the hysteretic behavior occurs and the strain decreases. At the coercive limit for the opposite direction, the dipoles reorient to their original polarization. The relative change in the dimension parallel to the electric field causes also decrease or increase in dimension perpendicular to the direction of the field. This change however is approximately 50% smaller as compared to the parallel direction [52].

Similarly to the behavior of ferromagnetic materials, poled ferroelectrics exhibit hysteresis and their temperature dependent dielectric constants are very high. A typical hysteresis curve illustrating the influence of the electric field, E , on the polarization, P , of the piezoelectric ceramics is given in Figure 2.4b).

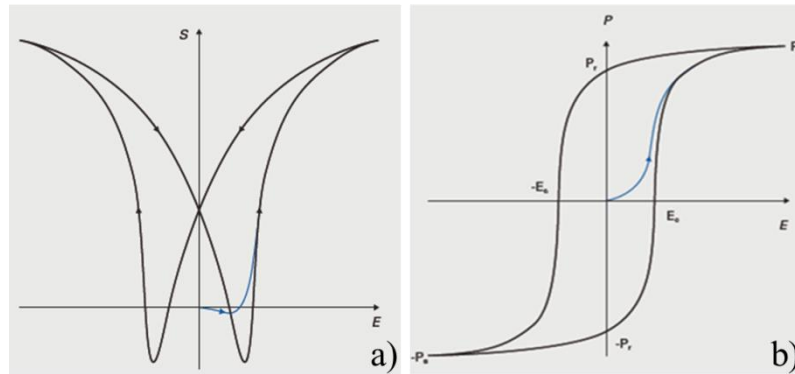


Figure 2.4: (a) Electromechanical behavior of the longitudinal strain, S , as a function of the electric field, E ; (b) influence of the electric field, E , on the polarization, P , of a piezoelectric ceramics [55].

The application of the electric field to the piezoelectric ceramics results in a maximum polarization at saturation P_s . When the field is reduced to zero, the remnant polarization P_r is determined. The application of the reverse field causes the negative maximum polarization, $-P_s$, of the material and negative remnant polarization $-P_r$. When the field is reversed again, the positive remnant polarization is restored [52]. The depolarization of the material is possible only if the opposing electric field exceeds the coercivity strength E_c [55].

Thanks to their physical structure, the piezoelectric ceramics can behave like generators and convert mechanical energy of compression or tension into electrical energy. This is due to the fact that when a poled piezoelectric ceramics is exposed to the mechanical stress, the dipole moment changes, and as a result, the voltage is generated. The compression of the material in the direction of polarization or tension perpendicular to the polarization direction causes the voltage generation of the same polarity as the poling voltage. Contrarily, when these ceramics are exposed to the tension along the polarization direction or to the compression perpendicular to the direction of the polarization, the polarity of generated voltage is opposed to the poling voltage. The value of voltage generated by compressive stress applied to the piezoelectric ceramics is linearly proportional to this stress up to a material-specific stress. These generator actions make the piezoelectric ceramics suitable for wide range of applications and they are used in the devices such as solid state batteries, fuel-igniting devices and many others. The influence of compression and tension on the direction of generated voltage, is given in Figure 2.5c-d), respectively.

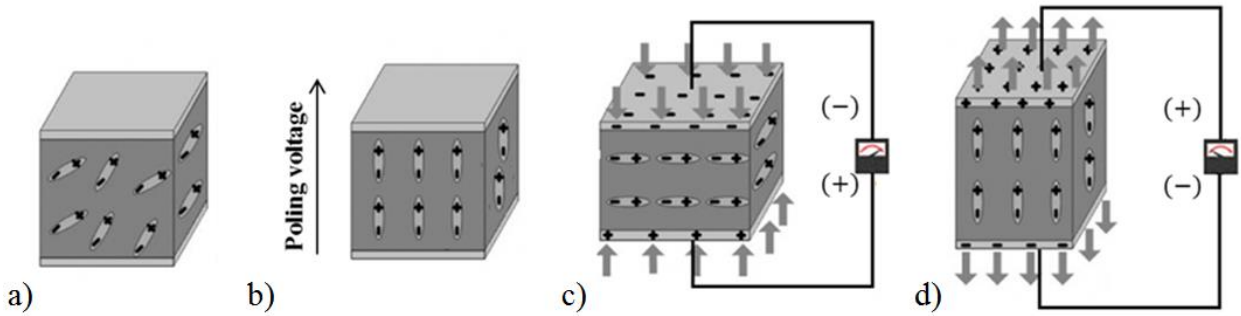


Figure 2.5: Piezoelectric ceramics (a) before poling; (b) after poling; (c) after compression along the poling direction; (d) after tension along the poling direction.

Piezoelectric materials exhibit also a motor behavior, during which the electrical energy is converted into mechanical energy. When the piezoelectric ceramics is exposed to a voltage of the same polarity as the poling voltage, it lengthens and its diameter decreases, as it is shown in Figure 2.6b). Analogously, the element shortens if the voltage that has the opposite polarity to the poling voltage is applied, which is given in Figure 2.6c). Figure 2.6d) shows the situation when the piezoelectric element is exposed to an alternating voltage, which results in cyclic lengthening and shortening of the material with the frequency of applied voltage. This behavior of ceramics is used in piezoelectric motors, as well as sound or ultrasound generating devices. The applied voltage is proportional to generated strain [52].

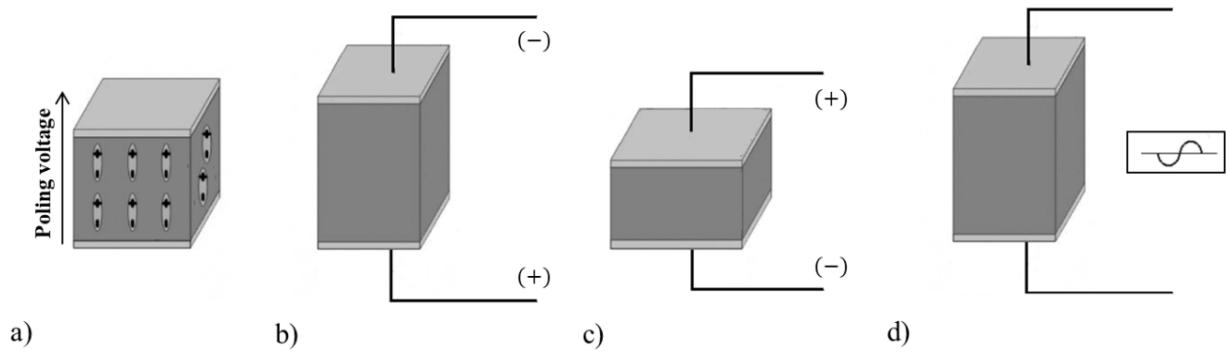


Figure 2.6: Piezoelectric ceramic (a) after poling; (c) after compression along the poling direction; (d) after tension along the poling direction.

In order to fabricate a piezoelectric ceramics, the mixture of the fine powder of the component metal oxides must be heated to a form of uniform powder. Later, the powder is mixed with an organic binder, pressed and molded into the desired shape. To obtain a dense crystalline structure, the shapes are sintered, cooled and trimmed. The last part of the production process is the deposition of the electrodes [52]. After this sintering process the ceramic element is in a thermally depolarized state and is isotropic due to almost uniform distribution of spontaneous polarization direction in the domains. A typical ceramic sample contains 10^9 to 10^{12} grains per cm^3 .

2.2.2. Organic piezoelectric materials

A number of organic materials such as silk, some species of wood, or even animal tendons display a piezoelectric behavior, but the effect that appears in natural materials is very weak as compared to piezoelectric ceramics [56]. However, despite the extensive design of piezoelectric ceramics as actuators and sensors that have been performed for recent decades, due to their fragility they are still not suitable for the devices requiring large displacement. This drawback was successfully overcome in 1969, when Kawai discovered a new type of piezoelectric polymer [57]. The advantages of these polymers, e.g.: polyvinyl fluoride PVF or polyvinylidene fluoride PVDF, stand at their huge flexibility, small impedance, low density and relatively high piezoelectric coefficient. The piezoelectric effect of polymers can be increased by the additional technological processes, such as stretching the film in high temperature and electric field or doping the synthetic material with piezoelectric ceramics. Piezoelectric polymers find their applications in pressure sensors, explosion igniting or in devices that are used for underwater ultrasonic measurements. The drawback of these materials is their low piezoelectric strain constant that limits their applications as active transducers [52,55].

2.2.3. Piezoelectric composites

Piezoelectric composites are the materials consisted of ceramics and polymers that are mechanically connected to form different constructions. As a result, they present enhanced

properties as compared to their initial components and, in some cases, even the features that do not exist in any of the component separately [53]. The composites present a number of advantages over conventional monolithic piezoelectric materials, such as better electromechanical properties and lower density, a very strong piezoelectric effect, large flexibility as well as the possibility of combining diverse features of the materials by using different connectivity patterns [58]. A large voltage coefficient together with a large charge coefficient result in the improvement of sensitivity and bandwidth of piezoelectric transducers, which make them attractive for sensors, actuators or energy harvesters in smart structures, medical science and ultrasonic transducers, as well as for hydroacoustic and electroacoustic applications [59]. The latest research focused on optimization of the composite components in terms of thermal stability and mechanical quality factors, allowed them to be considered as promising materials for high temperature and high power transducer applications e.g.: high power ultrasonic wire bonding, high temperature non-destructive testing or downhole energy harvesting. The benefits of piezoelectric transducers working based on piezoceramic-polymer-composites come also from their flexible nature that results in the durability, reliability, robustness and longer lifetime of piezoelectric devices [58].

2.3. Electro-mechanical properties of piezoelectric materials

2.3.1. Boundary conditions

There are two electrical and two mechanical boundary conditions typically used for piezoelectric measurements. The first type, defined by electrodes, circuit states and geometrical shape of the piezoelectric material, includes short-circuit boundary condition, for the situation when the electric displacement, D , varies but the electric field, E , is maintained zero, and open circuit boundary condition for constant electric displacement, D , and variable electric field, E , inside piezoelectric material. Stress-free and clamped are two types of mechanical boundary conditions. The combination of electrical and mechanical boundary conditions form four boundary condition groups that are typically applied for piezoelectric equations, and they are defined as follow:

- short-circuit – stress-free boundary condition group,
- short-circuit – clamped boundary condition group,
- open circuit – stress-free boundary condition group,
- open circuit – clamped boundary condition group.

2.3.2. Properties of piezoelectric materials and piezoelectric coefficients

Due to the anisotropy of piezoelectric materials, all physical coefficients are related to the directions of applied mechanical or electric force, as well as to the directions perpendicular to the force application. The usual direction of a polarization vector, P , is parallel to the direction 3 that corresponds to z-axis of the right-handed Cartesian coordinate system. The parameters

parallel to x, y and z axes are denoted by subscripts 1, 2 and 3, respectively, whereas subscripts 4, 5 and 6 represent shear about one of these axes [55], which identify rotations.

2.3.2.1. Elastic properties and coefficients of piezoelectric materials

Each object exposed to an external force, responds by a movement of its position, including translation and rotation, and by its plastic or elastic deformation. Taking into account, that the deformation of a piezoelectric material is small enough, it can be considered as elastic. There are two parameters, stress, \mathbf{T} , and strain, \mathbf{S} , which describe an elastic state of a piezoelectric material. Stress is understood as a force applied to a piezoelectric element per surface area of the element, whereas strain is a change of the element's length per its original length. Stress, that depends on force orientation and on plane of its action, is a second-rank tensor of 9 components, amongst which only six are independent. It can be expressed by a matrix presented in Eq.(2.1). Analogically, strain tensor contains six independent components forming a matrix described by Eq.(2.2) [53].

$$\mathbf{T} = [T_1 \ T_2 \ T_3 \ T_4 \ T_5 \ T_6]^t \quad \text{Eq.(2.1)}$$

$$\mathbf{S} = [S_1 \ S_2 \ S_3 \ S_4 \ S_5 \ S_6]^t \quad \text{Eq.(2.2)}$$

Both, mechanical stress and strain in piezoelectric materials require directional indexing, due to their anisotropy. According to the Hooke's law, within linear elastic range, strain component is a linear function of stress and these two parameters are correlated by a flexibility coefficient, s , or stiffness coefficient, c . The relation between strain and stress matrices for a piezoelectric material can be described by Eq.(2.3) or Eq.(2.4).

$$\mathbf{T} = \mathbf{cS} \quad \text{Eq.(2.3)}$$

$$\mathbf{S} = \mathbf{sT} \quad \text{Eq.(2.4)}$$

where s is a matrix of flexibility coefficients presented in Eq.(2.5) and c is a matrix of stiffness coefficients. The relation between s and c matrices can be expressed by $s = c^{-1}$ [53].

Young's Modulus Y

Young's Modulus, Y , is an indicator of a material elasticity and it is determined from a value of stress that is applied to the material over a value of resulting strain in the same direction [52]. The unit of this constant is typically expressed in $[\text{N/m}^2]$. Due to the fact that the stiffness of the material is different in direction 3 than in 1 and 2, both electrical conditions as well as the directions must be taken into consideration [60].

Elastic compliance or flexibility coefficient s

Elastic compliance, s , is the value of strain, S , produced by the element in response to applied mechanical stress, T , and it is dependent on the interactions between mechanical and electrical energy. The compliance under constant electric displacement and under constant electric field is expressed by s^D and s^E , respectively. The first subscript of this coefficient refers to the strain direction, whereas the second one to the direction of the stress. The matrix of compliance coefficient s is presented in Eq.(2.5) [51,59].

$$s = \begin{bmatrix} s_{11} & s_{12} & s_{13} & 0 & 0 & 0 \\ s_{12} & s_{11} & s_{13} & 0 & 0 & 0 \\ s_{13} & s_{13} & s_{33} & 0 & 0 & 0 \\ 0 & 0 & 0 & s_{44} & 0 & 0 \\ 0 & 0 & 0 & 0 & s_{44} & 0 \\ 0 & 0 & 0 & 0 & 0 & s_{66} \end{bmatrix} \quad \text{Eq.(2.5)}$$

For the directions 11 and 33 the compliance is reciprocal to the Young's Modulus.

2.3.2.2. Electrical properties and coefficients of piezoelectric materials

All piezoelectric materials present the dielectric behavior. In any dielectric exposed to an external electric field, polarization process occurs, resulting in the electric charges appearing on the outside surfaces of a material. The constant deformation inside piezoelectric material results in constant electric field, E , and it leads to Eq.(2.6).

$$\Delta V = E \cdot h \quad \text{Eq.(2.6)}$$

where h is the thickness of piezoelectric material [19].

Dielectric permittivity constant ϵ

The dielectric constant, ϵ , of isotropic materials is considered as scalar, so unpolarized crystalline ceramic presents the same values of constant in all directions. However, in anisotropic materials, which include piezoelectric elements, the coefficient, ϵ , that connects electric field, \mathbf{E} , and electric displacement, \mathbf{D} , is a second-rank tensor. The higher symmetry of the crystal structure is, the fewer independent components of a dielectric constant there are. The poled piezoelectric ceramics, which is anisotropic due to remnant polarization along the poling direction, presents different constant component in this direction than in the other directions [53]. The ferroelectric piezo ceramics present a symmetry similar to the symmetry of hexagonal crystal system, which means that they are approximate to the crystals from “6 mm” point group and they are non-centrosymmetric. For this class of crystals, the matrix of dielectric constants presents the form Eq.(2.7) [19].

$$\boldsymbol{\varepsilon} = \begin{bmatrix} \varepsilon_{11} & 0 & 0 \\ 0 & \varepsilon_{22} & 0 \\ 0 & 0 & \varepsilon_{33} \end{bmatrix} \quad \text{Eq.(2.7)}$$

The directionality of dielectric constant is described by the tensor components. Permittivity at constant stress and strain is expressed by $\boldsymbol{\varepsilon}^T$ and $\boldsymbol{\varepsilon}^S$, respectively. The amount of charge that can be stored by ceramic material, relative to the absolute dielectric constant ε_0 is known as relative dielectric constant K [51,59].

Piezoelectric charge or strain constant d

The piezoelectric charge constant, d , is a measure of the electric charge that is induced and collected on the electrodes as a response to applied mechanical stress T . The unit of this constant may be expressed in coulombs/square meter per newton/square meter. If the applied force is uniformly distributed over area fully covered by electrodes, the unit of the coefficient can be described as [C/N]. Due to the fact that piezoelectric ceramic materials are typically polarized along 3rd axis, the plane that is perpendicular to polaxis is isotropic, which means that in piezoelectric constant matrix there are only three independent components – d_{31} , d_{33} and d_{15} . Thus, the piezoelectric constant matrix can be expressed by Eq.(2.8).

$$\mathbf{d} = \begin{bmatrix} 0 & 0 & 0 & 0 & d_{15} & 0 \\ 0 & 0 & 0 & d_{15} & 0 & 0 \\ d_{31} & d_{31} & d_{33} & 0 & 0 & 0 \end{bmatrix} \quad \text{Eq.(2.8)}$$

Figure 2.7a-c) shows stress modes of piezoelectric ceramics for charge constants d_{33} , d_{31} , d_{15} , respectively [52].

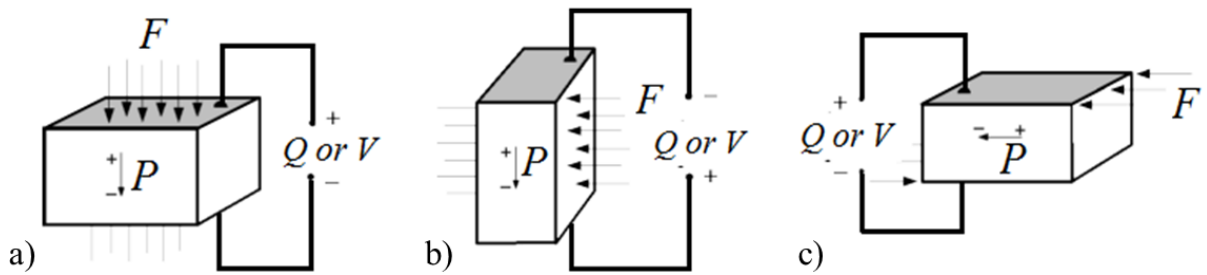


Figure 2.7: Stress modes of piezoelectric ceramics [60].

Conversely, the d constant can be understood as mechanical strain S produced by applied electric field and termed as strain coefficient, with the unit expressed in [m/V] [60]. Due to the fact that strain induced in the material by the electric field depends on the value of this field as well as on d , it is an important constant that has to be taken into account when the strain dependent applications, such as actuators, are considered [52].

Piezoelectric voltage constant g

Piezoelectric voltage constant, g , is related to the electric field, E , generated by piezoelectric material as a response to the mechanical stress, T , and it can be expressed in [Vm/N]. Voltage coefficient can also describe the ratio of mechanical strain, S , developed in a piezoelectric material over applied electric displacement, D . Its unit is then denoted by [m²/C]. Due to the fact that the strength of the induced electric field produced by piezoelectric element responding to applied stress is determined by Eq.(2.9) that includes the piezoelectric voltage coefficient, g , it is a significant factor for accessing the piezoelectric material suitability for sensing applications.

$$E = -(gT) + \frac{D}{\epsilon T} \quad \text{Eq.(2.9)}$$

Under static or near-static conditions, for input frequencies far below the resonance frequency of the piezoelectric material, the force, F , and stress, T , applied to a piezo ceramics, as well as the electric field, E , and generated charge, Q , are correlated according to Eq.(2.10) and Eq.(2.11).

$$E = -(g_{33}T) \quad \text{Eq.(2.10)}$$

$$Q = -(d_{33}F) \quad \text{Eq.(2.11)}$$

Eq.(2.12)-Eq.(2.15) present the relationships between changes in thickness, Δh , length, Δl , or width, Δw , of ceramic element and applied voltage V or electric field E that caused these changes.

$$\Delta h = d_{33}V \quad \text{Eq.(2.12)}$$

$$S = d_{33}E \quad \text{Eq.(2.13)}$$

$$\frac{\Delta l}{l} = d_{31}E \quad \text{Eq.(2.14)}$$

$$\frac{\Delta w}{w} = d_{31}E \quad \text{Eq.(2.15)}$$

where $S = \frac{\Delta h}{h}$ is strain and h , l and w are initial height, length and width of ceramic element, respectively [52].

Temperature dependence of piezoelectric coefficients g , d and ϵ

The permittivity, ϵ , the piezoelectric charge constant, d , and the piezoelectric voltage constant, g , are factors that depend on the temperature. Temperature-associated changes in

the domain orientations are usually transient within recommended operating temperature range. These changes, however, can cause charge displacements and electric fields generation, which could influence the accuracy of the measurements. Rare, but occasionally occurring, sudden temperature fluctuations result in high voltages generation, which could lead to the depolarization of piezoelectric ceramic.

The parallel connection of a capacitor to the piezoelectric element causes the increase of the total capacitance of the system and equivalent drop of the temperature coefficient for total capacitance. Due to the fact that permittivity, ϵ^T , charge, d , and voltage constants, g , are correlated, the temperature coefficient for g (which is the difference between the temperature coefficients for other two factors) is in general constant within a wide temperature range [52].

Electromechanical coupling factor k

The coupling coefficients are non-dimensional factors describing the ability of a particular piezoelectric to transform electrical energy into mechanical or contrarily, mechanical energy into electricity. It is thus a good indicator of piezoelectric effect effectiveness and can be used for comparing various materials regardless their different variable parameters such as permittivity or compliance. Under static or near-static conditions, when the input frequencies are far below the resonance frequency of the piezoelectric material, the coupling factor can be determined by a square root of the mechanical energy created by converse piezoelectricity over input electrical energy or by a square root of electrical energy generated by direct piezoelectric effect over input mechanical energy [51,54,52,59]. Depending on the type of the ceramics and the direction of the forces, at low frequencies, it can transform from 30% to 75% of stored energy into another form of energy. Although a high coupling factor k is required to perform efficient energy conversion, it is not a measure of efficiency. This is due to the fact that it does not take into account dielectric or mechanical losses. In order to determine the real efficiency of piezoelectric element, the ratio of usable energy provided by the piezoelectric material to the total energy taken up by the element must be established. In well-designed systems the efficiency of the ceramics can reach even 90% [52].

The electromechanical coupling factor can be also expressed in the function of charge constant d and dielectric constant ϵ , or as a function of Young's Modulus Y , if the material is in 31 or 33 mode, as it is described by Eq.(2.16) and Eq.(2.17), respectively [61].

$$k^2 = \frac{d}{\sqrt{S^E \epsilon^T}} \quad \text{Eq.(2.16)}$$

$$k^2 = d \sqrt{\frac{Y}{\epsilon^T}} \quad \text{Eq.(2.17)}$$

There are several types of coupling factors that depend on a shape of the piezoelectric element as well as on the vibratory modes. k_p is the planar electromechanical coupling factor for

a thin disc made of piezoelectric ceramics, which express the radial coupling between electric field parallel to the polarization dimension of the material and mechanical effects producing radial expanding and contracting vibrations [51,54,52,59]. For the frequencies much lower than resonant, the coupling factor for ceramic disc can be determined from Eq.(2.18) [52].

$$k_p^2 = \frac{2d_{31}^2}{(s_{11}^E + s_{12}^E)\epsilon_{33}^T} \quad \text{Eq.(2.18)}$$

2.3.3. Piezoelectric equations

The interactions between electric parameters – electric field, E , electrical displacement, D – and mechanical parameters – stress, T , and strain, S , – are known as the state equations for piezoelectric materials. The forms of piezoelectric equations depend on the boundary conditions, described in section 2.3.1, as well as on the forms of piezoelectric coefficient, elastic compliance and permittivity. Due to the fact that the independent components vary in the matrix depending on the structure of the crystal, the expressions of piezoelectric equations change adequately. The most common piezoelectric equations are related to short-circuit and stress-free boundary conditions as well as to the compliance coefficients s^E and dielectric constants ϵ^T and they are expressed by Eq.(2.19) and Eq.(2.20) [53].

$$S = s^E T + d^t E \quad \text{Eq.(2.19)}$$

$$D = d T + \epsilon^T E \quad \text{Eq.(2.20)}$$

There are two basic piezoelectric equations for piezoelectric ceramics that describe direct piezoelectric effect in short-circuit electrical boundary conditions ($E_1 = E_2 = E_3 = 0$) and converse effect at stress-free mechanical boundary conditions ($T_i = 0, i = 1, 2, 3, 4, 5, 6$). They are expressed by Eq.(2.21) and Eq.(2.22) respectively.

$$D = d T \quad \text{Eq.(2.21)}$$

where D is transposed electric displacement vector $D = [D_1 D_2 D_3]^t$, d is the matrix recaptured from piezoelectric constant tensor and it depends on the crystal structure of the material.

$$S = d^t E \quad \text{Eq.(2.22)}$$

If the piezoelectric ceramic is activated in mode 33 or 31 the piezoelectric equations can be simplified to forms Eq.(2.23) and Eq.(2.24).

$$D = d T + \epsilon E \quad \text{Eq.(2.23)}$$

$$S = \frac{T}{Y} + d E \quad \text{Eq.(2.24)}$$

2.4. Summary of the chapter

In this chapter the general information about piezoelectric phenomenon and the properties of different piezoelectric materials are given, which can be useful when choosing a suitable energy converter dedicated to the device proposed in this manuscript. The main information regarding piezoelectric materials, comprised in the chapter are:

- electric charge can be generated by certain crystals without a center of symmetry when they are subjected to mechanical stress. The voltage of opposite polarity generated due to tension and compression of the material is proportional to applied force,
- the piezoelectric materials are anisotropic and their properties strongly depend on the measurement direction,
- the direct and inverse piezoelectric effect are widely used in the industry for sensing and actuating applications, respectively,
- due to their physical structure, piezoelectric materials can be used also as generators,
- the new domain, in which the piezoelectric materials found their application recently, is energy harvesting, where they are used for energy conversion purposes,
- nowadays, the most widely used piezoelectric materials are BaTiO_3 and PZT ceramics, due to their strong piezoelectric effect, high dielectric constant and relatively simple fabrication technology,
- the main drawback of piezoelectric ceramics consists in their fragility, which excludes them from the applications where large displacements are required,
- the issue of high fragility does not exist for the PVF and PVDF polymers, which are characterized by a huge flexibility, low impedance, low density and relatively high piezoelectric coefficient.

Additionally, in this chapter the electromechanical properties of piezoelectric materials, piezoelectric coefficients and equations have been described.

The information listed above contributed to the decision that the two piezoelectric materials considered during the design process of the device presented in this work should be PZT ceramics and flexible PVDF polymer. The deep study on these converters are described in *Chapter 3*.

3. Analysis of piezoelectric converters exposed to pulse of pressure

3.1. Experimental setup description

The aim of the research presented in this chapter was to evaluate the energy generated by the piezoelectric elements of different types and geometries under the excitation pulse. In order to examine the electric response of diverse piezoelectric converters to a pulse of pressure created by decompressing air, an experimental setup given in Figure 3.1a) was developed. The main part of the setup, shown in Figure 3.1b), consisted of a tightly sealed, 50 mm high, cylindrical chamber with the diameter of 35 mm, made of Aluminum. To supply and later release compressed gas from the system, inlet and outlet holes with the diameters of 4 mm each, were drilled through the chamber walls. Two solenoid valves P2LBX312 were mounted to control the gas flow. The opening and closing time of each valve stood at 18 ms and 45 ms, respectively. In order to control the electro-valves, a USB 4714 data acquisition system was used. The changes of pressure inside the chamber were measured by a 40PC015G1A pressure sensor from Honeywell Inc. The sensor worked in the range between 0 and 6 bar with $\pm 2.6\%$ of full scale accuracy. A piezoelectric element was mounted inside the chamber using a cylindrical clamping support made of glass-reinforced epoxy laminate sheet (FR-4), in a way shown in Figure 3.1c). When air decompression occurred in the chamber, the pressure changes generated during this process affected the piezoelectric element mounted inside, causing its deformation. This resulted in the electric signal generation. Both piezoelectric voltage and pressure changes occurring inside the chamber were acquired by Dynamic Signal Analyzer (DSA) PCI-4462.

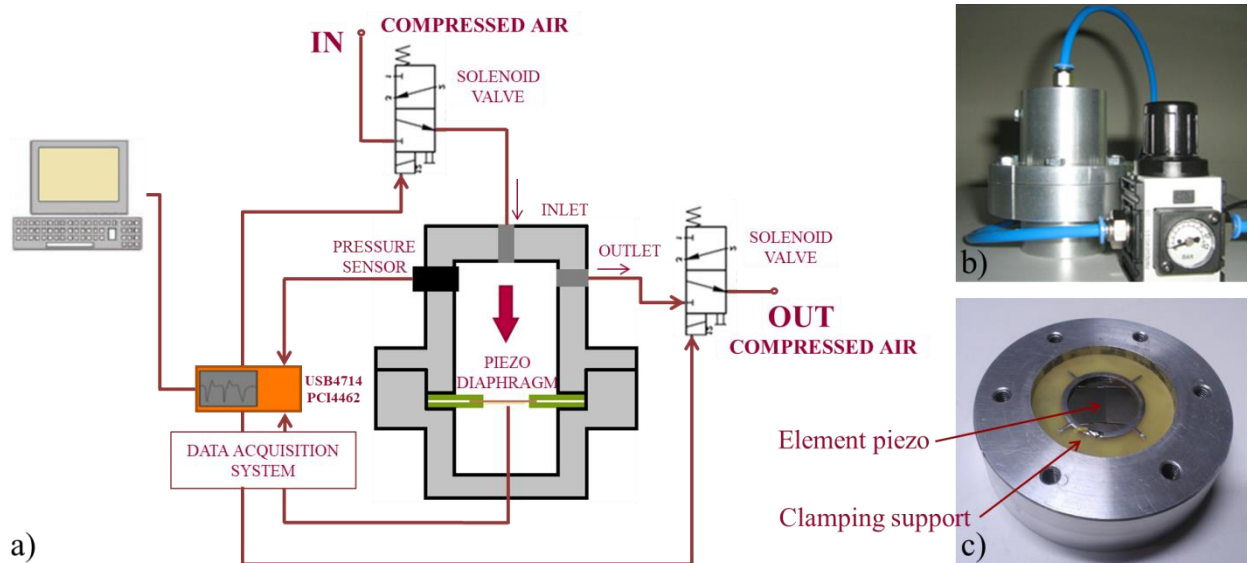


Figure 3.1: (a) Experimental setup developed to investigate the response of piezoelectric elements working under the pressure excitation pulse; (b) test chamber with pressure control element; (c) interior of the chamber with the removable clamping support containing a piezoelectric element.

In order to develop the device proposed in this manuscript, it was mandatory to verify how an assembly method and a type of a piezoelectric transducer influences the energy generated in response to a pulse of pressure applied to the element. For this purpose, the clamping support of piezoelectric element was designed in a form of diaphragm that could be arbitrarily modified or replaced. This gave the possibility of testing diverse piezoelectric elements using the same experimental setup.

The study was focused on two types of the material – flexible PVDF and rigid PZT-based ceramics described in section 3.2 and section 3.3, respectively. PVDF was considered as an interesting solution due to its elasticity and the fact that it can be easily cut and formed into diverse shapes. Hence, using this material would widen the scope of possibilities when designing the structural elements of the prototype. On the other hand, PZT-based materials are known, amongst others, for higher coupling factor, Young's Modulus and Curie temperature as compared to PVDFs. Due to the fact that these materials present interesting features but their electromechanical properties vary significantly, it was decided to test both of them in several operation modes. This helped to select the configuration and the assembly methods that ensured the most efficient design of the device in terms of energy generation. Each diaphragm forming the clamping support had a diameter of 4 mm and its shape depended on a type and an operation mode of the piezoelectric element that was to be investigated. In order to test the PVDFs operating either in a cantilever or in a membrane configuration, and the PZT in a strain mode the piezoelectric element was placed between two ring-shaped layers with a thickness of 1 mm each, in a way shown in Figure 3.2a-b) and Figure 3.2d), respectively. In case of PZT operating in a stress mode, the 1 mm thick, cylindrical-shaped diaphragm was applied, as it is presented in Figure 3.2c). To facilitate the measurement of the signal, the additional electrodes were sputtered on the selected areas of the clamping supports for PZT working in the stress mode as well as for both PVDFs in a way illustrated in Figure 3.2a-c). It was important especially in case of PVDFs due to their structural limitations and low temperature resistance that makes the soldering of a wire to its metalized surface not possible.

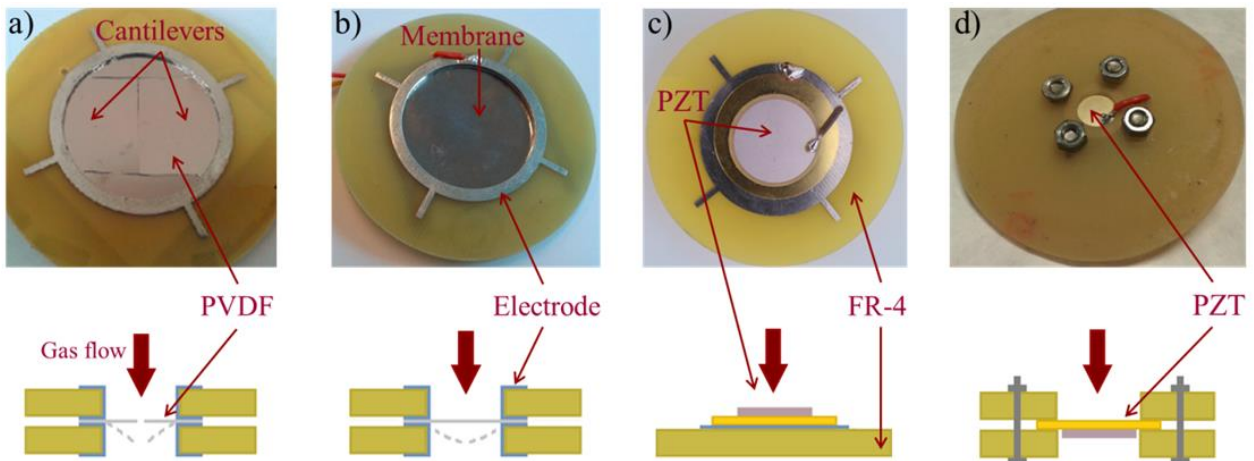


Figure 3.2: Diaphragm containing (a) two PVDF cantilevers; (b) PVDF membrane operating in strain mode; (c) PZT operating in stress mode; (d) PZT operating as a membrane in strain mode.

Given that the study described in present work had been conducted under the cooperation with CEA-Liten and the author had partially participated in the works of its research group, the part of the study that was aimed at analyzing the PZT behavior in the strain mode was performed independently in both facilities - at Lodz University of Technology (TUL) and in the laboratory of CEA. This gave the possibility of comparing the results obtained for the same experimental conditions but using two autonomous setups of different designs. Figure 3.3 shows the details of the clamping method given schematically in Figure 3.2d), which was applied at TUL to test PZT-based elements of different dimensions. The elements varied with respect to their thickness and they diameters were equal to 12 mm, 20 mm and 27 mm.

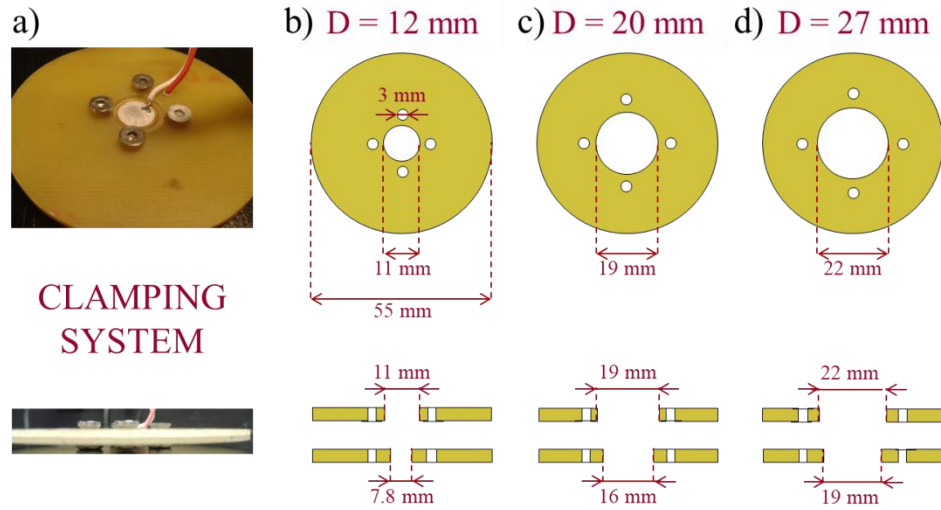


Figure 3.3: (a) Photographs of clamping system designed at TUL; dimensions of the clamping system for PZT-based elements of (b) 12 mm; (c) 20 mm and (d) 27 mm diameter.

A cross-section of the Aluminum pressure chamber proposed by CEA-Liten is given in Figure 3.4a). To mount the piezoelectric inside the chamber, it had been first attached to an Aluminum support by 4 or 6 screws with a fixed torque of 0.05cNm. The dimensions of the support, designed to clamp the piezoelectric elements of different sizes inside the pressure chamber, are given in Figure 3.4b-d).

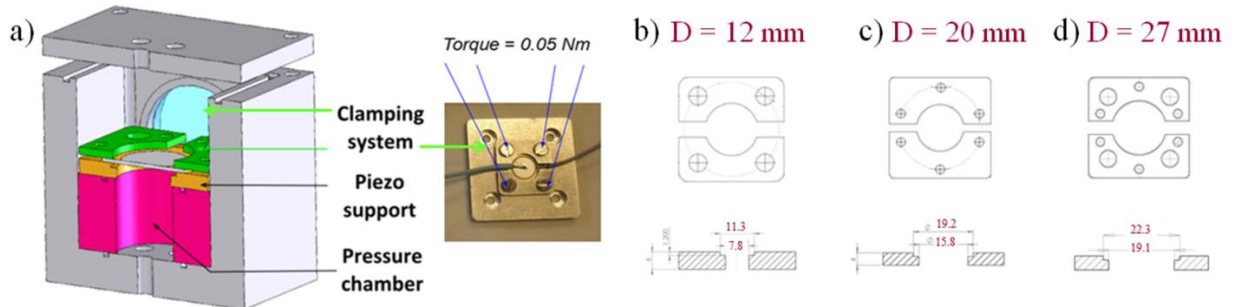


Figure 3.4: (a) Schematic cross-section of pressure chamber and a photograph of clamping system designed in CEA-Liten; clamping system for (b) 7BB-12-9; (c) 7BB-20-6 and 7BB-20-3; (d) 7BB-27-4.

In order to create possibly the same conditions for both experiments, the torque of the screws used for clamping was set to the fixed value of 0.05 cN.m by a screwdriver FACOM A300MTJ1 and the diameters of circular openings in the bottom and top part of FR-4 support were the same as in the design of CEA-Liten. The comparison of the results obtained in two independent series of experiments at TUL and CEA-Liten is presented in section 3.3.3.

3.2. Analysis of flexible PVDF transducers

3.2.1. Electrical response of PVDF to the pressure pulse: cantilever mode

In this section the analysis of piezoelectric transducers composed of two flexible PVDF cantilevers, depicted in Figure 3.2a), exposed to pulses of pressure is described. To verify if the thickness of the element plays a significant role in the value of energy generated during the process, the transducers were cut out of PVDF sheets (Measurement Specialties) having three different thicknesses: 28 μm , 52 μm and 110 μm . The total surface of two cantilever beams was equal to 4 cm^2 .

As the output piezoelectric voltage is a function of stress that is usually achieved by bending or displacing a piezoelectric beam, the cantilevered transducer was mounted inside the chamber, between two rigid layers and it was exposed to a pulse of pressure created by decompressing air. The pressure generated during decompression inside the chamber affected thin PVDF layers, causing the electric charge generation. Due to the fact that the results of the preliminary experiments showed relatively low values of generated voltage for the pressures below 3 bar, it was decided to analyze the response of PVDF when exposed to a pressure pulse equal to 3 bar. The main electromechanical parameters of the applied films are placed in Table 3.1. A value of capacitance for each transducer was calculated from Eq.(3.1).

$$C = \epsilon_r \epsilon_0 \frac{S}{t} \quad \text{Eq.(3.1)}$$

where ϵ_r is the relative permittivity of PVDF, ϵ_0 is the vacuum permittivity equal to 8.854×10^{-12} [F/m], S is the active area of the PVDF electrodes [m^2] and t is the thickness of the film [m].

Table 3.1: Electromechanical parameters of tested PVDF films.

Type	t [μm]	C [nF]	d_{31} [pC/N]	g_{31} [Vm/N]	k_{31} [%]	ϵ/ϵ_0 [-]	Y [GPa]
PVDF 1	28	1.52	23	0.216	11	12	2-4
PVDF 2	52	0.82					
PVDF 3	110	0.38					

Where d_{31} is a piezoelectric charge constant, g_{31} is a piezoelectric voltage constant, k_{31} is a coupling factor expressed in %, ϵ/ϵ_0 is a relative permittivity and Y is Young modulus.

An example waveform of pressure changes Δp inside the chamber, and the electrical responses of 28 μm , 52 μm , 110 μm thick PVDFs are placed in Figure 3.7a-c), respectively.

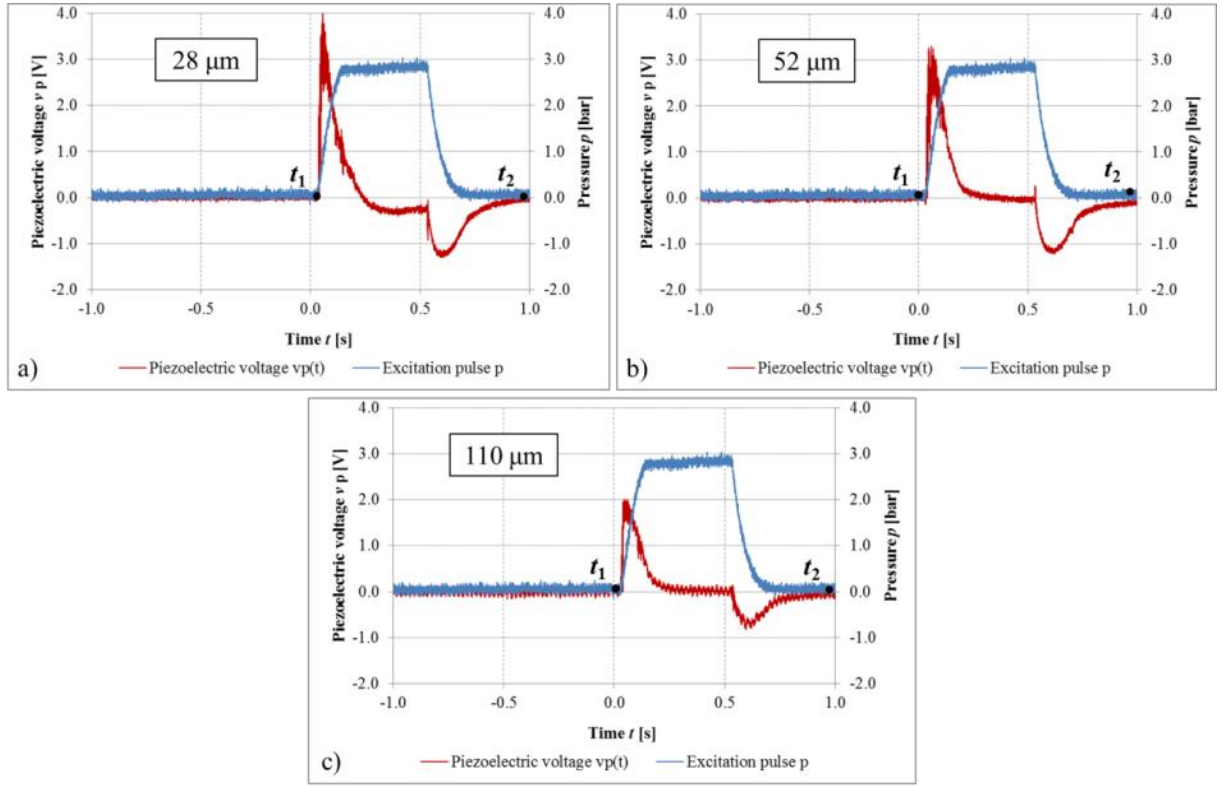


Figure 3.5: Changes of pressure Δp inside the chamber and piezoelectric voltage changes for the cantilevered PVDF with a thickness of (a) 28 μm ; (b) 52 μm and (c) 110 μm .

The results presented in Figure 3.5 were used for determining the maximum value of voltage, V_{Pmax} , and estimating the power, P , generated during a single excitation pulse, Δp , by each PVDF transducer. The values of energy were calculated from Eq.(3.2), and listed Table 3.2.

$$P = \frac{1}{t_2 - t_1} \int_{t_1}^{t_2} \frac{C v_p^2(t)}{2} dt \quad \text{Eq.(3.2)}$$

where $v_p(t)$ is piezoelectric voltage in discrete-time domain [V], t_1 and t_2 refer to the beginning and the end of the excitation pressure pulse, respectively [s].

Table 3.2: Values of maximum piezoelectric voltage V_{Pmax} , and power, P , for cantilevered transducers of three different thicknesses.

Type	t [μm]	V_{Pmax} [V]	P [nW]
PVDF 1	28	4.0	0.60
PVDF 2	52	3.3	0.20
PVDF 3	110	2.0	0.05

The chart given in Figure 3.6 shows graphically the dependance of maximum voltage and power generated by catilevered transducer during one pressure pulse of 3 bar on the PVDF thickness.

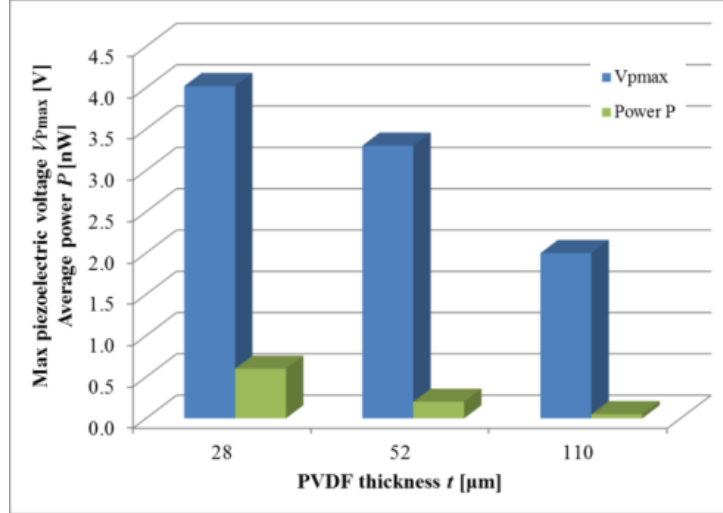


Figure 3.6: Maximum value of voltage $V_{p\text{max}}$, power, P , generated by cantilever transducer during single excitation pulse of maximum $\Delta p = 3$ bar, for three different thicknesses of PVDF.

The research presented in this section showed that the films with lower thickness generate higher values of voltage and power.

3.2.2. Electrical response of PVDF to the pressure pulse: strain mode

Another approach of the research concerning flexible piezoelectric films was to examine their behavior when they are mounted inside the chamber in a form of a circular membrane, in the way shown in Figure 3.2b). The preliminary experiments performed for PVDF transducer having a membrane form showed, that it can be easily destroyed when exposed to high pressures. This means that the very thin layers of PVDF, which usually present good electrical properties due to their high capacitance value, can operate only in a range of small pressures. On the other hand the voltage signals generated by thick layers were very low. Taking these two facts into account, a medium, 52 μm thick PVDF membrane of 7 cm^2 surface was selected for the experiments. The capacitance, C , of this transducer was calculated from Eq.(3.1) and it was equal to 1.43 nF. Likewise in experiments described in section 3.2.1 the main goal of this part of the research was to analyze the response of PVDF material to the excitation pulse created by decompressing air introduced to the chamber. A detailed description of the experimental setup, as well as the measurement method, is placed in section 3.1. The values of pressure affecting piezoelectric film in consecutive experiments were as follow: 0.2 bar, 0.3 bar, 1 bar, 1.5 bar, 2 bar, 2.5 bar, 3 bar up to 3.5 bar. In order to quantify repeatability of the results, 31 measurements for each pressure value were performed and a standard deviation was calculated and listed in Table 3.3. For pressures higher than 3 bar, the rupture of the PVDF occurred.

Table 3.3: Mean voltage, $V_{Pmax(AVG)}$, and its standard deviation, σ , for different values of pressure inside the chamber.

p [bar]	0.2	0.3	1.0	1.5	2.0	2.5	3.0	3.5
$V_{Pmax(AVG)}$ [V]	2.00	2.20	3.30	3.50	3.51	2.73	2.57	N/A
σ [V]	0.15	0.20	0.18	0.30	0.52	0.43	0.62	N/A

Based on the values listed in Table 3.3, the voltage dependence on pressure was plotted and presented in Figure 3.7.

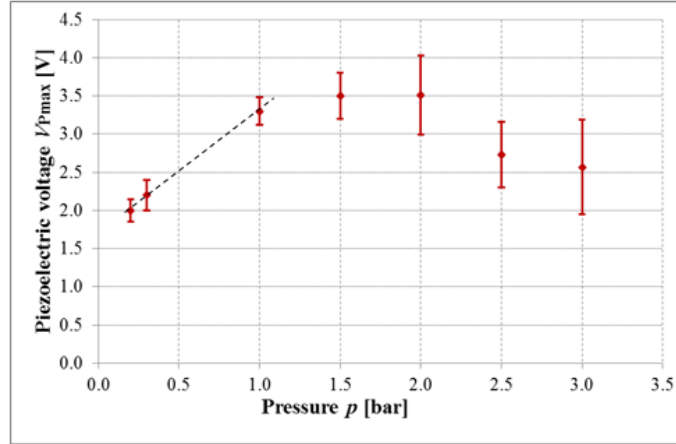


Figure 3.7: Voltage dependence on the value of pressure introduced to the chamber.

The characteristic of the chart allow assuming that there are three pressure intervals, within which the PVDF membrane presents different type of behavior. For values between 0.2 bar and 1 bar, the voltage was raising linearly with the increasing pressure. Above 1 bar however, the linear behavior declined and the results were less repeatable and more random, which is also visible in higher values of standard deviations. Finally, at a pressure value of 3.5 bar, a rupture of the PVDF occurred.

In order to find out if the pressure above certain value applied to the membrane could affect the structure of PVDF film irreversibly, resulting in lower reliability of the experiments, the three transducers were tested. One was exposed to a pulse of pressure equal to 0.7 bar, another to 2.5 bar and finally the third one to 3.5 bar. After the experiment, each element was removed from the air chamber and its shape was analyzed (Figure 3.8a-c)).

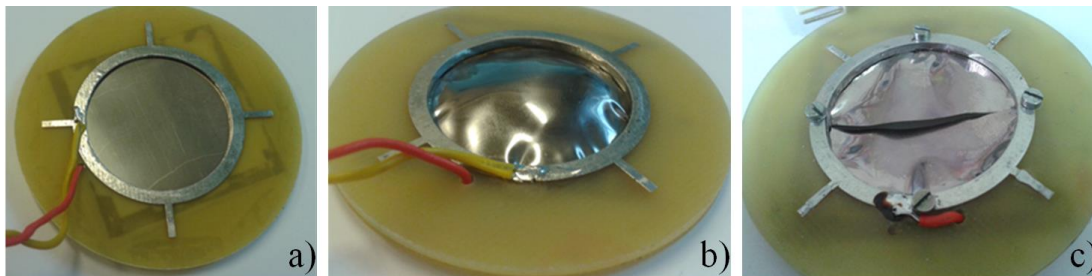


Figure 3.8: 52 μ m PVDF membrane after a contact with pressure of (a) 0.7 bar; (b) 2.5 bar; (c) 3.5 bar.

In case of PVDF exposed to pressure below 1 bar, no changes of the film had been observed, for higher value however, a visible, irreversible deformation of the element occurred. As for previous experiments, applying pressure of 3.5 bar resulted in the rupture of the transducer.

All these observations led to a conclusion that, unlike in case of cantilever construction, a tensile strength of testing film plays a significant role when it works in a form of membrane. It is thus essential to evaluate the highest tensions to which it can be exposed, without losing its initial mechanical properties.

In order to understand the general elastic behavior of PVDFs, the tensile tests of 52 μm thick film were performed. For this purpose the INSTRON 4204 universal testing instrument was applied. This tool is a highly reliable precision system for evaluating the mechanical properties of the materials and it is composed of two main elements: a crosshead drive that applies tensile or compressive loading to a specimen and a load weighing system that measures the loading of a specimen.

In order to evaluate mechanical properties of tested PVDF, five samples 20 cm long and 1 cm wide had been prepared. Each sample was placed between two vertical leadscrews, loaded in tension where it experienced the opposing forces located on the same axis. The measurements of specimen elongation ΔL and load F , were performed. Based on these results the values of stress σ , strain ε and Young Modulus were calculated. Figure 3.9 shows the three stages of this experiment – the beginning of elongation, when the sample was still in an elastic region and could come back to its initial shape; the elongation, when the sample was in a strain hardening region and irreversible changes to its structure occurred; and finally the rupture of the sample. At one moment of the elongation process the tension was released, in order to demonstrate the irreversible changes of the sample length in the strain hardening region, which is shown in Figure 3.9b). During the experiment it was observed that up to the force of $F = 31\text{ N}$, the PVDF strip did not change drastically its shape, however above this value the elongation of the PVDF started to be visibly irreversible and even after the release of the force it could not come back to its initial dimension.

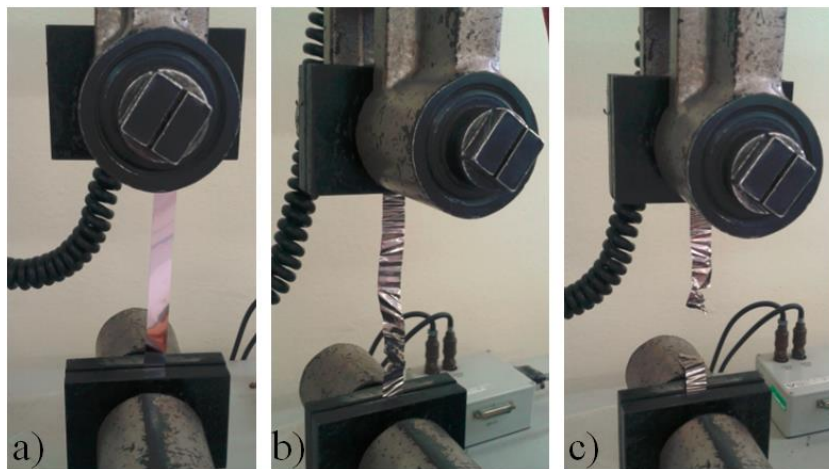


Figure 3.9: Specimen (a) at the beginning; (b) during elongation; (c) after rupture.

Figure 3.10 shows the chart representing the evolution of stress, σ , calculated from Eq.(3.3), in a function of strain ε expressed by Eq.(3.4).

$$\sigma = \frac{F}{S} \quad \text{Eq.(3.3)}$$

$$\varepsilon = \frac{\Delta L}{L} \quad \text{Eq.(3.4)}$$

where, L is the original length of the sample [m] and ΔL is a change of the length during elongation process.

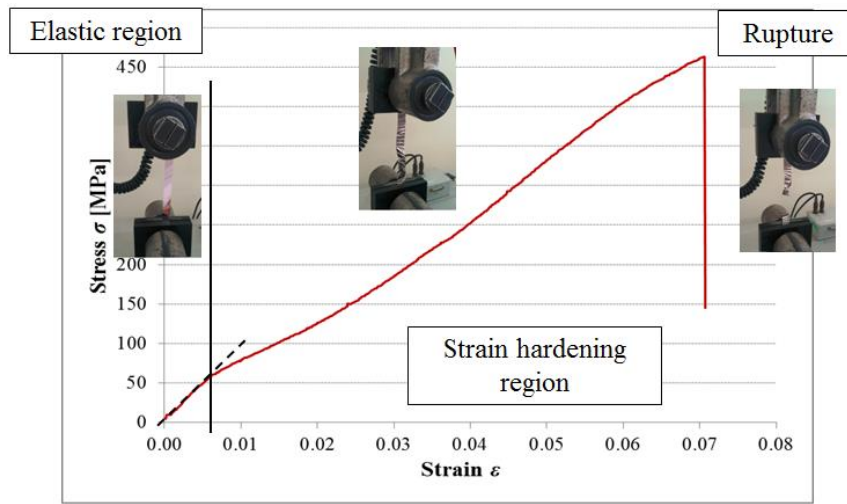


Figure 3.10: Stress-strain curve of the 52 μm , PVDF strip at tensile test.

The stress-strain curve is unique for each material and can be used for estimation of its mechanical properties. The data from stress-strain curve of PVDF given in Figure 3.10 were used to calculate the Young's Modulus of the material accordingly to Eq.(3.5).

$$Y = \frac{\sigma}{\varepsilon} \quad \text{Eq.(3.5)}$$

The value of Young's Modulus at the end of elastic region, calculated from Eq.(3.5) was equal to 9.1 GPa, which is higher than the typical values given by the manufacturers of PVDFs (usually between 2 GPa and 8 GPa), it sands however at the same order of magnitude.

The conclusion driven from these initial experiments with PVDF membranes as well as from the tensile tests are, that the value of force applied to the transducer must be carefully selected. This is due to the fact that when exposed to a force of a high value, the PVDF might lose its elastic properties or even get destroyed. Although the maximum value of the stress that can be applied to the sample is not constant and depends on many factors such as thickness and shape of

the sample or the direction of applied force, the tensile tests explained the non-linear behavior of the circular membrane, described at the beginning of this section and depicted in Figure 3.7 and Figure 3.8. It could be observed that, alike in case of tensile test, it was possible to specify the elastic range of PVDF membrane, inside which the pressure did not cause any harm to the material. However, above certain value of pressure, the PVDF film entered the strain hardening region and displayed non-linear properties, to be finally destroyed when the pressure was too high. These three situations are illustrated in Figure 3.11.

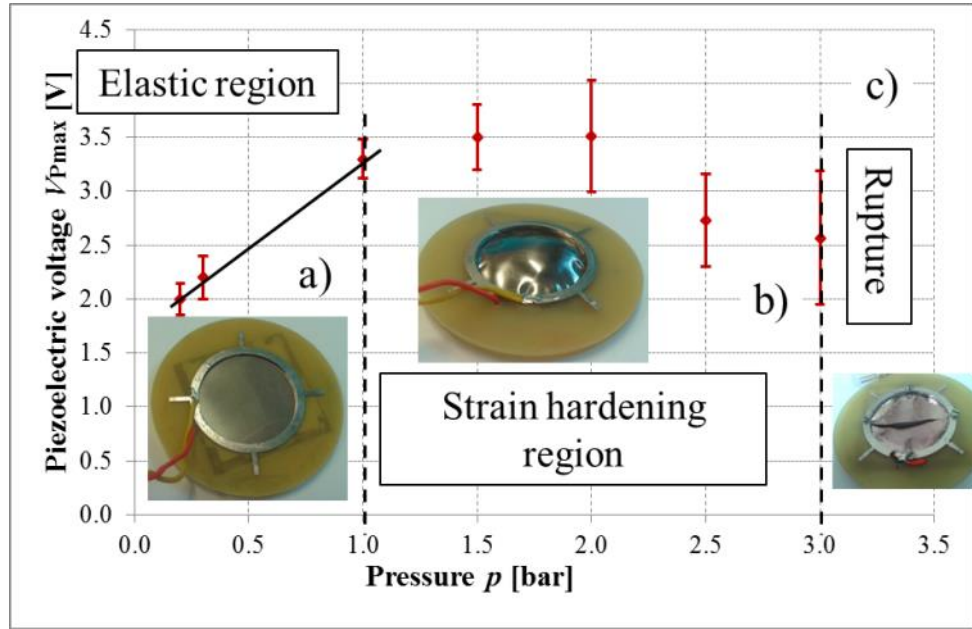


Figure 3.11: Piezoelectric voltage generated by 52 μm thick PVDF membrane; (a) elastic region; (b) strain hardening region; (c) rupture.

One can conclude that for the piezoelectric film membrane with these specific dimensions it is not relevant to work with pressures higher than 1 bar. Figure 3.12a-b) presents the electrical response 52 μm thick PVDF to pressure pulses of 0.3 bar and 1 bar respectively.

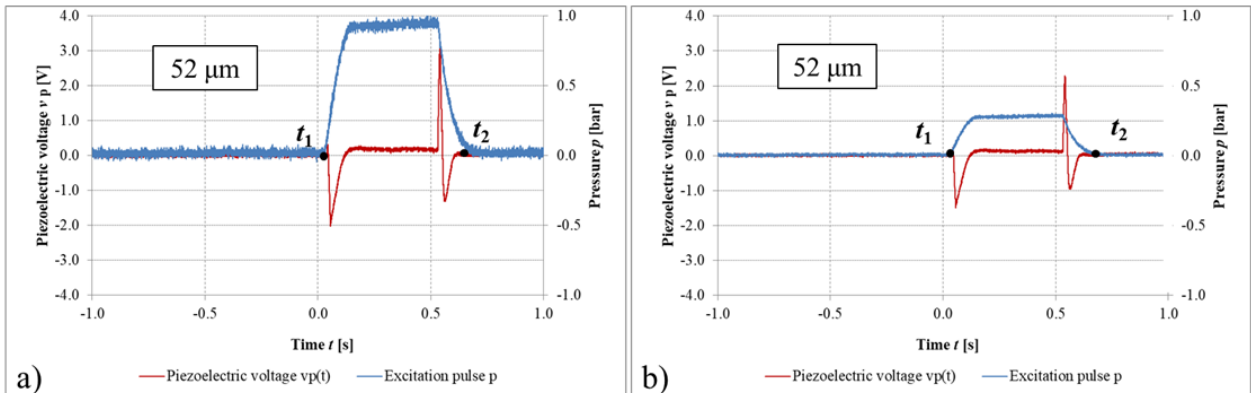


Figure 3.12: Voltage signal generated by 52 μm thick PVDF membrane exposed to a pressure pulse of (a) 0.3 bar and (b) 1 bar.

The data from Figure 3.12 were used for determining the maximum value of voltage V_{Pmax} generated by 52 μm PVDF membrane in a single pulse of excitation and for estimating the value of power, P , that was calculated from Eq.(3.2). These values are listed in Table 3.4.

Table 3.4: Maximum piezoelectric voltage V_{Pmax} , power, P , generated by membraned PVDF under the influence of two different pressure values.

Pressure p [bar]	t [μm]	V_{Pmax} [V]	P [nW]
0.3	52	2.3	0.08
1.0		3.0	0.15

3.2.3. Comparison of PVDF films operating in cantilever and strain mode

In order to compare the two operation modes of PVDF films, the values of maximum voltage, V_{Pmax} , and power, P , generated by 52 μm thick transducers of cantilever and membrane construction were listed in Table 3.5.

Table 3.5: Maximum piezoelectric voltage V_{Pmax} , power, P , generated by cantilevered and membraned PVDF under the influence of two different pressure values.

Operation mode	t [μm]	p [bar]	V_{Pmax} [V]	P [nW]
Cantilever	52	3	3.3	0.20
Membrane		1	3.0	0.15

Given that the PVDF transducer operating in the membrane mode was losing its elastic properties when exposed to high pressures, the results placed in Table 3.5 referred to the maximal reliable value of this parameter, which was 1 bar. The values of maximum voltage and power generated by 52 μm thick PVDF in cantilever and membrane mode are comparable, but the pressure applied to the membrane transducer was 3 times lower than in case of the cantilever construction. This allows expecting that, in general, the membrane structure is more efficient in terms of generated energy. However, the drawback of this solution stays in the fact that it is more fragile and it can be easily destroyed when the pressure affecting the membrane is too high. The conclusion drawn from the experiments described in section 3.2. is that the electrical properties of PVDF film are better when it works in a form of membrane, but due to a fragility of this construction it can operate only in the range of low pressures.

3.3. Analysis of circular piezoelectric ceramics PZT

The main goal of the research presented in section 3.3 was to analyze the behavior of PZT-based elements operating in stress or strain mode, when they are exposed to the excitation pulse caused by changing pressure. Each of the investigated elements consisted of a circular-shaped PZT layer with a silver electrode sputtered on one surface, which was bonded on top of a brass substrate being also the second electrode. For the large piezoelectric elements, the energy generation is simplified due to the large active surfaces. However, for small-scale

systems that are the subject of this work, the size of the piezoelectric should be drastically reduced and as a result, the values of voltage and current generated during the process are expected to be lower as well. The analysis aimed at understanding the influence of the element sizing on the amount of generated energy for slow pulse excitation were performed and described in this section. In the experiments, four commercially available, piezoelectric devices of different sizes (from MURATA) were tested. A schematic and a photograph of analyzed PZT diaphragms are given in Figure 3.13, whereas their main geometrical parameters and the capacitance values given by the manufacturer are listed in Table 3.6.

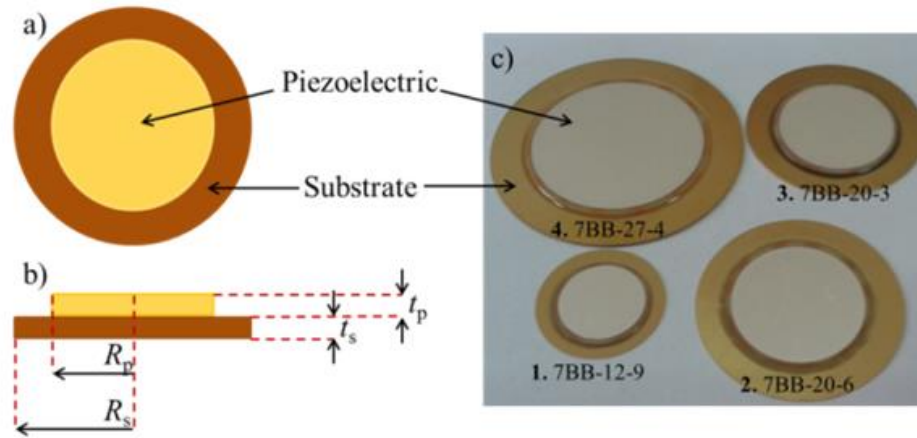


Figure 3.13: (a) Top view and (b) cross-section of PZT diaphragm, where R_p and R_s are the radii of piezoelectric and substrate respectively and t_p and t_s are their thicknesses; (c) photograph of different-sized PZT elements.

Table 3.6: Dimensional parameters of tested PZTs.

No.	Commercial name	R_s [mm]	R_p [mm]	t_s [mm]	t_p [mm]	C [nF]
1.	7BB-12-9	6.0	4.50	0.10	0.12	8 ($\pm 30\%$)
2.	7BB-20-6	10.0	7.00	0.20	0.22	10 ($\pm 30\%$)
3.	7BB-20-3	10.0	7.00	0.10	0.12	20 ($\pm 30\%$)
4.	7BB-27-4	13.5	9.85	0.30	0.24	20 ($\pm 30\%$)

The elements listed in Table 3.6 were placed inside a pressure chamber and subjected to a stable pressure variations of 25 mbar, 50 mbar, 100 mbar, 150 mbar, 200 mbar, 250 mbar and 300 mbar at low frequency (close to 1 Hz).

The elements given in Table 3.6 were selected due to their geometrical and electrical features that allowed studying the influence of three different parameters – radius, thickness and capacitance – on the value of voltage generated as a response to the pulse of pressure. In order to analyze the impact of PZT radius, the elements (1) and (2) from Table 3.5 were compared; the elements (2) and (3) were tested to understand the influence of the thickness and finally (2) and (4) were used in order to investigate the impact of different dimensions at constant capacitance value. The elements were studied in both, stress and strain mode.

3.3.1. Piezoelectric material determination

Due to the fact that, apart from geometrical dimensions and capacitance value, any other material parameters, such as dielectric and piezoelectric properties of PZT elements from Murata, were not provided in datasheets, it was necessary to find the method that would determine the type of the piezoelectrics composing this elements. Hooker [62] performed a wide range of measurements aimed at determining the dielectric, ferroelectric and electro-mechanical properties of four PZT-based materials when they are exposed to temperatures between -150°C and 250°C . The results of these experiments showed clearly that these parameters vary significantly depending on the type of piezoelectric material. The dielectric constant, ϵ_r , dependence on temperature for PZT-4, PZT-5A, PZT-5H and PLZT-9/65/35 are presented in Figure 3.14a-d), respectively.

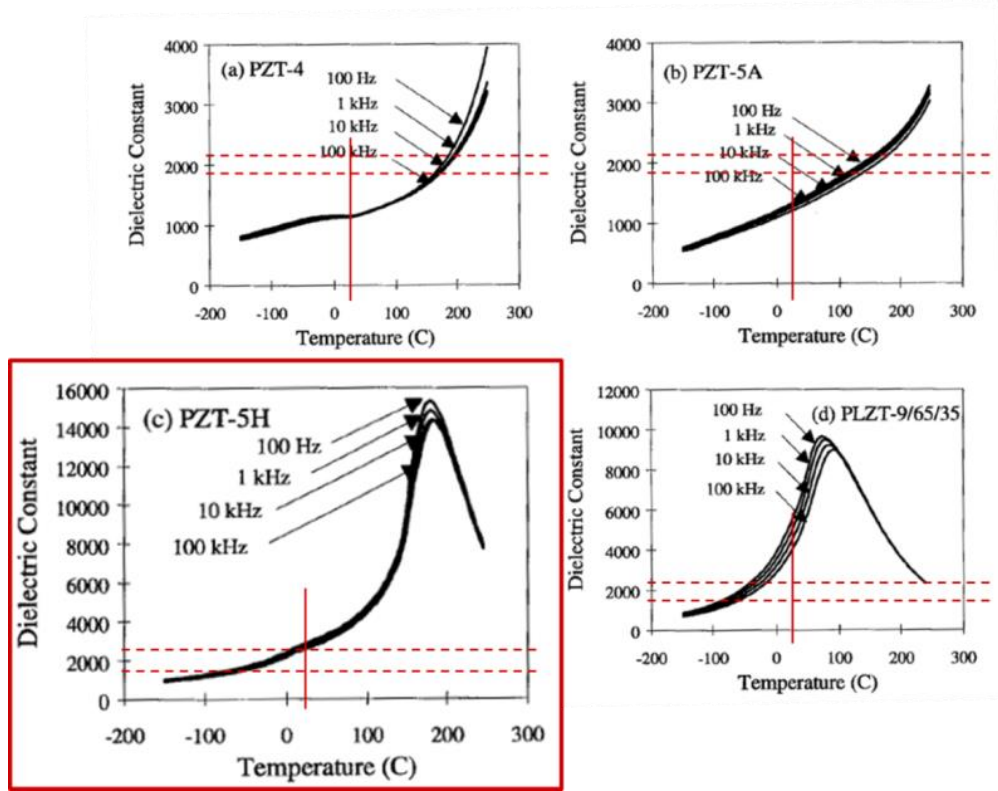


Figure 3.14: Dielectric constant versus temperature data for (a) PZT-4; (b) PZT-5A; (c) PZT-5H and (d) PLZT-9/65/35 [62].

Taking into account that different types of piezoelectric material express different evolution of relative permittivity, ϵ_r , in relation to temperature, it was possible to determine the piezoelectric type used in experiments presented in this work. For this purpose, the dielectric constant of each element was calculated based on Eq.(3.1). Due to the fact that the capacitance values for different PZT elements are given in datasheets with $\pm 30\%$ uncertainty it was decided to verify their real values using E4980A Precision LCR Meter. The capacitance of each element

was measured three times in the frequency range between 20 Hz and 100 Hz and its mean value was used to calculate the relative permittivity of each element. The geometrical parameters, measured values of capacitance and calculated dielectric constants of all tested piezoelectrics are listed in Table 3.7.

Table 3.7: Geometrical parameters, measured capacitance, C_m , and calculated relative permittivity, ϵ_r , of tested PZT elements.

No.	Commercial name	$S[\text{mm}^2]$	$t[\text{mm}]$	$C_m[\text{nF}]$	ϵ_r
1.	7BB-12-9	63.6	0.12	10.3	2191
2.	7BB-20-3	153.9	0.12	20.3	2124
3.	7BB-20-6	153.9	0.22	10.8	1749
4.	7BB-27-4	304.7	0.24	25.6	2282

The results of performed measurements and calculations show that in general the values of relative permittivity for all tested PZT-based materials oscillates around 2000. In order to compare the results of experiments with data presented in the literature, the horizontal dash lines representing the range of dielectric constants calculated for tested elements were added to the charts presenting data of Hooker [62], shown in Figure 3.14. Vertical lines added to the charts indicate room temperature.

Analyzing the charts from Figure 3.14 one can assume that all types of examined elements were closer to PZT-5H. Determining the type of PZT led to the knowledge of all the other piezoelectric coefficients that, at given temperature, are constant and depend only on the material type. Typical values of piezoelectric parameters for PZT-5H ceramics at the temperature of 25°C are listed in Table 3.8. In order to compare the properties of this PZT material, the table contains also the parameters related to other PZT-based ceramics tested by Hooker [62].

Table 3.8: Typical properties of different PZT-based ceramics at temperature of 25°C [62].

Type	k_p	k_{33}	k_{31}	d_{33}	d_{31}	g_{33}	g_{31}	$\epsilon T_{33}/\epsilon_0$
	[-]			[pC/N]		[10 ⁻³ Vm/N]		[-]
PZT-5H	0.59	0.59	0.36	585	-265	12.5	-8.5	3400
PZT-5A	0.56	0.53	0.40	350	-190	16.6	-13.7	1600
PZT-4	0.54	0.35	0.22	225	-85	8.5	-7.5	1400
PLZT-9/65/35	-	-	-	-	-	-	-	5000

Where k_p , k_{33} , k_{31} are coupling factors, d_{33} and d_{31} are piezoelectric charge constants, g_{33} and g_{31} are piezoelectric voltage constants, $\epsilon T_{33}/\epsilon_0$ is dielectric constants.

The values from Table 3.8 allow comparing the PZT-5H with other piezoceramic elements in terms of their efficiency. Amongst all the elements listed in the table, PZT-5H presents definitely the highest values of piezoelectric charge constants d that are measures of the electric charge induced and collected on the electrodes in response to applied mechanical stress. On the other hand, piezoelectric voltage constants g related to an electric field generated by a piezoelectric material as a response to mechanical stress are lower than for PZT-5A. However, the best indicator of the piezoelectric efficiency is a coupling factor k_p that is the nondimensional and

describes the ability of a particular piezoelectric under stress and electric field configuration to transform mechanical energy into electricity or contrarily, electrical energy into mechanical. Due to the fact that it is dimensionless, it can provide a very useful comparison between diverse piezoelectric materials, regardless of the variable values of permittivity compliance. Taking into account all the PZT elements listed in Table 3.8, PZT-5H is characterized by the highest value of coupling factor, which allow considering this element as the most efficient.

3.3.2. Electrical response of PZT to the pressure pulse: stress mode

In order to test the PZT-based ceramics listed in Table 3.6 when they operate in a stress mode, each element was mounted on the surface of the circular FR-4 diaphragm, in a way illustrated in Figure 3.2c), and placed inside the pressure chamber described in section 3.1. Then it was subjected to pressure pulses, as it was explained at the beginning of this section.

The example waveforms of pressure changes, Δp , having the maximum value equal to 300 mbar, inside the chamber, and the electrical responses of PZT elements from Table 3.6 are given in Figure 3.15.

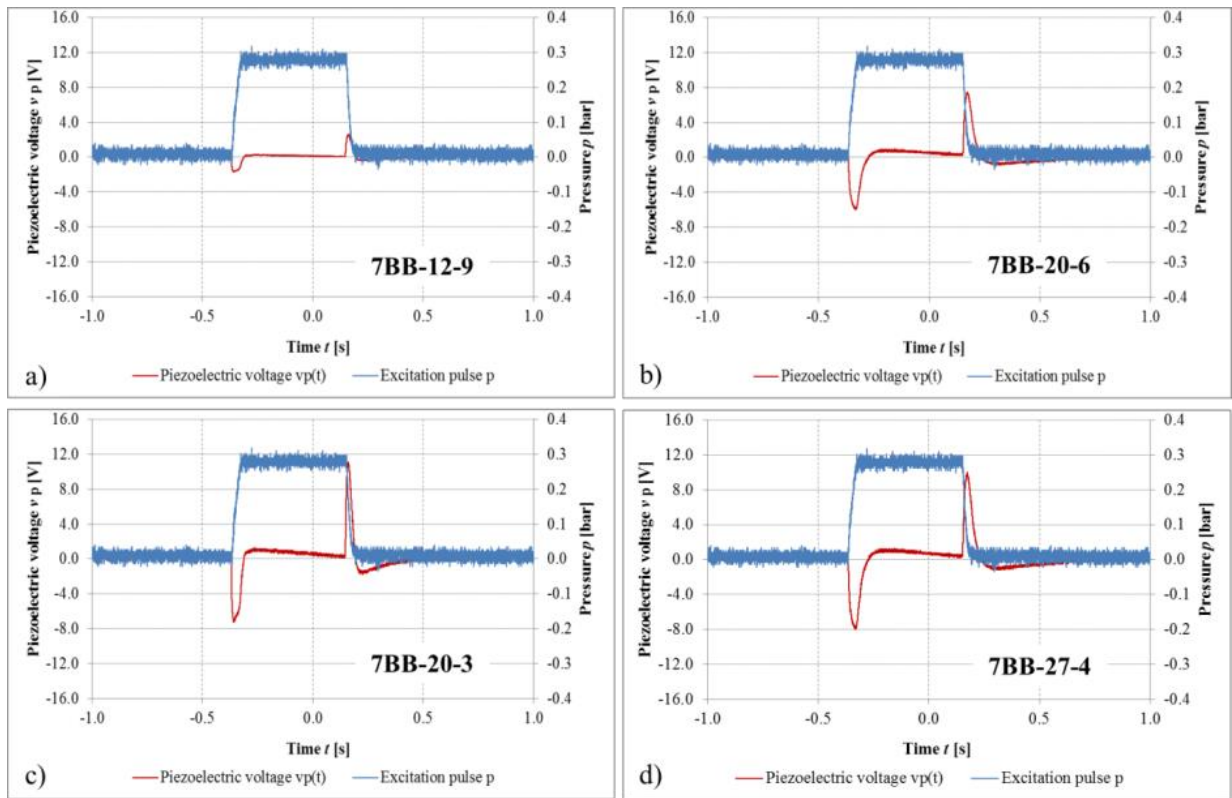


Figure 3.15: Changes of pressure Δp inside the chamber and piezoelectric voltage for the PZT-based elements (a) 7BB-12-9; (b) 7BB-20-3; (c) 7BB-20-6 and (d) 7BB-27-4 operating in stress mode.

The mean values of voltage generated as a response to applied pressure obtained in six independent experiments and their error bars corresponded to the minimal and maximal deviations from mean values are shown in Figure 3.16.

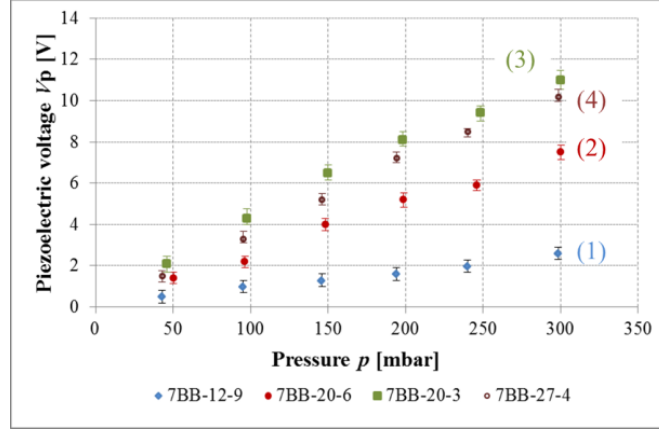


Figure 3.16: Mean values of piezoelectric voltage versus pressure for PZT ceramics operating in a stress mode.

The results from Figure 3.15 were used for determining the maximum value of voltage and estimating the power generated during one excitation pulse of 300 mbar, by each PZT element. The values of power were calculated from Eq.(3.2), and listed in Table 3.9. The values of capacitance used for calculations were taken from the measurements described in section 3.3.1.

Table 3.9: Geometrical parameters of tested PZT elements, values of maximum piezoelectric voltage V_{pmax} , and power, P , generated in the stress mode, under the pressure of 300 mbar.

Type	t_p [mm]	R_p [mm]	V_{pmax} [V]	P [nW]	C_m [nF]
7BB-12-9	0.12	4.50	2.6	1.3	10.3
7BB-20-6	0.22	7.00	7.5	12.0	10.8
7BB-20-3	0.12	7.00	11.0	45.0	20.3
7BB-27-4	0.24	9.85	10.2	72.0	25.6

For all tested elements the value of voltage evolved almost linearly with pressure. For the elements of the same thickness ((1) and (2) from Table 3.6) the voltage was higher for larger diameter. When the diameter of the element was identical (elements (2) and (3)) the voltage increased for thinner element. The values from Table 3.9 show that the highest voltage is generated for 7BB-20-3 that is a very thin element, with relatively large surface. This is related to the fact that thinner elements are more flexible and their deformation under the same pressure is higher as compared to thicker ones. However, it cannot be forgotten that apart from voltage, the power equation includes also a capacitance, C , that rises with the decreasing thickness and increasing surface of the piezo layer, which means that the value of generated power is a combination of these three parameters. This is proven by the results obtained for the largest element, 7BB-27-4, and the thinnest one 7BB-20-3. Even though the value of voltage for large 7BB-27-4 was lower than the one obtained for thin 7BB-20-3, which was due to its high thickness and small flexibility, the power obtained in the response to an excitation pulse of the same pressure was much higher for 7BB-27-4 thanks to its large surface. The chart given in Figure 3.17 shows graphically the maximum values of voltage and power generated by different PZT-based transducers during one pressure pulse of 300 mbar.

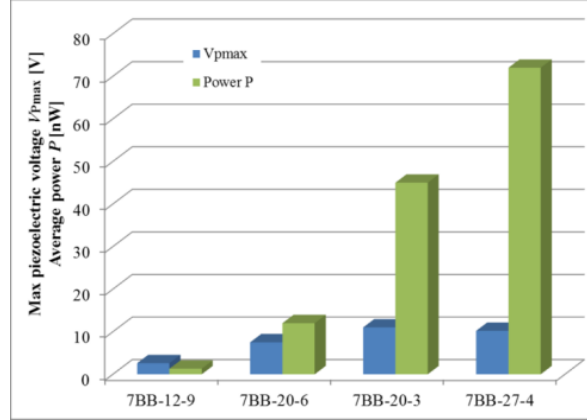


Figure 3.17: Maximum value of voltage V_{pmax} , power, P , generated by PZT-based transducers operating in a stress mode during one pressure pulse of 300 mbar.

3.3.3. Electrical response of PZT to the pressure pulse: strain mode

As it was mentioned in section 3.1, this part of the study was performed independently at TUL and in CEA-Liten and the experimental setups proposed by the two research groups are shown in Figure 3.3 and Figure 3.4, respectively. Figure 3.18a-d) present the comparison between the mean values obtained in six different experiments performed under the same conditions in two laboratories for the elements 7BB-12-9, 7BB-20-3, 7BB-20-6 and 7BB-27-4, respectively.

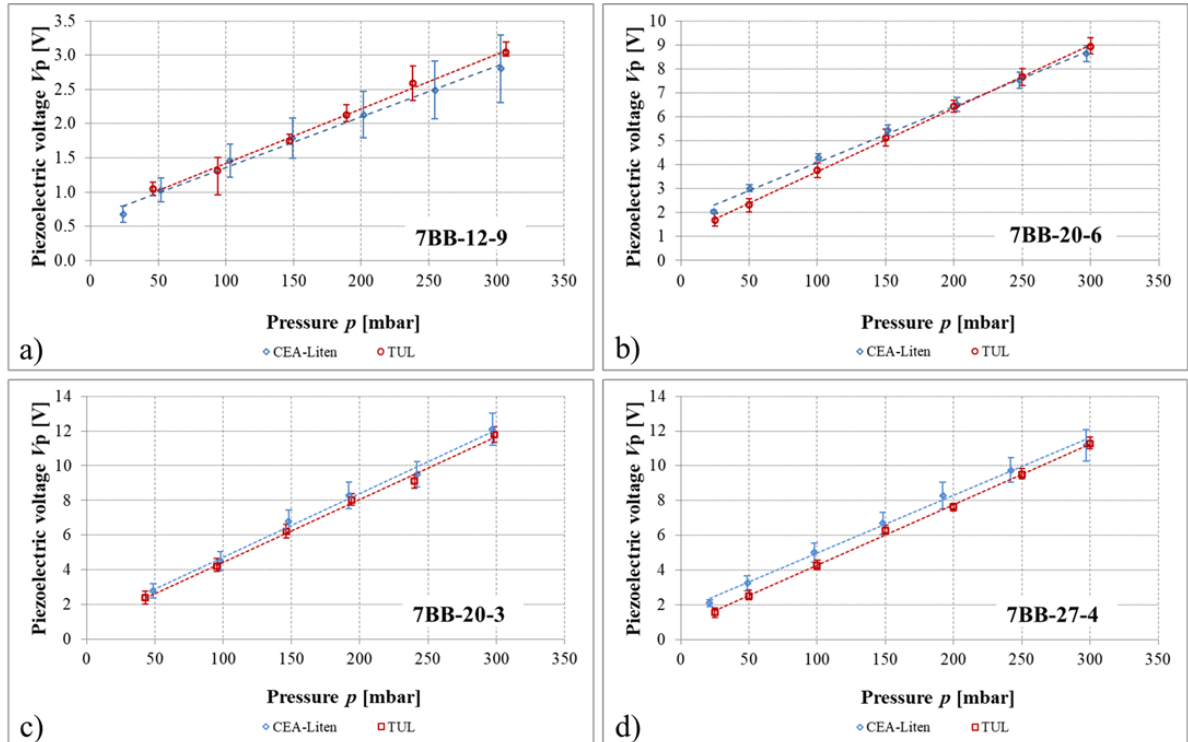


Figure 3.18: Piezoelectric voltage as a function of pressure generated by (a) 7BB-12-9, (b) 7BB-20-6, (c) 7BB-20-3 and (d) 7BB-27-4 obtained at Lodz University of Technology (red) and at CEA-Liten (blue).

The results given in Figure 3.18 show clearly that even though the design of two experimental setups differed, it is possible to obtain the reliable and repeatable results, when the experiments are performed under the same conditions. The evolution of voltage as a function of applied pressure for all elements tested at TUL are presented in Figure 3.19. The values of voltage plotted in the figures are the mean values obtained in six experiments and the error bars corresponded to the minimal and maximal deviations from mean values.

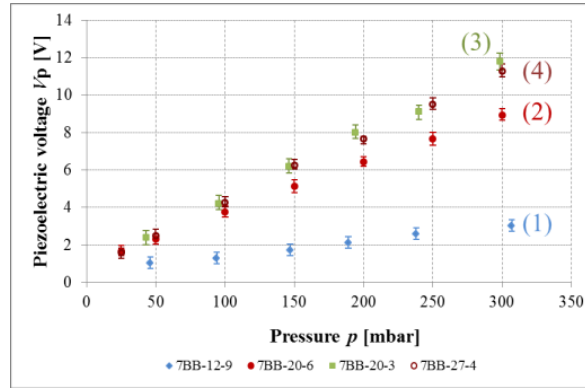


Figure 3.19: Mean values of piezoelectric voltage versus pressure for PZT ceramics operating in strain mode, measured at TUL.

The examples of electrical responses given by PZT elements tested at TUL to the pressure changes of the maximum value equal to 300 mbar, inside the chamber are placed in Figure 3.20.

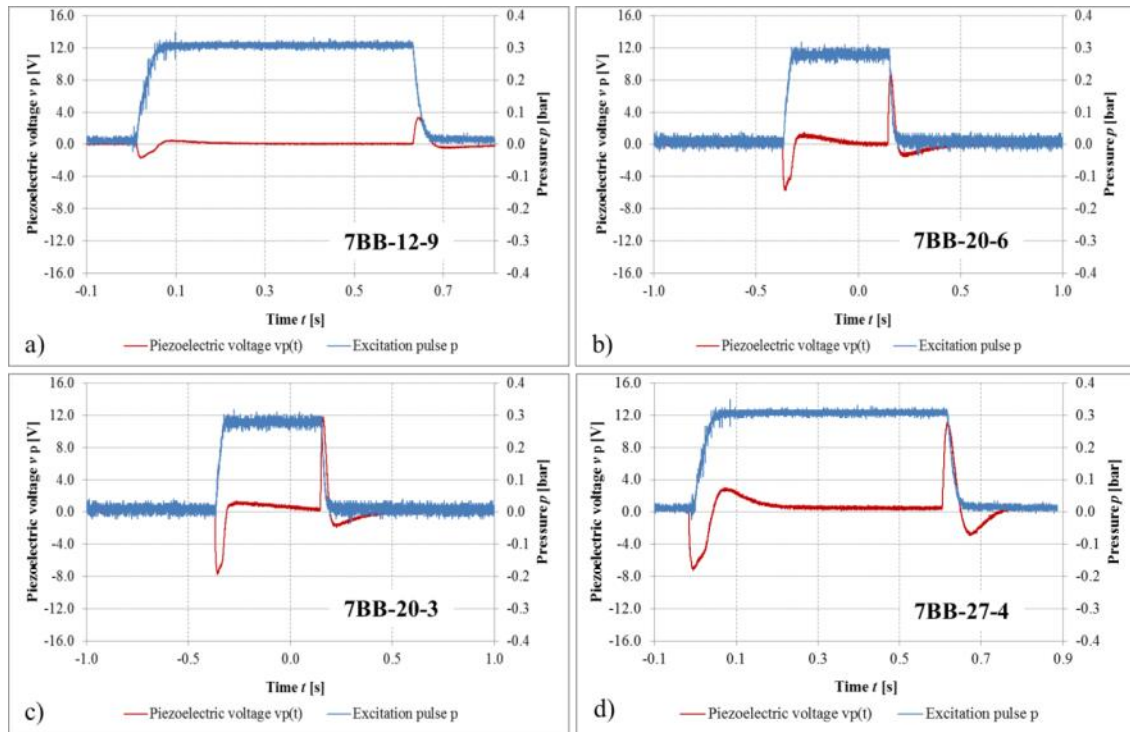


Figure 3.20: Changes of pressure Δp inside the chamber and piezoelectric voltage for the PZT-based elements (a) 7BB-12-9; (b) 7BB-20-3; (c) 7BB-20-6 and (d) 7BB-27-4 operating in strain mode.

The results given in Figure 3.20 were used for determining the maximum value of voltage and estimating the power generated during one excitation pulse of 300 mbar, by each PZT element. The values of power were calculated Eq.(3.2), and listed in Table 3.10. The values of capacitance used for calculations were taken from measurements described in section 3.3.1.

Table 3.10: Geometrical parameters of tested PZT elements, values of maximum piezoelectric voltage V_{Pmax} , and power, P , generated in stress mode, under the pressure of 300 mbar.

Type	t_p [mm]	R_p [mm]	V_{Pmax} [V]	P [nW]	C_m [nF]
7BB-12-9	0.12	4.50	3.1	1.4	10.3
7BB-20-6	0.22	7.00	8.9	14.0	10.8
7BB-20-3	0.12	7.00	11.8	51.0	20.3
7BB-27-4	0.24	9.85	11.0	126.0	25.6

The chart given in Figure 3.17 shows graphically the maximum values of voltage and average power generated by different PZT-based transducers during one pressure pulse of 300 mbar.

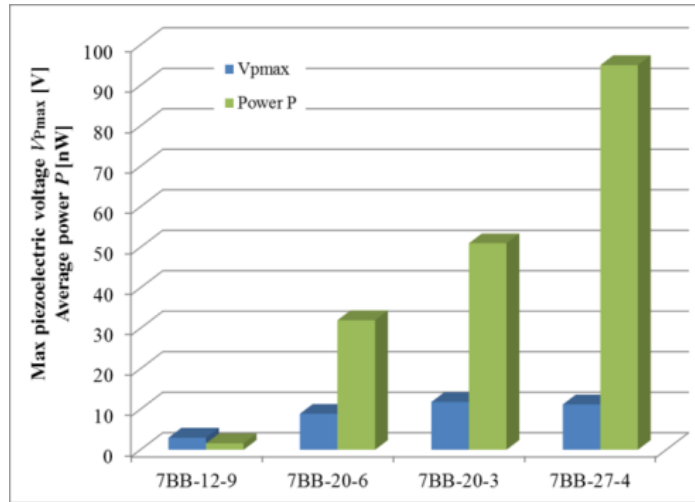


Figure 3.21: Maximum value of voltage V_{Pmax} , average power, P , generated by PZT-based transducers operating in strain mode, during one pressure pulse of 300 mbar.

Likewise in case of PZT elements operating in stress mode, the evolution of voltage value depending on applied pressure was almost linear. In case of the elements having the same thicknesses ((1) and (2) from Table 3.6) the voltage was higher for larger diameter. When the elements had the same diameters (elements (2) and (3)) the voltage slightly increased for thinner element. Also here, the results of experiments showed the strong between the geometrical parameters of the piezoelectric transducer and the value of generated power.

3.3.4. Comparison of PZT-based ceramics operating in stress and strain mode

To compare the two operation modes of PZT-based elements, the values of maximum voltage, V_{Pmax} , and average power, P , generated during a single pressure pulse of 300 mbar by different-sized transducers when they operate in stress and strain are listed in Table 3.11.

Table 3.11: Maximum piezoelectric voltage V_{pmax} , average power, P , generated by PZT-based transducers operating in stress and strain mode, when they were exposed to the 300 mbar pulse of pressure.

Type	V_{pmax} [V]		P [nW]	
	stress mode	strain mode	stress mode	Strain mode
7BB-12-9	2.6	3.1	1.3	1.4
7BB-20-6	7.5	8.9	12.0	14.0
7BB-20-3	11.0	11.8	45.0	51.0
7BB-27-4	10.2	11.0	72.0	126.0

The comparison given in Table 3.11 shows that the values of voltage and power generated due to the pressure pulse are higher, when the PZT element is mounted in a form of membrane, in a strain mode. This is due to the fact that such a way of montage ensures bigger possibility of element's bending and as a result higher value of voltage generated during the process.

3.4. Comparison between PVDF and PZT-based transducers

In order to select the most suitable piezoelectric material in terms of its application as a structural element of the device being the subject of this manuscript, the summary of the results presented in section 3.2 and 3.3 have been presented in Table 3.12. The table comprises the values of maximum voltage and average power generated under the influence of 300 mbar pulse of pressure, by the 52 μ m thick PVDF membrane, as well as the smallest and the largest of tested PZT-based transducers – 7BB-12-9 and 7BB-27-4, respectively – operating in stress and strain mode. Taking into account that a cantilevered PVDF transducer cannot be applied to the device that operates based on cyclic evaporation and condensation of the working fluid due to the leakage issue, it was excluded from this analysis.

Table 3.12: Comparison of the values of voltage and power generated in response to 300 mbar pressure pulse by PVDF and PZT materials operating in different modes.

Operation mode	Type of the material	V_{pmax} [V]	P [nW]
membrane	PVDF	2.3	0.08
stress	7BB-12-9	2.6	1.3
	7BB-27-4	10.2	72.0
strain	7BB-12-9	3.1	1.4
	7BB-27-4	11.0	126

Due to the fact that the values of power generated by the PZT-based elements are significantly higher as compared to the power generated by a PVDF membrane, it was decided to consider the PZT-transducers operating in strain mode as potential elements that shall be used as energy converters in the device proposed in present work.

3.5. Numerical modeling

Another attempt to analyze the significance of the piezoelectric element geometry was performed using COMSOL Multiphysics 4.4 with the structural mechanics module.

3.5.1. Comparison between simulation and experimental results

Initially, the simulations were carried out for piezoelectric diaphragms having the geometry of the elements provided by Murata. This study was aimed at creating a model that could be used for predicting the electrical behavior of PZT elements of diverse parameters. For this reason, in the first stage of the work, the model was verified by comparing the results of the simulations with the experimental study. In the first step, all the simulations were performed for the ideal case, where the real clamping method of the element was not considered. 3D model of the element consisted of PZT-5H cylinder placed on brass substrate, with fixed constraints on the edge and the uniform load applied to its bottom surface. The bottom surface of PZT had been chosen as an electric ground. The boundary conditions for ideal case are presented in Figure 3.22.

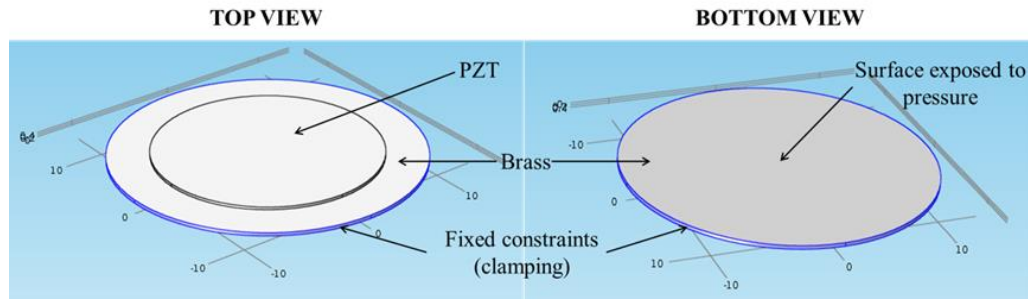


Figure 3.22: The boundary conditions for the ideal case, when the real clamping method is not considered.

Due to the fact that the first simulations were performed for ideal case, without considering the clamping conditions of PZT elements, as shown in Figure 3.23a), obtained results significantly differed from the experimental ones. This happened because the diameter of whole element, D , was introduced to the model. However, the construction of the experimental setup did not allow the whole element to actively participate in the deflection caused by applied pressure, which is schematically depicted in Figure 3.23b).

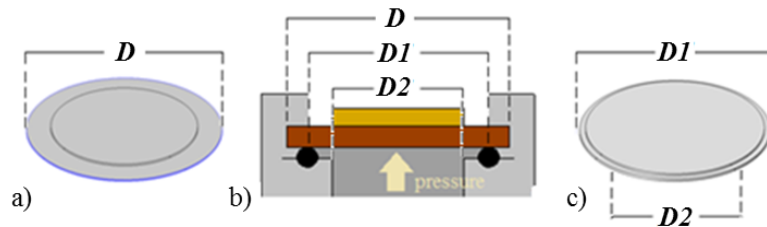


Figure 3.23: (a) Initial boundary conditions referred to the diameter of whole PZT element, D ; (b) experimental conditions; (c) modified boundary conditions corresponding to the diameter of active area, $D1$ and the diameter of the surface that was exposed to pressure $D2$.

Effectively, only a part that was not constrained by the clamping, was responsible for charge generation. These results showed, that the method of element montage and a clamping length plays a key role in the value of voltage generated during the process. For this reason, in the second attempt the boundary conditions were modified to face the real experimental case, which

means that the diameter of the element corresponded to the diameter of the clamping support relevant for each element, accordingly to the dimensions given Figure 3.23. The boundary conditions of the model, which corresponded to the real clamping conditions of tested elements are presented in Figure 3.24.

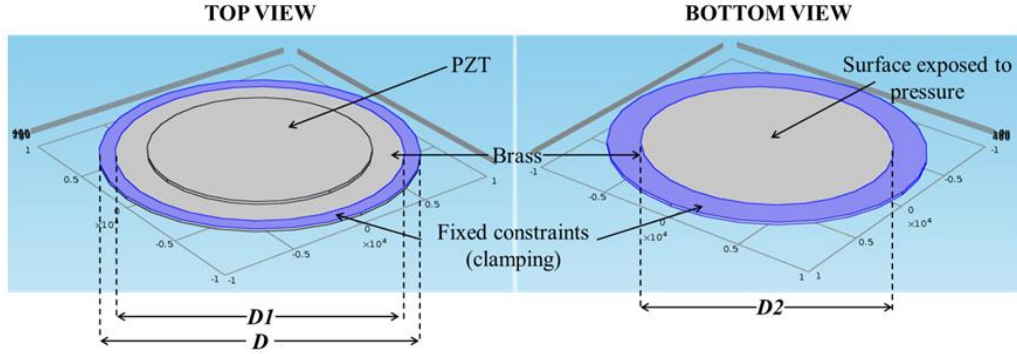


Figure 3.24: The boundary conditions, when the real clamping method is considered.

Figure 3.25 shows the values of voltage generated in response to the pressure variations obtained experimentally and the results of simulations performed for two different boundary conditions.

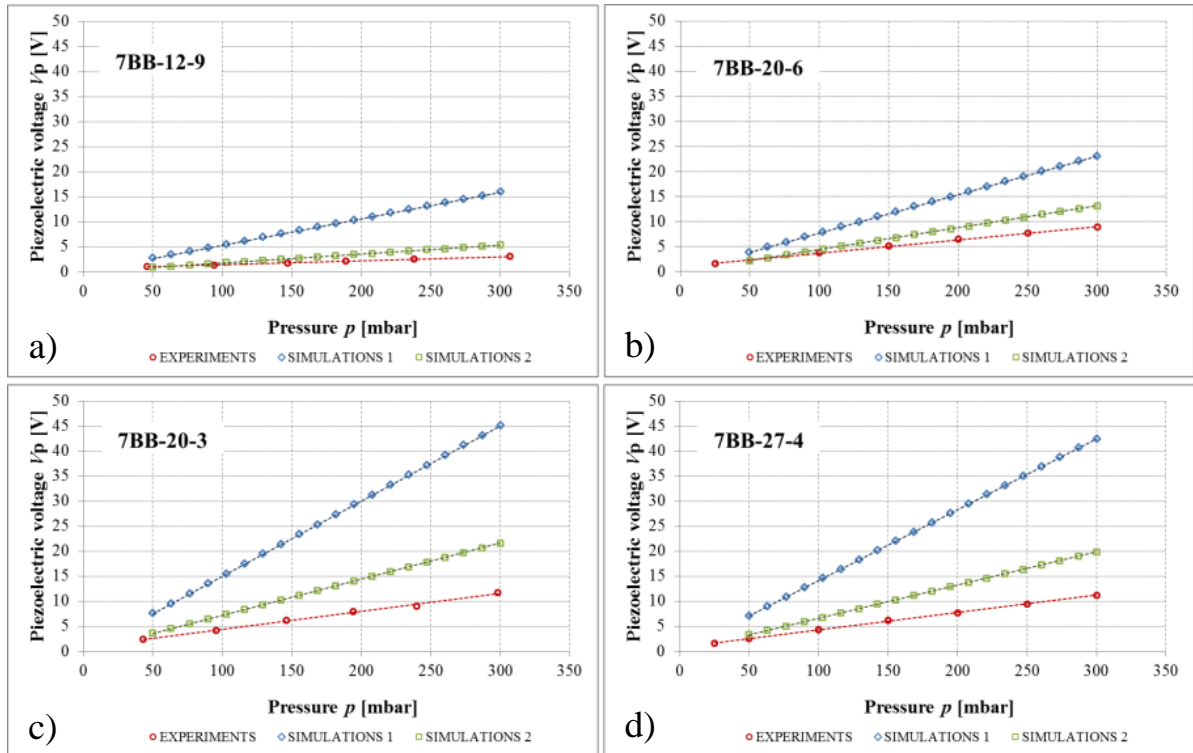


Figure 3.25: Comparison between values of voltage generated by PZT elements as a response to pressure variations obtained experimentally and as a results of simulations for (a) 7BB-12-9; (b) 7BB-20-6; (c) 7BB-20-3 and (d) 7BB-27-4.

The charts given in Figure 3.25 show the importance of the clamping in the process of charge generation and although the results of the simulations performed for boundary conditions close to the experimental setup did not match completely the results obtained experimentally, they were relatively close. The differences could be caused by the fact that also a way of tightening the piezoelectric element had an impact of its displacement and as a result, the generated voltage. As presented in Figure 3.26 there was a slight level difference between the clamping system and the PZT. This caused the modification of the clamping length, which was not included in the model, and this modification increase with the element thickness.

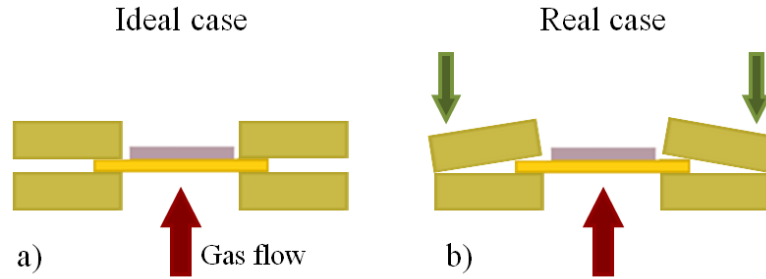


Figure 3.26: Schematic representation of tightening methods in (a) ideal and (b) real case.

3.5.2. Size optimization

Given that the goal of the present research was to create a device in a small scale, in the next step, the model was used for analyzing if it is relevant to reduce the size of the element. This could give a general idea if it is possible to miniaturize the whole structure keeping the same value of energy as given by a larger, commercially available element. To answer this the simulations of more complex cases concerning geometry modifications were performed. The boundary conditions used for the simulations corresponded to the ideal ones, shown in Figure 3.22.

The parameters that were considered in these simulations were as follow: the value of applied pressure, p , PZT thickness t_p and its radius R_p . Figure 3.27a) shows the evolution of voltage for pressure values between 50 mbar and 300 mbar for 7BB-20-6 element. The graph depicted in Figure 3.27a) shows that the value of piezoelectric voltage increases with the rise of pressure. The influence of PZT thickness t_p on the voltage generation is nonlinear. One can observe that the peak of voltage is generated for thicker layer, however with further increase of this parameter this value drops drastically.

Results of the simulations depicted in Figure 3.27c), showed that the value of electric potential remained at the same level for the low values of PZT radius R_p and it begins to decline when the radius of piezoelectric layer has the length of around 60% of the substrate radius R_s . Analyzing the value of piezoelectric voltage only, accordingly to Figure 3.27, it seemed to be reasonable to use the piezoelectric element with possibly the lowest volume of PZT. However, it has to be taken into account that if one consider piezoelectric material as a capacitor, the electric energy is proportional not only to the square of the voltage, but also to the capacitance of the

material. Contrarily, the capacitance is lower with the smaller surface of electrodes, hence with the smaller radius of the material R_p .

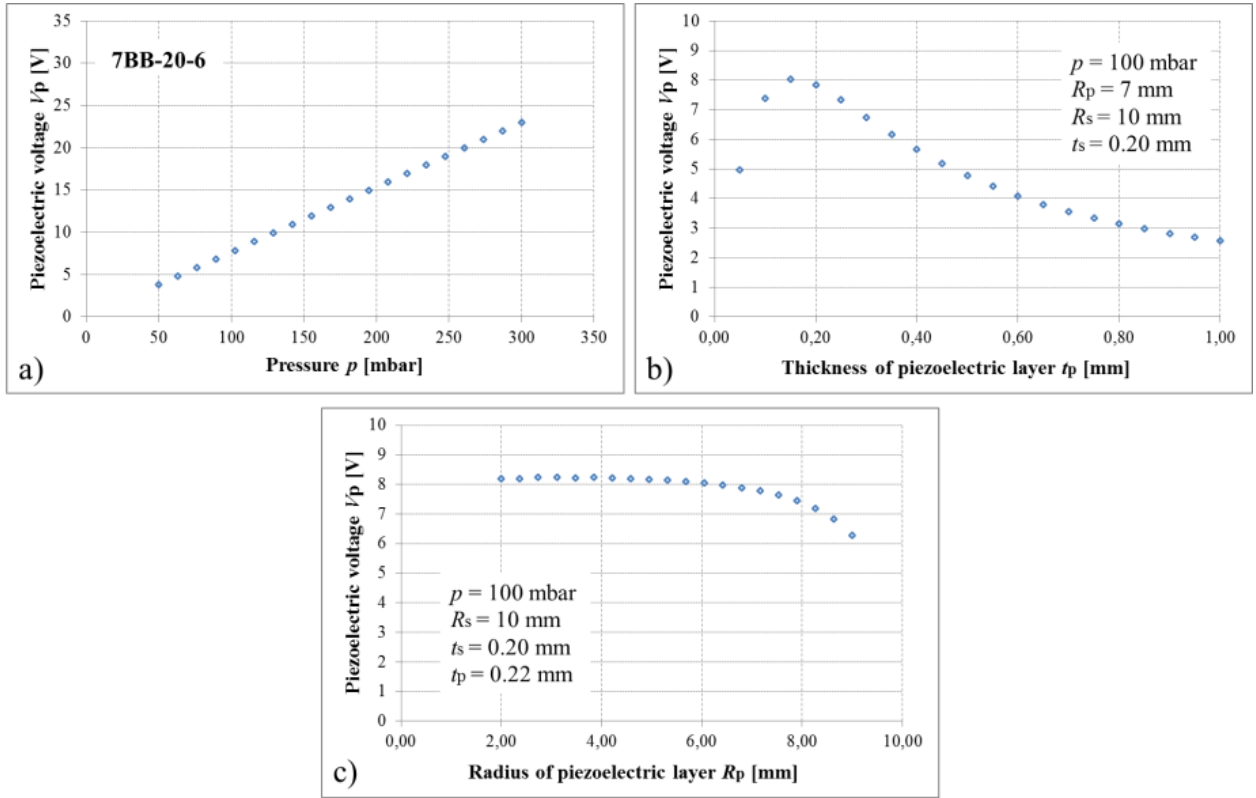


Figure 3.27: Piezoelectric voltage V_p as a function of pressure p for 7BB-20-6; (b) Piezoelectric voltage V_p as a function of piezoelectric thickness t_p at a constant substrate geometry value of pressure $p = 100$ mbar; (c) Piezoelectric voltage V_p as a function of piezoelectric radius R_p at a constant substrate geometry and a value of pressure $p = 100$ mbar.

All the observations lead to the conclusion that in the case of element composed of two layers of materials, with different mechanical parameters, the construction and the correlation between the geometries of these two layers have a huge impact on the energy generated by the structure. It is therefore essential to find the construction that is optimal from mechanical and thus electrical point of view.

3.5.2.1. Influence of PZT thickness

In order to establish the influence of PZT thickness on the value of generated voltage, the two diaphragms, 7BB-20-6 and 7BB-20-3, having exactly the same radius of piezoelectric layer $R_p = 7$ mm and substrate $R_s = 10$ mm, but different total thicknesses t_{tot} equal 0.42 mm and 0.22 mm respectively, had been simulated. The dimensions of these elements are specified in Table 3.1 and the results of the simulations are presented in Figure 3.28 that represents the electric potential V as a function of pressure p for these two elements. The results showed, that when the surface of two elements was the same, higher value of voltage was generated by

the element that had lower total thickness t_{tot} . However, it has to be taken into account that the diaphragm consists of two layers, made of different materials and even having the same total thickness of the element t_{tot} , the thickness of each layer t_p and t_s may vary. It was therefore important, to analyze what was the optimal value of this parameter for each layer. This would allow obtaining the highest possible value of voltage.

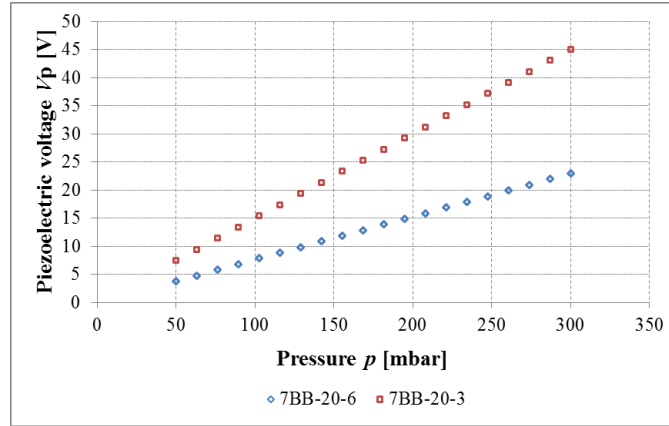


Figure 3.28: Electric potential V as a function of applied of pressure p for two diaphragms with different sizes.

In order to understand the correlation between thicknesses of two layers, t_p and t_s , the evolution of voltage with increasing PZT thickness t_p , but for constant total thickness of the diaphragm t_{tot} was plotted. The example of this correlation is depicted in Figure 3.29.

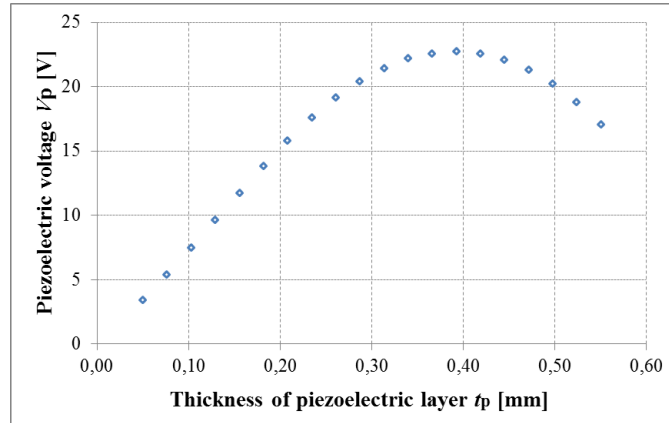


Figure 3.29: Electric potential V as a function of thickness of piezoelectric element t_p for constant thickness of the whole element $t_{\text{tot}} = 0.42$ mm.

The examination of several simulations results showed that high values of voltage were obtained always for the situation when the layer of PZT was thicker than the substrate layer. Moreover, irrespectively of diaphragm's radius, the peak of voltage occurred always when the thickness of PZT t_p stood at 64% of total thickness of the diaphragm t_{tot} . This led to the conclusion that, in order to enhance efficiency of piezoelectric element, it seems to be

reasonable to modify the geometry of the diaphragm by increasing the thickness of PZT layer t_p and reducing the thickness of a substrate t_s , keeping the relating ratio: $t_p = 64\% t_{tot}$.

3.5.2.2. Influence of PZT radius

Figure 3.30 presents the voltage dependence on pressure value for three different elements 7BB-20-3, 7BB-15-6 and 7BB-12-9. All the elements had exactly the same thickness of PZT $t_p = 0.12$ mm and substrate $t_s = 0.10$ mm, while radius of each element R varied having the value of 10 mm, 7.5 mm and 6 mm, respectively.

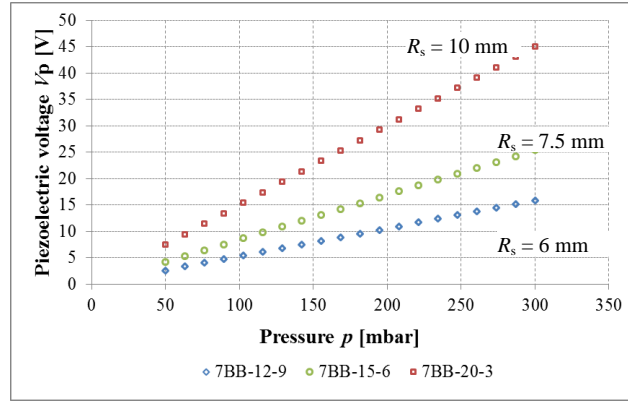


Figure 3.30: Electric potential V as a function of applied pressure p for three diaphragms with identical thicknesses t but different radiuses R .

The results of simulations showed, that for the elements having the same thickness but different values of radius, the voltage increased with increasing value of radius. This was therefore a drawback in terms of the entire system miniaturization.

3.5.2.3. Miniaturization

Presented analysis allowed to draw three conclusions that play significant importance in terms of size optimization:

- 1) when the thickness of PZT t_p stands at 64% of the total thickness t_{tot} of the diaphragm, the voltage V reaches its maximum value,
- 2) diaphragm's radius reduction leads to the drop of voltage value V ,
- 3) total thickness reduction t_{tot} results in voltage rise.

Further simulations performed based on these observations proved that, theoretically, for the same pressure p applied to a piezoelectric element it is possible to obtain higher value of voltage, when the size of the element is smaller.

Initial simulations were performed for commercially available 7BB-20-6 PZT-based element and the evolution of voltage with increasing pressure, represented by a blue line, was plotted in Figure 3.31a). Further, the thicknesses of the piezoelectric layer and the substrate were modified to 0.27 mm and 0.15 mm, respectively. This was to ensure that the piezoelectric thickness stands at 64% of total thickness t_{tot} of the element. The values of radius for both layers remained

unchanged. The voltage as a function of pressure p for this modified element is represented in Figure 3.31a) by a red line. One can observe that the voltage generated by modified element was slightly higher than for commercially manufactured 7BB-20-6. However, when one continued to modify the geometry of the element in order to reduce its radius, the decrease of the voltage occurred. This situation is presented in Figure 3.31b), where the green line represents the voltage V dependence on applied pressure p for the element with the radius of PZT R_p and substrate R_s , equal 6 mm and 9 mm, respectively. The third step of the simulations, aimed at size reduction of the system, was the reduction of the whole diaphragm thickness t_{tot} , but relation $t_p = 64\% t_{tot}$ was kept. Due to the fact, that thinner element is more flexible, its deflection is higher and, as a result, the expected voltage generated by piezoelectric layer should be higher as well. Total thickness of the diaphragm chosen for simulations had the value of 0.27 mm, which give 0.17 mm of PZT thickness t_p and 0.10 mm of substrate thickness t_s . This value was chosen due to the fact, that the substrate thickness cannot be reduced endlessly and the value of 0.10 mm is the lower thickness of substrate for commercially available elements. Purple line in Figure 3.31c) represents the voltage evolution depending on pressure p for the element with a total thickness t_{tot} of 0.27 mm.

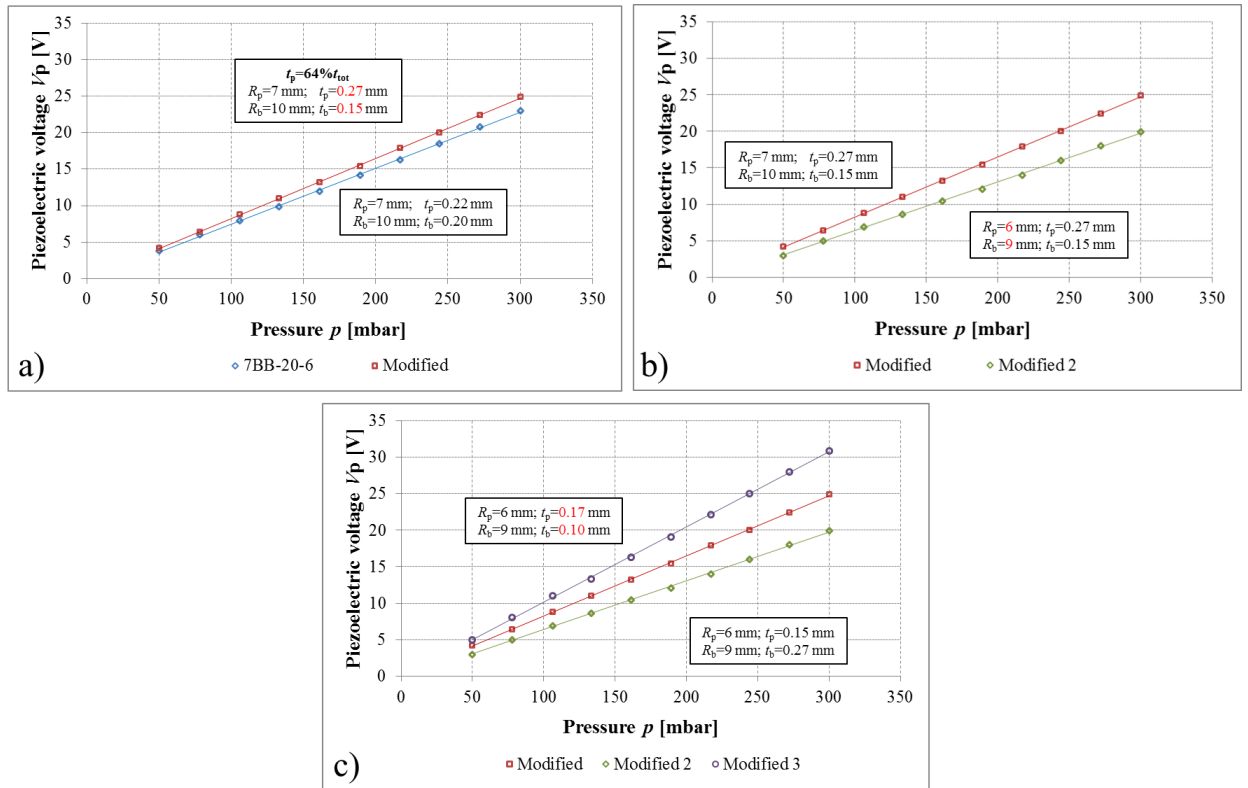


Figure 3.31: Electric potential V as a function of applied pressure p for (a) element 7BB-20-6 (blue line) and element with modified dimensions in a way that $t_p = 64\% t_{tot}$ (red line); (b) element with modified thickness in a way that $t_p = 64\% t_{tot}$ (red line) and element with smaller radius of PZT and substrate (green line); (c) element with modified thickness in a way that $t_p = 64\% t_{tot}$ (red line), element with smaller radius of PZT and substrate, (green line), and element with smaller total thickness.

The simulations showed that the reduction of the element thickness could result in a significant increase of generated voltage. Taking into account all performed simulations, one can conclude that, in theory, after several structural modifications, it is possible to reduce the size of the piezoelectric element and obtain higher value of voltage than in a case of larger element. This hypothetical situation is illustrated in Figure 3.32, where purple line represents the voltage V as a function of pressure p for the element with smaller dimensions compared to the element represented by the blue line, being commercially manufactured 7BB-20-6.

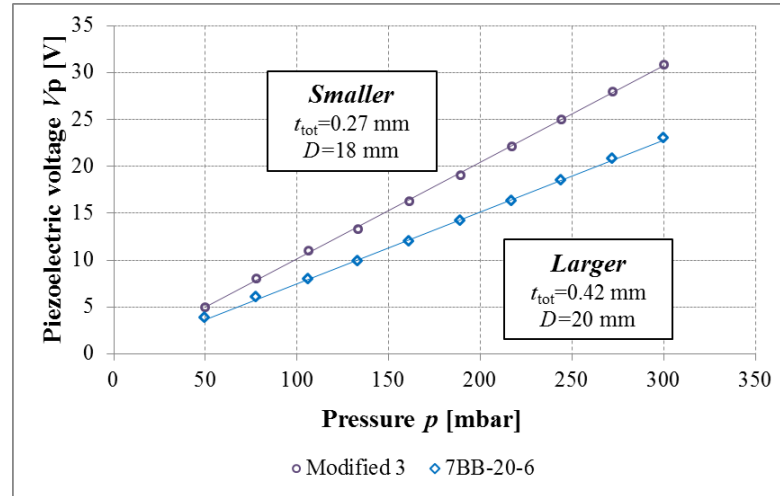


Figure 3.32: Electric potential V as a function of applied pressure p for element with total thickness t_{tot} of 0.27 mm and diameter D of 18 mm (purple line) and for element with total thickness t_{tot} of 0.42 mm and diameter D of 20 mm (blue line).

3.6. Summary of the chapter

In this chapter, the experimental setup enabled the study on the electrical behavior of PVDF and PZT-based piezoelectric materials, in response to a single pulse of pressure has been proposed. Additionally, a numerical modeling aimed at verifying if it is possible to increase the value of electrical energy generated by reducing the scale of PZT membrane has been performed. The presented analysis led to the following conclusions:

- higher values of voltage and power are generated for the transducers of lower thickness of piezoelectric layer,
- PVDF operating in a form of membrane generates higher values of voltage and power than cantilevered transducer, but it is more fragile,
- exceeding a specific value of pressure applied to the membraned transducer results in losing its elastic properties of the material or even its destruction. As a consequence, the PVDF membrane can give reliable and repeatable results only in a range of low pressures. For 52 μm thick membrane of 7 cm^2 surface, applied pressure could not exceed the value of 1 bar,
- for the same value of pressure, PZT-based ceramics generates much higher value of voltage and power than PVDF transducer,

- PZT operating in a strain mode gives higher value of voltage and power as compared to the same transducer operating in stress mode,
- clamping method strongly influences the electrical behavior of PZT membranes,
- theoretically, for specific dimensions of PZT-based elements it was possible to improve the energy generation by performing several modifications of PZT geometry.

Based on the results presented in this chapter it was decided to apply a PZT-based transducer operating in the strain mode for the structure of the device that was the subject of this manuscript. Amongst others, the detailed parameters of the transducer has been established in *Chapter 4*.

4. Concept of a thermal energy converter based on phase-change phenomenon

4.1. The prototypes applying phase-change phenomenon to harvest thermal energy

The research performed on the ground of the patent filed by Skotnicki [50], which was presented in *Chapter 2*, are described in sections 4.1.1, 4.1.2 and 4.1.3. Section 4.1.1 is related to the development of a microfluidic heat engine based on explosive boiling, section 4.1.2 corresponds to the development of a self-oscillating fluidic heat engine (SOFHE), both performed at the Sherbrooke University, Canada, whereas section 4.1.3 refers to the study of Solar energy, Harvesting, Thermal management research group of CEA-Liten, Grenoble, France, focused on the development of a thermo-mechanical oscillating system.

4.1.1. Microfluidic heat engine based on explosive boiling

A microfluidic heat engine proposed by Léveillé et al. [63] was based on explosive boiling phenomenon that allowed accumulating the energy in a liquid by heating it and rapidly releasing in a form of mechanical impulse. The engine presented by the authors operated in three main phases:

- 1) Liquid pre-heating.
- 2) Rapid liquid evaporation inside a confined chamber resulting in pressure increase.
- 3) Expansion providing mechanical work.

The abrupt evaporation can occur either due to a rapid contact of the liquid with a hot surface or due to exceeding its saturation conditions. This can be obtained by a sudden drop of pressure as well as by superheating the liquid above the saturation temperature. If the liquid is enclosed inside a chamber, its fast change into a gas phase results in a pressure increase. In order to obtain the explosive evaporation phenomenon in the system, the authors proposed the approach of a sudden pressure raise as a pressurization mechanism in the heat engine cycle. The mechanical work done by the expanding vapor during the whole cycle was converted into electricity by the deformation of a piezoelectric membrane, which induced the electric charges.

Figure 4.1 shows a schematic cross-section and a photograph of the microfluidic heat engine proposed by the authors. The device was mounted on a silicon substrate and it was composed of a planar expansion chamber with fluid ports, a thermocouple and a piezoelectric membrane covering a top part this chamber. In order to seal the device, it was coated with epoxy. A commercially available PZT-based piezoelectric consisted of 230 μm ceramics and 200 μm brass substrate was used as a transducer. The inlet and outlet fluid ports were composed of silica capillary tubes of 250 μm diameters. To provide water, playing a role of a working fluid, to the chamber via the inlet capillary, a syringe pump was used. The hot plate ensured the heating of a bottom wall of the device. To improve the heat exchange from the hotplate to the system, a copper plate and silicon thermal grease were used in a way shown in Figure 4.1b).

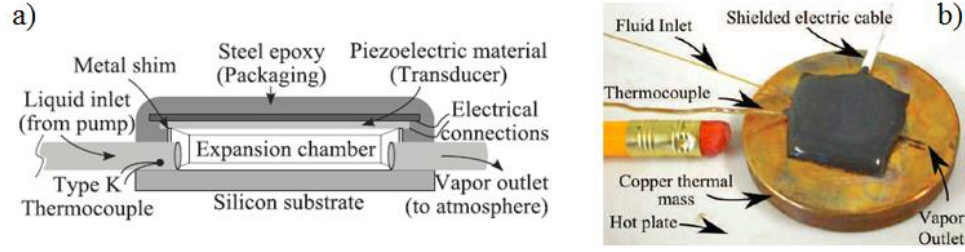


Figure 4.1: (a) Schematic cross-section and (b) a photograph of microfluidic heat engine [63].

The operation of the engine was initiated by water injection and its further heating in the expansion chamber. Inside the chamber a rapid vaporization of some portion of liquid occurred causing a fast, close to 10 ms, pressure increase. Then the vapor was being released to the ambient through the vapor outlet causing its expansion, until the atmospheric pressure was reached inside the chamber. Fresh water being provided continuously by the pump was replacing gradually the water evaporating from the system. Therefore, a condensation process that should occur in a closed system was not accomplished in this device and it was operating based on an open cycle mechanism. The cycle repeated systematically due to a continuous flow of water being provided to the chamber and a regular periodic operation of the engine was observed for several hours. Figure 4.2a-b) demonstrate one cycle of the engine represented by a piezoelectric voltage signal measured from one pulse, and several voltage pulses showing continuous operation of the device at the temperature of 145°C for a water flow of 10 $\mu\text{l}/\text{min}$, respectively.

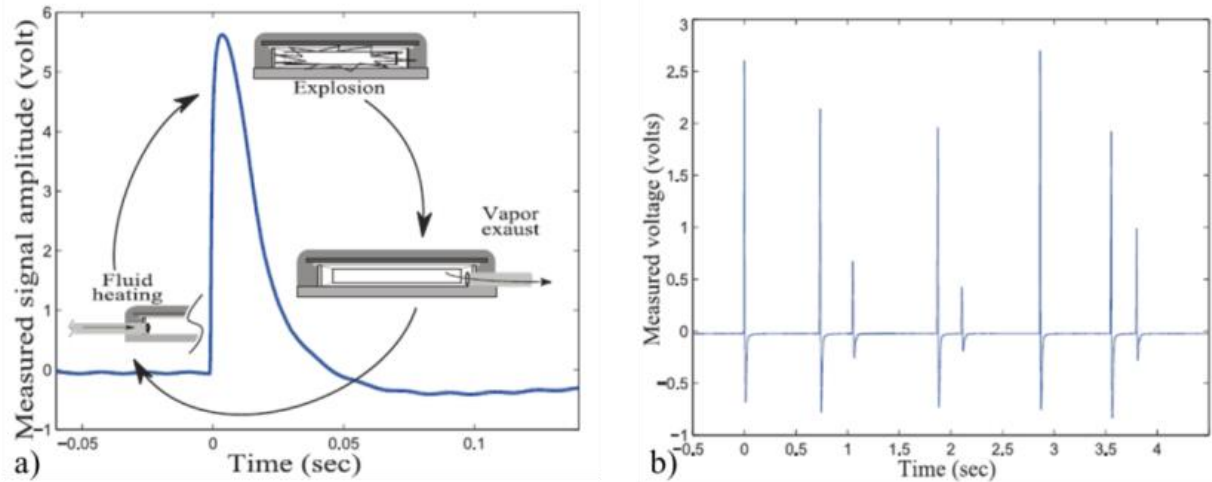


Figure 4.2: Phases of a cycle represented by a piezoelectric signal of one pulse [63].

The authors observed that the frequency and the amplitude values of generated signal varied depending on the flow rate as well as on the temperature of the surface. The influence of the input water flow on the characteristics of the signal was examined at the same temperature of a hot surface equaled to $130 \pm 10^\circ\text{C}$, for the flow rates between 5 $\mu\text{l}/\text{min}$ and 80 $\mu\text{l}/\text{min}$ and the results are presented in Figure 4.3a). One can see that the power increased with a water flow rate up to 25 $\mu\text{l}/\text{min}$, for which it reached its maximum. The authors observed that within this range of

rates, the amplitude of the signal remained almost constant, the frequency however raised rapidly. Above 25 $\mu\text{L}/\text{min}$ flow rate, the average power dropped and the cyclic pulses were gradually replaced by bursts of low amplitudes.

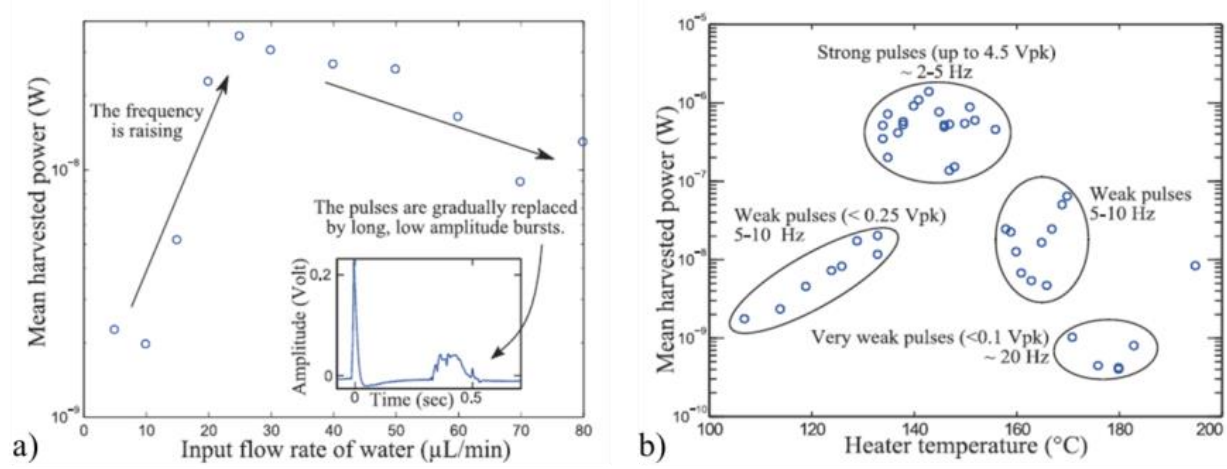


Figure 4.3: Influence of (a) the water flow rate on power, frequency and amplitude values of the generated signal, at constant temperature equal to $130\pm 10^{\circ}\text{C}$; (b) the hot temperature on power, frequency and amplitude values of the generated signal, at a constant water flow rate equal to $10 \mu\text{L}/\text{min}$ [63].

As demonstrated in Figure 4.3b) that illustrates the influence of the hot temperature on power, frequency and amplitude values of the generated signal, for the same liquid flow equaled to $10 \mu\text{L}/\text{min}$, the power at low temperatures, between 105°C and 135°C , increased clearly with the value of temperature. The frequency of the signal achieved high values of 5 Hz to 10 Hz, the amplitudes however were lower than 0.25 V. For higher temperatures, within the range of 135°C and 155°C , the maximum power increased significantly, the amplitudes raised up to 4.5 V, but the frequency dropped to the values between 2 Hz and 5 Hz. This sudden change of the signal characteristics showed a nonlinearity of this phenomenon. For example, at the temperatures close to 155°C the two different behaviors of the signal, namely strong and weak pulses alternating in time were observed. Finally, at high temperatures starting from 170°C , the frequency increased again up to a very high value of 20 Hz. Nonetheless, the amplitude dropped drastically to the values lower than 0.1 V.

The maximum power density of the device, calculated from the data presented in Figure 4.3, was around $1.6 \mu\text{W}/\text{cm}^2$. However, the authors underlined that the main goal of this research was to demonstrate the possibility of obtaining the explosive boiling phenomenon inside a microfluidic heat engine, and its optimization in terms of power generation was not the subject of their analysis. Nevertheless, they propose several improvements to enhance the energy transfer in the future. One of the solution is to match the mechanical impedance between the pulse of pressure and a piezoelectric membrane. In order to cause a larger membrane deflection, the flexible bimorph piezoelectric transducer could be used. Moreover, the reduction of the chamber volume would result in higher steam pressure and as a consequence, a higher amplitude of the signal. Additionally, the condensing chamber and the pumping mechanism

could be integrated, forming a closed system. Finally, in order to increase the frequency value, more capillary inlets could be assembled. Assuming that the reduction of the chamber thickness would result in an enhancement of mechanical coupling by 2-4 times and the flexible bimorph transducer would improve the extracted energy at least 2 times, the estimated power density could raise to values between $50 \mu\text{W}/\text{cm}^2$ and $100 \mu\text{W}/\text{cm}^2$.

4.1.2. Self-Oscillating Fluidic Heat Engine (SOFHE)

The innovative approach to harvest low-quality heat sources was proposed by Monin et al. [64]. Thermal energy was first converted into pressure pulsations by a self-excited thermo-fluidic oscillator driven by a periodic phase change of a working fluid enclosed in a channel. Then this mechanical energy was converted into an electrical power by a piezoelectric membrane. The SOFHE demonstrator is shown in Figure 4.4.

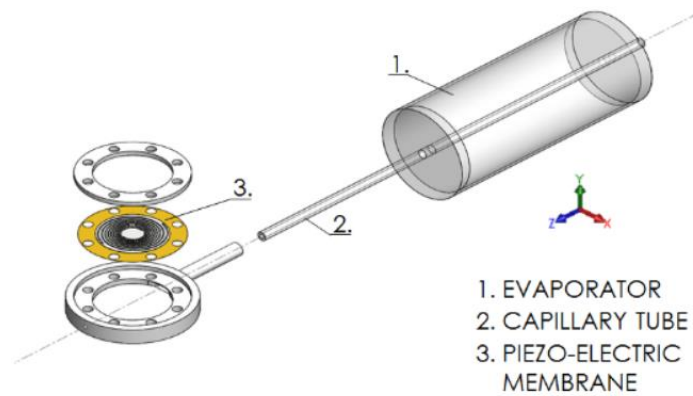


Figure 4.4: Self-Oscillating Fluidic Heat Engine [64].

The operation principle of the engine was divided into 2 main steps:

1) Thermal to mechanical energy conversion, where a constant source of heat supplied a passive, self-oscillating mechanism through an evaporator, resulting in a generation of mechanical energy via capillary tube.

2) Mechanical energy conversion into electricity by a piezoelectric membrane.

The first step of the conversion occurred due to a 2 mm/4 mm inner/outer diameters capillary tube, filled initially with deionized water, with one end closed and another one attached to the piezoelectric membrane. A part of the capillary was inserted into a larger glass tube, so-called evaporator of 30 mm diameter, filled with constant temperature glycerin. The remaining section was cooled by ambient air convection. In the hot zone, a vapor bubble was formed. Due to a heating process, the volume of vapor expanded until it reached its thermal equilibrium position. The meniscus started to oscillate depending on the thermal gradient at the interface of the liquid and vapor phases, as shown in Figure 4.5. The evaporation process started when the meniscus entered the hot zone. The pressure in the vapor bubble increased pushing the liquid towards the cold zone. Then, the vapor condensed, lowering the pressure in the bubble, which forced

the liquid column to come back into the hot zone. As a result, the self-sustained periodic oscillations occurred generating pressure fluctuations that could be used for mechanical work.

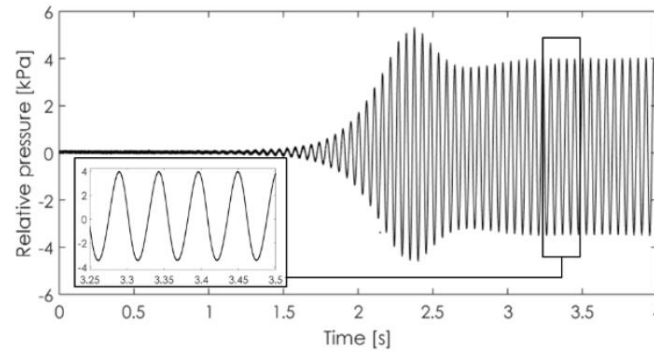


Figure 4.5: Oscillation start-up regime: no oscillations up to $t = 1$ s; transient regime at a time range between 1 s and 3 s; stabilization of meniscus oscillations' amplitude starting from the third second of the operation [64].

In order to ensure the second step of energy conversion a dedicated bimorph piezoelectric membrane, formed in a planar spiral, shown in Figure 4.6, was applied. To improve the efficiency of the conversion, the mechanical impedances of the thermo-fluidic engine and the transducer should be matched. The planar spiral form of the piezoelectric allowed controlling the mechanical stiffness and adapting its impedance.

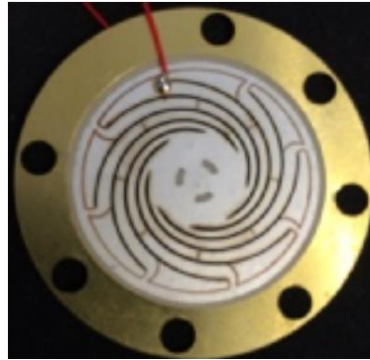


Figure 4.6: Piezoelectric bimorph spiral electromechanical transducer [64].

Figure 4.7a) shows the pressure-volume diagram for a hot source temperature set at 115°C . These results refer to the first stage of energy conversion – thermal to mechanical. The mechanical power calculated for the thermodynamic cycle was 3.3 mW. Even though the power was consumed through viscos energy dissipation of the liquid and the capillary walls, it gave the order of magnitude of the thermodynamic power that could be delivered by this cycle. Regarding the dimensions of the oscillator, the density power was $5 \text{ mW}/\text{cm}^3$. Figure 4.7b) corresponds to mechanical to electrical conversion and it shows the output voltage measured by an oscilloscope of $1 \text{ M}\Omega$ impedance at the temperature of 140°C with respect to time.

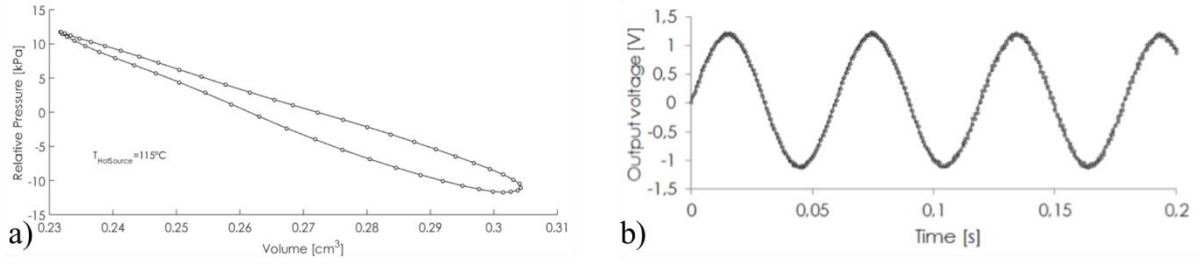


Figure 4.7: (a) P-V diagram of a free-loaded SOFHE thermo-fluidic oscillator; (b) SOFHE voltage output in a 1 M Ω load [64].

The power dissipated through the electrical load was 0.69 μW . The power generation could be greatly increased by finding an optimal electrical load for generator as well as further optimization of the piezoelectric membrane.

4.1.3. Thermo-mechanical oscillating system at macroscale

The objective of the research conducted by Soupremanien et al. [64,65,66] was to design and optimize a thermo-mechanical energy harvesting system operating based on phase-change phenomenon of a working fluid in a closed environment under the passive conditions. The device of the dimensions up to a few centimeters was considered as macroscopic. The main goals of this study was to fabricate a system that:

- generates controlled pressure variations in closed environment,
- does not contain any rotational elements and is based on piezoelectric effect,
- opens the possibility of miniaturization in terms of geometry architecture.

In this study, the oscillations occurring due to a sudden pressure decrease in a close chamber were obtained for passive conditions, which means that the heat was constant.

Although during the project several prototypes of the device were proposed, the operation principle was always the same and it was based on the patent of Skotnicki [50]. A device was composed of three parts – an evaporator being in contact with a hot surface, a condenser related to a cold surface and a channel spanning these two elements. Additionally, a PZT-based ceramics was mounted on top of the condenser. Figure 4.8 shows a schematic cross-section of the device.

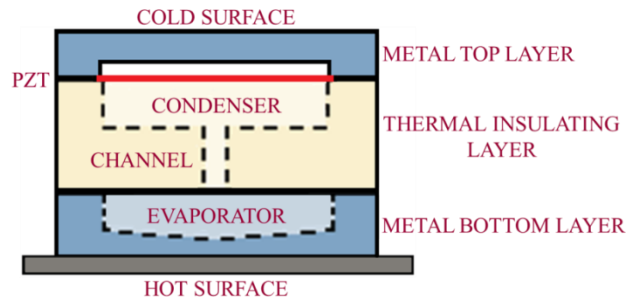


Figure 4.8: Schematic cross-section of the device.

In order to obtain a cyclic, rapid evaporation and condensation of the working fluid enclosed inside the system, specific working conditions had to be provided. To make the process effective, the space within which the fluid was enclosed should be confined and the whole device had to be tightly sealed. Additionally, the boiling temperature of the fluid should be higher than the temperature of a hot bottom layer and at the same time lower than the temperature of a top part of the device. According to the hypothesis, the operation mechanism was supposed to be divided into 5 steps:

- 1) Due to a contact with a surface hotter than the boiling temperature of the liquid enclosed in the system, it rapidly moves from liquid to vapor phase, leading to a high local overpressure and mechanical stress in the portion of liquid.
- 2) This mechanical stress is transmitted through the channel to the top part of the device, where it affects the piezoelectric element.
- 3) The mechanical stress is then transformed into electric signal due to the deflection of the piezoelectric.
- 4) The vapor condensed due to a contact with a top surface that is colder than the boiling temperature of the fluid.
- 5) Drops of liquid fall back to the evaporator and the whole process could be repeated.

In order to enable the oscillation existence, a sufficient ΔT between hot and cold surface should be provided. For this reason, the channel that spanned the evaporator and the condenser was fabricated in a thermal insulation layer made of Teflon. Additionally, to ensure that the temperature of the top part of the device was always lower than the boiling temperature of the working fluid, a cooling fan was applied in the experimental setup, above the device.

One of the first prototype designed and fabricated by the authors, shown in Figure 4.9, had the dimensions of 35 mm \times 35 mm \times 20 mm and its operation was enhanced by a small metal sphere placed on top of the channel. This element was used in order to obtain higher values of signal amplitudes generated by the piezoelectric. In this operation mode vapor passing through the channel caused the motion of the sphere towards the piezoelectric element. Considering that the mass of the sphere is much larger than the mass of vapor hitting piezoelectric, the expected amplitude of the signal was higher as well.

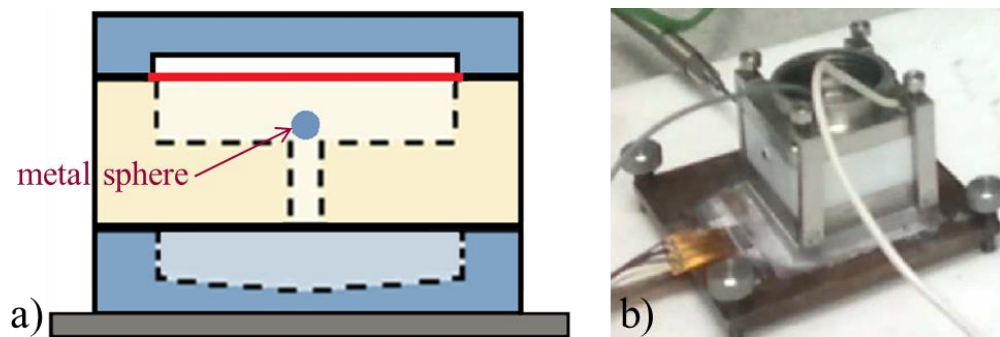


Figure 4.9: (a) Schematic cross-section and (b) a photograph of the prototype [65].

Figure 4.10 shows an example of the voltage signal generated by the device versus time. In general, the values of amplitudes were comprised between 1.5 V and 7 V, whereas the frequency of the signal varied between 0.5 Hz and 1.2 Hz.

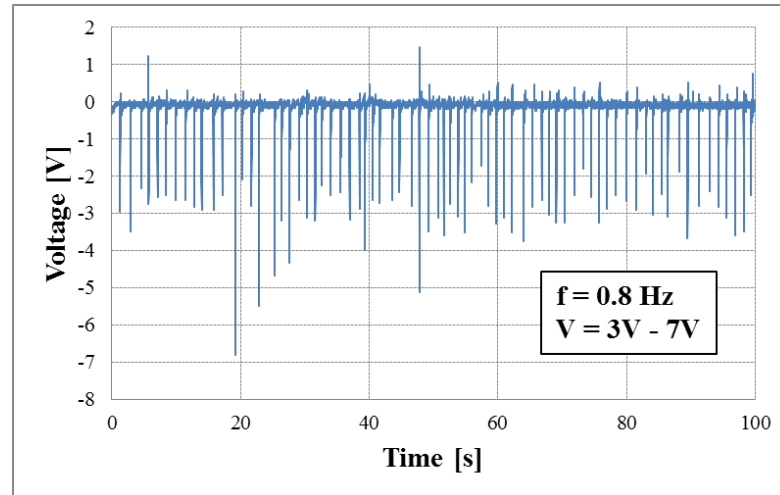


Figure 4.10: Voltage signal generated by the system versus time at heat flux equal to 3970 W/m^2 [66].

Using this device, the authors were able to charge a capacitor ($C = 10 \text{ }\mu\text{F}$; $U = 16 \text{ V}$). An electronic circuit and a capacitor applied for the tests are shown in Figure 4.11a), whereas Figure 4.11b) presents the voltage changes during the charging process. After 200 s it was possible to flash a LED.

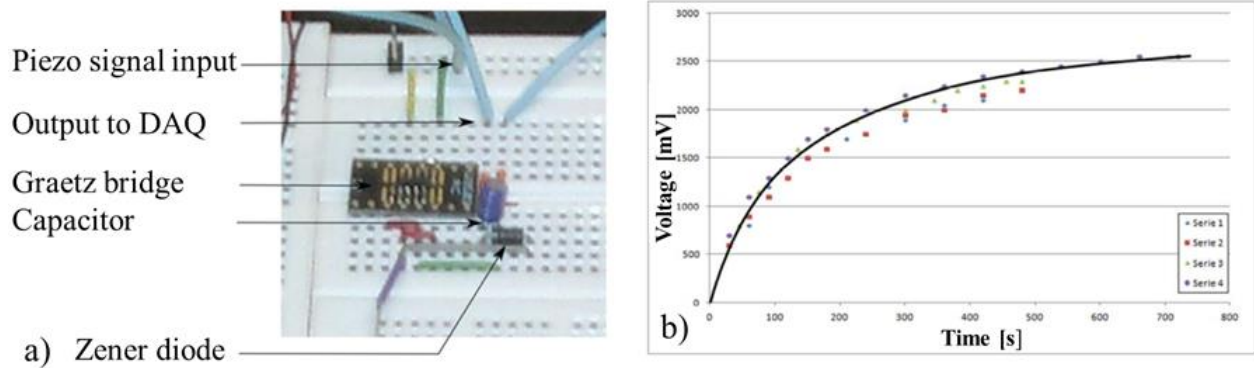


Figure 4.11: (a) Electronic circuit composed of Schottky diodes of threshold voltage equal to 550 mV; (b) charging curve of a capacitor [66].

In the next step, it was decided to reduce the size of the system from $35 \times 35 \times 20 \text{ mm}$ to $20 \times 20 \times 15 \text{ mm}$ as depicted in Figure 4.12. The analysis of the signals generated under the same conditions showed that the size reduction resulted in a significant drop of amplitude. The values of frequency were similar. In general, the value of voltage obtained during experiments was between 2 V – 2.5 V and the frequency oscillated around 1.3 Hz.

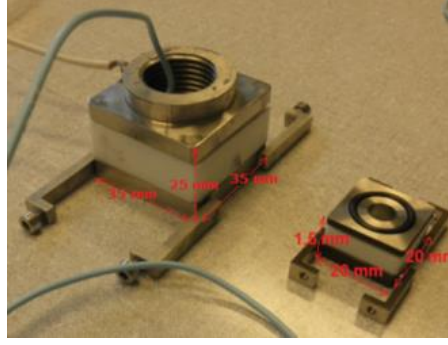


Figure 4.12: The volume of the device decreased 6 times [66].

The next part of this research was conducted with a participation of the author of this manuscript and it was aimed at optimizing the device operation. In the first step it was decided to verify if it is relevant to use the sphere to enhance the oscillation process. Although the presence of this element gave the advantage of relatively high amplitude of the signal, there was a significant issue related to this solution, namely a deterioration of the signal frequency.

In order to compare two possible operation modes – with and without the sphere, a number of experiments under the same conditions – heat flux 3955 W/m^2 , and the power of a cooling fan equaled to 0.6 W , were performed. The examples of the voltage signals versus time obtained during these experiments for the small device operating with or without the sphere are presented in Figure 4.13a-b), respectively.

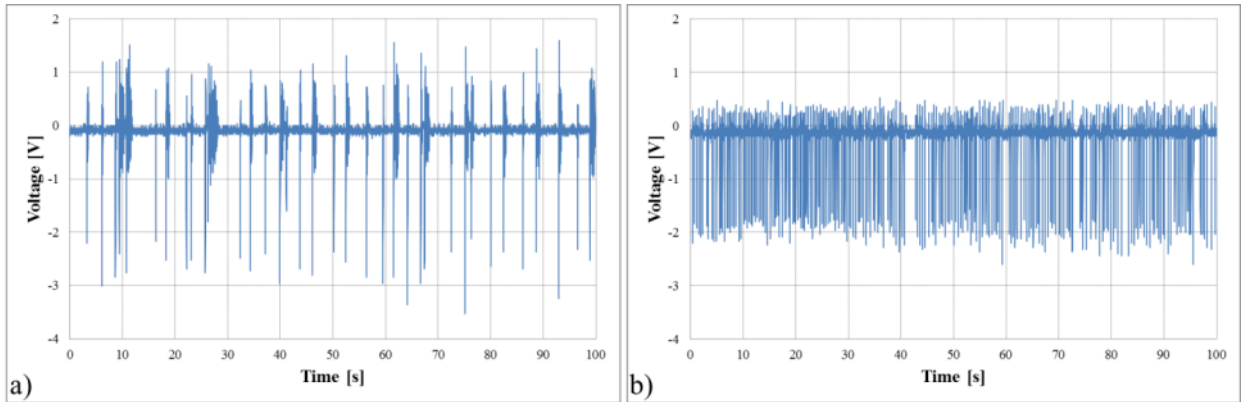


Figure 4.13: Voltage signal generated by the device operating (a) with and (b) without metal sphere at heat flux equal to 3955 W/m^2 and the power of a cooling fan equal to 0.6 W .

The results showed that the amplitude, in line with expectations, was lower compared to the device working with the sphere and its value oscillated usually between $1.5 \text{ V} - 2 \text{ V}$. The frequency however significantly increased, even up to the value of 2.8 Hz .

The comparison of the signal frequency and amplitude values obtained under the same experimental conditions for the large device operating with the enhancement of metal sphere, and for the small device operating with and without the sphere is given in Table 4.1.

Table 4.1: Frequency and amplitude of the signal generated by large and small device for different operation modes.

	LARGE DEVICE	SMALL DEVICE	
Sphere	YES	YES	NO
Frequency [Hz]	0.3 - 1.2	0.4 - 1.3	up to 2.8
Voltage amplitude [V]	1.5 - 7	2 - 2.5	1.5 - 2

During a number of measurements it was also observed that the oscillation nature might be improved by applying different heat flux to the hot surface. In general, for higher frequency values, the voltage amplitude dropped and contrarily, when the frequency was relatively low, the amplitude was higher. For example, for the value of heat flux equal to 4179 W/m^2 the value of amplitude oscillated around 2.5 V and the frequency was 1.3 Hz. For the lower value of heat flux (3995 W/m^2), the frequency raised significantly up to 2.8 Hz but the signal amplitude was not higher than 2 V. Hence, it was clear that a compromise between these two parameters must be established.

4.2. Concept of the silicon-based demonstrator in microscale

The aim of present work was to design and fabricate an oscillating device of small dimensions as compared to the existing solutions. The conversion of thermal energy should occur in two steps applying liquid to gas phase-change phenomenon and piezoelectric effect. The device should be characterized by a simple construction and be easy to manufacture with the conventional equipment and common materials. Due to the fact that this research was partially conducted based on the knowledge obtained during the collaboration with CEA-Liten, the architecture of proposed demonstrator is similar to the device developed by the Solar energy, Harvesting, Thermal management research group. The significant differences between the prototypes of CEA-Liten and TUL consisted in the scale of the devices and the material used for their fabrication. From fundamental point of view, to ensure possibly high ΔT between the hot and cold surfaces, the layer containing a channel should be made of thermal insulator, as it was done in the device proposed by CEA-Liten (Figure 4.8). In present work however it was decided to use silicon that is a thermal conductive material. A schematic cross-section of the proposed device is given in Figure 4.14.

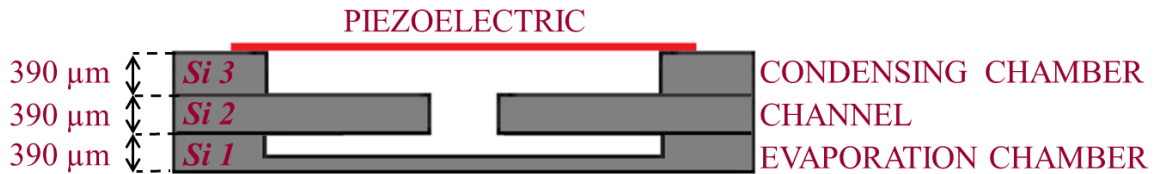


Figure 4.14: Cross-section of a single cell of the harvester comprising the evaporation and condensing chambers, a channel and a piezoelectric layer.

The decision of using silicon to create the layer containing the channel was technology driven and it was aimed at verifying if it is possible to fabricate an oscillating system of a small scale,

which is fully composed of this material. Hence, it was decided to etch an evaporating chamber in one silicon wafer, a channel in another wafer and a condensing chamber in the third silicon wafer. The three wafers should be then bonded together into one structure. The thickness of this element was expected to be close to the value of 1.23 mm and it could vary slightly depending on the wafers thicknesses provided by the supplier. Such a structure should be filled with some amount of working fluid and covered with a piezoelectric material.

The principle of the device operation is the same as in case of the macro-demonstrator fabricated in CEA-Liten and has been already described in section 4.1.3. The stages of one cycle of the energy conversion process are illustrated in Figure 4.15.

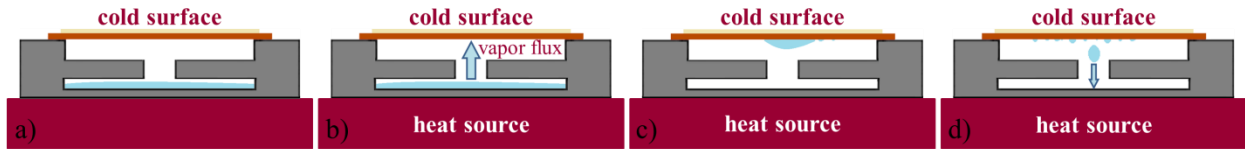


Figure 4.15: Stages of one cycle of the process: (a) the device filled with before the heating process; (b) evaporation of the fluid; (c) gas condensation; (d) return of the liquid to the evaporation chamber.

4.2.1. Technological challenges

The development of the device, the concept of which is proposed in section 4.2, entails a number of technological challenges that must be considered during the design process. There are several factors that may influence the oscillations initiation and play a significant role in their characteristics. The analysis of the potential issues that could appear at the technological stage of the work and the possible solutions to some of them are discussed. It has to be underlined that although some thermo-fluidic aspects are mentioned further in the chapter, this section was strongly aimed at overcoming the technological challenges related to the fabrication process of the device and the deep analysis of thermo-fluidic behavior of the system was not the main intention of the author. The parameters identified as influential, referring to the design and fabrication process are:

- type of the working fluid,
- surface wettability,
- channel design,
- type of piezoelectric element.

4.2.1.1. Type of the working fluid

Considering that at atmospheric pressure every substance exhibits different physical parameters such as boiling temperature or density, the selection of a proper working fluid that was supposed to be used in the device could be crucial for its operation. Additionally, it has to be taken into account that the working fluid selection impacts the whole mechanical design of the device. For instance, as explained distinctly in section 4.2.1.2, the channel design and its

surface wettability strongly depend on a capillary length as well as on the contact angle formed between liquid and the channel walls, and these two parameters differ depending on the type of the liquid. Hence, any change of a working fluid would necessitate a modification of the structure design, with particular emphasis on the channel characteristics. This means that all the experiments must be set up in regard to this choice. For all these reasons, the selection of a proper working fluid was one of the most important decisions that had to be taken in the initial part of the practical work with the prototype.

Due to the fact that the device designed in this research was dedicated to electronic applications, a relatively low boiling temperature of the liquid, possibly below 120°C, was desired. Additionally, the signal of high amplitude was required, which means that a high overpressure inside the system should be created. According to the mechanism of evaporation in a closed environment, the quantity of liquid that is being transformed into vapor should contribute in the increase of pressure inside an enclosure. In order to evaluate which fluid was able to generate high overpressure, the ratios between liquid and vapor densities at atmospheric pressure, for several fluids typically used in technological processes were calculated. In this analysis it was assumed that in each case the same volume of liquid evaporated. The comparison of different liquids regarding their boiling temperature and their mass density ratio at atmospheric pressure is shown in Figure 4.16a-b), respectively.

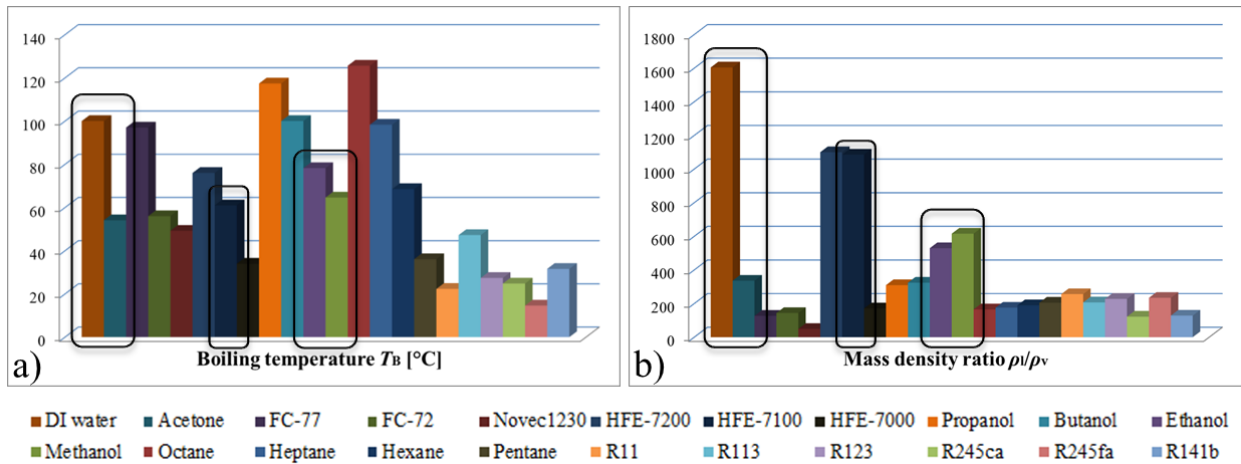


Figure 4.16: (a) Value of boiling temperature and (b) mass density ratio for various liquids at atmospheric pressure.

Based on the data presented in Figure 4.16 as well as on the experimental results of Soupremanien et al. [65], who designed a thermo-mechanical system generating pressure variations due to phase-change phenomenon of several working fluids, the following types of liquid were selected for further analysis: acetone, ethanol, methanol, HFE-7100 and water. The values of boiling temperatures, T_B , liquid and volume densities ρ_l , ρ_v and ratios of mass densities ρ_l/ρ_v at atmospheric pressure for selected fluids are listed in Table 4.2.

Table 4.2: Boiling temperature T_B , liquid and volume densities ρ_l , ρ_v and ratio of mass densities ρ_l/ρ_v at atmospheric pressure.

Fluid	T_B [°C]	ρ_l [kg/m ³]	ρ_v [kg/m ³]	ρ_l/ρ_v
Acetone	54.1	750	2.23	336
Ethanol	78.3	757	1.43	529
Methanol	64.7	752	1.22	616
HFE-7100	61.0	1520	1.39	1086
Water	100.0	958	0.60	1597

On the grounds of presented analysis, three of the fluids listed in Table 4.2 – methanol, HFE-7100 and water – could be considered as the ones with relatively high liquid/vapor density ratio (616, 1086 and 1507, respectively). This allowed expecting a satisfactory amplitude value of the oscillations. This choice seemed to be confirmed also by the results of [65], who tested all the liquids from Table 4.2 and observed the oscillation behavior only for methanol, HFE-7100 and water. However, in case of HFE-7100 different problem appeared, namely due to its high volatility an issue of leakage occurred and as a result, the fluid had a tendency to escape from the device during the evaporation process. For this reason HFE-7100 was excluded from the study presented in this work. Although methanol had been initially considered as a possible choice due to its low boiling temperature, it was finally decided that its mass density ratio is too low to expect high amplitudes of generated oscillations. Eventually, taking into account the simplicity of water application and all the previous experimental work (Soupremanien et al. [65]) performed with this liquid, it was selected as a working fluid.

4.2.1.2. Channel design

Oscillation incipience

According to the research performed in the domain of PHP systems, which is wider described in section 1.3.3.5, there is a critical value of the channel diameter, D_{crit} , expressed by Eq.(1.9), above which the oscillation generation does not occur. On the other hand, in order to enable the oscillation flow, the diameter cannot be too low.

Soupremanien et al. [65] designed a system that generated pressure variations, where a constant hot temperature provided to the surface was the only source of energy. Similarly to the system presented in this work, the device was divided into three sections: an evaporator, a condenser and a channel that spanned these two elements. The tests described by the authors, related to the repeatable condensation peaks in a closed chamber, were performed for three different channel diameters – 2, 3 and 4 mm, where water was used as a working fluid. The results showed that there is an optimal range of channel diameter that ensures the oscillations occurrence. Specifically, they observed regular pressure variations generated due to phase change of water inside the system composed of 3 mm and 4 mm channel, as opposed to not continuous oscillations of random nature for 2 mm channel diameter. The random pressure changes detected for two different temperatures in the system of 2 mm channel are illustrated in Figure 4.17. This may be explained by the fact that in order to ensure the repeatable and cyclic operation of the

device it was essential to enable the free flow of the working fluid from condenser through the channel towards the evaporator. In other words, the portion of water returning to the evaporator should not be trapped inside the channel. Due to the fact that following analysis were based on an assumption that there was no water inside the evaporation chamber, the influence of the forces related to a vaporization process were neglected. In such case, there are two forces that play an important role in this process – capillary force that depends on water contact angle on channel walls and is related to capillary pressure, P_{cap} , and the force referred to a weight of the fluid and its pressure, P_f .

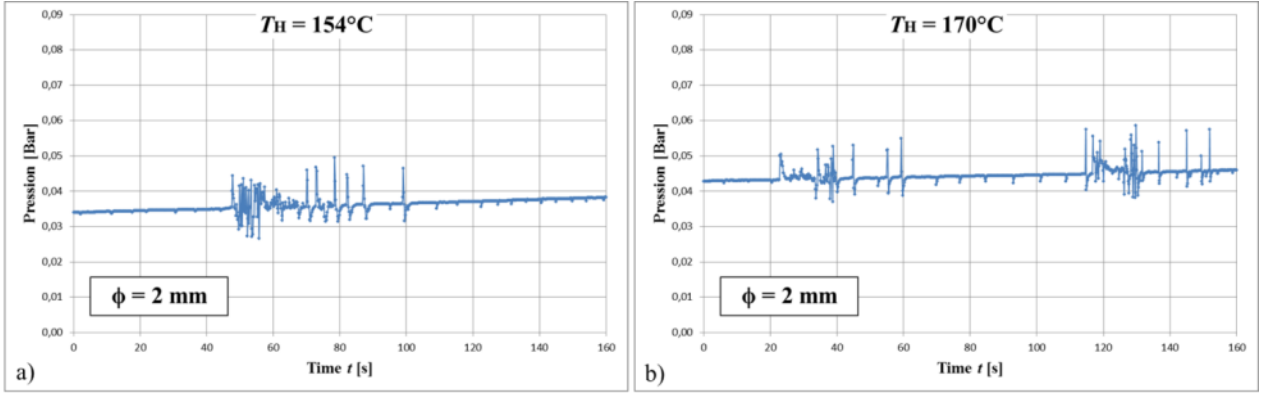


Figure 4.17: Pressure changes inside the system of 2 mm channel at the temperature (a) $T_{HOT} = 154^{\circ}\text{C}$ and (b) $T_{HOT} = 170^{\circ}\text{C}$.

Considering that the channel of the device filled with water has a shape of a tube, the capillary force F_{cap} , that acts on a periphery of the meniscus is proportional to a surface tension, γ , and a circle length, L , accordingly to Eq.(4.1).

$$F_{cap} = \gamma L = 2\pi\gamma R_{tube} \quad \text{Eq.(4.1)}$$

where γ is surface tension of a working fluid [N/m], L is the length of a line that the force operates on perpendicularly [m] and R_{tube} is the radius of the capillary tube [m]. The force that acts in the direction parallel to the tube walls $F_{up} = F_{down} = F_{||}$, can be expressed by Eq.(4.2) and its orientation depends on the contact angle, θ , between liquid and the tube surface. When the liquid reservoir is placed on top of capillary, for $\theta < 90^{\circ}$, the force is directed downwards, as opposed to upwards force in case of $\theta > 90^{\circ}$ [66,67].

$$F_{||} = F_{cap} \cos \theta = 2\pi\gamma R_{tube} \cos \theta \quad \text{Eq.(4.2)}$$

Due to the fact that this force can be oriented both upwards and downwards, it can serve as an opposing or a driving force for fluid transport.

The second force that participates in a fluid transport inside the tube, F_f , is related to the weight of the fluid. It is always directed downwards and it is described by Eq.(4.3).

$$F_f = \pi R_{\text{tube}}^2 g H (\rho_l - \rho_v) \quad \text{Eq.(4.3)}$$

where g is the gravitational acceleration [m/s^2]; ρ_l and ρ_v are liquid and vapor densities [kg/m^3] and H is the height of the fluid column, so-called pressure head [m]. In practice, the vapor density, ρ_v , at surface condition is very small and can be neglected [70].

In the situation when the value of a fluid contact angle ensures the upward orientation of the force $F_{||}$, in order to maintain an equilibrium in the capillary tube, this force must be balanced by the opposite force, F_f , accordingly to Eq.(4.4).

$$\begin{aligned} F_{||} &= F_f \\ 2\pi\gamma R_{\text{tube}} \cos \theta &= \pi R_{\text{tube}}^2 g H \rho_l \end{aligned} \quad \text{Eq.(4.4)}$$

Pressure related to the force described by Eq.(4.1), so-called capillary pressure is defined as a difference between the pressures in two fluids forming an interface and it is proportional to a surface tension, γ . Capillary pressure in a tube can be calculated from Eq.(4.5).

$$P_{\text{cap}} = \frac{2\gamma \cos \theta}{R_{\text{tube}}} \quad \text{Eq.(4.5)}$$

Due to the fact that P_{cap} is inversely proportional to R_{tube} , its value decreases with the raise of the tube radius. Eq.(4.6) expresses the fluid pressure, P_f , which refers to a weight of a fluid:

$$P_f = g(\rho_l - \rho_v)H \quad \text{Eq.(4.6)}$$

In practice, as in case of Eq.(4.3), the vapor density, ρ_v , can be neglected.

All presented analyses led to a conclusion that in order to ensure the return of the liquid from condenser through the channel towards the evaporator, the upward capillary forces must be overcome by the opposite forces related to the fluid weight, as expressed in Eq.(4.7).

$$g\rho_l H > \frac{2\gamma \cos \theta}{R_{\text{tube}}} \quad \text{Eq.(4.7)}$$

The illustration presented in Figure 4.18 depicts the distribution of forces playing the role in water transport in the channel of the device designed in this work, when the value of contact angle is lower than 90° . To facilitate the demonstration of this phenomenon, the scale of the silicon device shown in the schematic has been changed and it do not correspond to the dimensions of the real system.

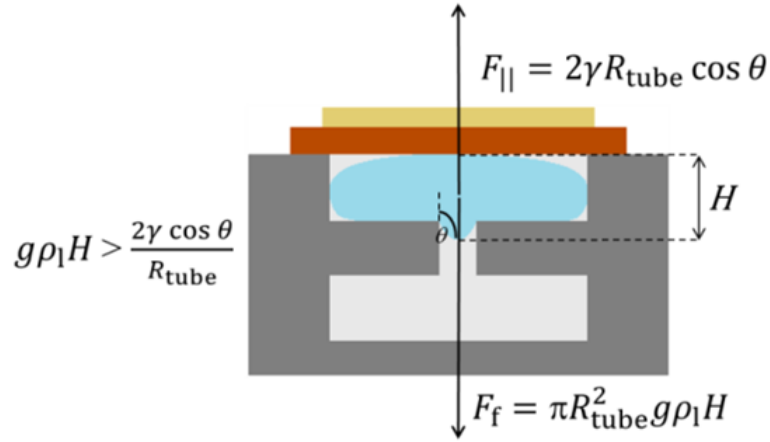


Figure 4.18: Forces distribution in the device for wetting water that ensures a contact angle between liquid and a channel surface lower than 90° .

Assuming that the pressure head, H , is close to the height of the condensing chamber being around $400 \mu\text{m}$, it was possible to determine the maximum value of contact angle that enabled the water to come back through the channel into evaporation chamber. Converting Eq.(4.8) we obtain:

$$\cos \theta < \frac{g \rho_l H R_{\text{tube}}}{2\gamma} \quad \text{Eq.(4.8)}$$

Solving Eq.(4.8) for the following values of parameters: $g = 9.81 \text{ N/kg}$; water density at 25°C $\rho_l = 997 \text{ kg/m}^3$; $H = 4 \cdot 10^{-4} \text{ m}$; $R_{\text{tube}} = 1.5 \cdot 10^{-3} \text{ m}$ and surface water tension at 25°C $\gamma = 0.072 \text{ N/m}$ we obtain value of contact angle $\theta < 87.7^\circ$. If we consider this phenomenon at the temperature of 130°C that is an expected value of temperature applied to the structure in experiments, the values of water density and its surface tension will change into 935 kg/m^3 and 0.053 N/m , respectively. In this situation the contact angle calculated from Eq.(4.8) drops to $\theta < 87.1^\circ$. This means that in order to ensure the conditions allowing the water to come back to the evaporation chamber, it is necessary to fabricate a structure that creates the contact angle between water and channel walls, which is lower than 87° in case of wetting surface of the device.

To sum up, there are several factors that may interfere the occurrence of regular oscillations. One of them could be too small channel diameter in relation to weight of the working fluid, which leads to the situation where the surface tension forces become dominant and as a result, the liquid is trapped inside the channel, which seems to be confirmed by the results of Soupremanien et al. [65]. Additionally, due to the fact that both, contact angle and surface tension, playing a significant role in the oscillation mechanism, are strongly related to the wettability of the channel surface, it was essential to analyze type of the material, which should be used to fabricate this element.

Impact of channel diameter on amplitude and frequency

In the same experiments Soupremanien et al. [65] established also that the channel diameter had an impact on the pressure generated inside the system as well as on the frequency of the oscillations at given temperature. This is shown in Figure 4.19 presenting the pressure variations inside the systems of two different channel diameters, at the similar temperatures. Figure 4.19a-b) and Figure 4.19c-d) represent the data recorded for 3 mm and 4 mm channel device, respectively. The results given in Figure 4.19 show clearly that although in both cases regular oscillations appear, the frequency and amplitude values at similar temperatures significantly differ. Regarding frequency, its value is much higher for wider, 4 mm, channel, the amplitude however is significantly lower as compared to the channel of 3 mm. This shows explicitly that when choosing the channel diameter, a compromise in terms of frequency and amplitude of the oscillations is required.

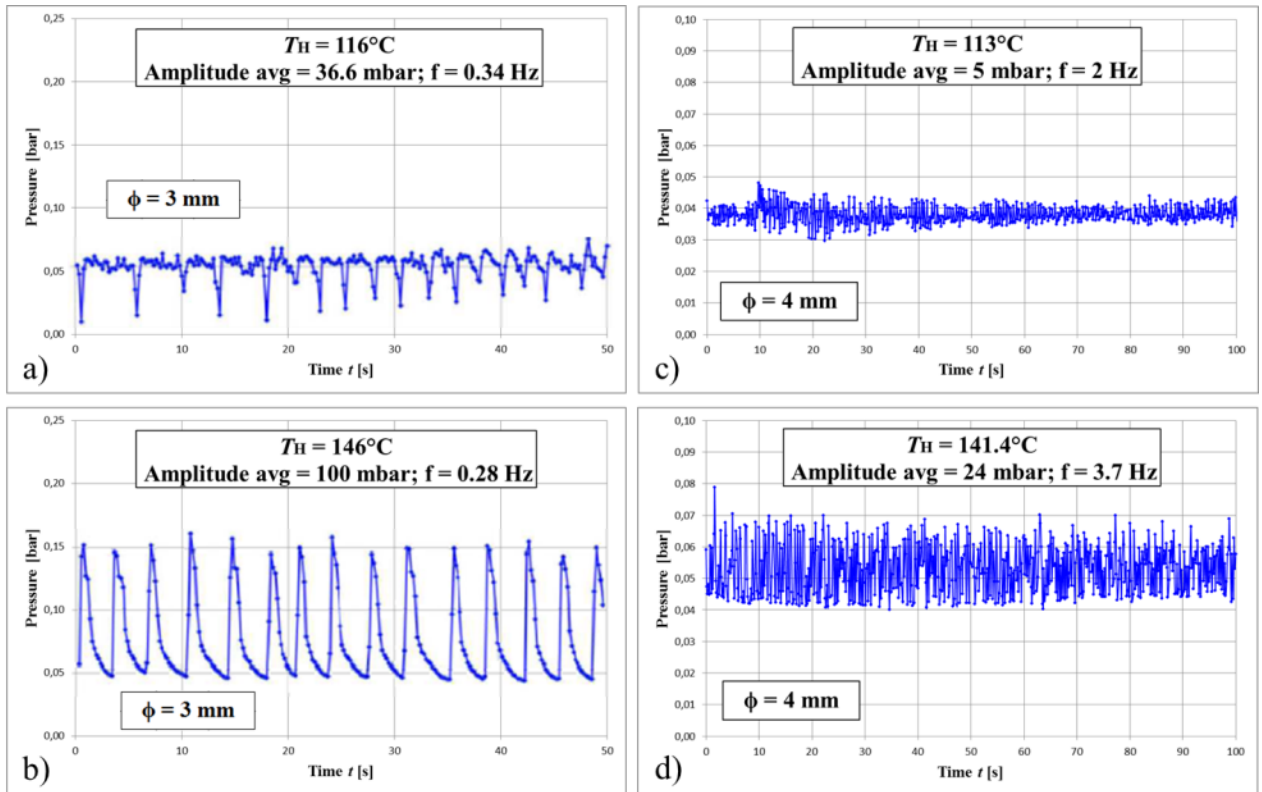


Figure 4.19: Pressure changes inside the system of 3 mm channel at hot temperature equal to (a) $T_{HOT} = 116^{\circ}\text{C}$ and (b) $T_{HOT} = 146^{\circ}\text{C}$; for 4 mm channel at the temperature (c) $T_{HOT} = 113^{\circ}\text{C}$ and (d) $T_{HOT} = 141.4^{\circ}\text{C}$ [65].

The authors analyzed also how the hot temperature variations influence the frequency values of oscillations generated by two systems that differed with respect to their channel diameter. Figure 4.20a-b) present the dependence of the oscillation frequency on the value of hot temperature for 3 mm and 4 mm channel, respectively.

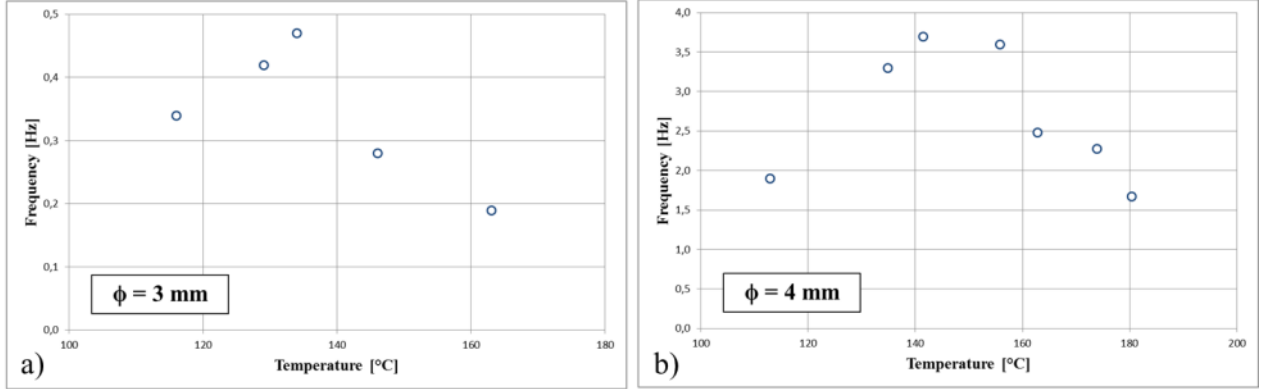


Figure 4.20: Influence of the hot temperature on the oscillation frequency for (a) 3 mm and (b) 4 mm channel [65].

The results presented by the authors show that this parameter strongly depends on the surface temperature as well as on the channel diameter. Moreover, they observed that, regardless the channel dimensions, there is an optimal value of temperature, for which oscillations frequency reaches the maximum, as shown in Figure 4.20.

Presented analysis showed that the diameter of the channel is a significant parameter that influences the operation of the device and it must be considered in the design. A very important conclusion that can be drawn from experimental results of [65] is that, when one consider different channel diameters, a clear compromise between the oscillations frequency and amplitude is required. The authors observed that in general, at the same temperature the frequency is higher for larger channel, the amplitude however drops significantly. Due to the fact that the oscillation amplitudes for much smaller device described in presented work were expected to be lower as well, obtaining a relatively high value of this parameter could be challenging. On the other hand, the oscillation frequencies are generally higher for small-scale systems. Taking this two facts into consideration, it had been decided to focus at achieving possibly high signal amplitudes and for this reason a 3 mm wide channel was designed.

4.2.1.3. Filling ratio

The filling ratio, α , that can be expressed by Eq.(4.9) is the ratio between the volume of the liquid, V_l , enclosed in the system and the total volume of enclosure, V_{tot} .

$$\alpha = \frac{V_l}{V_{tot}} \quad \text{Eq.(4.9)}$$

The study regarding pulsating heat pipes, presented in section 1.3.3.5, showed that the characteristics of the oscillations strongly depend on the filling ratio and, in order to initiate the pulsation mechanism, this parameter must be comprised within a specific range of values between 20% and 80%. Additionally, within this range there, there is an optimal filling ratio that

ensures the best behavior of the device from thermal point of view. This value depends, amongst other, on the working fluid type and in case of water it is close to 50%.

Similar behavior was observed by Soupremanien et al. [67] in their thermo-mechanical system that was partially filled with water and had been designed to generate pressure variations due to constant heat flux being provided to the system. The authors tested two devices – D1 and D2 that differed with respect to their sizes. Each of the device was divided into three sections – evaporator made of stainless steel, PEEK (polyether ketone) insulator and stainless steel cover with a pressure sensor installed on top. To bring the droplets back to the evaporator after the condensation process using gravity forces a channel created in the insulator was designed to be slightly larger (3 mm) than capillary length (2.7 mm). The geometries of both devices are shown in Figure 4.21 and in Table 4.3.

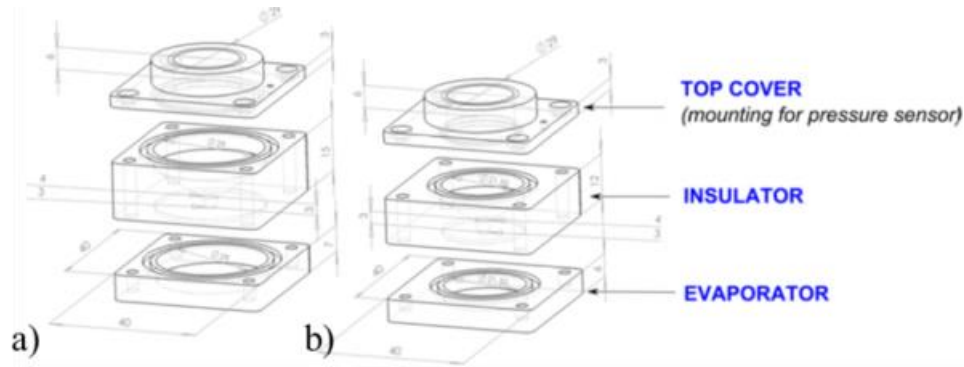


Figure 4.21: Schematic of the devices used for the experiments; (a) D1; (b) D2 [67].

Table 4.3: Comparison of devices geometry [67].

	h_{total} [mm]	$h_{insul.}$ [mm]	V_{total} [ml]	$V_{cond.}$ [ml]	$V_{evap.}$ [ml]	Ratio V_{cond}/V_{evap}
D1	31	15	15.14	12.38	2.64	4.68
D2	27	12	6.45	5.23	1.09	4.81

For both systems the authors observed, irregularity, discontinuity and specific stopovers of the oscillations when the filling ratio was below a certain value. This situation was observed also by Khandekar et al. [49] but the authors related this behavior to the temperature gradient and for this reason it is wider described in section 4.2.1.4. The critical values of filling ratio, which ensured the continuous oscillation mechanism were 6.61% for a larger device and 12.41% for a smaller one. The authors assumed that these stopovers might be related to the fact that at low filling ratio, the water could evaporate totally from the hot surface. Although the partial pressure was not high enough to suspect that whole water turned into vapor, the droplets could be trapped in the condenser. The pressure could raise drastically inside the system before the last stage of evaporation. This behavior seems to be confirmed by the results of measurements, given in Figure 4.22, where some bulges can be observed in a pressure signature at the moments of stopovers.

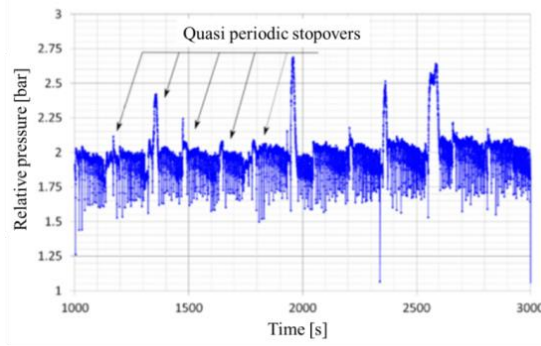


Figure 4.22: Pressure variations with stopovers versus time for D2 and $\alpha = 12.41\%$ at $T_{\text{hot}} = 130.6^\circ\text{C}$ [67].

In general, the authors observed that with the increase of the filling ratio value the amplitude of pressure raises, however the value of frequency decreases, as shown in Figure 4.23. They assumed that the increase of the frequency could be related to the fact that for larger volume of liquid the condensation process is slowed down.

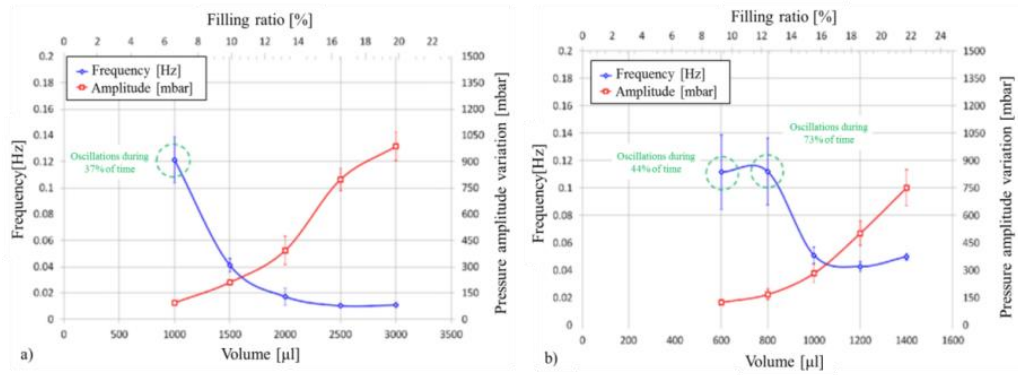


Figure 4.23: Volume impact on pressure amplitude and oscillations frequency for (a) D1 and (b) D2 at $T_{\text{hot}} = 130^\circ\text{C}$ [67].

Additionally, the authors noticed that with the size reduction of the device, the oscillations frequency raises as opposed to the pressure amplitude that is lower for smaller system. These tendencies are shown in Figure 4.24.

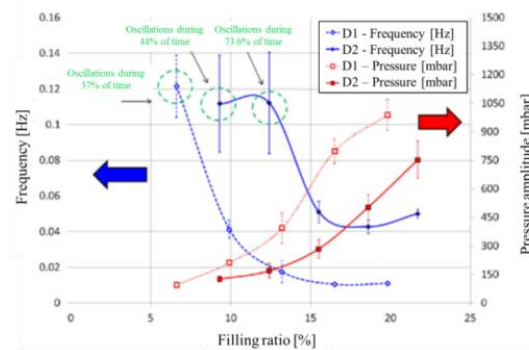


Figure 4.24: Filling ratio impact on oscillating behavior [67].

All these observations show that the filling ratio is a parameter of a significant importance for the systems that base their operation on the oscillation mechanism and its optimal value vary depending on the type of the device. Hence it was essential for this research to determine the volume of liquid that ensures the desired behavior of the device of particular geometry designed in this study. The thorough analysis aimed at determining its optimal value is presented in sections 6.2 and 6.3.

4.2.1.4. Hot surface temperature

The parameter that influences strongly the occurrence and characteristics of the oscillation is the temperature of the bottom part of the device, T_H , being also the temperature of a heat source. Most of all, in order to initiate the evaporation process of a working fluid, it has to be higher than its boiling temperature. Additionally, according to the results of Soupremanien et al. [67] the examined systems described in section 4.2.1.3, expressed oscillation mechanisms only within a certain range of temperatures, so if the temperature of the heat source was too high and exceeded the range limit, the oscillations stopped. Moreover, Soupremanien et al. noticed that the value of this parameter has a significant impact on the frequency and the amplitude of the pressure generated inside their devices. Additionally, the authors observed a specific behavior with stopovers during which no oscillations occurred in the device. They established that it was mainly related to a filling ratio parameter, as explained in 4.2.1.3, however the influence of the hot temperature could also impact the oscillation behavior. They observed that, when the hot temperature dropped to 120°C, the waiting times of stopovers for D2 disappeared completely for $\alpha = 12.41\%$ and lowered from 64% to 44% for $\alpha = 9.91\%$.

In general, the authors analyzed the influence of the hot temperature within a range between 115°C and 140°C and the example of their results is given in Figure 4.25, where (a) shows the pressure signal evolution for different values of hot temperatures versus time and (b) illustrates how the hot temperature influences oscillations frequency and amplitude.

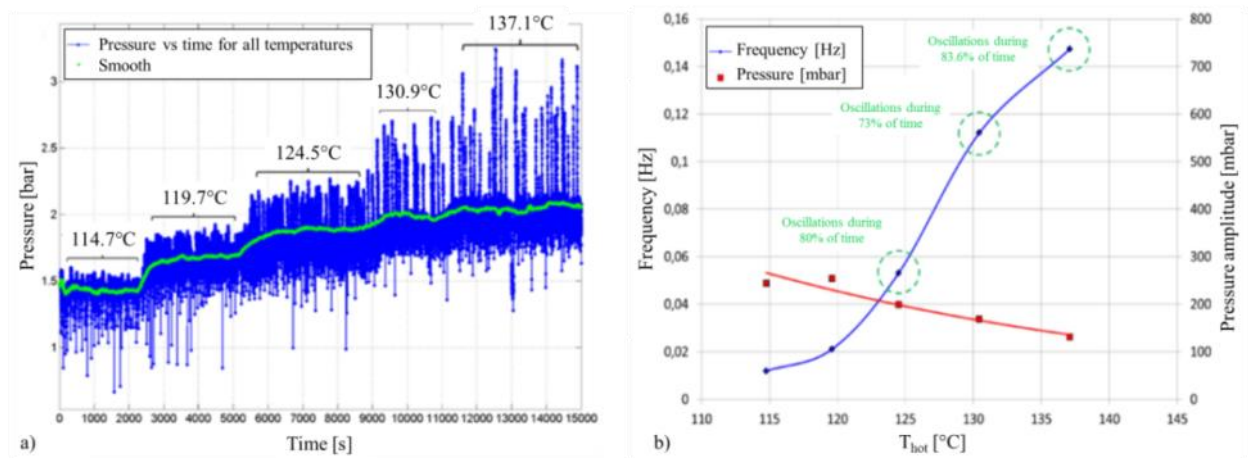


Figure 4.25: (a) Pressure signature evolution with the increase temperature increase; (b) impact of the hot temperature on the oscillations behavior for $\alpha = 12.41\%$ for D2 [67].

These results showed clearly that the oscillation frequency highly increased with the raise of the hot temperature from 0.012 Hz at 115°C to 0.147 Hz at 137°C. Contrary to the frequency, the value of pressure amplitude decreased with the hot temperature from 250 mbar at 115°C to 120 mbar at the temperature of 137°C.

The specific behavior of the oscillations characterized by the quasi periodic stopovers was observed also by Khandekar et al. [49]. The authors performed a wide analysis of a single two-phase capillary loop that represented a structural element of a multi-turn pulsating heat pipe. Amongst a number of other observations they noticed that after obtaining a steady state in the loop, the altering periods of movement and stopover occur. The authors explained that in order to obtain this steady state, a sufficient temperature gradient between the condenser and the evaporator ΔT_{E-C} must be established. When the oscillations began, the process of mixing fluid portion in the condenser and evaporator was facilitated. This resulted in an immediate drop of the driving temperature gradient ΔT_{E-C} leading to the oscillation stop. Due to the fact that the fluid was continuously provided to the evaporator, this break caused again the increase of the evaporator temperature. Thus, the cycle repeated in a quasi-periodic manner. One of the interesting observations made by the authors is that a complete stopover of fluid motion, occur in a single loop, but they had never been noticed in a multi-turn PHP. This suggests that the level of perturbations increases with a number of turns, which lowers the probability of this phenomena almost to zero.

All these analysis show that there is not only a specific interval of hot temperature values, within which the oscillations occur but also that a compromise between their amplitude and frequency must be reached. For this reason it was necessary for this work to establish the most optimal value of the hot temperature that would ensure the generation of the oscillations characterized by a satisfactory level of both frequency and amplitude. The analysis focused at obtaining this compromise is described in 6.2 and 6.3.

4.2.1.5. Type of piezoelectric

A detailed experimental study of two piezoelectric materials, flexible PVDF and PZT-based ceramics is presented in *Chapter 3* of this work. That analysis showed explicitly that, although PVDF is a very interesting material due to its flexibility and could be successfully used for specific applications, it cannot be used as a structural element of the device presented in this chapter. A PVDF cantilever construction analyzed in 3.2.1, is completely unacceptable in case of the device proposed in this work, due to the fact that in order to avoid any leakage issues, it must be tightly sealed. Additionally, the energy efficiency of PVDF films are drastically lower as compared to piezoelectric ceramics based on PZT. Thus, PVDFs were not considered to be applied in this work. For these reasons, the other material, namely circular, easily available and well known cylinder-shaped piezoelectric diaphragms composed of PZT ceramics and metal plate was chosen.

Soupremanien et al. conducted a very wide research including numerical modeling as well as experimental study, which was focused at determining how a geometry and a clamping method of

PZT-based ceramics influence the value of the voltage generated by these elements. As it was expected, the results of the analysis showed that the voltage evolve almost linearly with pressure. It was observed that for the same thickness of the piezoelectric, t_p , and the brass substrate, t_s , the voltage increased with the raise of the element diameter. On the other hand, for constant diameter the voltage improved with the thickness reduction. The authors observed also that clamping method had a very strong impact on the results.

Also Mo et al. [24] performed a very detailed analytical and experimental study on piezoelectric circular diaphragms based on PZT material, and they focused on the assessment of these elements in terms of their application in pressure fluctuating energy harvesting systems. The authors created a theoretical model of a simply supported unimorph PZT-based element and performed a parametric study of the various factors, which had an influence on the optimal power generated by this element. The element was subjected to a uniformly distributed pressure load of a frequency much lower than their fundamental mode. The authors presented that, regarding the generated power, there is an optimal ratio of the piezoelectric and the substrate radius, R_p/R_s . This ratio differed depending on the piezoelectric and surface materials and it shifted depending on the thickness ratio of these layers, t_p/t_s . Additionally, the studies proved that the clamping conditions can significantly influence the generated voltage output.

Hence, one can conclude that, in general, the geometrical parameters of PZT are of huge importance in terms of its electrical behavior. However, the particular construction of the device presented in this work allow expecting that for the specific assembly, the size of PZT would not play a role in the value of generated voltage. The experiments described in section 6.2 confirm this assumption.

4.3. Summary of the chapter

In this chapter the following elements have been presented:

- the concept of a small scale silicon-based device being the subject of present work,
- the principle of the device operation, which was to generate the repetitive pressure oscillations due to the cyclic evaporation and condensation of the working fluid enclosed inside the system,
- the design of the device, which assumed that it should be composed of three Si wafers comprising the evaporation and condensing chambers, and the channel spanning these two elements. The PZT-based transducer mounted on top of the structure should be applied to ensure energy conversion,
- the prototypes of existing innovative devices transforming thermal energy into electricity based on phase-change phenomenon,
- the main challenges related to the practical realization of the prototype that is the subject of this work. The challenges that have been recognized as the most important and the solutions to two of them, determined based on previous studies on the similar subject, described in section 4.1, are as follow:

- type of the working fluid: water,
- channel design: 3 mm diameter, possibly hydrophilic surface,
- type of piezoelectric element,
- filling ratio,
- hot surface temperature,

The analysis of the remaining questions only opened the discussion and their actual values were established experimentally in *Chapter 5* and *Chapter 6* related to the technological realization of the demonstrator and its characterization, respectively.

5. Technological realization of the silicon-based demonstrator

A well-known silicon technology, commonly used for microfabrication has been chosen to create the small-sized device, the concept of which has been described in section 4.2. This technology was selected to open out wide perspectives of its implementation in the various silicon microsystems.

Due to the fact that the device was supposed to consist several elements fabricated in silicon, it was mandatory to determine the most appropriate method of silicon etching. During the research, three etching techniques were tested – reactive-ion etching, deep reactive-ion etching and wet etching in KOH solution. Another technological issue that had to be considered during the fabrication process was a choice of a method enabling to bond together three silicon wafers characterized by a non-standard surface structure. For this purpose, four bonding techniques, namely fusion, low temperature, vacuum and adhesive bonding were tested and analyzed. Equally important was to choose an assembly method of a piezoelectric element on top of a silicon wafer. In spite of appearances, it was a very challenging task, first of all due to a high smoothness of the wafer's surface and secondly due to the fact that, to avoid the fluid evaporation, the sealing process could not occur at high temperatures. Moreover, after the montage, the structure should be able to operate at high temperatures during the process, where any leakage is unacceptable, so the selected adhesive should be characterized by a high heat resistance. In the experiments a number of high temperature glues were examined.

All the technological processes applied during the device fabrication were performed in a microelectronic laboratory of the Department of Semiconductor and Optoelectronics Devices (DSOD), at Lodz University of Technology. The laboratory is a clean room environment of class 10000 in the main room and 100 class in the photolithography facilities, which are shown in Figure 5.1a-b), respectively.



Figure 5.1: (a) Class 10000 main room and (b) class 100 photolithography section (b) of clean room laboratory of the Department of Semiconductor and Optoelectronics Devices at Lodz University of Technology.

The laboratory is equipped in a number of technological appliances, amongst which mask aligner Karl Suss MJB-55, oxidation furnace SD-3, Diener plasma reactor FEMTO 90966, bonding pressure chamber and chemical stand, were used in the fabrication process of the device.

5.1. Selection of technological processes

5.1.1. Silicon etching process

In order to find the most suitable way to fabricate the cavities in a silicon wafer, both dry and wet etching processes were considered. The results of the tests performed using both techniques are presented in this section.

5.1.1.1. Dry etching approach

Reactive-ion etching

The very first attempts of the silicon structures etching were performed with the application of a plasma reactor FEMTO 90966 (Diener), available in the laboratory of DSOD. The results however, accordingly to the predictions, were not satisfactory and a huge irregularity of etched surface, as well as a complete degradation of Aluminum mask used in the process were observed. This was due to the fact that this technique is not dedicated to deep silicon etching, but it is typically used for cleaning of the wafer's surface. The full procedure applied for these experiments and their results are presented in Appendix A.1.

Deep reactive – ion etching

The deep reactive-ion etching (DRIE) is another, more effective etching technique that uses a highly anisotropic process to perform deep penetration into silicon wafers, usually with high aspect ratios. In the experiments, a plasma reactor ADIXEN AMS100 of the Institute of Electron Technology (ITE) was applied. The system used the Bosch technology that is time-multiplexed etching, which alternates repeatedly between two modes, to achieve nearly vertical structures. The two stages of the process were as follow: standard, nearly isotropic plasma etching, during which the ions attack the wafer's surface from a direction close to vertical; deposition of a chemically inert passivation layer that protects the entire substrate from further chemical attack and prevents further etching. Each stage of the process lasts several seconds. Due to the fact, that they are repeated alternately many times, a large number of very small, isotropic etching steps takes place only at the bottom of the etched pits. In the process performed in this experiment, the SF₆ (sulfur hexafluoride) was used for an etching step and C₄F₈ (octafluorocyclobutane) for a planarization step. The process was carried out at a pressure of 100 mTor, with the power equaled to 2.8 kW. To protect the part of the silicon structure that was not supposed to be etched, the Aluminum mask was applied. A SEM (Scanning Electron Microscope) picture of a 250 μm chamber etched inside a silicon wafer using DRIE technique is shown in Figure 5.2.

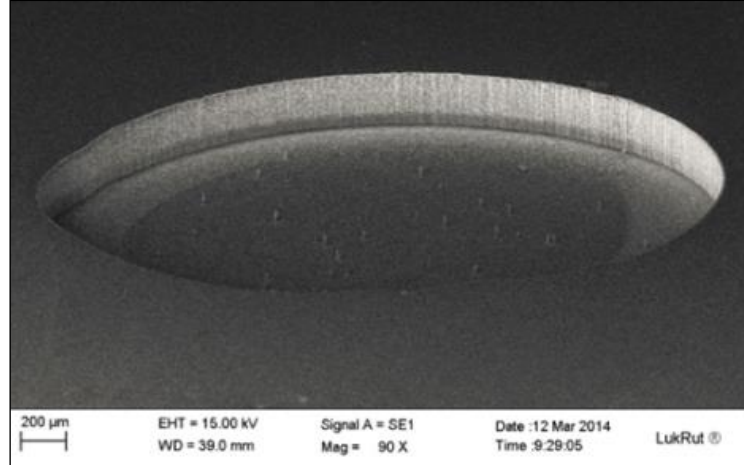


Figure 5.2: Chamber etched in Si wafer by DRIE.

Due to the anisotropy of this process, the etching occurred in desired directions only, which resulted in the fabrication of a 250 μm deep cavity of desired shape. Moreover, thanks to the short time of the process, close to 0.5 h (as compared to 20 h RIE etching), no damage was done to the Al mask and as a consequence, to the silicon surface surrounding the etched part. A comparison between RIE and DRIE etching results are given in Appendix A.2.

The dry etching experiments indicated that from the two investigated techniques, the deep reactive-ion etching technique has indisputable advantages and could be used in order to form the harvester chambers of expected quality.

5.1.1.2. Wet etching approach

Due to the fact that a wet chemical etching is an easily accessible process, typically used in the microelectronic laboratories, also this technique was considered for the fabrication of the designed energy harvester demonstrators. All the experiments presented in this section, fully conducted by the author of present work, were performed using a heated KOH (potassium hydroxide) solution. An SiO_2 (silicon dioxide) layer was playing a role of a mask in the experiments and it was obtained in a wet oxidation process, carried out at the temperature of 1150°C. A long time of the oxidation lasting 5 hours allowed forming a thick layer of silicon dioxide equaled to around 1.7 μm . The simplified process flow of the typical KOH etching occurs in 8 steps, shown in Figure 5.3.

- 1) RCA cleaning procedure of a silicon wafer.
- 2) Wet oxidation process resulting in the SiO_2 mask formation required for KOH etching (Figure 5.3b).
- 3) Photoresist deposition (Figure 5.3c).
- 4) Photoresist development aimed at opening the window of a desired shape of the structure (Figure 5.3d).
- 5) Etching of the SiO_2 that is not covered with a photoresist layer, using buffered hydrofluoric acid solution NH_4F -HF (ammonium fluoride-hydrofluoric acid) (Figure 5.3e).

- 6) Photoresist layer removal using acetone.
- 7) Etching of the desired structures in silicon using KOH solution (Figure 5.3f).
- 8) SiO₂ removal (Figure 5.3h)).

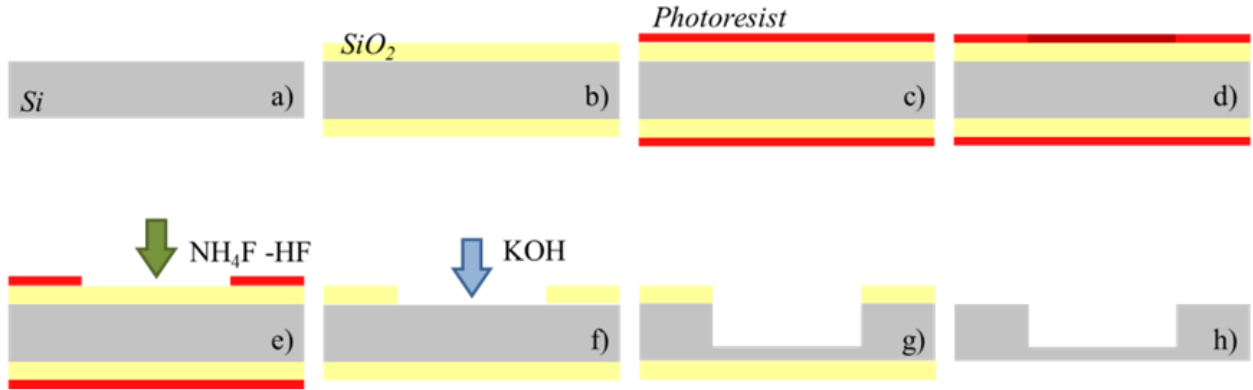


Figure 5.3: Process flow of KOH etching: (a) Si wafer after cleaning procedure; (b) wet oxidation; (c) photoresist deposition; (d) photoresist development; (e) SiO₂ etching and photoresist removal; (f) Si etching with KOH solution; (g) etched Si structure after KOH process; (h) Si structure after SiO₂ removal.

The KOH wet etching is anisotropic and it consumes both Si and SiO₂ layers. The etch rates of both materials strongly depend on the temperature and the percent weight of KOH in a solution, and in case of Si wafer, on its crystallographic orientation. In order to fabricate the deep structures of desired shape without consuming the mask during the process, all these factors must be taken into account and several combinations of the process parameters should be considered. In general, for higher temperatures of the solution, the etching occurs faster for both, Si and SiO₂. Thus, in order to perform a fast etching that would allow fabricating a very deep structure, the temperature of the solution should be high enough to obtain the assumed depth of the cavity, but not higher than the temperature that could cause the degradation of the SiO₂ mask before the end of the process. It should be also taken into account that with more aggressive etch rates, the quality of the etched surface decreases, so to obtain the satisfying results, the temperature of the process, and as a consequence, its rate, should not be too high. The etch rate strongly depends also on the percent weight of KOH in the solution; it rises together with the KOH concentration and obtains its peak at the value of 20%. Further increase of the concentration results in a drop of the process rate. However, during the experimental study of Resnik et al. [71] the authors observed that at the concentration of 20%, the surface smoothness was spoiled by the formation of micropyramides. They concluded from optical observations that the samples etched in 35% KOH were superior concerning the smoothness.

Seidel et al. [72] calculated and verified experimentally the values of etch rates R [$\mu\text{m/h}$] for Si $\langle 100 \rangle$ and $\langle 110 \rangle$ as well as for thermally grown silicon dioxide depending on the KOH concentration and the temperature of the etching process. The etch rates determined by the authors are listed in Table B.1-Table B.3 of Appendix B, respectively.

The influence of the process temperature and the concentration of KOH solution on the etch rate of the silicon wafers with $\langle 100 \rangle$ and $\langle 110 \rangle$ crystallographic orientations established based on Table B.1 and Table B.2 are shown in Figure 5.4a-b), respectively.

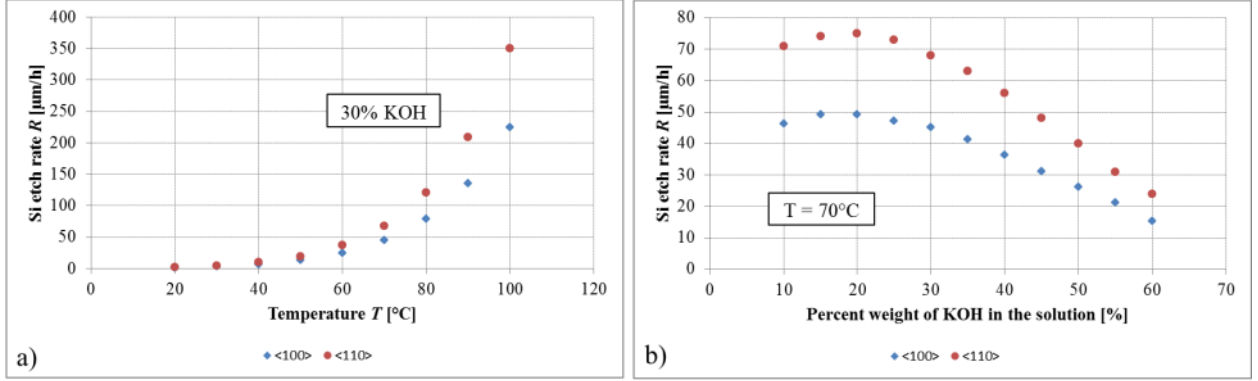


Figure 5.4: The dependence of Si $\langle 100 \rangle$ and Si $\langle 110 \rangle$ etch rate on (a) process temperature at a constant 30% KOH concentration; (b) percent weight of KOH in the solution at a constant temperature of 70°C.

Another factor that had to be considered was the silicon crystallographic orientation, which strongly affects the etch rate. Due to the fact that the pure $\langle 110 \rangle$ surface has more corrugated atomic structure as compared to $\langle 100 \rangle$ and $\langle 111 \rangle$ primary surfaces, the etching is much faster in Si wafers with this crystallographic structure. Contrarily, tightly packed $\langle 111 \rangle$ plane results in an extremely slow etching process [73]. Seidel et al. [72] determined that at the temperature of 100°C, the relation between etch rates of $\langle 110 \rangle$, $\langle 100 \rangle$, $\langle 111 \rangle$ Si orientation is 50:30:1, respectively. At a room temperature these values stand at about 160:100:1. Due to a very low etch rate in case of $\langle 111 \rangle$ silicon, the wafers of this crystallographic orientation were not considered to be used in the experiments.

To sum up, the information that must be taken into consideration when choosing the parameters of the KOH etching process are as follow:

- the etch rate rises with the temperature of the process (Figure 5.4a),
- the increase of etch rate results in the decrease of the surface quality,
- the etch rate rises for percent weight of KOH solution up to 20% and decreases for its higher values Figure 5.4b),
- the largest smoothness of the etched surface is observed for 35% KOH solution [71],
- the highest etch rate is obtained for $\langle 110 \rangle$ Si crystallographic orientation and the lowest for $\langle 111 \rangle$ [73].

Further in this section the analysis aiming at determining the optimal temperature, percent rate of a KOH solution and a crystallographic orientation of Si wafer that would allow etching very deep cavities are presented.

Based on the data presented in Table B.1-Table B.3, several combinations of the process parameters were selected for tests aiming at fabrication the energy harvester demonstrator. As specified in section 4.2, the goal of the investigation was to create in silicon, 250 μm deep

evaporation chambers and the condensing chambers as well as the channels that pass through the Si wafer. For the initial experiments the easily available, 390 μm thick, 3'' silicon wafers of <100> crystallographic orientation, that are the most commonly used in semiconductor microtechnology were chosen. Due to the fact that a very deep etching was required, the process had to be relatively fast, therefore, it should be performed at high temperatures. On the other hand, it is known, that although the etch rate increases with temperature, the quality of the surface drops. For this reason, the compromise between the rate and the quality of the process should be established.

Knowing that the smoothness of the surface is the largest for KOH concentration between 20% and 35% and the process rate must be high, due to the large thickness of the wafer that was supposed to be etched through, the first etching was performed in 30% KOH solution at a relatively high temperature of 80°C. For these parameters the etch rate of <100> Si equals to 79 $\mu\text{m}/\text{h}$ (Table B.1) , which means that in order to create a channel in 390 μm Si wafer, 294 min are required. Unfortunately, under these conditions the etch rate of SiO_2 mask is high as well, and it stands at 435 nm/h (Table B.3), meaning that 1.7 μm of layer would be degraded after 234 min of the process. Therefore, the etching performed for selected parameters resulted in a very low quality of created cavities and a complete degradation of SiO_2 mask, which made the structures unacceptable.

Due to the fact that the first results were not satisfying, it was decided to modify the parameters of the process in the way that would allow obtaining undamaged structures. The only parameter that was modified compared with the first experiment, was a lower temperature of the solution, which was set at 70°C. This change resulted in a lower rate of SiO_2 etching equal to 193 nm/h instead of 435 nm/h occurring in previous case. Although the etch rate of Si dropped as well, to become 45 $\mu\text{m}/\text{h}$, and the time of the process lengthen drastically to almost, 540 min, the times required to degrade the whole layer of SiO_2 and to etch through Si wafer were comparable being 528 min and 516 min, respectively. Unfortunately, the experiments proved that these parameters of the etching process had not been adapted yet for the fabrication of the structures of satisfying quality. The photographs placed in Figure 5.5a-b) depict the surface of <100> silicon wafer after the etching process of the channels, performed with 30% KOH solution at the temperatures of 80°C and 70°C, respectively.

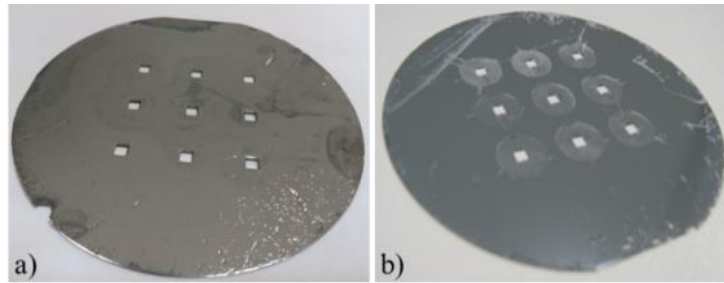


Figure 5.5: Surface of the silicon wafer containing chambers and channels etched in 30% KOH concentration, for <100> Si at the temperature of (a) 80°C and (b) 70°C.

Figure 5.6a-b) shows the thickness of the etched Si and SiO₂ depending on the process time at the temperatures of 70°C and 80°C, respectively. A blue line represents the time after which the SiO₂ mask is degraded, whereas a red line corresponds to the time required to etch through the Si wafer.

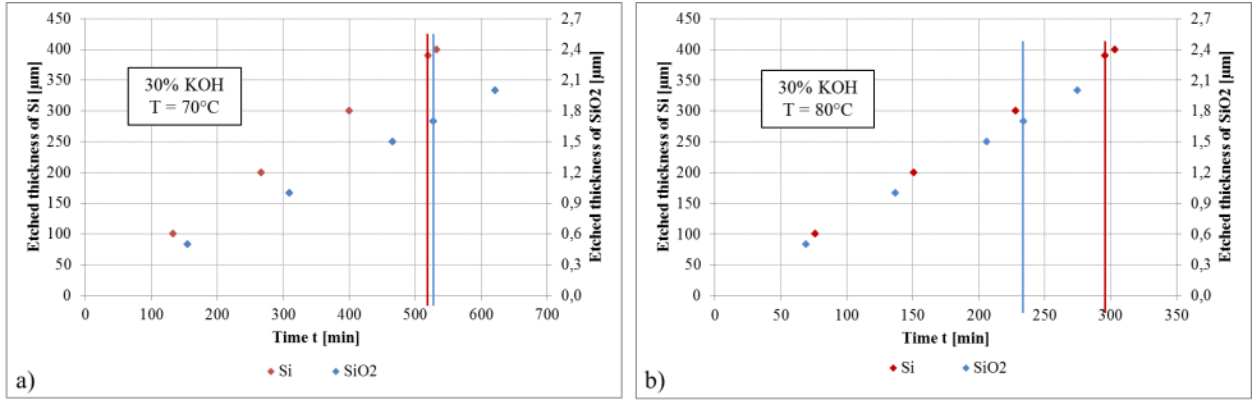


Figure 5.6: Thickness of the etched Si and SiO₂ dependence of the process time at (a) 70°C and (b) 80°C.

Further reduce of the temperature was pointless, since it led to an extremely long time of process. For example, the drop of temperature from 70°C to 60°C would result in a 960 min Si etching process instead 516 min.

In order to solve this issue, it was decided to use the less common, <110>, Si wafers that are characterized by the fastest etch rates amongst the three crystallographic orientations. In case of <110> silicon wafers, the etch rate at the temperature of 70°C and 30% concentration of KOH solution has the value of 68 μm/h (Table B.2), which means that creating the channel in 390 μm deep Si wafer, would last around 342 min. During this time, about 1.1 μm of SiO₂ mask could be etched. Taking into account, that the thickness of the mask is 1.7 μm one can conclude that the parameters chosen for this process, namely were adequate to fabricate each element of the structure, which was verified experimentally. Additionally, the roughness of the etched surface was determined by profilometer. The average roughness established in 6 independent measurements of different chambers stayed at 0.47 μm at the distance of 1 mm. For comparison, the surface of the chamber of the same depth fabricated during etching process performed under the same conditions but in <100> Si wafer gave the average roughness of 0.18 μm at the distance of 1 mm.

Although the results of this experiment was satisfactory, it was decided to verify if it is possible to reduce the time of etching process without losing the quality of fabricated structures. For this reason, the etching was performed at higher temperature of 80°C and 30% concentration of KOH solution. In this case the etch rate has the value of 125 μm/h, which means that creating the channel in 390 μm deep Si wafer, would last around 186 min. During this time, about 1.3 μm of SiO₂ mask can be consumed. The average roughness of fabricated structure was equal 0.56 μm at the distance of 1 mm.

Figure 5.7a-b) shows the chambers etched in $\langle 110 \rangle$ Si wafer, in the 30% KOH solution having the temperature of 70°C and 80°C, respectively, whereas Figure 5.8a-b) presents the thickness of the etched Si and SiO₂ depending on the process time at the temperatures of 70°C and 80°C, respectively. A blue line represents the time after which the SiO₂ mask is degraded whereas a red line corresponds to the time required to etch through the Si wafer.

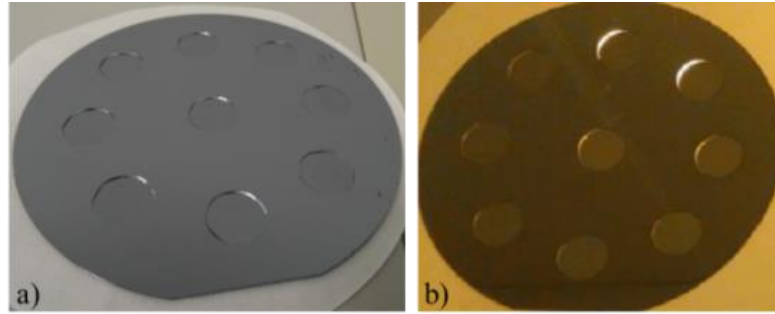


Figure 5.7: Surface of the silicon wafer containing chambers etched in the 30% KOH solution, for $\langle 110 \rangle$ Si at the temperature of (a) 70°C and (b) 80°C.

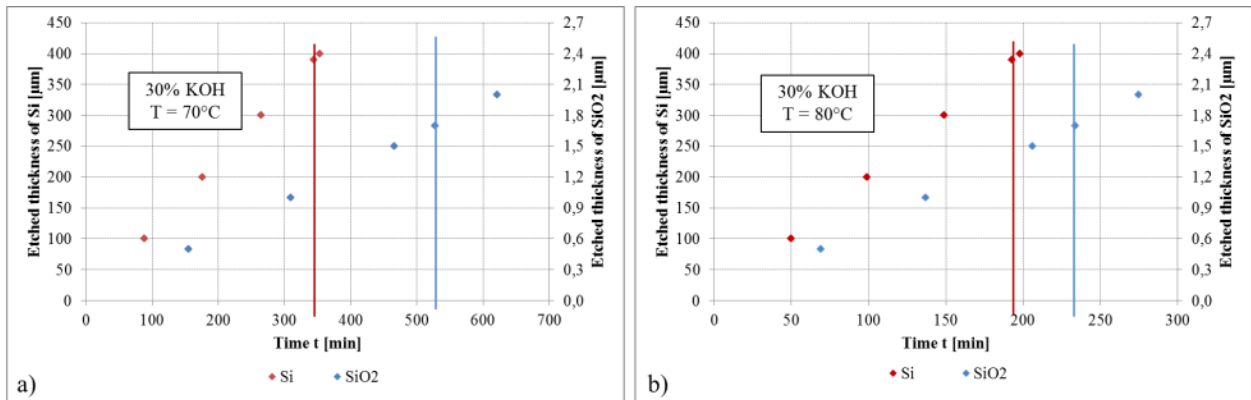


Figure 5.8: Thickness of etched Si and SiO₂ dependence of the process time at (a) 70°C and (b) 80°C.

Due to the fact that the quality of the etched structure and the surface surrounding the cavity were comparable to the surface obtained by the etching process performed at 70°C, it was decided to use the parameters that ensure shorter time of the whole process for further experiments.

The data listed in Table 5.1 summarize the results of the performed experiments. The first three columns contain the information about the crystallographic orientation of the Si wafer as well as the values of the concentrations of the KOH solution and the temperatures, respectively. The etch rates of Si and SiO₂ as well as the time required to etch through a 390 μm thick Si wafer and to degrade completely the 1.7 μm of SiO₂ mask are listed in the next four columns of the table. The last column refers to the quality of the structure after the etching process and contains the information whether the parameters selected for the experiment ensured the fabrication of a non-damaged element or not.

Table 5.1: Parameters of the etching process used in four experiments, etch rates of SiO₂ and Si for tested temperatures and concentrations of KOH; time required to etch through a 390 µm thick Si wafer and to consume 1.7 µm layer of SiO₂ mask.

Cryst. orient.	KOH con. [%]	Temp. [°C]	Si etch rate [µm/h]		Time to etch 1.7 µm of SiO ₂ and 390 µm of Si [min]		Damage
			Si	SiO ₂	Si	SiO ₂	
<100>	30	80	79	0.435	294	234	YES
<100>	30	70	45	0.193	516	528	YES
<110>	30	80	125	0.435	186	234	NO
<110>	30	70	68	0.193	342	528	NO

All the etching methods presented in this section have both, advantages and disadvantages, however after a number of experiments, it was decided to select the wet KOH etching in further research as the most easily available technique, suitable to create all the silicon elements of the harvester. It was established that the most efficient way to create the desired structures was to use the <110> Si wafers, in which the chambers were etched by the 30% KOH solution at the temperature of 80°C and these parameters of the process was applied to fabricate all the silicon elements of the future harvester.

5.1.2. Surface wettability

One of the parameter that should be taken into consideration when the work encompasses the interaction between a liquid and a surface, is a surface wettability that is the feature defining the ability of a fluid to wet a solid surface in a presence of another, immiscible fluid. Figure 5.9a) shows the general case of two immiscible fluids on a solid surface at an initial, unstable state. If the molecules of one fluid are attracted towards the solid stronger than the molecules of the other fluid, the first one expands and starts to occupy the majority of the surface, creating an equilibrium state, as shown in Figure 5.9b). A balance between the various cohesive forces is characterized by the contact angle, θ , that is defined as the angle created by the intersection of the liquid-solid and liquid-vapor interface. This interface of solid, liquid and vapor co-existence is known as three-phase contact line.

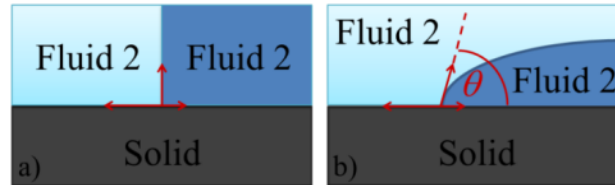


Figure 5.9: Surface wettability at (a) initial, unstable state; (b) equilibrium state [70].

Surface is considered as hydrophilic when the contact angle between water droplet and the surface is comprised between almost 0° up to 90°, depending on the level of hydrophilization. This means that the water has a tendency to spread out on the surface. On the contrary, the contact angle between a hydrophobic surface and a drop of water is larger than 90° and a fluid

tends to bead up on it. Superhydrophobic surfaces are usually characterized by the contact angles greater than 150° . When the contact angle equals to 90° , the wettability is classified as neutral. Figure 5.10a-c) shows the hydrophilic, neutral and hydrophobic states of surface wettability, respectively.

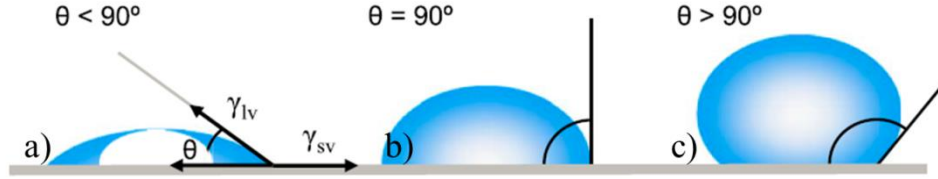


Figure 5.10: Contact angles formed by liquid droplets on (a) hydrophilic; (b) neutral and (c) hydrophobic surface [74].

In ideal case, each molecule inside the liquid droplet is attracted equally in every direction by neighboring molecules, which results in a zero net force. However, the molecules at the surface do not have the neighboring molecules in all the directions, so they are attracted to the inside of the droplet, creating an internal pressure. As a consequence, in order to maintain the lowest surface free energy, the liquid voluntarily contracts its surface area. This intermolecular force, F_{cap} , operating perpendicularly to a line of a fluid interface divided by the length of this line, L , so-called surface tension or surface energy, is described by Eq.(5.1), and it determines the shape of a liquid droplet [49,74].

$$\gamma = \frac{F_{cap}}{L} \quad \text{Eq.(5.1)}$$

The illustration of unbalanced forces of liquid molecules at the surface, which are the reason of a surface tension occurrence is given in Figure 5.11.

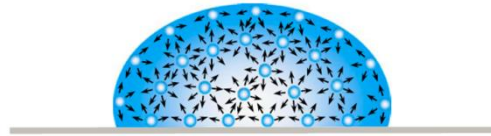


Figure 5.11: Unbalanced forces of liquid molecules at the solid surface [74].

The interfacial surface tensions and the work of adhesion between liquid and solid are directly related to the contact angle and this relation is described by Young-Dupré equation, Eq.(5.2).

$$W_{SL} = \gamma_{SV} + \gamma_{LV} - \gamma_{SL} = \gamma_{LV}(1 + \cos\theta) \quad \text{Eq.(5.2)}$$

where W_{SL} is work of adhesion [J/m^2] and γ_{SV} , γ_{LV} , γ_{SL} are surface tensions between solid and vapor, liquid and vapor, solid and liquid, respectively [N/m].

Depending on the type of the involved materials, the droplet spreads on the surface for some distance until it obtains an equilibrium shape that is determined by the contact angle. For small contact angles, the work of adhesion is high and as a result, a considerable energy must be spent to separate the liquid from the solid. When contact angle equals to $\theta = 0^\circ$, $W_{SL} = 2\gamma_{LV}$, in case of $\theta = 90^\circ$, $W_{SL} = \gamma_{LV}$ and if $\theta = 180^\circ$, $W_{SL} = 0$. The last expression means that no work is required in order to separate a drop from a solid surface, which occurs for super-hydrophobic surfaces [75,76,77].

Due to the fact that both, the surface tension, γ , and the contact angle, θ , created between liquid and a channel walls of designed device play a fundamental role in the oscillation mechanism, they are deeply analyzed in section 4.2.1.2 that is dedicated entirely to the channel design. The analysis presented in that section showed that the best way to ensure the return of the droplet through the channel into evaporation chamber is to create a hydrophilic channel surface characterized by a contact angle lower than 87° .

Another aspect of the surface wettability is its impact on the evaporation time of the fluid, and as a result, on the rapidity of the oscillations occurring in the system. There are several publications showing that in general, the evaporation of water is faster on a hydrophilic surface [78,79,80,81]. On the other hand, Hsu et al. [42] observed that, contrarily to the conventional view of natural evaporation, the hydrophilic surface does not enhance the evaporation process when considered superheated surface. The authors confirmed that the surface wettability plays a significant role in the vapor-liquid heat transfer on superheated surfaces when the vapor bubbles formation impacts the evaporation behavior. Soupremanien et al. [65] performed a brief experiment aiming at understanding if the surface wettability of the channel influences anyhow the oscillation mechanism occurring inside their thermo-mechanical device. The system, likewise the one presented in this work, was composed of evaporator, condenser and a channel connecting these two elements. In order to compare two types of the surface – hydrophobic and hydrophilic – SiO₂ was deposited on the channel to create a hydrophobic surface. For hydrophobic version, the surface of the channel remained unchanged. Although the result obtained in this experiment showed that the oscillations were initiated faster for a hydrophilic surface, the authors underline that the question of wettability was of little importance in their study and the experiment had only a tentative character. The authors did not classify this parameter as the one of a great importance for their macro-demonstrator. Nonetheless, they emphasized that the surface type could have a huge significance in terms of vaporization dynamics, for the devices fabricated at a small scale, where the gravity phenomena becoming negligible, contrary to the surface tension.

In order to decide which type of surface should be created in technological fabrication process, two samples of silicon structures were prepared. In one case, the silicon wafers creating the full structure had been pre-processed during the fabrication process in terms of the surface hydrophilisation, as described in section 5.1.3.1. The typical water contact angle for silicon surface after SC-1 and SC-2 cleaning (known also as RCA-1 and RCA-2), which was performed during the fabrication process of device presented in this work, is 10° [82]. The wafers forming

another structure stayed unchanged, which means that typical silicon wafers processing including HF involvement had been applied during the fabrication. This allowed to expect that the contact angle was close to 70° [82]. During the initial experiments, a practical issue related to the level of surface wettability appeared, namely for higher contact angles, the water distribution inside the system was hindered and as a result, it could not fill completely the evaporation chamber, as shown in Figure 5.12a). The schematic of the silicon device has a tentative character and its scale do not correspond to the dimensions of the real system. In case of surface characterized by the contact angle close to 10° this problem disappeared as shown in Figure 5.12b).

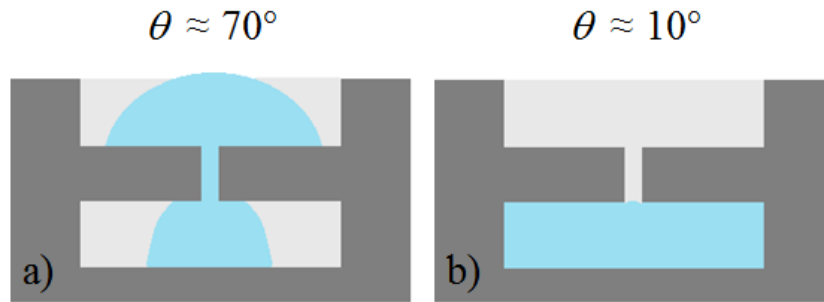


Figure 5.12: Water distribution inside the system of the contact angle θ close to (a) 70° and (b) 10° .

Hence, for this practical reason, it was decided to perform all the experiments with the devices characterized by the low contact angle, close to 10° .

5.1.3. Silicon bonding

Due to the fact that the structure of the harvester was supposed to consist of the three silicon wafers it was mandatory to find out a way to bond these elements. Figure 5.13a-c) shows the photographs of three silicon wafers containing the evaporation chambers, the channels and the condensing chambers, respectively. These three elements were supposed to be connected to create a silicon part of the harvester structure in a way shown in Figure 5.13d) that depicts a schematic cross-section of bonded layers.

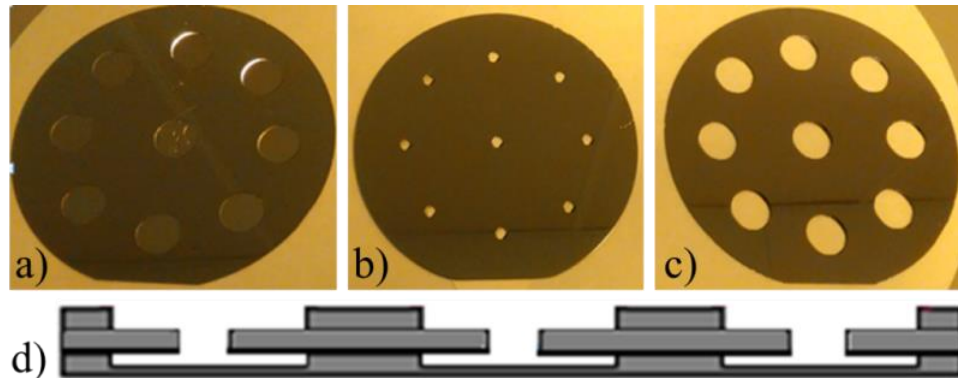


Figure 5.13: Si wafer containing (a) evaporation chambers; (b) channels and (c) condensing chambers; (d) cross-section of the three Si wafers after the bonding process.

5.1.3.1. Wafer preprocessing

Although the process of etching was performed in the clean room environment, where the wafers were prevented from coming into contact with contaminations, each bonding technique requires the substrates to be subjected to a cleaning process. This procedure bases on a sequence of chemistries that selectively removes the organic and inorganic contaminations residing on the surface of the wafer. Additionally, to obtain a uniform distribution of the fluid inside the evaporation chamber, its surface should be close to hydrophilic. These two requirements can be obtained at the same procedure by performing the steps listed in Table 5.2 [83]:

Table 5.2: Technological steps for cleaning and hydrophilisation of Si wafers.

	Technological step	Procedure details
1.	Piranha etch (Caro's etch) - general cleaning procedure, especially useful for removing hardened photoresist	the wafers are immersed in a hot mixture of H_2O_2 (hydrogen peroxide) and H_2SO_4 (sulfuric acid) in the proportion 1:4; time: 20 min
2	Thorough rinse	the wafers are rinsed under flowing DI (deionized) water; time: 5 min
3.	Drying	the wafers are spun in spin coater; time: 60 s; frequency of rotation: 3000 rpm
4.	SC-1 (Standard Clean) - procedure removing traces of organic residues from the wafer surface [84]	the wafers are immersed in a mixture of NH_4OH (ammonium hydroxide), H_2O_2 and deionized water, in the ratio of 1:1:5; time: 10 min; temp: 80°C
5.	Thorough rinse	the wafers are rinsed under flowing DI water; time: 5 min
6.	Drying	the wafers are spun in spin coater; time: 60 s; frequency of rotation: 3000 rpm
7.	SC-2 cleaning - procedure removing all the ionic contaminations, specifically metals, from the wafer [84]	the wafers are immersed in a mixture of HCL (hydrochloric acid), H_2O_2 and DI water in 1:1:6 proportion; time: 10 min; temp: 80°C
8.	Thorough rinse	the wafers are rinsed under flowing DI water; time: 5 min
9.	Drying	the wafer are spun in spin coater; time: 60 s; frequency of rotation: 3000 rpm

5.1.3.2. Silicon bonding techniques

In order to select the most suitable way to bond the three Si wafers, several techniques were considered and experimentally examined. The methods of bonding that taken into account during the research were: high temperature Silicon Fusion Bonding (SFB), known also as Silicon Direct Bonding (SDB) or Silicon Thermal Bonding (STB), low temperature bonding, vacuum bonding and adhesive bonding. Amongst all tested methods the most reliable and reproducible results were obtained for the adhesive bonding and this procedure is presented in the following section.

The description of the experiments and the results obtained during fusion, low temperature and vacuum bonding are placed in Appendix C.

5.1.3.3. Adhesive bonding

After a deep study, it was concluded that in order to connect the three silicon wafers of a non-standard geometry into one structure of the harvester, the adhesive bonding technique using an intermediate layer should be applied. This method enables joining silicon wafers at the temperatures lower than 200°C and it does not depend on the surface roughness, particles, material of the substrate or planarity of the bonding surfaces [85]. During the research, SU-8 photoresist that is widely used as an adhesive between the silicon wafers, was selected as an intermediate layer [97,98]. SU-8 is an epoxy based, negative photoresist that shows one of the best results in bonding experiments and it has numerous advantages, such as flexibility of its layer thickness up to several hundreds of micrometers, high chemical and thermal stability and good mechanical properties [88]. Taking into account the principles of the device operation, this material has a number of features that make it suitable for its application in the structure. The main advantages that legitimate its usage for a fabrication process of this particular structure consist in:

- a very low thermal conductivity (0.2 W/mK) [88],
- the fact that it is dedicated especially for microfluidic systems,
- the fact that it does not require polished surfaces of the elements to be bonded.

In the experiments leading to the fabrication of the device, several steps shown in Figure 5.14 were employed. The parameters of the process had been established based on the literature, as well as on a number of experiments performed during the study, which helped to adapt this technique to a non-standard bonding of the three Si wafers. In the first step of the process, a 4" silicon wafer playing a role of a substrate, was treated in HNO_3 . This allowed creating a hydrophilic surface of the wafer, which was supposed to facilitate a transfer of the adhesive layer at a later stage of the experiment. In the next step, 4 ml of SU-8 2007 photoresist was deposited on its surface (1 ml for each inch of the wafer's diameter) and, to obtain a uniform thickness of the photoresist layer, it was spun in two steps of different parameters: 500 rpm/15 s and 3000 rpm/60 s, respectively. Later, an adhesive layer was transferred from the 4" wafer to the surface of Teflon cylinder. After that, the cylinder was rolled on the surface that was supposed to be bonded – in the first stage of the experiment it was the surface of the wafer containing the evaporation chambers – and as a result, the adhesive layer was partially transferred on this surface. Later, the wafer containing the evaporation chambers, covered with a thin layer of SU-8 was aligned and brought in contact with the silicon wafer comprising the channels. This way, the first part of the harvester composed of the evaporation chambers and the channels was created. In the next steps, the structure was placed for 90 min at 160°C inside a pressure chamber that was designed for this particular procedure. The pressure inside the chamber equaled to

10^3 mbar and the force applied to the structure equaled to 1000 N. In order to complete the device, the condensing chambers were needed. For this reason, the first steps of the procedure were repeated, and the Teflon cylinder was used in order to deposit the layer of photoresist on the surface of the wafer containing the condensing chambers. Further, the wafer was aligned and brought in contact with the structure created by the evaporation chambers and the channels. The whole structure was placed inside the pressure chamber and subjected to the same procedure.

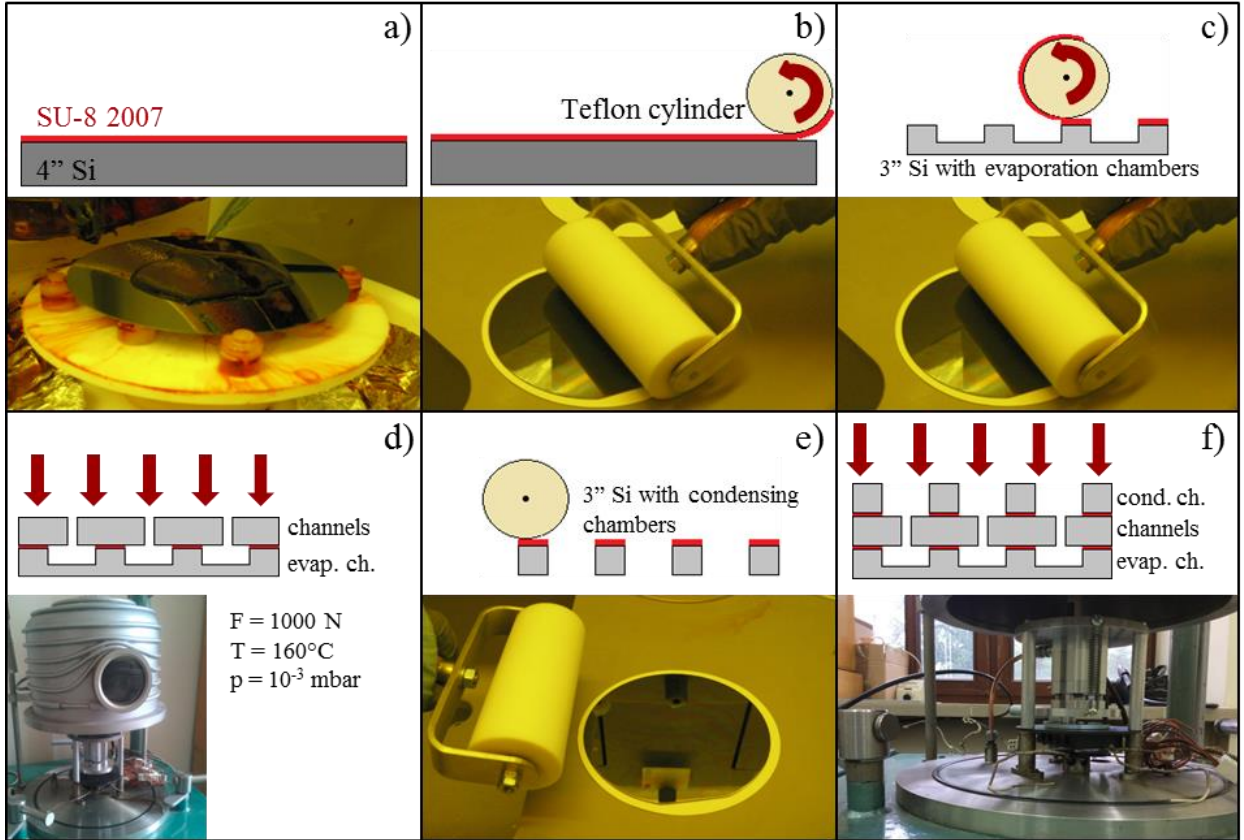


Figure 5.14: Technological steps of SU-8 bonding process: (a) spinning of SU-8 photoresist on 4" Si wafer; (b) transfer of SU-8 from Si wafer onto Teflon cylinder; (c) transfer of the adhesive layer from the cylinder to a wafer containing evaporation chambers; (d) a structure with channels brought in contact with the wafer containing evaporation chambers, covered with SU-8 and placed inside a pressure chamber; (e) transfer of SU-8 onto a wafer with condensing chambers; (f) all three layers brought in contact and placed inside the pressure chamber.

In order to verify the strength of the bonding and to optimize the parameters of the process two types of tests were performed. Firstly, the bonded layers were dipped in a buffered HF for one hour. After this process, the structure stayed unchanged and no disconnection was observed. In the second approach, several tests with the usage of ultrasonic cleaner were carried out. It was observed that all the wafers bonded in the process shorter than one hour disconnected after around 30 min of test, while for the longer bonding process the connection was permanent and no wafers separation occurred. Therefore, in all the further bonding processes, the bonded elements were kept in the pressure chamber for 90 min.

The SEM photograph given in Figure 5.15 shows the cross-section of the manufactured harvester structure covering three silicon layers bonded with the usage of SU-8 2007 photoresist of around 5 μm as an adhesive layer.

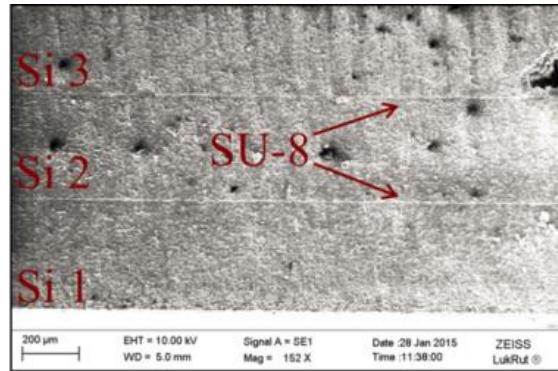


Figure 5.15: Cross-section of three Si wafers bonded by a layer of SU-8 photoresist.

5.1.4. PZT montage – challenges and limitations

The last step of the fabrication process was to mount a piezoelectric element on top of the structure that had been partially filled with a working fluid. There were several challenges related to the process of a piezoelectric layer bonding to the surface of silicon wafer. First of all, due to the fact that before the sealing, the device had already contained some liquid, it was not possible to apply any high temperature bonding process because it would result in an evaporation of the fluid. For this reason, it was decided to connect these two elements with the usage of an adhesive material. It had to be also taken into account that the harvester was supposed to operate at high temperatures and it was mandatory to avoid fluid leakage, which means that the structure of the glue and its properties could not degrade with temperature and time. Moreover, the surface of the silicon wafer was manufactory polished, which made it very smooth and not all the types of the glue were able to connect elements that did not contain any roughness. In order to select the adhesive that would be able to meet all these demands, several prospective candidates listed in Table 5.3 was examined.

Table 5.3: Types and parameters of tested adhesives.

	Adhesive type	Temperature operating range [°C]	Water resistance
1.	Pro Seal	-56 ÷ 204	YES
2.	LOCTITE Hysol 3450 A&B	-55 ÷ 120	YES
3.	Mega Strong Sader	-30 ÷ 130	YES
4.	3M DP490 Scotch-Weld	-55 ÷ 120	YES

The first tests were carried out with Pro Seal high temperature silicon gasket that can operate continuously at the temperatures from -56°C up to 204°C and can withstand a temperature of 260°C in case of intermittent work. Moreover, it resists different types of fluids, including water, which allowed expecting that this gasket could be a suitable solution of the bonding issue. Unfortunately, after the application of the gasket, its surface remains flexible so the changing pressure inside the harvester, which affected the piezoelectric element, caused its displacement to finally cause a disconnection of the gasket and a smooth silicon wafer.

The second approach was to use a two component epoxy adhesive that is characterized by a high strength of the bonding. It was decided to choose LOCTITE Hysol 3450 A&B that can operate at the temperatures up to 120°C and it is resistant to water. However, although at the beginning of each experiment the glue was working properly, with rising temperature and pressure inside the harvester, the silicon wafer had a tendency to crack along the crystal axes. This could be a result of a mechanical stress in a silicon wafer, which was caused by a thick layer of the strong adhesive attached to its surface.

Another type of glue selected for experiments was MS polymer (Mega-strong SADER) that is resistant to water and can work successfully in the temperatures between -30°C and 130°C . The results of the experiments performed with structures bonded by this glue were much more promising than in previous cases and even several hours operation in high temperatures did not result in a leakage of fluid from the device. However, with rising time of experiment the properties of the glue worsen and after around three hours of continuous operation at the temperature of approximately 130°C , a layer of the glue was defected. As a result, a fluid leak from the harvester occurred. Despite this drawback it was decided to use MS glue for most of the further experiments due to the fact that it made it possible to observe and analyze each time the continuous electric signal during around three hours.

The last type of glue that was tested at the very end of a practical work, was 3M DP490 Scotch-Weld that is a thixotropic, two component epoxy adhesive with an excellent heat and environmental resistance. The experiments showed that regardless the time of the continuous operation at high temperatures no damage to the structure of the glue and no leakage occurred. As a result, the same structure could be tested a number of times, which gave the possibility to observe and analyze the continuous electric signal without the reduce of the amplitude even after several days of operation.

5.2. Process flow of energy harvester fabrication

All the experiments described in this section resulted in the elaboration of a process flow of the silicon device fabrication. The production process of a single cell of the system composed of the evaporation and condensing chambers, the channel and the piezoelectric element was divided into several technological steps shown graphically in Figure 5.16. The scale of the device given in the figure do not correspond to its real dimensions and the schematic has only an illustrative character.



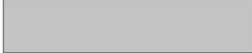
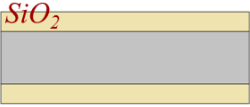
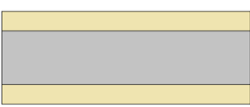
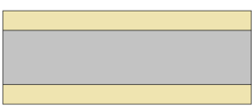
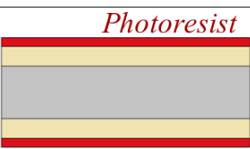
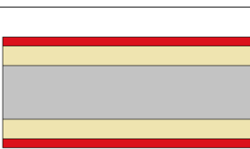
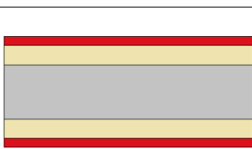
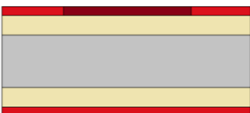


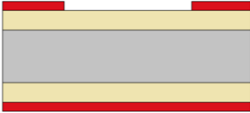








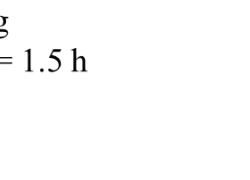
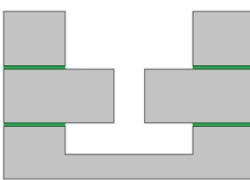

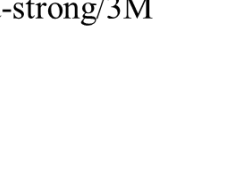
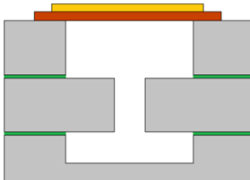

	Boiling chamber	Channel	Condensing chamber
a) Three Si <110> wafers RCA cleaning			
b) Wet oxidation T = 1150°C; t = 5 h			
c) Spin coating of ma-P 2010 positive photoresist			
d) Exposure of photoresist to a pattern of light			
e) Photoresist development			
f) SiO2 etching in NH4F-HF			
g) Si wet etching in 30% KOH solution; T = 80°C			
h) Hydrophilisation; bonding SU-8 2007; T = 160°C; t = 1.5 h F = 1000 N			
i) PZT montage – MS Mega-strong/3M Scotch-Weld			

Figure 5.16: Process flow of silicon energy harvester fabrication: (a) wafers preparation; (b) wet oxidation; (c) photoresist deposition; (d) photoresist exposure to a pattern of intense light; (e) development of photoresist; (f) SiO₂ etching in NH₄F-HF; (g) Si etching in KOH solution; (h) hydrophilisation and bonding of the wafers; (i) montage of piezoelectric element to a surface of Si wafer.

At the beginning three Si <110> wafers had to be subjected to a full RCA cleaning procedure, after which they were placed inside the oxidation furnace, where the wet oxidation process occurred. The process was performed at the temperature of 1150°C and it lasted 5 hours, which allowed creating approximately 1.7 µm thick layer of SiO₂ on both sides of each wafer. This layer played the role of a mask in the KOH etching process. The photolithography started by a spin coating of ma-P 2010 positive photoresist on the back and front side of each wafer. The photoresist was further prebaked at the temperature of 100°C and exposed in Mask Aligner to a pattern of intense light. The pattern was composed of nine evaporation chambers, channels or condensing chambers. Later the post-exposure baking and the development of the photoresist was performed. After that, a part of SiO₂ that was not covered with the photoresist layer was etched in a buffered hydrofluoric acid solution NH₄F-HF (ammonium fluoride-hydrofluoric acid). This way, the desired shapes of the chambers and the channels could be etched in Si wafers. To this end, the 80°C solution of 30% KOH was used. In the next steps, SiO₂ was removed and three silicon wafers, after a procedure of cleaning and hydrophilisation, were aligned and bonded together to create the harvester structures. The bonding process with the usage of SU-8 2007 as an adhesive was performed inside the pressure chamber where the whole structure was being kept during 90 min under the force of 1000 N at the temperature of 160°C, under the pressure of 10³ mbar. In order to obtain independent cells of the device from the construction containing nine of them, the laser was used. The last part of the fabrication process was to fill the structure with some amount of fluid and to cover it with a piezoelectric element. It was decided to use PZT circular ceramics and to attach it to the surface of the cell by MS polymer (Mega-strong SADER). At the end of the research a two component epoxy adhesive (3M Scotch-Weld EPX Adhesive DP490) was applied for several experiments.

5.3. Summary of the chapter

In this chapter the technological steps required for fabrication of the prototype that was proposed in section 4.2 are presented. The experiments were performed in the clean room environment, where different technological processes have been tested and the final parameters for the structure fabrication were determined (Figure 5.3):

- three <110> Si wafers subjected to RCA cleaning procedure; hydrophilisation,
- wet oxidation process ($T = 1150^{\circ}\text{C}$; $t = 5\text{ h}$),
- spin coating of the ma-P 2010 positive photoresist,
- exposure of the photoresist to a pattern of light,
- photoresist development,
- SiO₂ etching in NH₄F-HF,
- Si wet etching in a 30% KOH solution ($T = 80^{\circ}\text{C}$),
- bonding of the three wafers with etched elements of the device into one structure with the usage of the SU-8 2007 intermediate layer ($T = 160^{\circ}\text{C}$; $t = 1.5\text{ h}$; $F = 1000\text{N}$)
- PZT montage (MS-Mega strong/3M Scotch Weld).

The characterization of a prototype has been described in *Chapter 6*.

6. Characterization of the prototype structures

The aim of the research presented in this chapter was to examine if the structures fabricated in the process flow described in section 5.2 were able to generate continuous pressure oscillations when exposed to temperatures higher than 120°C. It has to be underlined that the work presented in this manuscript was strongly focused on the technological aspects and the deep analysis aimed at understanding the thermo-fluidic behavior of the system was not included to this study.

The oscillation mechanism occurring in the system was determined by analyzing the electric signal given by the piezoelectric ceramics, PZT. A SEM picture and a schematic cross-section of the structures that were examined during the study are presented in Figure 6.1a-b), respectively. The scale of the device given in Figure 6.1b) do not correspond to its real dimensions and the schematic has only an illustrative character.

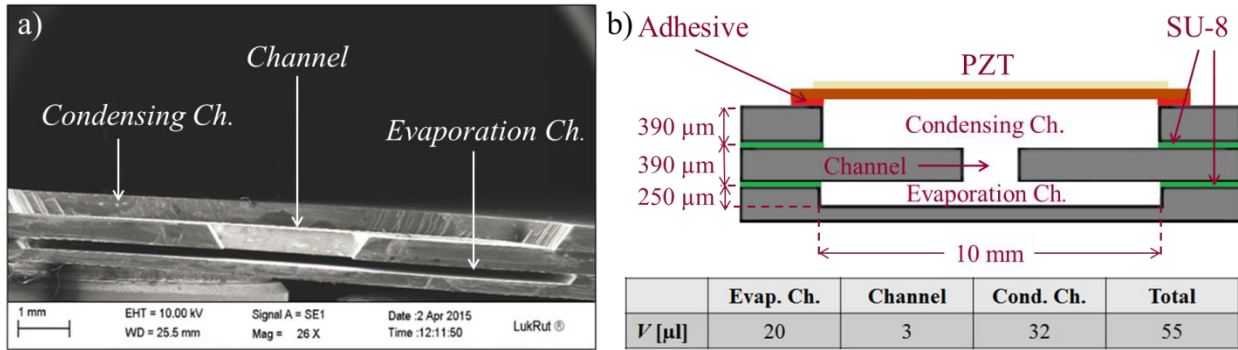


Figure 6.1: (a) SEM picture of the device's cross-section; (b) schematic of the device.

Many parameters may influence the system performances, especially the material used for assembly. All the constitutive elements of the device were assembled using SU-8 photoresist, except for the piezoelectric that was a top cover of the whole structure, as shown in Figure 6.1b). The application of another adhesive to mount this particular element was related to the fact that the assembly process with the usage of SU-8 requires a temperature of 160°C that is higher than expected operating temperature. As a result, the fluid placed inside the structure would boil and evaporate before the sealing process is completed. For this reason, the piezoelectric was attached to the silicon structure with the use of an adhesive that was applied in a form of a thin layer on a surface surrounding the condensing chamber, as shown in Figure 6.1b). In the first part of the experimental work, described in sections 6.2 and 6.3, MS polymer, also referred to as silyl-modified polyether or modified silicone, (Mega-strong SADER) was used. According to the data provided by the supplier, this adhesive is resistant to the temperatures up to 130°. In some experiments however, it was required to provide higher temperature to a bottom part of the device. Hence, to reduce the thermal stresses, it was decided to apply a cooling system to the experimental setup. In order to verify if it is possible to maintain a continuous operation of the device without a cooling system support, at the end of a practical work some complementary, tentative tests described in section 6.4 were performed. In these experiments a two component

epoxy adhesive (3M Scotch-Weld EPX Adhesive DP490), presenting much better heat resistance, was applied.

6.1. Parameters of influence: hierarchy of importance

The factors that play a significant role in the oscillations characteristics are analyzed in section 4.2.1. Due to the fact that some of them are interdependent, it was necessary to list them and to establish their hierarchy of importance. The parameters identified as influential are:

- type of the working fluid,
- surface wettability,
- channel design,
- type of the piezoelectric element,
- value of the hot temperature, T_H , required for the oscillations occurrence,
- volume of the working fluid in relation to total volume of the structure (filling ratio, α).

6.1.1. Ranking of the parameters

The analysis described in section 4.2.1 contributed towards the establishment of the parameters hierarchy that was ranked as follow:

1) Working fluid

The parameter defined as the most important was the type of the fluid introduced to the system. This was due to the fact that the physical properties of the liquid not only influence the operational temperatures and oscillations efficiency, but also define a whole mechanical design of the device.

2) Channel design

Due to the fact that a proper choice of a channel diameter and its surface is an essential factor for the oscillations occurrence, was ranked as a second most influential parameter.

3) Hot surface temperature and filling ratio

These two parameters were placed on the third place in the hierarchy and they are considered as equally important. This is due to the fact that, in order to obtain any kind of oscillations both, the hot temperature and the filling ratio, must be comprised within a specific range of values and in case of exceeding the range limits, no oscillations appear. Moreover, within this range there is a specific value of filling ratio that ensures an optimal oscillation behavior.

4) Surface wettability

This parameter was ranked fourth on the list of parameters due to the fact that although its impact on the evaporation kinetics was confirmed in the literature, it appears that it is significant

only in terms of optimization of the oscillations. Contrary to the parameters placed higher in the hierarchy, it does not determine whether the oscillations occur or not.

5) PZT geometry

The analysis performed in sections 3.3 and 3.5 regarding the size of the piezoelectric ceramics allowed to assume that although in general the dimensions of PZT play a huge role in the value of generated voltage, it should not have this significance when one take into account the particular geometry of the device presented in this work.

6.2. Preliminary experiments

The main research aimed at profound analysis of the hot temperature, T_H , and the filling ratio, α , impact on the oscillation nature for two different configurations of experimental setup – with and without a cooling system – are thoroughly described in sections 6.3 and 6.4, respectively. However, before this study could be performed, it had been essential to determine a final form of the device, the working conditions as well as the relevant ranges of the hot temperature and the filling ratio. For this reasons some preliminary experiments and theoretical analysis had been carried out.

6.2.1. Determining the working conditions ensuring oscillation mechanism

Due to the fact that, as described in the previous sections, there is a number of parameters that significantly influence not only the occurrence but also the nature of the oscillations, it was decided that some of them should be classified as fixed. It was assumed that all the factors related to the device structure and its components, namely channel diameter, surface wettability, working fluid and piezoelectric element should be considered as constant. The parameters that strictly refer to the nature of the oscillations and influence significantly the value of their amplitude and frequency – filling ratio, α , and hot temperature, T_H , – should be thoroughly examined in the wide range of values.

6.2.1.1. Fixed parameters: device structure

As it was explained in section 6.1.1 the most important decision to be taken at the very beginning of this research was to choose a working fluid type. Based on the analysis presented in 4.2.1.1, it was decided that water should be used for all the experiments. In the next step, the diameter of the channel connecting the evaporation and the condensing chambers had to be established. Taking into account all the information from 4.2.1.2 it was chosen to create a channel of 3 mm. Another important decision to be taken was the type of the silicon structure of the device in terms of wettability. Accordingly to the study from 5.1.2 it was decided to perform all the experiments with the devices characterized by a low contact angle, close to 10° .

The next step of the preliminary experiments was aimed at selecting the PZT type that could generate the highest value of voltage and power when exposed to pressure changes occurring

inside the device. Taking into account the analysis presented in section 4.2.1.5, as well as in *Chapter 3* it seemed to be relevant to verify how the geometry of PZT element influences the electrical properties of the device. For this reason three hydrophilic structures containing 20% of water were covered each one with different-sized piezoelectric and placed on a hotplate heated to a temperature of 125°C. Each PZT was attached to a structure using the same method, namely with the use of MS polymer adhesive (Mega-strong SADER) that was applied in a form of thin layer on a surface surrounding the condensing chamber, as shown in Figure 6.1b). According to the literature and to the experiments described in *Chapter 3*, a thinner piezoelectric layer generates higher value of voltage, and as a result, its efficiency is better as compared to thick elements. This is due to the fact that the capacitance of the element rises with a drop of thickness. Additionally, a thin piezoelectric is more flexible and when mechanical stress is applied, the element deflection is much higher than in case of a thick layer. Although there are many advantages of using very thin piezoelectrics, it must be taken into account that its thickness cannot be reduced endlessly, as it becomes fragile and higher pressures could cause its irreversible deformation. However, taking into consideration a small size of the device presented in this research, it was decided to analyze the thinnest commercially available PZT of the same thicknesses equal to 0.1 mm. Thus, the parameter that varied was the diameter of the element. The geometrical parameters of PZT-based ceramics (from MURATA) selected for the experiments are listed in Table 6.1.

Table 6.1: Dimensional parameters of tested PZT.

No.	Commercial name	R_s [mm]	R_p [mm]	t_s [mm]	t_p [mm]
1.	7BB-12-9	6.0	4.5	0.10	0.12
2.	7BB-15-6	7.5	5.0	0.10	0.12
3.	7BB-20-3	10.0	7.0	0.10	0.12

R_s being the radius of the substrate, R_p the radius of the piezoelectric layer, t_s the thickness of the substrate and t_p the thickness of the piezoelectric layer.

Although it could be expected that higher value of voltage should be generated by the structure covered with the PZT of a larger diameter, no difference in signal amplitude was observed for all the tested devices. This result could be explained by the clamping method that was the same for the all cases, as shown in Figure 6.2. As a result the active area of PZT that participated in the electric charge generation was unchanged, regardless the actual size of the element. Due to the fact that the project presented in this work assumed the fabrication of a low-scale device and knowing that in this particular case the larger dimension of PZT would not result in a higher value of generated voltage, it was decided to select the 7BB-15-6 piezoelectric of 15 mm diameter, which is the second smallest from commercially available, to the best of the author's knowledge. As its diameter did not extend the diameter of the whole silicon part of the device it was not relevant to choose even smaller 7BB-12-9.

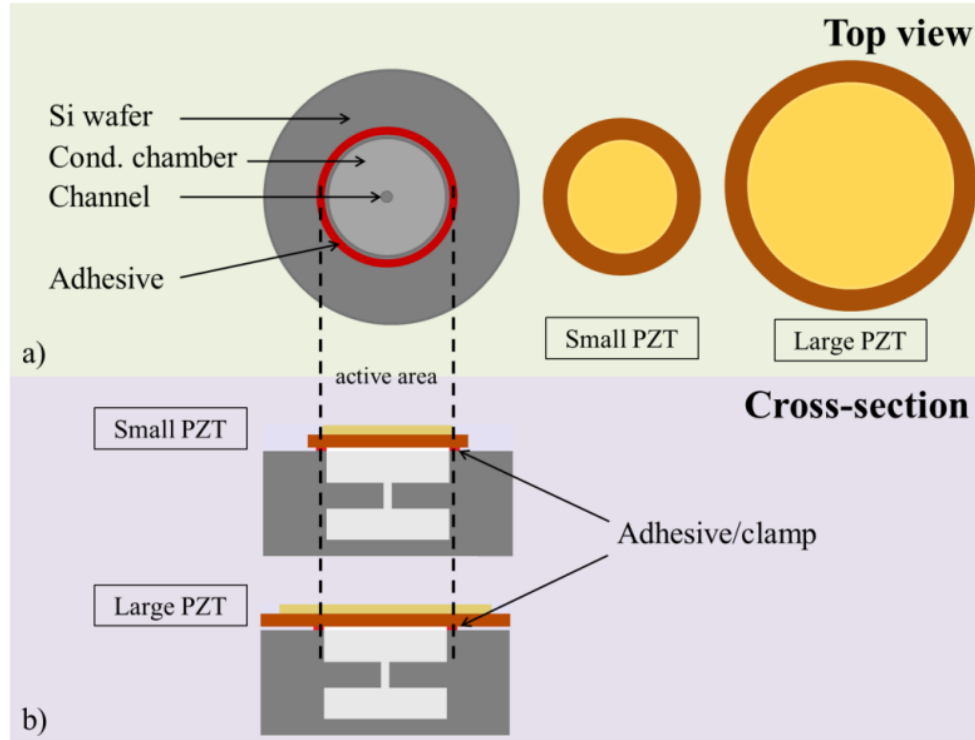


Figure 6.2: (a) Top view of the Si structure with an adhesive layer applied around the condensing chamber as well as of small-sized and large-sized PZT; (b) cross-sections of two Si structures – one covered with small another with large PZT.

At this point the final structure of the device was established and treated as constant.

6.2.1.2. Variable parameters: oscillations nature

The next part of preliminary research was aimed at determining the general ranges of the temperatures and the filling ratios for which any kind of oscillations occur. Their optimization was not the goal of this study. In these initial experiments a number of silicon structures after a hydrophilisation procedure creating close to 10° water contact angle, with 3 mm wide channel, covered by 7BB-15-6 PZT and filled with different amounts of water (5%-60%) were exposed to a wide range of temperatures (between 100°C and 160°C). During these experiments, some of the structures presented oscillation behavior and some did not. After the theoretical analysis presented in 4.2.1.3 and 4.2.1.4 it can be assumed that the devices that did not generate any oscillations were either exposed to the hot temperature or filled with the amount of water that exceeded the range limits of these parameters. In other words, the working conditions did not ensure the oscillations occurrence. However, even for the operating devices the oscillations never appeared below 120°C and above 135°C , as it is shown in Table 6.2. Therefore preliminary results helped to establish the range of temperatures within which the following experiments were supposed to be performed.

Table 6.2: Oscillations occurrence depending on hot surface temperature, T_H .

T_H [°C]	100÷120	120÷135	135÷160
Oscillations	NO	YES	NO

Regarding the filling ratio, it was established that in general, when operating within the correct range of the hot temperatures, the oscillations were generated if the volume of water enclosed inside the system comprised no less than 10% and no more than 30% of the total enclosure volume (56μl), as presented in Table 6.3.

Table 6.3: Oscillations occurrence depending on filling ratio, α .

α [%]	5	10	20	30	40	60
Oscillations	NO	YES			NO	

According to the literature related to PHP's being also the systems dependent on the filling ratio, in order to ensure the oscillation mechanism the value of this parameter must be comprised between 20% and 80% [49]. For minimization of the overall thermal resistance it should be in the range of 40%-60% [44] and its optimal value stands at around 50% [43]. In general these values differ from the ones obtained experimentally in presented work. However, in case of the thermo-mechanical device of Soupremanien et al. [67], the oscillations were initialized for much lower values of this parameter, even close to 6.5%. Moreover, the authors observed that this value varies depending on the size of the device. All these publications show that filling ratio is the parameter that strongly depends on the type of the working fluid [46] and above all, on the construction and the geometry of the device. For these reasons, every device of particular structure should be analyzed separately and can give results incomparable with another oscillating systems.

The analysis summarized in Table 6.2 and Table 6.3 led to the conclusion that, in order to enable the device operation, it is essential to provide simultaneously both, correct amount of water and hot temperature value. If even one of these parameters exceeds its range limits, no oscillations appears.

For all the experiments, a specific behavior of the generated signal was observed, namely for a fixed value of filling ratio the oscillation mechanism occurred for two different ranges of temperatures. Generally, the first oscillations appeared at the temperatures between 120°C÷128°C then after some time they stopped to occur again at the temperature of around 130°C÷135°C. This kind of behavior, to the best of author's knowledge, has not been noticed in any other oscillating systems and the profound thermo-physical analysis aimed at understanding this phenomenon should be performed in the future work.

In sections 6.3 and 6.4 the study of filling ratio and hot temperature influence of the oscillations behavior has been deepen. It aimed at determining the value of these parameters that ensure the generation of oscillations of optimal characteristics.

6.2.2. Working conditions summary

To sum up, all the preliminary experiments were aimed at determining the working conditions ensuring the oscillations occurrence inside the system. This allowed starting the thorough analysis of two main parameters, filling ratio and hot temperature, which are strictly related to the oscillation characteristics, especially to the frequency and the amplitude value of the signal generated by the piezoelectric element. The list of structural features as well as relevant ranges of the hot temperatures and the filling ratios established during preliminary experiments and the analysis are listed in Table 6.4.

Table 6.4: Summary of parameters selected for the experiments.

Working fluid	Channel diameter [mm]	Temperature T_H [°C]	Filling ratio α [%]	Surface type	PZT type
Water	3	120 ÷ 135	10 ÷ 30	Hydrophilic	7BB-15-6

6.3. Operation of the device with a cooling system

6.3.1. Uncertainty analysis and experimental repeatability

In this research the influence of the hot temperature, T_H , and the filling ratio, α , on the voltage signal characteristics generated by the piezoelectric, with particular emphasis of its frequency and amplitude, was analyzed. Thanks to the preliminary experiments described in section 6.2, three values of filling ratio that enables the oscillation occurrence when exposed to the temperatures between 120°C and 135°C, were determined – 10%, 20% and 30%. For each value of filling ratio three independent experiments under exactly the same conditions were performed. The first series of the three experiments was performed for $\alpha = 10\%$. Three silicon hydrophilic structures of 3 mm channel filled with the same amount of water and covered with 7BB-15-6 PZT-based ceramics were exposed to the same range of temperatures. The values of voltage generated in each experiment were similar and they oscillated around $0.4 \text{ V} \pm 25\%$. In the second series, the experiments were carried out under the same conditions, with the only difference being the value of $\alpha = 20\%$. The voltage amplitudes were generally equal to $1.5 \text{ V} \pm 30\%$. The third stage of this work aimed at analyzing the structures filled with $\alpha = 30\%$ resulted in signal amplitudes of $0.4 \text{ V} \pm 25\%$.

6.3.2. Experimental setup description

In order to examine the electrical behavior of created structures, the experimental setup shown in Figure 6.3 was used. In order to provide heat to the structure of the device, a digital hotplate SD 160 was used. The temperature variations across the plate are $\pm 0.2^\circ\text{C}$ at 37°C and $\pm 1^\circ\text{C}$ at 150°C , whereas the temperature stability stands at $\pm 0.25^\circ\text{C}$. For conducting the heat flow to the structure, a 5 cm high Aluminum cylinder of 1.5 cm diameter was placed on the hotplate surface. The energy harvesting device, partially filled with water was mounted on top of the cylinder. Due to the fact that first examined elements contained MS polymer adhesive

(Mega-strong SADER), a cooling system was required to ensure that the top surface temperature stay lower to 130°C. Thus a heatsink and a fan, powered by DF1743005C NDN generator, were mounted on top of the whole system, as shown in Figure 6.4a) and Figure 6.4c). The values of the hot temperature, T_H , at the bottom, and the cold temperature, T_C , on top of the device were measured and stored using Extech Instruments SDL 200 data acquisition system. Each thermocouple was placed inside a thin copper plate mounted between Aluminum block and a bottom part of the device in case of the hot temperature measurement (first thermocouple – T-couple₁), and between the top part of the device and the heat sink for the cold temperature measurement (second thermocouple – T-couple₂), as shown in Figure 6.4d).

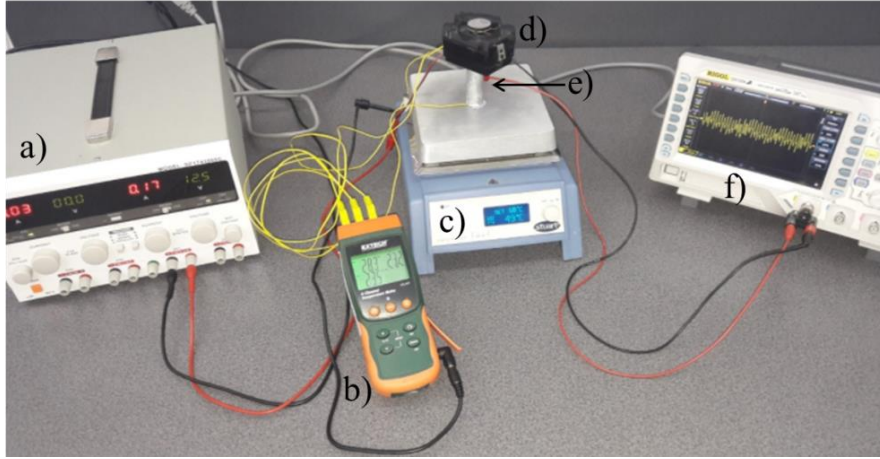


Figure 6.3: Experimental setup – (a) DF1743005C NDN generator; (b) Extech Instruments SDL 200 data acquisition system; (c) digital hotplate SD 160; (d) Aluminum cylinder; (e) heatsink with a fan; (f) Digital Oscilloscope (Rigol DS1054Z).

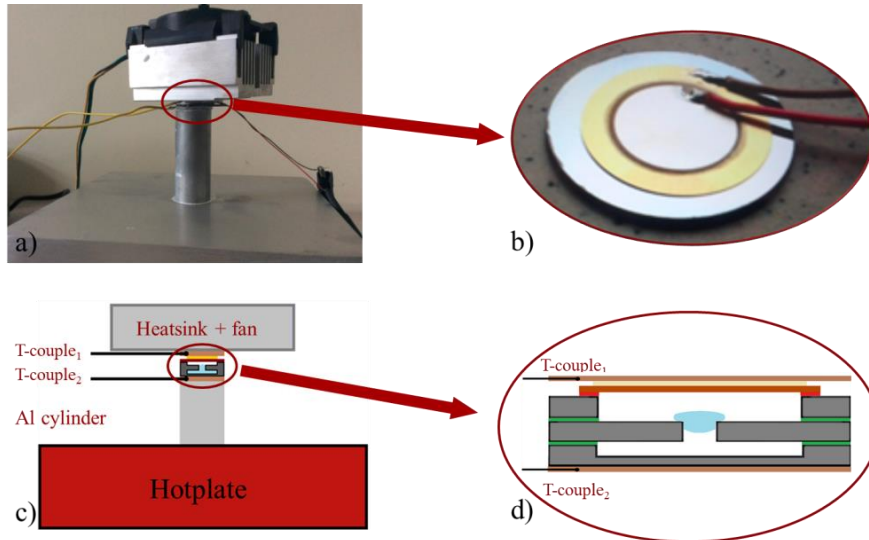


Figure 6.4: Photograph of (a) main elements of experimental bench and (b) prototype of the silicon device covered with PZT-based element; schematic representation of (c) experimental setup elements and (d) cross-section of silicon device prototype.

In order to ensure a good thermal contact, a thermal conductive paste ($\kappa = 4.1 \text{ W/mK}$) was applied between the hotplate and the Aluminum cylinder, on top of the cylinder, between the first thermocouple (T-couple₁), and bottom part of the device, on top part of the device, and finally between the second thermocouple (T-couple₂) and the heat sink. Experiments were always initialized at a room temperature. The temperature was then being increased with time up to a selected value. When the temperature provided by the hotplate to the bottom part of the examined structure was high enough, the evaporation of the water enclosed inside the evaporation chamber occurred and the vapor flow was transmitted through the channel to a top part of the device to affect the piezoelectric element causing its deflection. After the contact with the surface of the piezoelectric element, that was colder than the bottom part of the harvester, the vapor started to condensate. When the small droplets of water accumulated to form a certain mass, it broke away the PZT surface and came back to the hotter part of the cell. Both, the evaporation and the condensation processes were causing the deformation of the piezoelectric element and as a result the conversion of mechanical stress into electric signal occurred. The signal given by the piezoelectric element was observed with a Digital Oscilloscope (Rigol DS1054Z) of $1 \text{ M}\Omega$ input impedance.

6.3.3. Electric response to the pressure pulses

In order to analyze the electrical behavior of the designed device, a number of experiments were performed. Parameters that were studied are:

- filling ratio, α ,
- hot temperature, T_H .

Due to the fact that preliminary experiments described in section 6.2, showed that the oscillations appear only when the filling ratio, α , was comprised between 10% and 30%, as presented in Table 6.3 and in the range of temperatures between $120^\circ\text{C} \div 135^\circ\text{C}$ (Table 6.2), the study was carried out for parameters listed in Table 6.5.

Table 6.5: Values of filling ratio α , liquid volume V_l and hot temperature T_H applied in experiments.

Series no.	α [%]	V_l [μl]	T_H [$^\circ\text{C}$]
1.	10	5	120 \div 135
2.	20	10	
3.	30	16	

6.3.3.1. Impact of T_H for 10% filling ratio

The first series of experiments was performed for the devices filled with $5 \mu\text{l}$ of water, which represented 10% of their total volume, V_{tot} . It was observed that the regular oscillations of the frequency higher than 1 Hz, which were lasting for minimum 1 min, were generated within two ranges of hot temperatures, T_H - first between 121°C and 125°C and later between 134°C and 135°C . For the temperatures slightly above 120°C , the amplitudes, V , of the generated signal were very low and varied between 50 mV and 100 mV. The signal frequency, f , was comprised

between 5.5 Hz and 6 Hz. Charts presented in Figure 6.5a-b) show the changes of the voltage, v_p , and the hot temperature, T_H , over time, for the temperatures that do not ensure the oscillations occurrence and for the temperature of 121°C, at which the first oscillations were observed, respectively. The signal stopped at the temperature of 125°C, after 22 min of the continuous operation.

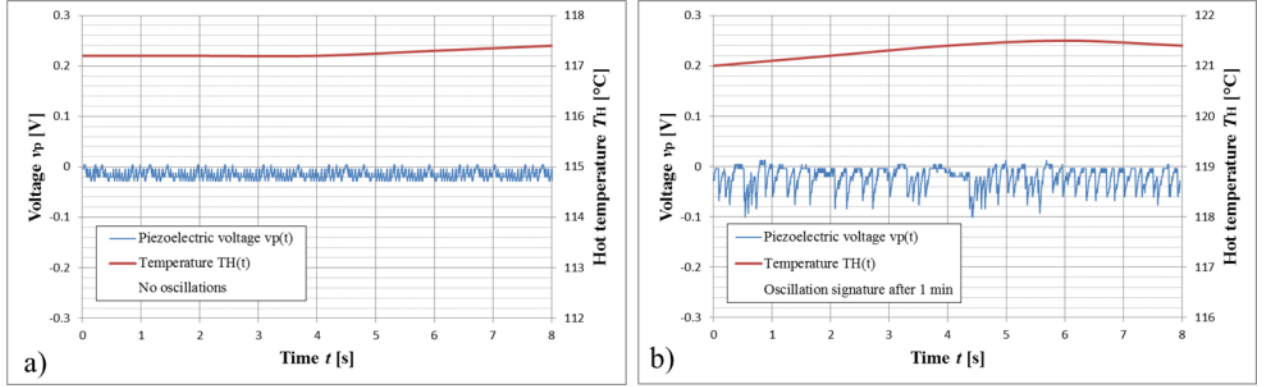


Figure 6.5: Changes of the voltage, v_p , and the hot temperature, T_H , over time, for $\alpha = 10\%$, (a) when no oscillations occur and (b) at the beginning of oscillations.

In the first step, the power was calculated for the voltage signal given in Figure 6.5b). The capacitance of piezoelectric element, C , used for calculations was measured three times in the frequency range between 20 Hz and 100 Hz by E4980A Precision LCR Meter and its mean value equaled to 12.3 nF. As it was expected, given the low values of the voltage generated by the device, the power of the signal, P , was extremely low and stood at 0.006 nW.

Within a second range of temperatures, between 134°C and 135°C, the values of voltage generated by the piezoelectric element were higher and varied between 300 mV and 500 mV, whereas the frequency of the signal changed from 5 Hz to 6.5 Hz. Figure 6.6a) shows the voltage signal at the temperature of 133°C, just before the oscillations incipience. The chart placed in Figure 6.6b) demonstrates the voltage changes at the temperature, T_H , slightly higher than 134°C, one minute after the oscillations had started. Figure 6.6c-d) presents the voltage signals generated at the same temperature but after one and two hours of continuous oscillations, respectively. The calculated power, P , equaled to 0.11 nW.

The signal had been lasting continuously for four hours, during which the characteristics of the oscillations did not changed significantly. After 4 hours of the continuous operation, the values of amplitudes started to decrease, as shown in Figure 6.7a), to finally stop completely (Figure 6.7b)). In order to understand the reason of this behavior, the whole structure was cooled down and disassembled. It turned out, that there was no water remained inside the device. This was due to the fact that the glue connecting piezoelectric element with the silicon structure loses its adhesive properties when operating at the temperatures above 130°C, which was also observed during dismantling. This means, that with a long operation time at high temperatures, the water started to evaporate outside the system to finally disappear.

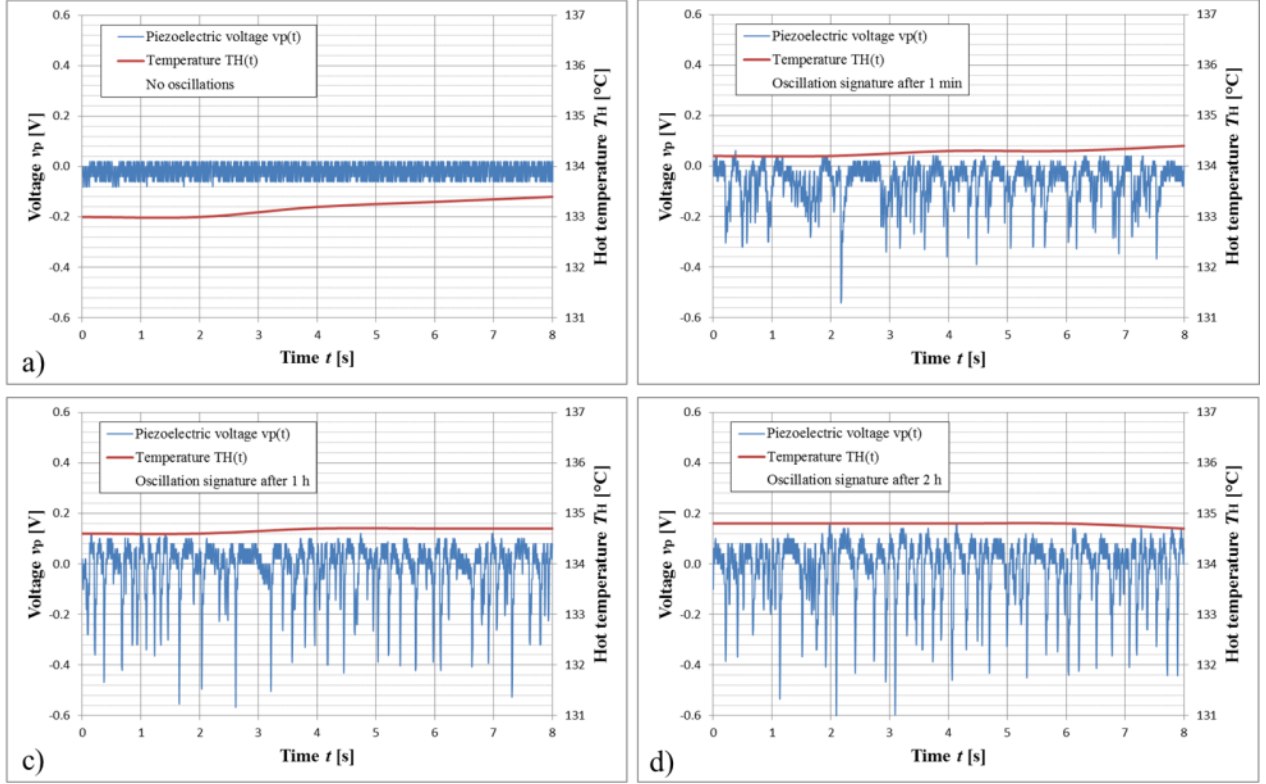


Figure 6.6: Changes of the voltage, v_p , and the hot temperature, T_H , over time, for $\alpha = 10\%$, (a) when no oscillations occur, (b) after one minute, (c) one hour and (d) two hours of continuous signal.

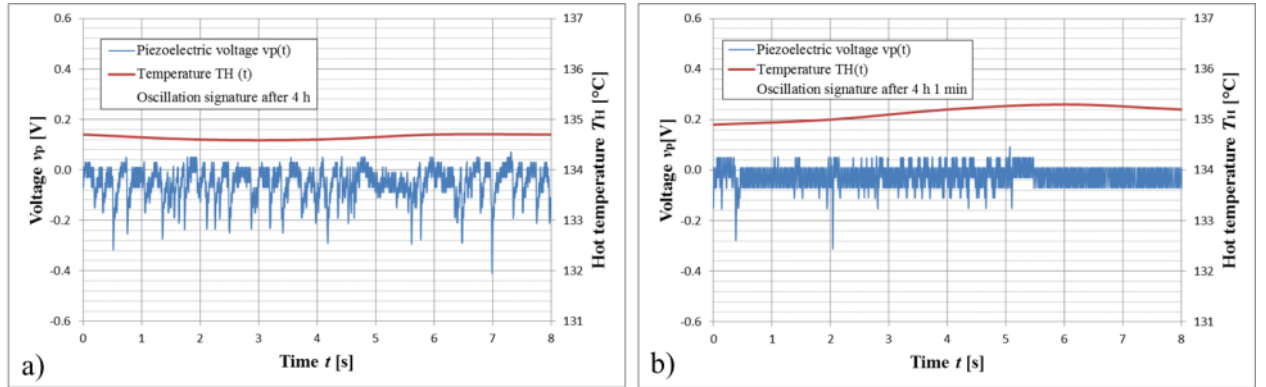


Figure 6.7: Changes of the voltage, v_p , and the hot temperature, T_H , over time, for $\alpha = 10\%$, at the end of oscillations, after four hours of continuous operation.

6.3.3.2. Impact of T_H for 20% filling ratio

Another series of the study was carried out for the devices filled with 10 μ l of water, which represented 20% of its total volume. Likewise, in case of the experiments performed with the devices filled with smaller amount of water, the oscillations were generated for two ranges of hot temperatures, T_H : between 122°C and 128°C and later for the range of 130°C and 131°C. This time no significant differences of amplitudes were observed and within both temperature

intervals they oscillated between 1 V and 2 V, which means that they were higher as compared to the structures filled with the lower volume of water.

Figure 6.8a-d) shows the voltage, v_p , and the temperature, T_H , versus time before the oscillations, at the very beginning of the signal, one hour and two hours after it had started, respectively. All the oscillations showed in Figure 6.8 were generated at the temperatures between 122°C and 128°C. The behavior of the signal had not changed significantly for 2 hours, during which the frequency values varied between 6.5 Hz and 7.1 Hz. After 2.5 hours of continuous operation the signal stopped. The calculated power, P , equaled to 1.1 nW.

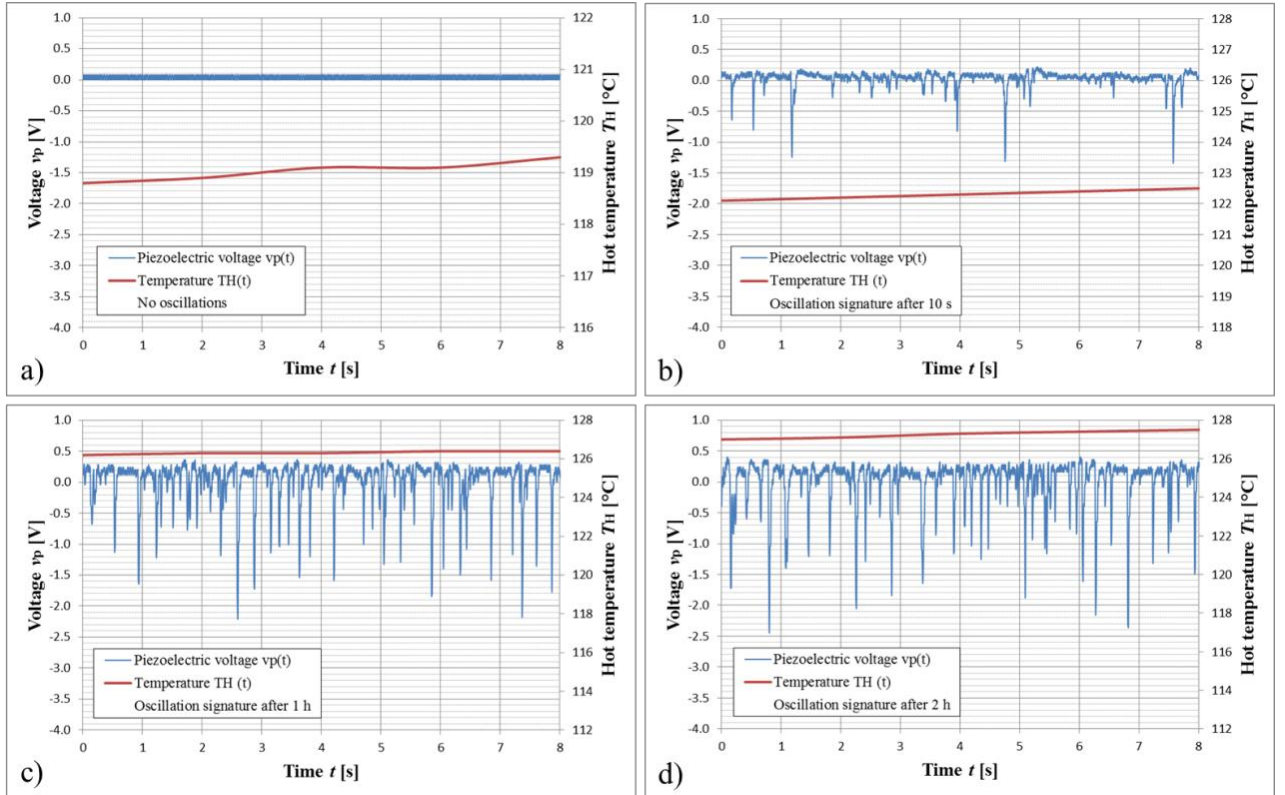


Figure 6.8: Changes of the voltage v_p and the hot temperature T_H over time, for $\alpha = 20\%$, (a) at the beginning of oscillations, (b) after one hour and (c) two hours of continuous signal.

The voltage variations versus time for second range of temperatures, comprised between 130°C and 131°C, are given in Figure 6.9a-d) and they represent the signals before, at the beginning, after 20 min and after 30 min of the oscillations, respectively. In this case, the signal was less regular than for the range of lower temperatures and the oscillations stopped after 32 min of operation at the temperature around 131°C. The calculated power, P , equaled to 0.8 nW. This time however it was not relevant to use simple estimation for the value of power generated during the operation of the device, due to aperiodical characteristic of the signal and its irregularity.

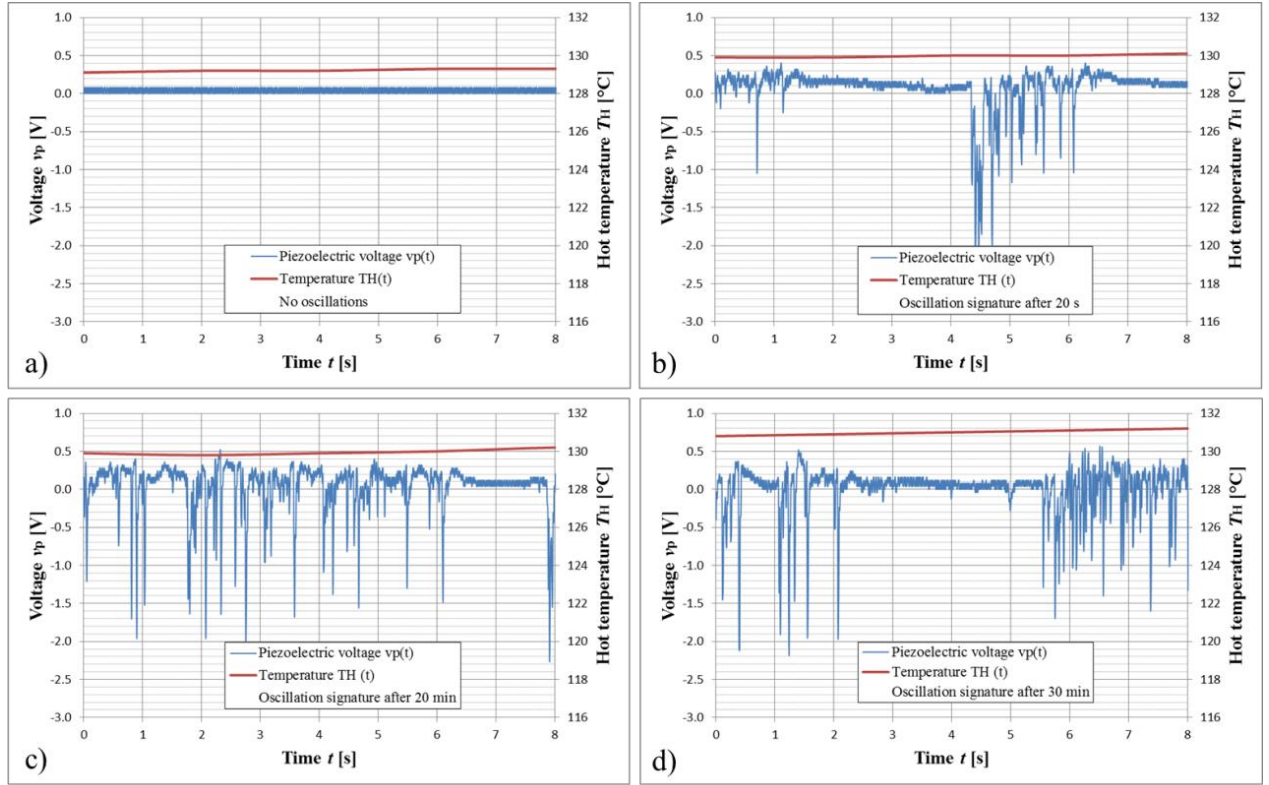


Figure 6.9: Changes of the voltage v_p and the hot temperature T_H over time, for $\alpha = 20\%$, (a) before, (b) at the beginning, (c) after 20 min and (d) after 30 min of the oscillations.

Additionally, another phenomenon that did not exist in case of the previous structures was observed – for higher range of temperatures, the stopovers between the oscillations appeared, as shown in Figure 6.10. This behavior was noted also by Khandakar et al. [49] in their experiments regarding PHP and by Soupremanien et al. [67] in the work related to the thermo-mechanical oscillation system, which is described in sections 4.2.1.3 and 4.2.1.4.

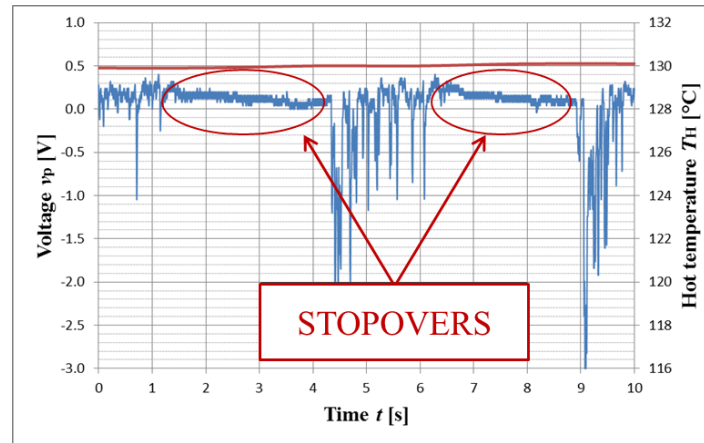


Figure 6.10: The breaks between the oscillations observed at the temperatures higher than 130°C for the devices filled with $10\ \mu\text{l}$ of water ($\alpha = 20\%$).

6.3.3.3. Impact of T_H for 30% filling ratio

In the third series of experiments the influence of the hot temperature on the signal behavior generated by the structure filled with 16 μl of water, representing 30% of the total device's volume was examined. Also here, it was visible that there are two intervals of the hot temperatures, within which the oscillation mechanism occurs. In the first stage of the experiments the signal fluctuations started at T_H close to 121°C and lasted around 45 min to stop at 126°C. The amplitudes and frequencies were changing between 300 mV and 600 mV, and 6 Hz and 8 Hz, respectively. The oscillations started again when the temperature was increased up to 130°C and they were working continuously for almost 3 hours to stop at 135°C. Figure 6.11a-b) shows the piezoelectric voltage, v_p , and the hot temperature, T_H , changes versus time after 1 min and 45 min of operation at the temperatures of 121°C and 126°C, respectively. The calculated power, P , equaled to 0.087 nW.

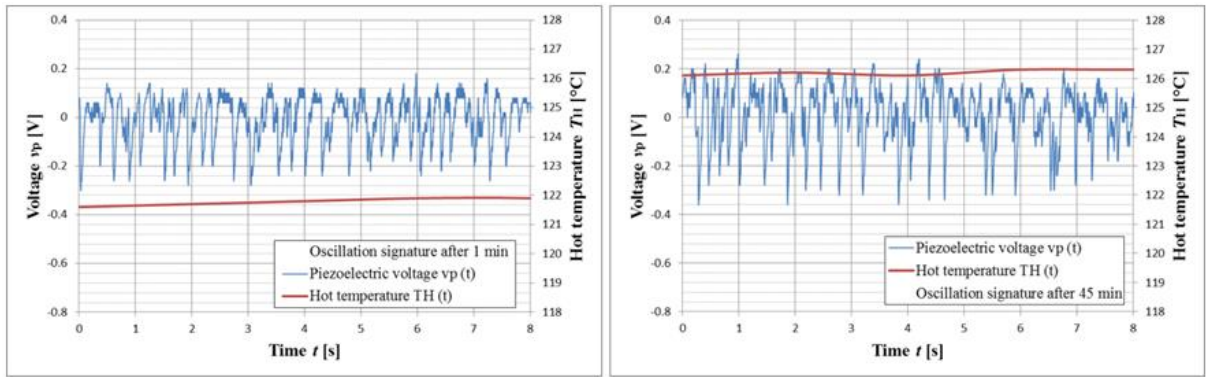


Figure 6.11: Changes of the voltage v_p and the hot temperature T_H over time, for $\alpha = 30\%$, (a) at 121°C after 1 min, (b) at 126°C, after 45 min of continuous operation.

The example of the voltage variations versus time for the range of higher temperatures, comprised between 130°C and 135°C, are shown in Figure 6.12. They represent the signals, at the beginning of the oscillations and after 2.5 hours of continuous device operation, respectively.

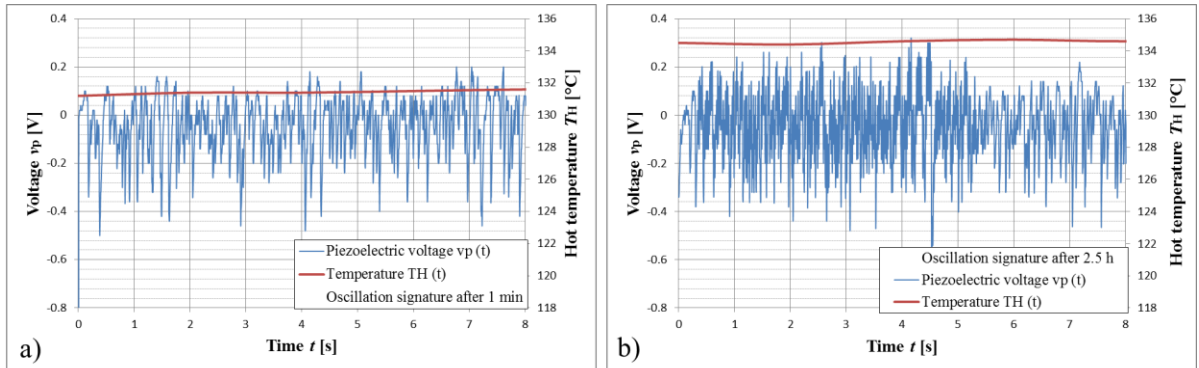


Figure 6.12: Changes of the voltage v_p and the hot temperature T_H over time, for $\alpha = 30\%$, (a) at 131°C after 1 min, (b) at 134°C, after 2.5 min of continuous operation.

The amplitudes of the voltage signal during the oscillation process varied between 300 mV and 700 mV, and they were slightly higher than for the range of low temperatures. The frequency however visibly increased at higher temperatures and its value was comprised between 11 Hz and 13 Hz. It is also important to note, that for this filling ratio the signal was continuous and specific stopovers observed in case of the filling ratio equal to 20% appeared only sporadically. The calculated power, P , equaled to 0.1 nW.

6.3.3.4. Summary of the experiments

To sum up the results of the experiments presented in this section the minimum, maximum and average amplitudes, V , and frequencies, f , of the signal, generated by the prototypes characterized by 10%, 20% and 30% filling ratio, α , operating in the ranges of low and high temperatures are listed in Table 6.6. Additionally, the table contains the values of power, P , generated by each device. The last row of the table gives the information whether specific stopovers between the oscillations appeared.

Table 6.6: Summary of the results.

α [%]	10		20		30	
T [°C]	121-125	134-135	122-128	130-131	121-126	130-135
V_{MIN} [V]	0.050	0.3	1.0	1.0	0.30	0.3
V_{MAX} [V]	0.100	0.5	2.0	2.0	0.60	0.7
V_{AVG} [V]	0.075	0.4	1.5	1.5	0.45	0.5
f_{MIN} [Hz]	5.50	5.00	6.5	2.50	6.0	11.0
f_{MAX} [Hz]	6.00	6.50	7.1	5.00	8.0	13.0
f_{AVG} [Hz]	5.75	5.75	6.8	3.75	7.0	12.0
P [nW]	0.006	0.110	1.000	0.812	0.087	0.108
Operation Time t [min]	22	240	150	32	45	180
STOPOVERS	NO		NO	YES	NO	

Based on the data listed in Table 6.6 the changes of amplitude, V , frequency, f , and power, P , in relation to the filling ratio, α , were plotted for the range of low and high temperatures, which is shown in Figure 6.13 and Figure 6.14, respectively. In the figures the mean values of amplitudes and frequencies are shown and the error marks refer to the minimal and maximal values of these parameters. The results obtained for the device characterized by $\alpha = 20\%$, when it worked in a range of higher temperatures, presented in Figure 6.14 are not representative and they cannot be used for establishing the general relation between the filling ratio and the studied parameters. This is due to the fact that under these particular conditions of the experiment the oscillations generated by the device were irregular and the stopovers between them appeared. This means that the values of frequency and power generated during the operation time of the device varied and were not reliable. The points that should be excluded from the analysis are marked in Figure 6.14.

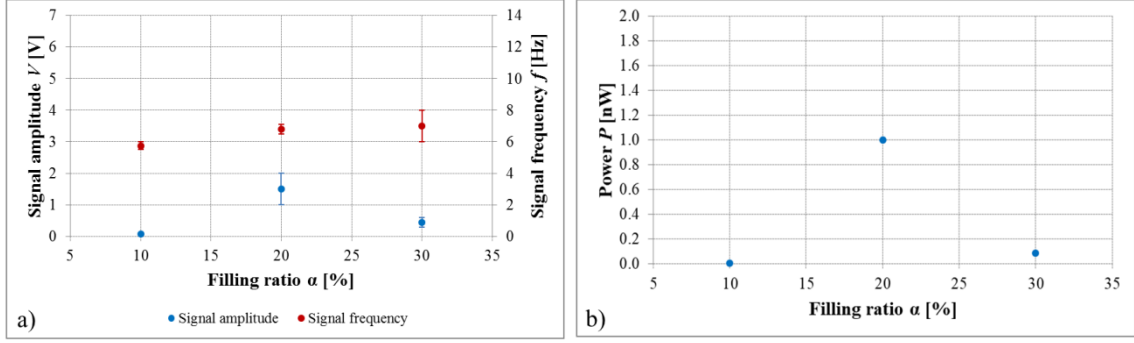


Figure 6.13: Changes of (a) the amplitude, V , and the frequency, f ; (b) the power, P , in relation to the filling ratio, α , for the range of low temperatures.

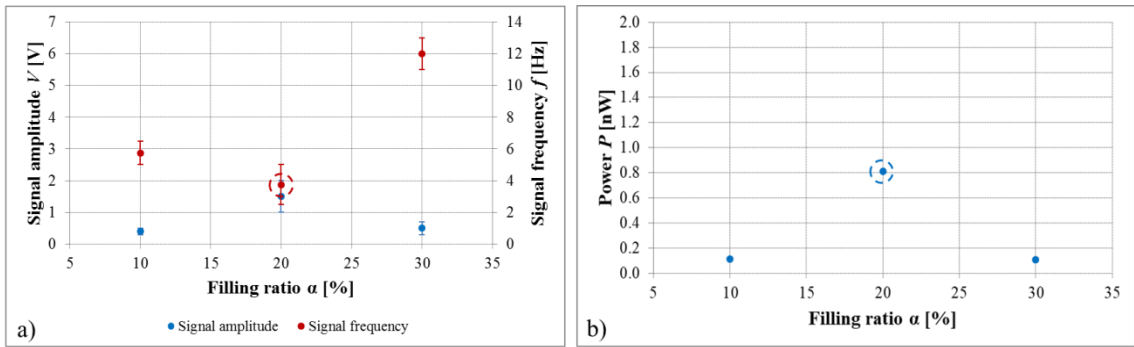


Figure 6.14: Changes of (a) the amplitude, V , and the frequency, f ; (b) the power, P , in relation to the filling ratio, α , for the range of high temperatures.

6.4. Operation of the device without a cooling system

The research described in this section had a tentative character and was aimed at verifying if it is possible to maintain a continuous operation of the device without any support of a cooling system. For the work performed in this study the epoxy adhesive (3M Scotch-Weld EPX Adhesive DP490) presenting much better heat resistance as compared to previously used MS polymer, was applied to assemble the PZT-based ceramics to the silicon structure. The experimental setup used in order to perform these experiments was very similar to the one described precisely in section 6.3.2 and shown in Figure 6.3 and Figure 6.4. The only difference between setups was the lack of a heat sink, a fan and a second thermocouple T-couple₂ measuring the cold temperature of the device.

Due to the fact that during experiments described in section 6.3.2 for the devices filled with 30% of water no stopovers in signal were observed, it was decided to choose this value of filling ratio to study the device operation with no cooling system applied. For this research three independent experiments were carried out under the following conditions:

- water as a working fluid,
- hydrophilic surface structure,
- channel diameter equal to 3 mm,

- PZT type: 7BB-15-6,
- filling ratio equal to 30%,
- temperature range: 120°C-160°C.

In all three cases, the oscillations were detected and they had been continuously operating for a time range between 4 h and 5 h. The first regular signal of the amplitudes between 0.4 V and 1 V were observed at the hot temperature of 125°C and it did not express irregularities or stopovers. After 30 min of continuous operation the temperature was increased up to 135°C but no change in the characteristic of signal was detected. The value of the temperature was being increased every half an hour by 10°C to finally reach 160°C. Since this moment no higher temperature was applied in order to avoid the structure destruction. The device had been operating continuously for 4 hours in case of one structure and close to 5 hours for two other elements. The example of the voltage changes versus time at the temperature of 122°C, just before the oscillations had occurred and at the very beginning of the oscillations incipience (125°C) is given in Figure 6.15a-b), respectively. Figure 6.16a-b) illustrates the voltage signal detected at the temperature of 135°C after 30 min of continuous operation and at the temperature equal to 160°C, 240 min since the beginning of the oscillations, respectively.

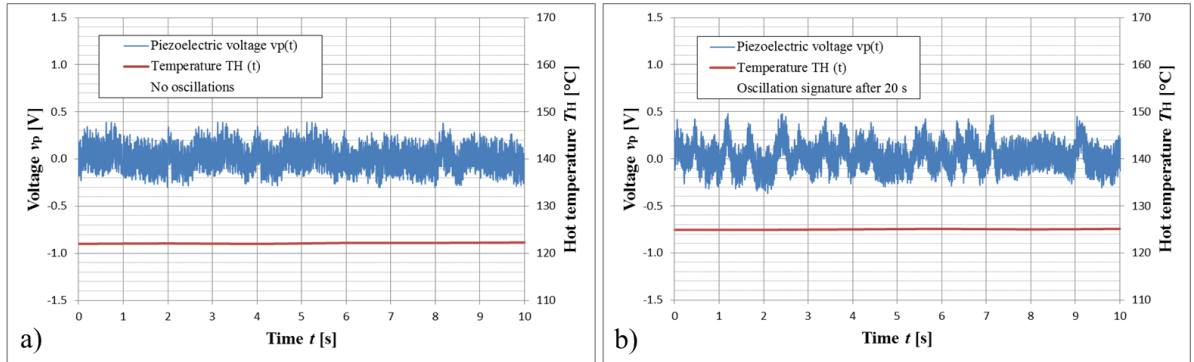


Figure 6.15: Changes of the voltage v_p and the hot temperature T_H over time, for $\alpha = 30\%$, (a) before, (b) at the beginning of the oscillations for the device operating without cooling fan.

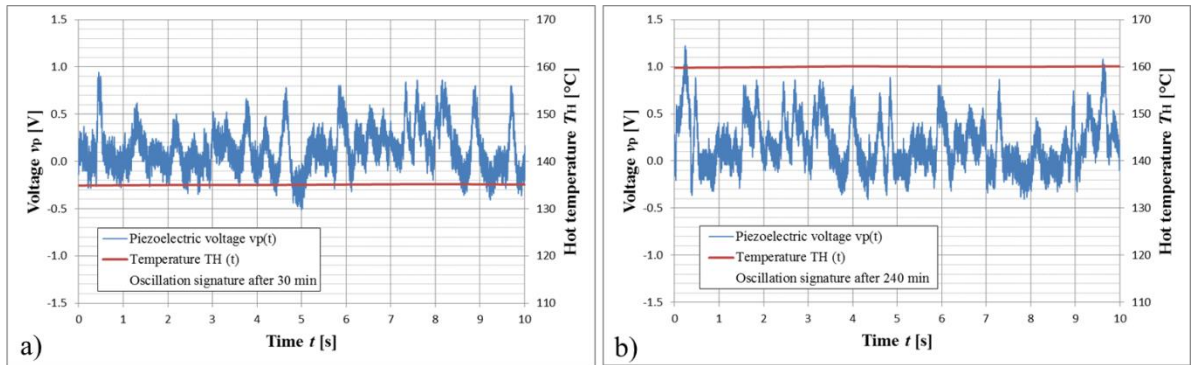


Figure 6.16: Changes of the voltage v_p and the hot temperature T_H over time, for $\alpha = 30\%$, (a) after 30 min and (b) after 240 min of the oscillations for the device operating without cooling fan.

The experiments described in section 6.3 and 6.4 proved that it is possible to develop an oscillating system that generates an electric signal using a constant source of heat, which is fully fabricated in silicon technology. However, the silicon is a thermal conductive material, hence, in order to ensure better thermal performance of the device it is desirable to apply a thermal insulating layer between the hot and the cold part of the structure. This would allow obtaining higher temperature difference ΔT between these two parts. For this purpose, the intermediate layer, comprising the channel, could be fabricated in glass that has much lower thermal conductivity as compared to silicon. Such a prototype, showed in Figure 6.17, was designed and fabricated at the end of this research.

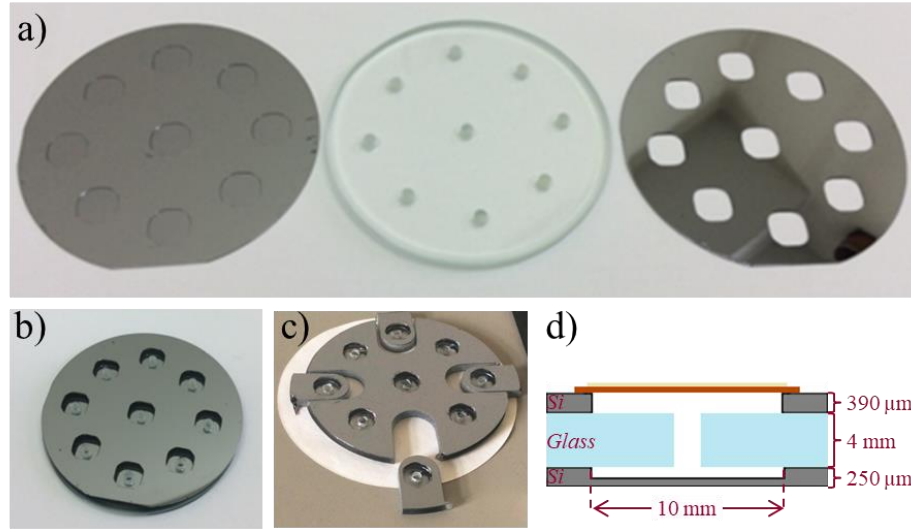


Figure 6.17: (a) Photograph of two Si wafers containing nine evaporation or condensing chambers and 4 mm thick layer of glass, with nine channels drilled through; (b) nine structures before cutting; (c) four independent cells cut out by flow water jet; (d) schematic cross-section of one cell of the harvester.

The only differences in the process flow described in section 5.2 consist in the method of channel fabrication and cells separation. The channel was fabricated by drilling and the cells were cut out by a flow water jet. The fabricated structures consisted of the evaporation and the condensing chambers etched in $\langle 110 \rangle$ silicon wafers and of channel drilled through a layer of glass. Each evaporation chamber had a diameter of 10 mm and the thickness equal 250 μm, the 3 mm wide channels were drilled in a 4 mm thick layer made of glass and the condensing chambers of 10 mm diameter were etched through the 390 μm thick silicon wafer. All the layers were bonded together with the usage of SU-8 2007 photoresist and the cells were cut out by the flow water jet. Figure 6.17a-d) shows three main elements of the structure before and after the bonding process, four independent cells and a schematic of a single cell of the device.

This design opens out the possibilities for a development and optimization of an oscillating energy harvesting system that operates with higher ΔT as compared to fully silicon structure. However, the deep analysis and the optimization of the proposed prototype were not a subject of this work and are not included in present manuscript.

6.5. Summary of the chapter

This chapter is related to the characterization of the device that was fabricated based on the study described in *Chapter 5*. The main observations and conclusions driven from this chapter are the following:

- the parameters that influence the initiation and the nature of the oscillations are ranked according to the list:

- 1) Working fluid.
- 2) Channel design.
- 3) Filling ratio, α , and the temperature of the hot surface, T_H .
- 4) Surface wettability.
- 5) PZT geometry.

- given the particular geometry of the proposed device and a clamping method of a piezoelectric element, the size of the transducer does not influence the voltage value generated in response to the pressure variations,

- in order to enable the oscillating mechanism inside the device, it is essential that it operates simultaneously in the specific range of filling ratio and hot temperature,

- for the fixed value of α , the oscillation mechanism occur for two different ranges of temperature: between $120^{\circ}\text{C} \div 128^{\circ}\text{C}$ and $130^{\circ}\text{C} \div 135^{\circ}\text{C}$,

- the value of α strongly influences the amplitude, the frequency and the nature of generated signal,

- for $\alpha = 20\%$, in the range of high temperatures, aperiodical stopovers between the oscillations appear,

- it is possible to fabricate a small scale, fully silicon device that is able to generate the continuous oscillations without an enhancement of a cooling system.

In the last part of this chapter, the design of the device that could ensure higher temperature difference between the hot and the cold surface, was proposed. This design opens out the perspectives for the optimization of an oscillating energy harvesting system, described in this manuscript.

Conclusions

a. Review of the work

The work presented in this manuscript was a contribution to the continuously developing subject of energy harvesting that is focused on extracting small amounts of energy, normally wasted in the environment and close vicinity of human, and converting it into electricity. This electric energy can be used afterwards for supplying Ultra-Low Power devices such as WSN (wireless sensor networks). Taking into account that nowadays a WSN node consumes typically up to 100 μW in an operation mode, the application of the energy harvesting devices for powering purposes is an achievable challenge. As stated in *Chapter 1*, there is a large number of energy sources existing both, in the environment and in the industry, that can be used for energy harvesting applications. The easily available energy that can contribute towards supplying low power electronic is kinetic energy. Due to a high density and efficiency of power conversion, the kinetic transducers operating based on piezoelectric effect are one of the most attractive solutions for the energy harvesting purposes. Another approach in energy harvesting domain is to convert solar energy into electricity or, in case of places that do not ensure enough light, thermal energy into electricity. One of the widely used and classical methods of thermal conversion, which consists in direct conversion of heat into electricity, applies Seebeck effect. The main drawbacks of this method are related to the materials applied in the thermoelectric generators. First of all, they must exhibit at the same time high electric conductivity and low thermal conductivity, which are material characteristics of the opposite nature. For this reason, to generate a significant amount of energy, it is necessary to enhance the temperature difference of the thermoelectric generators by using the cooling systems. This inconvenience limits their use regarding the small-scaled applications. Moreover, the materials that have the best properties are usually rare, toxic or expensive. The other disadvantage that appears commonly in the devices aimed at thermal energy conversion is their complex mechanical construction.

At the end of *Chapter 1* a new concept of the device capable of generating electrical energy from a constant source of heat by means of phase-change phenomenon and piezoelectric effect was featured. The concept implied two steps of energy conversion – (1) thermal energy into mechanical energy due to the repetitive evaporation and condensation of the working fluid and (2) mechanical energy into electricity by using piezoelectric transducers. The uniqueness of this idea consisted in applying phase-change phenomenon inside a micro-confinement to create a local overpressure that could be transformed afterwards into electric energy. According to the assumptions, the system was able to generate electric energy from a constant source of heat, without a need of any other external power supply and was easy to manufacture at low scale by using conventional equipment. This concept was the motivation to initiate the study presented in this manuscript.

The objective of present work was to design and fabricate in well-known silicon technology an oscillating device applying phase-change phenomenon and piezoelectric effect, which could be used for energy harvesting applications. The device should be characterized by simplicity of construction, ease of manufacture with the conventional equipment and common materials and was not supposed to contain any moving parts. It should have small dimensions as compared to

the existing devices – up to 2 cm of diameter and 2 mm of thickness and could possibly work without a cooling system.

One of the interests of this study was focused on mechanic energy conversion performed by means of piezoelectric transducers. Although the direct and inverse piezoelectric effects have been widely used for many years, mainly for sensing and actuating applications, recently the piezoelectric materials found their application also in energy harvesting, where they are used for the energy generation purposes. The most common piezoelectric materials are BaTiO₃ and PZT ceramics, which are characterized by strong piezoelectric effect, high dielectric constant and relatively simple fabrication process. The main inconvenience of the ceramics is related to their fragility, which excludes their application from the solutions that require large displacements. The group of piezoelectric materials that is not affected by this inconvenience is created by polymers, amongst which the most well-known is PVDF. Their main advantages consist in huge flexibility, low density and relatively high piezoelectric coefficients. The polymers find their applications mainly in the pressure sensors. However, their low piezoelectric strain constant limits their applications as active transducers. Additionally, their low Curie temperature, excludes them from the solutions operating at temperatures higher than 90°C. The electromechanical properties of the piezoelectric materials, as well as the main piezoelectric coefficients and equations were described in *Chapter 2*.

Due to the different properties of PZT-based ceramics and PVDF polymers, it was decided to study both materials in terms of their possible applications for the device presented in this work. For this purpose, the experimental setup presented in *Chapter 3*, which enabled the study on electromechanical behavior of different piezoelectric materials was built. The aim of the experiments was to evaluate the energy generated by the elements of different types and geometries when they were subjected to a pulse of pressure created by decompressing air. The first part of the work referred to the PVDF flexible sheets operating in a cantilever or a membraned mode. It was observed that the membrane converter generated higher power as compared to the one composed of cantilevers, but it was also more fragile. Additionally, it was noted that when exceeding a certain value of pressure the membrane losses its elastic properties. This led to the conclusion that in order to give the repeatable and reliable results, a membrane should operate only below a threshold pressure value. Particularly, the transducer composed of 52 µm thick membrane of 7 cm² surface could not be exposed to pressures higher than 1 bar. In the second part, four PZT-based transducers of different size were tested in a stress and a strain mode. The analysis showed, that in all cases the thinner transducers generated higher values of voltage and power, which was related to the higher flexibility and capacitance of these elements. The analysis showed, that the PZT-based transducers generate much higher powers than PVDF elements and they are more effective when they operate in the strain mode. Additionally, it was observed that the clamping method strongly influenced the electrical properties of the PZT membranes. To enhance the knowledge about the impact of the geometrical parameters of PZT-based converters on the electric energy generated by this elements, a numerical modeling was performed. The results confirmed the significance of the clamping method and showed that, theoretically, for specific dimensions of PZT-based elements, it was possible to improve

the energy generation by performing several modifications of PZT geometry. The experiments described in *Chapter 3* contributed to the decision that the PZT-based transducer operating in the strain mode was the best integration for energy conversion.

In order to open out the perspectives of its implementation in variety of silicon microsystems, the silicon technology was selected for the device fabrication. In *Chapter 4* the precise concept of the silicon-based device, being the subject of this work was proposed. The principle of its operation was to generate the repetitive pressure oscillations being the result of the cyclic evaporation and condensation of the working fluid enclosed inside the system. The device was composed of three Si wafers comprising the evaporation and the condensing chambers, and a channel connecting these two elements. The PZT-based transducer mounted on top of the structure was applied to ensure energy conversion. Thanks to the analysis of previous studies on the similar subject, the following challenges and questions regarding a technological realization of the prototype were appointed: what should be the type of the working fluid, the channel design, the type of the piezoelectric element, the filling ratio and the hot surface temperature? The analysis presented in this chapter brought the answers to some of these questions and opened the discussion for remaining ones. Further study on this subject was presented in *Chapter 5* and *Chapter 6*. Finally, it was decided to use water as a working fluid; to design a 3 mm wide channel of a hydrophilic surface; apply the 7BB-15-6 PZT-based element, test the prototypes in three values of the filling ratio – 10%, 20% and 30%, at the hot temperatures between 120°C and 135°C.

b. Scientific and technical contributions

The technological steps of the prototype fabrication, which were performed in the clean room environment were presented in *Chapter 5*. During this work different technological processes were tested and the final parameters of the fabrication process were determined. It was decided to use three <110> Si wafers and subject them to RCA cleaning procedure, connected with a hydrophilisation process. After that, the standard procedures that precede silicon etching – wet oxidation; spin coating, exposure and development of a photoresist, SiO₂ mask removal – were conducted. Si etching aimed at fabricating the chambers and the channel of the prototype was performed in a 30% KOH solution at the temperature of 80°C. The last two parts of the device fabrication was to bond the three Si wafers together into one structure using SU-8 photoresist as an intermediate layer and to mount a PZT on top of the device.

Later the fabricated devices were tested in terms of an oscillation mechanism and the electrical properties, and the results of this work were described in *Chapter 6*. The hierarchy of importance for the parameters of influence was determined. It was observed that, given the particular geometry of the prototype and the clamping method of PZT-based converter, the diameter of this element did not influence the voltage value generated in response to the pressure variations occurring inside the system. A number of experiments that were performed with the presence of a cooling system showed, that in order to initiate the oscillating mechanism inside the device, it was essential to operate simultaneously in the specific range of the filling ratios and the hot temperatures. Additionally, for the fixed value of the filling ratio, the oscillation mechanism occurred for two different temperature ranges: between 120°C ÷ 128°C

and $130^{\circ}\text{C} \div 135^{\circ}\text{C}$. The amplitude, the frequency and the nature of generated signal strongly depended on the amount of water enclosed inside the system. Furthermore, for $\alpha = 20\%$, in the range of high temperatures, aperiodical stopovers between the oscillations appeared. At the end of a practical work, the cooling system was removed from the experimental setup and the tentative experiments performed under these conditions showed that it was possible to fabricate a fully silicon device being able to generate the continuous oscillations without an enhancement of a heat sink. However, the amplitudes and the frequencies of the signal decreased due to a low temperature difference between the hot and the cold surface. This showed that the system had a potential to work without a heat sink but to ensure better properties, the optimization of the device is required.

To sum up, the assumptions for the study presented in this manuscript was to design and fabricate the device of the following features: it is able to convert thermal energy coming from a constant source of heat into electricity, by means of phase-change phenomenon and piezoelectric effect; it does not contain any moving mechanisms, has a simple construction and is easy to manufacture with the conventional equipment; its diameter is not higher than 2 cm and it is not thicker than 2 mm; it could possibly work without a cooling system and finally, it could be used for energy harvesting applications.

The device fabricated during this study faced most of these requirements and opened up the prospects for its optimization. The prototype being the final result of the study had a relatively simple geometry, was fabricated in a very well-known and conventional silicon technology, transformed thermal energy into electric signal applying piezoelectric effect and the cyclic evaporation and condensation of the working fluid. The maximum diameter of the prototype was equal to 1.5 cm and its thickness did not exceed the value of 1.4 mm. Even though the values of power generated by the prototype were not high enough to use it successfully for the energy harvesting purposes, the device was prospective and its further optimization could result in the improvement of the signal frequency and the power generation. Although most of the experiments were performed with the usage of the cooling system, the final part of a practical work demonstrated that it was possible to fabricate a fully silicon device being able to generate the continuous oscillations without an enhancement of a heat sink but due to a small temperature difference between hot and cold surfaces the electric properties of generated signal dropped significantly.

c. Proposed future work

In order to enhance the signal duration, in the future work the evaporation issue should be solved and the improvement of thermal properties of the device should be proposed. This could be done by an application of a thermal insulating layer between the hot and the cold surfaces of the structure. This would allow obtaining a higher temperature difference ΔT between these two parts. Such a prototype was designed and fabricated at the end of this research. This opened the opportunities of its further optimization.

Additionally, the profound thermo-physical analysis and the theoretical study on scaling laws should be performed in the future. Moreover, the significant work aimed at increasing the value of generated power must be done.

Appendix A

A.1 Reactive-ion etching

In the reactive-ion etching technique (RIE), typically used in microfabrication, high-energy ions from chemically reactive plasma attack a substrate and react with it, causing the removal of material from the surface of processing substrate. Although this etching method is widely used in microtechnology, the first results of RIE, performed with the usage of FEMTO 90966 provided by Electronic Diener, given in Figure A.1a), clearly show that this technique is not suitable for etching deep structures of the harvester. In Figure A.1b), a photograph of a silicon wafer after the RIE process applied to a 250 μm deep chamber creation is given.

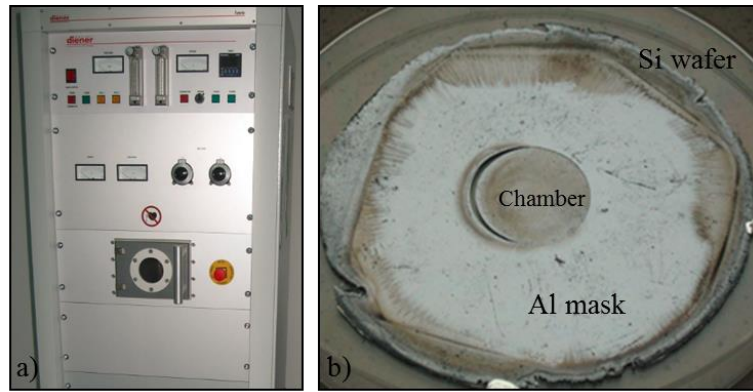


Figure A.1: (a) Plasma system FEMTO 90966; (b) 250 μm deep chamber etched by RIE in silicon wafer.

One can observe a huge irregularity of etched surface and complete degradation of Al (aluminum) mask used in the process. This is mainly due to the fact that this technique is not dedicated to deep silicon etching, but it is typically used for cleaning the surface of the wafers. Moreover, the plasma system that was used for the experiment is characterized by relatively low power that stands at a value of 100 W for 3" wafer and in addition, the temperature of a table, on which the sample was placed, is not controllable. Furthermore, the process is isotropic, which means that it occurs in all, even undesired directions. A combination of these features results in an extremely long time of etching (20 h in case of 250 μm deep structures) and makes the process impossible to control.

A.2 Comparison between reactive-ion etching and deep reactive-ion etching techniques

Deep reactive-ion technique (DRIE) has several advantages over RIE. First of all, it is dedicated to deep silicon etching, secondly it is highly anisotropic, which results in a very high regularity of fabricated structures. Moreover, the temperature of the table inside the etching chamber is fully controllable and the power used during the process is very high. As a consequence, the time needed to create 250 μm deep cavity was close to 0.5 hour, which was a huge advantage as compared to 20 hours required in case of reactive-ion etching.

Figure A.2a-b) shows the comparison between two sidewalls of a chamber etched in silicon wafer by RIE and DRIE techniques, respectively. As one can notice, the quality of the deep structures fabricated by DRIE is very high, and due to isotropy of this process, the etching occurs in desired directions only. Moreover, thanks to the short time of the process, no damage to the Al mask and, as a consequence, to the surface of the silicon wafer in the vicinity of the etched part is observed.

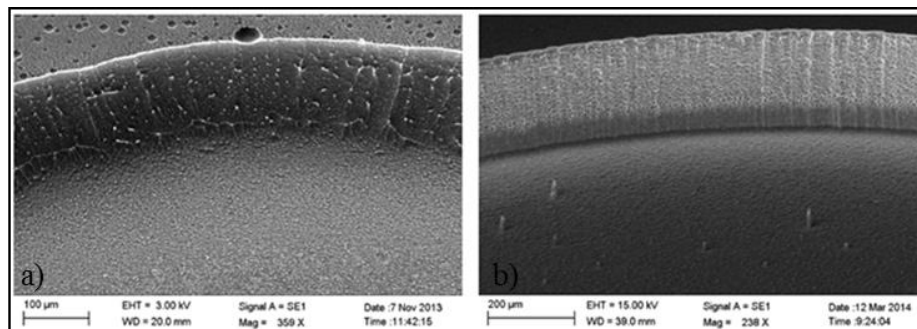


Figure A.2: Sidewall of a chamber etched in Si wafer by RIE (a); DRIE (b).

The dry etching experiments indicated that from the two investigated techniques, the deep reactive-ion etching technique has indisputable advantages over RIE.

Appendix B

The silicon and silicon dioxide etch rates of various KOH concentrations and temperatures were determined by Seidel et al. [72]. The values of etch rates R [$\mu\text{m/h}$] for Si $\langle 100 \rangle$ and $\langle 110 \rangle$ as well as thermally grown silicon dioxide calculated and verified experimentally by the authors are listed in Table B.1-Table B.2, respectively. For the calculations, the following empirical formula Eq.(B.1) was used by the authors:

$$R = k_0 [\text{H}_2\text{O}]^4 [\text{KOH}]^{\frac{1}{4}} e^{-\frac{E_a}{kT}} \quad [72] \quad \text{Eq.(B.1)}$$

where R is etch rate, k is Boltzmann's constant, T is the temperature [K] and E_a is the activation energy [eV]. The activation energy values E_a of around 0.61 eV and 0.59 for $\langle 110 \rangle$ and $\langle 100 \rangle$, respectively, were determined according to Arrhenius law Eq.(B.2):

$$R = R_0 e^{-\frac{E_a}{kT}} \quad [72] \quad \text{Eq.(B.2)}$$

where R_0 is pre-exponential factor.

The values of the parameters taken to calculate the etch rates for different KOH concentrations and temperatures were $E_a = 0.595$ eV and $k_0 = 2480 \mu\text{m/h} \cdot (\text{mol/l})^{-4.25}$ for a $\langle 100 \rangle$ surface and $E_a = 0.60$ eV and $k_0 = 4500 \mu\text{m/h} \cdot (\text{mol/l})^{-4.25}$ for a $\langle 110 \rangle$ surface [72].

Table B.1: Dependence of $\langle 100 \rangle$ silicon etch rates R [$\mu\text{m/h}$] on KOH concentration and temperature, for $E_a = 0.595$ eV and $k_0 = 2480 \mu\text{m/h} \cdot (\text{mol/l})^{-4.25}$ [72].

%KOH	Temperature [°C]								
	20	30	40	50	60	70	80	90	100
10	1.49	3.2	6.7	13.3	25.2	46	82	140	233
15	1.56	3.4	7.0	14.0	26.5	49	86	147	245
20	1.57	3.4	7.1	14.0	26.7	49	86	148	246
25	1.53	3.3	6.9	13.6	25.9	47	84	144	239
30	1.44	3.1	6.5	12.8	24.4	45	79	135	225
35	1.32	2.9	5.9	11.8	22.3	41	72	124	206
40	1.17	2.5	5.3	10.5	19.9	36	64	110	184
45	1.01	2.2	4.6	9.0	17.1	31	55	95	158
50	0.84	1.8	3.8	7.5	14.2	26	46	79	131
55	0.66	1.4	3.0	5.9	11.2	21	36	62	104
60	0.50	1.1	2.2	4.4	8.4	15	27	47	78

APPENDIX B

Table B.2: Dependence of <110> silicon etch rates R [$\mu\text{m/h}$] on KOH concentration and temperature, for $E_a = 0.60$ eV and $k_0 = 4500 \mu\text{m/h} \cdot (\text{mol/l})^{-4.25}$ [72].

%KOH	Temperature [°C]								
	20	30	40	50	60	70	80	90	100
10	2.2	4.8	10.1	20.1	38	71	126	216	362
15	2.3	5.1	10.6	21.2	40	74	132	228	381
20	2.3	5.1	10.7	21.3	41	75	133	229	383
25	2.3	5.0	10.4	20.6	39	73	129	222	372
30	2.1	4.7	9.8	19.4	37	68	121	209	350
35	2.0	4.3	8.9	17.8	34	63	111	192	321
40	1.7	3.8	8.0	15.9	30	56	99	171	285
45	1.5	3.3	6.9	13.7	26	48	85	147	246
50	1.2	2.7	5.7	11.3	22	40	71	122	204
55	1.0	2.2	4.5	9.0	17	31	56	96	161
60	0.7	1.6	3.4	6.7	13	24	42	72	121

The etch rates of thermally grown silicon dioxide R [$\mu\text{m/h}$] listed in Table B.3 were achieved by the assumption of linear dependence on the molar KOH up to 35% KOH and decrease proportional to the square of the molar water concentration for higher concentrations and they were calculated based on best numerical fit of experimental data. The mean value of activation energy $E_a = 0.85$ eV was used for the calculations [72].

Table B.3: Etch rates of thermally grown SiO_2 R [nm/h] depending on KOH concentrations and temperatures, for $E_a = 0.85$ eV [72].

%KOH	Temperature [°C]								
	20	30	40	50	60	70	80	90	100
10	0.40	1.22	3.5	9.2	23	54	123	266	551
15	0.63	1.91	5.4	14.4	36	85	193	416	862
20	0.88	2.66	7.5	20.0	50	118	268	578	1200
25	1.14	3.46	9.8	26.0	65	154	348	752	1560
30	1.42	4.32	12.2	32.5	81	193	435	940	1950
35	1.44	4.37	12.4	32.8	82	195	440	949	1970
40	1.33	4.03	11.4	30.3	76	180	406	876	1820
45	1.21	3.67	10.4	27.5	69	163	369	797	1650
50	1.08	3.28	9.3	24.6	62	146	330	713	1480
55	0.95	2.87	8.1	21.6	54	128	289	624	1290
60	0.81	2.45	6.9	18.4	46	109	246	532	110

Appendix C

C.1 Fusion bonding

Silicon Fusion Bonding (SFB), known also as Silicon Direct Bonding (SDB) or Silicon Thermal Bonding (STB) is a high temperature process occurring due to chemical bonds between two surfaces and it is dedicated to join on a permanent basis silicon substrates without any intermediate layer or external electric field [83]. In order to avoid unbonded areas, so-called voids, perfectly flat and smooth wafers must be prepared by standard clean purification RCA. Following this preparation, the substrates are brought in contact by gently pressing the two elements together at one central point, which results in an initial bonding between the surfaces thanks to hydroxyl radicals that are present on the wafer. A contact wave, initiated at the point of pressure, sweeps across the substrates, bringing them into intimate connection over the entire surface. The propagation velocity of the wave stands at a few cm/s and rises with the smoothness as well as with chemical and physical purity of the substrate. The contacting process is critical to prevent from trapping any particle or air between the surfaces. The strength of the connection rises with annealing the connected pair at high temperature [89].

Si-Si bonding

When the two silicon substrates with hydrophilic surfaces are brought in contact at room temperature, they attract each other and they bond spontaneously. A thin unprompted oxide layer of around 0.4 nm, a few layers of molecular water, 1 or 2 monolayers of Si-OH, numerous hydrogen bonds Si-H and free hydroxyl groups OH are formed between the connected surfaces. Weak hydroxyl and hydrogen bonds are responsible for the bonding, whose strength depends on the thickness of water layer trapped between the surfaces. After the initial connection, the silicon substrates must be anneal at high temperature [100].

In order to verify if this bonding technique could be successfully used in the clean room laboratory of TUL, several tests have been performed. For this purpose, five samples with the surface of 10 mm² were cut out from a silicon wafer with the usage of laser and subjected afterwards to RCA cleaning procedure. In each experiment the polished side of the sample was brought in contact with the smooth, cleaned surface of a 3" silicon wafer. After that, initially bonded elements were placed inside the oxidation furnace. The process of annealing was divided into several steps. Firstly, the connected pair was being slowly inserted into the furnace at the temperature of 300°C with the speed of 0.5 mm/s, later the temperature was being gradually (5°C/min) increased up to 1100°C. The actual annealing, during which the nitrogen and oxygen were provided to the system with the flow rate of 10 l/min in proportion 3:1, lasted 1 hour. In the last stage of the process, the temperature was being gradually decreased to the value of 300°C.

Although five independent experiments using different samples had been performed, it was not possible to obtain a permanent connection between the bonded surfaces.

In order to enhance this process it has been decided to insert one droplet of hydrofluoric acid HF between the silicon surfaces before the bonding. After the contact with HF, the silicon is

covered with hydrogen and fluorine and the attraction between silicon surfaces occurs due to the connection between Si-F and H-Si across the wafers [90]. After the initial bonding, the connected pair was inserted to the oxidation furnace and annealed according to the procedure described before. In five experiments only one pair of substrates was connected after the process, unfortunately after several minutes it was possible to detach the samples.

Si/SiO₂-Si and Si/SiO₂-SiO₂/Si bonding

In the next step of the research it has been decided to perform a fusion bonding following the same procedure, with and without the presence of HF, but for the situation where either one (Si/SiO₂-Si) or two (Si/SiO₂-SiO₂/Si) of silicon surfaces were covered with 100 nm layer of SiO₂ obtained in dry oxidation process. The mechanism of Si/SiO₂-Si bonding is similar to Si-Si one. The main differences consists in higher diffusion of water and hydrogen in layers of SiO₂, as well as in the fact that the oxides covers the microconfinements of the material and their surface is smoother as compared to the surface of silicon wafer.

In ten attempts only one temporary bonding has been obtained for the pair Si/SiO₂-Si enhanced by small amount of HF and one pair of Si/SiO₂-SiO₂/Si with HF droplet trapped between the substrates have been bonded on a permanent basis. However, it was not possible to reproduce this result.

Summarizing described above experiments, one can conclude that in the conditions offered by TUL laboratories, all the experiments performed in the domain of fusion bonding proved, that even though it is possible to sporadically obtain the permanent connection between two silicon surfaces, the results are completely unpredictable. The reason of such a situation consists probably in the fact that, in order to successfully perform a fusion bonding process, perfectly clean ultra-smooth surfaces with roughness lower than 10 Å are required [89]. Taking into account, that the oxidation furnace, inside which the main part of the process was performed, is situated in the room of class 10000, it is possible that the contamination gathered on the substrate is too high to perform a successful bonding. Typically, this type of process is carried out in the clean room laboratory of higher class or inside a precise, high-reliability wafer bonder, unfortunately, the laboratory of Department of Semiconductor and Optoelectronic Devices does not have such an equipment at its disposal.

C.2 Low temperature bonding

Another attempt to obtain permanent connection between the substrates was performed at room temperature. All the samples were prepared in the way described in section C1. In each case, the droplet of HF had been placed at one of the surfaces before the actual bonding process. After an initial bonding, the connected pair was subjected to the force of 1000 N for 24 hours. Although for each type of the samples (Si-Si, Si/SiO₂-Si and Si/SiO₂ - SiO₂/Si) five tests were performed, no success have been achieved.

Due to the fact that, according to the literature [91], the strongest attraction between the surfaces at room temperature and high reactivity with water and other chemicals, which results in

a formation of strong silanol bonds, was observed for the wafers activated using O_2 plasma processing, it appeared to be a promising enhancement for the bonding process.

Taking into account that in case of fusion bonding performed in previous experiments, the only promising result have been obtained for the $Si/SiO_2 - SiO_2/Si$ connected with the assistance of HF, the last assay of bonding at room temperature was carried out for this type of connection, but before the process, the surfaces had been activated in Plasma system FEMTO 90966 by O_2 plasma.

Unfortunately, despite a number of experiments no success has been achieved in a process of bonding performed at room temperature. Like in case of fusion bonding, the main requirement that was not met during this process was a perfectly clean surface of the substrate. Additionally, due to the fact that the strength of the connection rises with annealing, the bonding process performed at room temperature might not be efficient enough to result in a strong permanent connection of the substrates.

C.3 Vacuum bonding

Another tested idea of bonding consisted in the use a vacuum pump to create the bonding forces and simultaneously, to increase the join thermal resistivity in the structure. The concept of this kind of bonding is presented in Figure C.1.

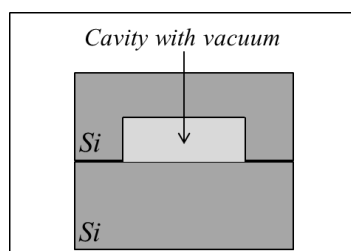


Figure C.1: The concept of a vacuum bonding.

In order to perform the process, in one of the smooth bonded surfaces, a small cavity had been fabricated. The elements to be bonded have been placed inside the vacuum pump that was further de-aerated. This resulted in much lower value of pressure inside the pump in comparison with the ambient air pressure. As a consequence, the pressure difference should have created the forces pressing one component against another. Due to a very low pressure value, close to vacuum, the strength of the connection was supposed to be very high and the thermal insulation between both components, for diffusion heat flow processes should be very high.

The process was carried out in several steps: firstly, two silicon wafers, amongst which one contained a small cavity, separated from one side by a blocking element in the way presented in Figure C.2a), were placed inside a vacuum pump and the pumping process started. When the pressure close to vacuum had been achieved, the separator block was removed and the two wafers were brought in contact as it is depicted in Figure C.2b). Afterwards, the chamber venting occurred.

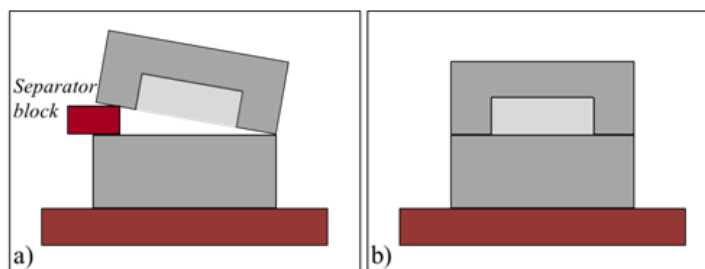


Figure C.2: (a) Two Si wafers with a separator block between them before bonding process;
(b) after connection.

Although numerous attempts of this process have been performed, the obtained connections were rather weak and no permanent connection has been achieved. There are two main reasons of such a situation: first of all, the surfaces of the wafers used during experiments were not perfectly smooth, while it is a necessary condition for the implementation of such a connection; secondly, the venting process was not sufficiently fast, due to the fact that the vacuum pump system was not adapted to this particular application. Therefore, although the first experiments confirmed the rightness of idea, the further investigation were not continued.

The goal of the present work was to design and fabricate a fully silicon oscillating device that converts thermal energy into electricity, applying phenomena of liquid to gas phase-change and piezoelectricity. It should be characterized by simplicity of construction, small size, and ease of manufacture. The diameter should not exceed 2 cm, while the thickness should be within 2 mm.

The device was composed of three Si wafers comprising the evaporation and condensing chambers, and a channel connecting these two elements. A PZT-based transducer mounted on top of the structure was applied to ensure the energy conversion.

The design process included the establishment of the device geometry, the type of the working fluid enclosed inside the system, a type, size and assembly technique of a piezoelectric element, as well as a bonding method of several silicon wafers of the device.

The practical realization of the designed prototypes was aimed at selecting the most suitable technological processes for the structure fabrication. All the experiments were performed in a clean room environment and employed wet oxidation, photolithography, a well-known, easily available wet chemical etching in a KOH solution, and a silicon bonding technique with the use of SU-8 photoresist as an intermediate layer. Additionally, during the practical work a few tools were designed and developed to enhance the device fabrication, amongst which a vacuum pump dedicated to bond the three silicon wafers as structural elements of the prototypes.

The fabricated prototypes were tested in terms of the oscillation mechanism and electrical properties. The influence of the filling ratio and the hot temperature value on the generated signal was established. Additionally, the power range of the prototypes was evaluated. In the last part of the study, optimization steps for the devices developed in the present work were proposed.

L'objectif du présent travail a été de concevoir et de fabriquer des dispositifs sur silicium pour convertir de l'énergie thermique en une énergie électrique en utilisant le changement de phase liquide-gaz dans le but de générer une variation subite de pression suivie d'une conversion d'énergie mécanique vers une énergie électrique à l'aide d'un piézoélectrique. La construction des dispositifs a dû rester simple, avec des matériaux courants et en respectant des limites dimensionnelles. Empreinte inférieure à un diamètre de 20 mm et une épaisseur en dessous des 2 mm.

Les prototypes fabriqués sont composés de 3 plaques en silicium, contenant une chambre d'évaporation, une chambre de condensation et un canal réunissant les deux. Un transducteur piézoélectrique a été reporté sur la chambre de condensation et assure l'étanchéité ainsi que la génération d'énergie électrique.

Le processus de conception inclut plusieurs étapes, dont la définition de la géométrie et du type de fluide de travail utilisé en tant qu'agent thermique. Le travail effectué a permis de sélectionner le type de piézoélectrique, sa taille ainsi que sa méthode d'intégration. Une étude a également été conduite pour déterminer la méthode optimale d'assemblage des plaques en silicium.

La réalisation pratique des dispositifs a été orientée vers la sélection des meilleurs procédés technologiques pour la fabrication des structures. Toutes les expériences ont été conduites en salle blanche avec utilisation de l'oxydation humide, la photolithographie, la gravure KOH, ainsi que d'une technique d'assemblage des plaques silicium avec utilisation de la résine SU-8 comme couche intermédiaire. En plus, quelques outils spécifiques ont été conçus lors du présent travail, pour faciliter la fabrication des dispositifs, dont un système sous vide dédié à l'assemblage des plaques en silicium.

Les dispositifs ont été testés afin d'établir leur mécanisme d'oscillation thermique ainsi que leurs propriétés électriques. L'influence du taux de remplissage et de la température de surface chaude sur le signal en sortie ont également été étudiées. Le calcul de l'énergie générée a aussi été effectué. Dans la dernière partie de l'étude, des étapes d'optimisation pour les dispositifs développés dans le présent travail sont proposées.

Bibliography

- [1] Siemens AG, “Waste Heat Recovery with Organic Rankine Cycle Technology: Power Generation with Siemens ORC-Module,” 2014.
- [2] Energetics Inc. and E3M Inc., “Energy Use, Loss and Opportunities Analysis: : U.S. Manufacturing & Mining,” 2004.
- [3] “Waste Heat Recovery Technology Assessment,” 2015.
- [4] J. Kim, B. L. Grisso, J. K. Kim, D. S. Ha, and D. J. Inman, “Electrical modeling of Piezoelectric ceramics for analysis and evaluation of sensory systems,” *Sensors Appl. Symp.*, 2008.
- [5] G. Fagas, L. Gammaitoni, D. Paul, and G. A. Berini, *ICT - Energy concepts towards zero power information and communication technology*. InTech, 2014.
- [6] P. D. Mitcheson, E. M. Yeatman, G. K. Rao, A. S. Holmes, and T. C. Green, “Energy Harvesting From Human and Machine Motion for Wireless Electronic Devices,” *Proc. IEEE*, vol. 96, no. 9, pp. 1457–1486, 2008.
- [7] A. Khaligh, P. Zeng, X. Wu, and Y. Xu, “A hybrid energy scavenging topology for human-powered mobile electronics,” in *Proceedings - 34th Annual Conference of the IEEE Industrial Electronics Society, IECON 2008*, 2008, pp. 448–453.
- [8] Y. Kheng, *Sustainable Energy Harvesting Technologies – Past , Present and Future*. InTech, 2011.
- [9] “ARM The architecture for the Digital World.”
- [10] N. Salamon, R. Gozdur, M. Turczyński, Z. Lisik, U. Soupremanien, E. Ollier, S. Monfray, and T. Skotnicki, “Case study of piezoelectric flexible thin films in pulse excited electromechanical transducers,” vol. 9291, no. 1, p. 92910M, 2014.
- [11] M. a. Pasha, S. Derrien, and O. Sentieys, “A novel approach for ultra low-power WSN node generation,” *IET Irish Signals Syst. Conf. (ISSC 2010)*, pp. 204–209, 2010.
- [12] T. Torfs, V. Leonov, and R. J. M. Vullers, “Pulse Oximeter Fully Powered by Human Body Heat,” *Sensors Transducers J.*, vol. 80, no. 6, pp. 1230–1238, 2007.
- [13] R. Elfrink, V. Pop, D. Hohlfeld, T. M. Kamel, S. Matova, C. De Nooijer, M. Jambunathan, M. Goedbloed, L. Caballero, M. Renaud, J. Penders, and R. Van Schaijk, “First autonomous wireless sensor node powered by a vacuum-packaged piezoelectric MEMS energy harvester,” *Tech. Dig. - Int. Electron Devices Meet. IEDM*, pp. 543–546, 2009.
- [14] F. Yildiz, “Potential Ambient Energy-Harvesting Sources and Techniques,” *J. Technol. Stud.*, pp. 40–48, 2007.
- [15] S. Priya, “Advances in energy harvesting using low profile piezoelectric transducers,” *J. Electroceramics*, vol. 19, no. 1, pp. 165–182, 2007.
- [16] L. Mateu and F. Moll, “Review of energy harvesting techniques and applications for microelectronics,” *Proc. SPIE 5837 VLSI Circuits Syst. II*, pp. 359–373, 2005.
- [17] H. Vocca and F. Cottone, “Kinetic Energy Harvesting,” *ICT - Energy - Concepts Towar. Zero - Power Inf. Commun. Technol.*, pp. 25–48, 2014.
- [18] S. Boisseau, G. Despesse, and B. A. Seddik, “Electrostatic Conversion for Vibration Energy Harvesting,” *Small-Scale Energy Harvest.*, pp. 1–39, 2012.
- [19] O. Puscasu, “Dispositifs innovants pour la récupération de l’énergie thermique,” PhD Thesis 2014.

BIBLIOGRAPHY

- [20] N. N. H. Ching, G. M. H. Chan, W. J. Li, H. Y. Wong, and P. H. W. Leong, "PCB Integrated Micro-Generator for Wireless Systems," *Proc. Int. Symp. Smart Struct.*, vol. 1, 2000.
- [21] H. Liu, C. J. Tay, C. Quan, T. Kobayashi, and C. Lee, "Piezoelectric MEMS energy harvester for low-frequency vibrations with wideband operation range and steadily increased output power," *J. Microelectromechanical Syst.*, vol. 20, no. 5, pp. 1131–1142, 2011.
- [22] M. Stewart, P. M. Weaver, and M. Cain, "Charge redistribution in piezoelectric energy harvesters," *Appl. Phys. Lett.*, vol. 100, no. 7, 2012.
- [23] L. Dhakar, H. Liu, F. E. H. Tay, and C. Lee, "A new energy harvester design for high power output at low frequencies," *Sensors Actuators A Phys.*, vol. 199, pp. 344–352, 2013.
- [24] C. Mo, L. J. Radziemski, and W. W. Clark, "Experimental validation of energy harvesting performance for pressure-loaded piezoelectric circular diaphragms," *Smart Mater. Struct.*, vol. 19, no. 7, p. 75010, 2010.
- [25] D. F. Berdy, P. Srisungsitthisunti, X. Xu, J. Rhoads, B. Jung, and D. Peroulis, "Compact low frequency meandered piezoelectric energy harvester," *Power MEMS*, pp. 71–74, 2009.
- [26] V. Quaschnig, "Renewable Energy and Climate Change." p. 344, 2010.
- [27] S. Boisseau, *Récupération d'énergie vibratoire à électrets*. PhD Thesis 2011.
- [28] N. Bourgoine, "Harvest Energy from a Single Photovoltaic Cell," *LT J. Analog Innov.*, vol. 21, no. 1, 2011.
- [29] H. Jabbar, Y. S. Song, and T. T. Jeong, "RF Energy Harvesting System and Circuits for Charging of Mobile Devices," *IEEE Trans. Consum. Electron.*, vol. 56, no. 1, pp. 247–253, 2010.
- [30] D. Bouchouicha, F. Dupont, M. Latrach, and L. Ventura, "Ambient RF Energy Harvesting," in *International Conference on Renewable Energies and Power Quality*, 2010, no. January 2016.
- [31] H. Hong, X. Cai, X. Shi, and X. Zhu, "Demonstration of a highly efficient RF energy harvester for Wi-Fi signals," in *Microwave and Millimeter Wave Technology (ICMMT)*, 2012, p. 4.
- [32] J. H. Goldsmid, *Introduction to thermoelectricity*. 2010.
- [33] D. T. Do and Michigan State University, "Thermoelectric generator." .
- [34] G. J. Snyder and E. S. Toberer, "Complex thermoelectric materials," *Nat. Mater.*, vol. 7, no. February, pp. 105–114, 2008.
- [35] N. Mingo, "The nanoparticle in alloy approach to efficient thermoelectrics: silicides in SiGe," *Nano lett.*, vol. 9, no. 711, 2009.
- [36] S. Whalen, M. Thompson, D. Bahr, C. Richards, and R. Richards, "Design , fabrication and testing of the P 3 micro heat engine," *Sensors Actuators A Phys.*, vol. 104, no. 104, pp. 290–298, 2003.
- [37] T. Huesgen, J. Ruhhammer, G. Biancuzzi, and P. Woias, "Detailed study of a micro heat engine for thermal energy harvesting," *Journal of Micromechanics and Microengineering*, vol. 20, no. 10. p. 104004, 2010.
- [38] F. Formosa and L. G. Fréchette, "Scaling laws for free piston Stirling engine design : Benefits and challenges of miniaturization," *Energy*, vol. 57, pp. 796–808, 2013.
- [39] F. Formosa, "MicroStirling preliminary design for power generation and thermal energy harvesting," in *Energy Harvesting Workshop*, 2010.
- [40] J. C. Hsieh, J. L. Lin, S. C. Shen, and T. W. Lin, "The Study of the Enhancement of Micro-Vibration-Induced Harvester based on Vapor Impacting," in *NEMS*, 2013, pp. 3–6.
- [41] S. Khandekar, "Thermo-hydrodynamics of closed loop pulsating heat pipe," University of Stuttgart, Germany, 2004.

- [42] C. Hsu, T. Su, C. Wu, L. Kuo, and P. Chen, "Influence of surface temperature and wettability on droplet evaporation," vol. 141602, no. 2015, 2017.
- [43] Z. Lin, S. Wang, J. Chen, J. Huo, Y. Hu, and W. Zhang, "Experimental study on effective range of miniature oscillating heat pipes," *Appl. Therm. Eng.*, vol. 31, no. 5, pp. 880–886, 2011.
- [44] S. Lips, A. Bensalem, Y. Bertin, V. Ayel, C. Romestant, and J. Bonjour, "Experimental evidences of distinct heat transfer regimes in pulsating heat pipes (PHP)," *Appl. Therm. Eng.*, vol. 30, no. 8–9, pp. 900–907, 2010.
- [45] P. R. Pachghare and A. M. Mahalle, "Thermo-hydrodynamics of closed loop pulsating heat pipe : an experimental study †," vol. 28, no. 8, pp. 3387–3394, 2014.
- [46] J. L. Xu and X. M. Zhang, "Start-up and steady thermal oscillation of a pulsating heat pipe," *Heat Mass Transf. und Stoffuebertragung*, vol. 41, no. 8, pp. 685–694, 2005.
- [47] S. Khandekar, "Multiple Quasi-Steady States in a Closed Loop Pulsating Heat Pipe," pp. 1–35, 2008.
- [48] Y. F. Maydanik, V. I. Dmitrin, and V. G. Pastukhov, "Compact cooler for electronics on the basis of a pulsating heat pipe," *Appl. Therm. Eng.*, vol. 29, no. 17–18, pp. 3511–3517, 2009.
- [49] S. Khandekar, A. Prasad, and P. K. Sharma, "Multiple quasi-steady states in a closed loop pulsating heat pipe," *Int. J. Therm. Sci.*, vol. 48, no. 3, pp. 535–546, 2009.
- [50] T. Skotnicki, "Thermoelectric Generator," 12/911,287, 2011.
- [51] H. Yang, S. Khandekar, and M. Groll, "Performance characteristics of pulsating heat pipes as integral thermal spreaders," *Int. J. Therm. Sci.*, vol. 48, no. 4, pp. 815–824, 2009.
- [52] APC International Ltd, *Piezoelectric Ceramics, Principles and Applications*. 2011.
- [53] C. Zhao, "Fundamentals of Piezoelectricity and Piezoelectric Materials for Ultrasonic Motors," in *Ultrasonic Motors Technologies and Applications*, Springer Publication, 2011, pp. 21–49.
- [54] University of Liverpool, "Piezoelectric Materials and Applications." .
- [55] PI Piezo Technology, *Piezoelectric Ceramic Products, Fundamentals, Characteristics and Applications*. 2014.
- [56] Politechnika Wrocławska Lab. Nowoczesna diagnostyka Materiałowa, "Materiały piezoelektryczne: pomiar prostego i odwrotnego zjawiska piezoelektrycznego," pp. 1–11.
- [57] J. Cheng, B. Wang, and S. Y. Du, "A theoretical analysis of piezoelectric/composite anisotropic laminate with larger-amplitude deflection effect, Part I: Fundamental equations," *Int. J. Solids Struct.*, vol. 42, no. 24–25, pp. 6166–6180, 2005.
- [58] H. J. Lee, S. Zhang, Y. Bar-Cohen, and S. Sherit, "High Temperature, High Power Piezoelectric Composite Transducers," *Sensors*, vol. 14, pp. 14526–14552, 2014.
- [59] Fraunhofer Institute for Ceramic and IKTS Technologies and Systems, "Piezoelektrische komposite und wandler." pp. 2–3.
- [60] Piezo Systems Inc, "Introduction to piezoelectricity," in *Piezoceramic Application Data*, no.8, 2011, pp. 59–61.
- [61] *IEEE Standard on Piezoelectricity*. 1988.
- [62] M. . W. Hooker, "Properties Ceramics of PZT-Based Piezoelectric and 250 ° C," Virginia, 1998.
- [63] E. Léveillé et al., "A microfluidic heat engine based on explosive evaporation," *Power MEMS 2012*, pp. 2–5, 2012.
- [64] T. Monin, A. Tessier-Poirier, E. Léveillé, A. Juneau-Fecteau, T. Skotnicki, F. Formosa, S.

- Monfray, and L. . Fréchette, "First experimental demonstration of a Self-Oscillating Fluidic Heat Engine (SOFHE) with piezoelectric power generation," *J. Phys. Conf. Ser.*, vol. 773, no. 12039, pp. 1–4, 2016.
- [65] U. Soupremanien, "Réalisation de démonstrateurs de récupération d'énergie aptes à être intégrés dans les puces ou architectures 3D de la microélectronique," Grenoble, 2011.
- [66] U. Soupremanien, "Réalisation de démonstrateurs de récupération d'énergie aptes à être intégrés dans les puces ou architectures 3D de la microélectronique," Grenoble, 2012.
- [67] U. Soupremanien, E. Ollier, N. Salamon, S. Monfray, T. Skotnicki, C. E. A. Dtnm, S. Lrme, A. Martyrs, and G. Cedex, "Experimental device designed to obtain repeatable condensation peaks in a close system .," no. 1, pp. 1–12.
- [68] K. Rębilas, "Wyznaczanie współczynnika napięcia powierzchniowego cieczy metodą wznoszenia w kapilarze," Kraków.
- [69] "Multiphase Phenomena." .
- [70] P. Glover, "Fluid Saturation and capillary pressure," in *Petrophysics MSc Course Notes*, pp. 32–54.
- [71] D. Resnik, U. Aljancic, D. Vrtacnik, and S. Amon, "Surface smoothness of anisotropically etched (100) silicon," *Inf. MIDEM*, vol. 23, pp. 10–16, 1993.
- [72] H. Seidel, L. Csepregi, and A. Heuberge, "Anisotropic Etching of Crystalline Silicon in Alkaline Solutions," *J. Electrochem. Soc.*, vol. 137, no. 11, pp. 249–260, 1990.
- [73] Virginia Semiconductor Inc., "Wet-Chemical Etching and Cleaning of Silicon," 2003.
- [74] Y. Yuan and T. R. Lee, "Surface Science Techniques," Berlin, 2013.
- [75] KINO Industry Co, "Work of adhesion and Young-Laplace equation-Theory of surface tension, contact angle, wetting and work of adhesion." .
- [76] E. Gutierrez-Miravete, "Adhesion between Contacting Surfaces," 2009. .
- [77] M. Żenkiewicz, "Analiza głównych metod badania swobodnej energii powierzchniowej materiałów polimerowych," *Polimery*, vol. 52, no. 10, pp. 760–767, 2007.
- [78] M. Lee, D. Lee, N. Jung, M. Yun, C. Yim, S. Jeon, M. Lee, D. Lee, N. Jung, M. Yun, and C. Yim, "Evaporation of water droplets from hydrophobic and hydrophilic nanoporous microcantilevers," vol. 13107, 2011.
- [79] B. Sobac and D. Brutin, "Triple-Line Behavior and Wettability Controlled by Nanocoated Substrates : Influence on Sessile Drop Evaporation," pp. 14999–15007, 2011.
- [80] D. H. Shin, S. H. Lee, J.-Y. Jung, and Y. J. Yoo, "Evaporating characteristics of sessile droplet on hydrophobic and hydrophilic surfaces," *Microelectron. Eng.*, vol. 86, no. 4–6, pp. 1350–1353, 2009.
- [81] L. Grandas, C. Reynard, R. Santini, and L. Tadrist, "Étude expérimentale de l'évaporation d'une goutte posée sur une plaque chauffante. Influence de la mouillabilité," *Int. J. Therm. Sci.*, vol. 44, no. 2, pp. 137–146, 2005.
- [82] S. Franssila, "Introduction to Microfabrication," in *Introduction to Microfabrication*, Second., Chichester, 2010, p. 505.
- [83] J. A. Dziuban, *Technologia i zastosowanie mikromechanicznych struktur krzemowych i krzemowo-szkłanych w technice mikrosystemów*. Wrocław: Oficyna Wydawnicza Politechniki Wrocławskiej, 2002.

- [84] Ucirvine, "Cleaning Procedures for Silicon Wafers Cleanin," no. Di. pp. 2–5.
- [85] M. Wiemer, J. Frömel, C. Jia, and T. Gessner, "Bonding and contacting of MEMS-structures on wafer level," *Proc. Electrochem. Soc.*, pp. 58–60, 2003.
- [86] C. Iliescu and F. E. H. Tay, "Tay' 2," 2005.
- [87] H. Bin Fang, J. Q. Liu, Z. Y. Xu, L. Dong, L. Wang, D. Chen, B. C. Cai, and Y. Liu, "Fabrication and performance of MEMS-based piezoelectric power generator for vibration energy harvesting," *Microelectronics J.*, vol. 37, no. 11, pp. 1280–1284, 2006.
- [88] L. Yu, F. E. H. Tay, G. Xu, B. Chen, M. Avram, and C. Iliescu, "Adhesive bonding with SU-8 at wafer level for microfluidic devices," *J. Phys. Conf. Ser.*, vol. 34, pp. 776–781, 2006.
- [89] M. a. Schmidt, "Wafer-to-wafer bonding for microstructure formation," *Proc. IEEE*, vol. 86, no. 8, pp. 1575–1585, 1998.
- [90] Q.-Y. Tong, E. Schmidt, and U. Ggosele, "Hydrophobic silicon wafer bonding," vol. 64, no. 5, pp. 625–627, 1994.
- [91] G. Kissinger and W. Kissinger, "Void-free silicon-wafer-bond strengthening in the 200-400°C range," *Sensors and Actuators*, vol. 36, no. 2, pp. 149–156, 1993.

List of figures

Figure 1.1: Estimation of energy losses for major energy use areas in manufacturing [2].	3
Figure 1.2: (a) Comb gap-closing and (b) overlap electrostatic energy harvester [17].	6
Figure 1.3: Charge-constrained and voltage-constrained energy conversion cycles for electret-free electrostatic devices [18].	6
Figure 1.4: The model of the magnetic induction transducer [20].	7
Figure 1.5: Simplified configuration of silicon and oxygen ions inside the quartz (a) when there is no stress applied to the crystal; (b) when the crystal is exposed to the stress.	8
Figure 1.6: Design of a piezoelectric energy harvester working in a form of a cantilever beam [23].	9
Figure 1.7: Resonance frequency evolution regarding the circular diaphragm diameter [15].	10
Figure 1.8: The principal structure of a single solar cell [26].	11
Figure 1.9: Time evolution of photovoltaic cells efficiency depending on their fabrication technology [NREL].	12
Figure 1.10: (a) Diverse sources of radio waves [30]; (b) principle of a of typical RF energy harvesting system.	13
Figure 1.11: (a) Principle of Seebeck effect; (b) pn junction thermoelectric generator [33].	15
Figure 1.12: (a) The evolution of Bi ₂ Te ₃ figure of merit zT in a function of dopants concentration; (b) figure of merit of different thermoelectric materials in temperature function [34].	17
Figure 1.13: Cross-section of a unit-cell micro heat engine prototype [36].	18
Figure 1.14: Working cycle of unit-cell micro heat engine [36].	19
Figure 1.15: (a) Open-circuit voltage versus time and (b) power dependence on the load resistance generated by the micro heat engine [36].	19
Figure 1.16: Schematic cross-section of the micro heat engine operating in (a) “down-state” and (b) “up-state”[37].	20
Figure 1.17: The simplified schematic of FPSE geometry [39].	21
Figure 1.18: Schematic cross-section of vapor-generator [40].	22
Figure 1.19: Schematic of (a) an open loop without a flow check valve and (b) a closed loop with a flow check valve; (c) operation mechanism of PHP [41].	23
Figure 1.20: Simplified cross-section of the thermoelectric device.	25
Figure 1.21: Operating principle of the invention.	25
Figure 2.1: Mechanism of (a) direct piezoelectric effect – piezoelectric element responding to an external force; (b) inverse piezoelectric effect – piezoelectric element responding to an external electric field [53].	28
Figure 2.2: Crystal structure of a piezoelectric ceramics (a) above Curie temperature – symmetrical, cubic Perovskite structure; (b) below Curie temperature – tetragonal structure with electric dipole.	30
Figure 2.3: (a) Unpolarized dipoles in ferroelectric domains when no electric field is being applied; (b) reorientation of the domains in the strong electric field; (c) remnant polarization after the removal of the electric field [55].	31
Figure 2.4: (a) Electromechanical behavior of the longitudinal strain, S, as a function of the electric field, E; (b) influence of the electric field, E, on the polarization, P, of a piezoelectric ceramics [55].	31
Figure 2.5: Piezoelectric ceramics (a) before poling; (b) after poling; (c) after compression along the poling direction; (d) after tension along the poling direction.	32
Figure 2.6: Piezoelectric ceramic (a) after poling; (c) after compression along the poling direction; (d) after tension along the poling direction.	33
Figure 2.7: Stress modes of piezoelectric ceramics [60].	37
Figure 3.1: (a) Experimental setup developed to investigate the response of piezoelectric elements working under the pressure excitation pulse; (b) test chamber with pressure control element; (c) interior of the chamber with the removable clamping support containing a piezoelectric element.	42
Figure 3.2: Diaphragm containing (a) two PVDF cantilevers; (b) PVDF membrane operating in strain mode; (c) PZT operating in stress mode; (d) PZT operating as a membrane in strain mode.	43
Figure 3.3: (a) Photographs of clamping system designed at TUL; dimensions of the clamping system for PZT-based elements of (b) 12 mm; (c) 20 mm and (d) 27 mm diameter.	44

Figure 3.4: (a) Schematic cross-section of pressure chamber and a photograph of clamping system designed in CEA-Liten; clamping system for (b) 7BB-12-9; (c) 7BB-20-6 and 7BB-20-3; (d) 7BB-27-4.	44
Figure 3.5: Changes of pressure Δp inside the chamber and piezoelectric voltage changes for the cantilevered PVDF with a thickness of (a) 28 μm ; (b) 52 μm and (c) 110 μm	46
Figure 3.6: Maximum value of voltage $V_{P\text{max}}$, power, P , generated by cantilever transducer during single excitation pulse of maximum $\Delta p = 3$ bar, for three different thicknesses of PVDF.	47
Figure 3.7: Voltage dependence on the value of pressure introduced to the chamber.	48
Figure 3.8: 52 μm PVDF membrane after a contact with pressure of (a) 0.7 bar; (b) 2.5 bar; (c) 3.5 bar.	48
Figure 3.9: Specimen (a) at the beginning; (b) during elongation; (c) after rupture.	49
Figure 3.10: Stress-strain curve of the 52 μm , PVDF strip at tensile test.	50
Figure 3.11: Piezoelectric voltage generated by 52 μm thick PVDF membrane; (a) elastic region; (b) strain hardening region; (c) rupture.	51
Figure 3.12: Voltage signal generated by 52 μm thick PVDF membrane exposed to a pressure pulse of (a) 0.3 bar and (b) 1 bar.	51
Figure 3.13: (a) Top view and (b) cross-section of PZT diaphragm, where R_p and R_s are the radiuses of piezoelectric and substrate respectively and t_p and t_s are their thicknesses; (c) photograph of different-sized PZT elements.	53
Figure 3.14: Dielectric constant versus temperature data for (a) PZT-4; (b) PZT-5A; (c) PZT-5H and (d) PLZT-9/65/35 [62].	54
Figure 3.15: Changes of pressure Δp inside the chamber and piezoelectric voltage for the PZT-based elements (a) 7BB-12-9; (b) 7BB-20-3; (c) 7BB-20-6 and (d) 7BB-27-4 operating in stress mode.	56
Figure 3.16: Mean values of piezoelectric voltage versus pressure for PZT ceramics operating in a stress mode.	57
Figure 3.17: Maximum value of voltage $V_{P\text{max}}$, power, P , generated by PZT-based transducers operating in a stress mode during one pressure pulse of 300 mbar.	58
Figure 3.18: Piezoelectric voltage as a function of pressure generated by (a) 7BB-12-9, (b) 7BB-20-6, (c) 7BB-20-3 and (d) 7BB-27-4 obtained at Lodz University of Technology (red) and at CEA-Liten (blue).	58
Figure 3.19: Mean values of piezoelectric voltage versus pressure for PZT ceramics operating in strain mode, measured a TUL.	59
Figure 3.20: Changes of pressure Δp inside the chamber and piezoelectric voltage for the PZT-based elements (a) 7BB-12-9; (b) 7BB-20-3; (c) 7BB-20-6 and (d) 7BB-27-4 operating in strain mode.	59
Figure 3.21: Maximum value of voltage $V_{P\text{max}}$, average power, P , generated by PZT-based transducers operating in strain mode, during one pressure pulse of 300 mbar.	60
Figure 3.22: The boundary conditions for the ideal case, when the real clamping method is not considered.	62
Figure 3.23: (a) Initial boundary conditions referred to the diameter of whole PZT element, D ; (b) experimental conditions; (c) modified boundary conditions corresponding to the diameter of active area, D_1 and the diameter of the surface that was exposed to pressure D_2	62
Figure 3.24: The boundary conditions, when the real clamping method is considered.	63
Figure 3.25: Comparison between values of voltage generated by PZT elements as a response to pressure variations obtained experimentally and as a results of simulations for (a) 7BB-12-9; (b) 7BB-20-6; (c) 7BB-20-3 and (d) 7BB-27-4.	63
Figure 3.26: Schematic representation of tightening methods in (a) ideal and (b) real case.	64
Figure 3.27: Piezoelectric voltage V_p as a function of pressure p for 7BB-20-6; (b) Piezoelectric voltage V_p as a function of piezoelectric thickness t_p at a constant substrate geometry value of pressure $p = 100$ mbar; (c) Piezoelectric voltage V_p as a function of piezoelectric radius R_p at a constant substrate geometry and a value of pressure $p = 100$ mbar.	65
Figure 3.28: Electric potential V as a function of applied of pressure p for two diaphragms with different sizes.	66
Figure 3.29: Electric potential V as a function of thickness of piezoelectric element t_p for constant thickness of the whole element $t_{\text{tot}} = 0.42$ mm.	66
Figure 3.30: Electric potential V as a function of applied pressure p for three diaphragms with identical thicknesses t but different radiuses R	67

List of figures

Figure 3.31: Electric potential V as a function of applied pressure p for (a) element 7BB-20-6 (blue line) and element with modified dimensions in a way that $t_p = 64\% t_{tot}$ (red line); (b) element with modified thickness in a way that $t_p = 64\% t_{tot}$ (red line) and element with smaller radius of PZT and substrate (green line); (c) element with modified thickness in a way that $t_p = 64\% t_{tot}$ (red line), element with smaller radius of PZT and substrate, (green line), and element with smaller total thickness.	68
Figure 3.32: Electric potential V as a function of applied pressure p for element with total thickness t_{tot} of 0.27 mm and diameter D of 18 mm (purple line) and for element with total thickness t_{tot} of 0.42 mm and diameter D of 20 mm (blue line).	69
Figure 4.1: (a) Schematic cross-section and (b) a photograph of microfluidic heat engine [63].	72
Figure 4.2: Phases of a cycle represented by a piezoelectric signal of one pulse [63].	72
Figure 4.3: Influence of (a) the water flow rate on power, frequency and amplitude values of the generated signal, at constant temperature equal to $130 \pm 10^\circ\text{C}$; (b) the hot temperature on power, frequency and amplitude values of the generated signal, at a constant water flow rate equal to $10 \mu\text{l/min}$ [63].	73
Figure 4.4: Self-Oscillating Fluidic Heat Engine [64].	74
Figure 4.5: Oscillation start-up regime: no oscillations up to $t = 1$ s; transient regime at a time range between 1 s and 3 s; stabilization of meniscus oscillations' amplitude starting from the third second of the operation [64].	75
Figure 4.6: Piezoelectric bimorph spiral electromechanical transducer [64].	75
Figure 4.7: (a) P-V diagram of a free-loaded SOFHE thermo-fluidic oscillator; (b) SOFHE voltage output in a $1 \text{ M}\Omega$ load [64].	76
Figure 4.8: Schematic cross-section of the device.	76
Figure 4.9: (a) Schematic cross-section and (b) a photograph of the prototype [65].	77
Figure 4.10: Voltage signal generated by the system versus time at heat flux equal to 3970 W/m^2 [66].	78
Figure 4.11: (a) Electronic circuit composed of Schottky diodes of threshold voltage equal to 550 mV ; (b) charging curve of a capacitor [66].	78
Figure 4.12: The volume of the device decreased 6 times [66].	79
Figure 4.13: Voltage signal generated by the device operating (a) with and (b) without metal sphere at heat flux equal to 3955 W/m^2 and the power of a cooling fan equal to 0.6 W	79
Figure 4.14: Cross-section of a single cell of the harvester comprising the evaporation and condensing chambers, a channel and a piezoelectric layer.	80
Figure 4.15: Stages of one cycle of the process: (a) the device filled with before the heating process; (b) evaporation of the fluid; (c) gas condensation; (d) return of the liquid to the evaporation chamber.	81
Figure 4.16: (a) Value of boiling temperature and (b) mass density ratio for various liquids at atmospheric pressure.	82
Figure 4.17: Pressure changes inside the system of 2 mm channel at the temperature (a) $THOT = 154^\circ\text{C}$ and (b) $THOT = 170^\circ\text{C}$	84
Figure 4.18: Forces distribution in the device for wetting water that ensures a contact angle between liquid and a channel surface lower than 90°	86
Figure 4.19: Pressure changes inside the system of 3 mm channel at hot temperature equal to (a) $THOT = 116^\circ\text{C}$ and (b) $THOT = 146^\circ\text{C}$; for 4 mm channel at the temperature (c) $THOT = 113^\circ\text{C}$ and (d) $THOT = 141.4^\circ\text{C}$ [65].	87
Figure 4.20: Influence of the hot temperature on the oscillation frequency for (a) 3 mm and (b) 4 mm channel [65].	88
Figure 4.21: Schematic of the devices used for the experiments; (a) D1; (b) D2 [67].	89
Figure 4.22: Pressure variations with stopovers versus time for D2 and $\alpha = 12.41\%$ at $Thot = 130.6^\circ\text{C}$ [67].	90
Figure 4.23: Volume impact on pressure amplitude and oscillations frequency for (a) D1 and (b) D2 at $Thot = 130^\circ\text{C}$ [67].	90
Figure 4.24: Filling ratio impact on oscillating behavior [67].	90
Figure 4.25: (a) Pressure signature evolution with the increase temperature increase; (b) impact of the hot temperature on the oscillations behavior for $\alpha = 12.41\%$ for D2 [67].	91
Figure 5.1: (a) Class 10000 main room and (b) class 100 photolithography section (b) of clean room laboratory of the Department of Semiconductor and Optoelectronics Devices at Lodz University of Technology.	95

Figure 5.2: Chamber etched in Si wafer by DRIE	97
Figure 5.3: Process flow of KOH etching: (a) Si wafer after cleaning procedure; (b) wet oxidation; (c) photoresist deposition; (d) photoresist development; (e) SiO ₂ etching and photoresist removal; (f) Si etching with KOH solution; (g) etched Si structure after KOH process; (h) Si structure after SiO ₂ removal.	98
Figure 5.4: The dependence of Si <100> and Si <110> etch rate on (a) process temperature at a constant 30% KOH concentration; (b) percent weight of KOH in the solution at a constant temperature of 70°C.	99
Figure 5.5: Surface of the silicon wafer containing chambers and channels etched in 30% KOH concentration, for <100> Si at the temperature of (a) 80°C and (b) 70°C.	100
Figure 5.6: Thickness of the etched Si and SiO ₂ dependence of the process time at (a) 70°C and (b) 80°C.	101
Figure 5.7: Surface of the silicon wafer containing chambers etched in the 30% KOH solution, for <110> Si at the temperature of (a) 70°C and (b) 80°C.	102
Figure 5.8: Thickness of etched Si and SiO ₂ dependence of the process time at (a) 70°C and (b) 80°C.	102
Figure 5.9: Surface wettability at (a) initial, unstable state; (b) equilibrium state [70].	103
Figure 5.10: Contact angles formed by liquid droplets on (a) hydrophilic; (b) neutral and (c) hydrophobic surface [74].	104
Figure 5.11: Unbalanced forces of liquid molecules at the solid surface [74].	104
Figure 5.12: Water distribution inside the system of the contact angle θ close to (a) 70° and (b) 10°.	106
Figure 5.13: Si wafer containing (a) evaporation chambers; (b) channels and (c) condensing chambers; (d) cross-section of the three Si wafers after the bonding process.	106
Figure 5.14: Technological steps of SU-8 bonding process: (a) spinning of SU-8 photoresist on 4" Si wafer; (b) transfer of SU-8 from Si wafer onto Teflon cylinder; (c) transfer of the adhesive layer from the cylinder to a wafer containing evaporation chambers; (d) a structure with channels brought in contact with the wafer containing evaporation chambers, covered with SU-8 and placed inside a pressure chamber; (e) transfer of SU-8 onto a wafer with condensing chambers; (f) all three layers brought in contact and placed inside the pressure chamber.	109
Figure 5.15: Cross-section of three Si wafers bonded by a layer of SU-8 photoresist.	110
Figure 5.16: Process flow of silicon energy harvester fabrication: (a) wafers preparation; (b) wet oxidation; (c) photoresist deposition; (d) photoresist exposure to a pattern of intense light; (e) development of photoresist; (f) SiO ₂ etching in NH ₄ F-HF; (g) Si etching in KOH solution; (h) hydrophilisation and bonding of the wafers; (i) montage of piezoelectric element to a surface of Si wafer.	112
Figure 6.1: (a) SEM picture of the device's cross-section; (b) schematic of the device.	114
Figure 6.2: (a) Top view of the Si structure with an adhesive layer applied around the condensing chamber as well as of small-sized and large-sized PZT; (b) cross-sections of two Si structures – one covered with small another with large PZT.	118
Figure 6.3: Experimental setup – (a) DF1743005C NDN generator; (b) Extech Instruments SDL 200 data acquisition system; (c) digital hotplate SD 160; (d) Aluminum cylinder; (e) heatsink with a fan; (f) Digital Oscilloscope (Rigol DS1054Z).	121
Figure 6.4: Photograph of (a) main elements of experimental bench and (b) prototype of the silicon device covered with PZT-based element; schematic representation of (c) experimental setup elements and (d) cross-section of silicon device prototype.	121
Figure 6.5: Changes of the voltage, v_p , and the hot temperature, T_H , over time, for $\alpha = 10\%$, (a) when no oscillations occur and (b) at the beginning of oscillations.	123
Figure 6.6: Changes of the voltage, v_p , and the hot temperature, T_H , over time, for $\alpha = 10\%$, (a) when no oscillations occur, (b) after one minute, (c) one hour and (d) two hours of continuous signal.	124
Figure 6.7: Changes of the voltage, v_p , and the hot temperature, T_H , over time, for $\alpha = 10\%$, at the end of oscillations, after four hours of continuous operation.	124
Figure 6.8: Changes of the voltage v_p and the hot temperature T_H over time, for $\alpha = 20\%$, (a) at the beginning of oscillations, (b) after one hour and (c) two hours of continuous signal.	125

List of figures

Figure 6.9: Changes of the voltage v_p and the hot temperature T_H over time, for $\alpha = 20\%$, (a) before, (b) at the beginning, (c) after 20 min and (d) after 30 min of the oscillations.	126
Figure 6.10: The breaks between the oscillations observed at the temperatures higher than 130°C for the devices filled with $10\ \mu\text{l}$ of water ($\alpha = 20\%$).	126
Figure 6.11: Changes of the voltage v_p and the hot temperature T_H over time, for $\alpha = 30\%$, (a) at 121°C after 1 min, (b) at 126°C , after 45 min of continuous operation.	127
Figure 6.12: Changes of the voltage v_p and the hot temperature T_H over time, for $\alpha = 30\%$, (a) at 131°C after 1 min, (b) at 134°C , after 2.5 min of continuous operation.	127
Figure 6.13: Changes of (a) the amplitude, V , and the frequency, f ; (b) the power, P , in relation to the filling ratio, α , for the range of low temperatures.	129
Figure 6.14: Changes of (a) the amplitude, V , and the frequency, f ; (b) the power, P , in relation to the filling ratio, α , for the range of high temperatures.	129
Figure 6.15: Changes of the voltage v_p and the hot temperature T_H over time, for $\alpha = 30\%$, (a) before, (b) at the beginning of the oscillations for the device operating without cooling fan.	130
Figure 6.16: Changes of the voltage v_p and the hot temperature T_H over time, for $\alpha = 30\%$, (a) after 30 min and (b) after 240 min of the oscillations for the device operating without cooling fan.	130
Figure 6.17: (a) Photograph of two Si wafers containing nine evaporation or condensing chambers and 4 mm thick layer of glass, with nine channels drilled through; (b) nine structures before cutting; (c) four independent cells cut out by flow water jet; (d) schematic cross-section of one cell of the harvester.	131

List of tables

Table 1.1: Examples of energy sources depending on the type of provided energy.....	5
Table 1.2: Luminous power density and electric power density provided by a single solar cell with 15% of efficiency [27].	11
Table 1.3: Electric power density provided by different energy transducers.	14
Table 2.1: Examples of typical applications of piezoelectric materials [54].	29
Table 3.1: Electromechanical parameters of tested PVDF films.	45
Table 3.2: Values of maximum piezoelectric voltage V_{Pmax} , and power, P , for cantilevered transducers of three different thicknesses.	46
Table 3.3: Mean voltage, $V_{Pmax}(AVG)$, and its standard deviation, σ , for different values of pressure inside the chamber.	48
Table 3.4: Maximum piezoelectric voltage V_{Pmax} , power, P , generated by membraned PVDF under the influence of two different pressure values.	52
Table 3.5: Maximum piezoelectric voltage V_{Pmax} , power, P , generated by cantilevered and membraned PVDF under the influence of two different pressure values.	52
Table 3.6: Dimensional parameters of tested PZTs.	53
Table 3.7: Geometrical parameters, measured capacitance, C_m , and calculated relative permittivity, ϵ_r , of tested PZT elements.	55
Table 3.8: Typical properties of different PZT-based ceramics at temperature of 25°C [62].	55
Table 3.9: Geometrical parameters of tested PZT elements, values of maximum piezoelectric voltage V_{Pmax} , and power, P , generated in the stress mode, under the pressure of 300 mbar.	57
Table 3.10: Geometrical parameters of tested PZT elements, values of maximum piezoelectric voltage V_{Pmax} , and power, P , generated in stress mode, under the pressure of 300 mbar.	60
Table 3.11: Maximum piezoelectric voltage V_{Pmax} , average power, P , generated by PZT-based transducers operating in stress and strain mode, when they were exposed to the 300 mbar pulse of pressure.	61
Table 3.12: Comparison of the values of voltage and power generated in response to 300 mbar pressure pulse by PVDF and PZT materials operating in different modes.	61
Table 4.1: Frequency and amplitude of the signal generated by large and small device for different operation modes.	80
Table 4.2: Boiling temperature T_B , liquid and volume densities ρ_l , ρ_v and ratio of mass densities ρ_l/ρ_v at atmospheric pressure.	83
Table 4.3: Comparison of devices geometry [67].	89
Table 5.1: Parameters of the etching process used in four experiments, etch rates of SiO_2 and Si for tested temperatures and concentrations of KOH; time required to etch through a 390 μm thick Si wafer and to consume 1.7 μm layer of SiO_2 mask.	103
Table 5.2: Technological steps for cleaning and hydrophilisation of Si wafers.	107
Table 5.3: Types and parameters of tested adhesives.	110
Table 6.1: Dimensional parameters of tested PZT.	117
Table 6.2: Oscillations occurrence depending on hot surface temperature, T_H	119
Table 6.3: Oscillations occurrence depending on filling ratio, α	119
Table 6.4: Summary of parameters selected for the experiments.	120
Table 6.5: Values of filling ratio α , liquid volume V_l and hot temperature T_H applied in experiments.	122
Table 6.6: Summary of the results.	128